HYBRID MATERIALS DESIGN TO CONTROL CREEP IN PIPES

A thesis

submitted in partial fulfillment

of the requirements for the Degree of

DOCTOR OF PHILOSOPHY IN MECHANICAL ENGINEERING

IN THE

UNIVERSITY OF CANTERBURY

by

BENJAMIN PETER REYNGOUD

University of Canterbury

2015

PREFACE

This thesis is submitted as a partial requirement for the degree of Doctor of Philosophy in Mechanical Engineering in the University of Canterbury. This research was conducted under the supervision of Senior Supervisor Professor Milo V. Kral and Co-Supervisor Dr. Catherine M. Bishop in the Mechanical Engineering Department, University of Canterbury, between March 2010 and April 2015.

ACKNOWLEDGEMENTS

I would like to acknowledge the following people and organizations that have made this research work possible:

- My supervisor, Professor Milo V. Kral, for presenting me with this research opportunity, for technical and personal support throughout, and for always expecting the best from me.

- My co-supervisor, Dr Catherine M. Bishop, for her eagerness, patience and dedication to providing technical insight and thoughtful feedback.

- The generous financial support of Schmidt+Clemens (Spain) S.A.U. and Methanex NZ, as well as the enthusiasm and industry insight from Peter Tait (Methanex) and Pedro Imizcoz Goni (Schmidt+Clemens).

- Members of the Materials Engineering Group (MEG): Dr. Mark Staiger, Dr. Takanori Sato, Emeritus Professor Les Erasmus, Mike Flaws and Kevin Stobbs; MEG visitors Dr. Chris Hutchinson, Dr. Norman Dowling and Dr. Anthony Petrella; in addition to fellow MEG students for all their questions, critical thought, and for the gift of perspective.

- Professor Yves Bréchet, for his generous invitation to the ArchiMat workshop and willingness to share his insight into architectured materials.

- The administrative and technical staff of the Mechanical Engineering Department; in particular Julian Phillips, Scott Amies and Ken Brown for their wizardry and kind assistance.

- The people of Christchurch for weathering the trials presented by earthquakes, and responding with courage and resilience.

- To my family, for their love, prayers and encouragement.

- To my wife, Devon, for your sunshine which cuts through the gloom, stress and anxiety. Your love and support lifted me up, and reminded me what a tremendous accomplishment this PhD is.

- And greatest of all, to the Lord God, for setting everything in place and for giving meaning to life.

"You are worthy, our Lord and God, to receive glory and honour and power, for you created all things, and by your will they were created and have their being."

– Revelation 4:11

ABSTRACT

A hybrid material design has been developed to improve creep performance in pressurized metallic pipes subjected to high temperatures. Metallic pipes were reinforced with various arrangements of external wires which have substantially greater creep resistance than the pipe material. This research was conducted to explore the field of reinforcement of piping for creep reduction, exploit the creep strength of refractory metals, and investigate structure-property relationships in architectured materials.

Two basic wire reinforcement architectures were tested, simple helical windings and braided sleeves. By adjusting the architecture of the reinforcement, apparent tangential (hoop) and longitudinal stresses on the pipe are altered, thereby allowing multiaxial creep strains to be controlled.

The utilization of a reinforcement layer in a *hybrid* layup, where it is not bonded or embedded in a matrix is a relatively unexplored field. Hybridization allows the most desirable properties to be extracted from each component and have them work together in parallel. The use of *braided refractory* reinforcement is also a particularly novel concept, with refractory materials for reinforcement purposes traditionally being utilized in particle, whisker and discontinuous fibre form. Rather than testing in a uniaxial stress state, the present approach to creep testing *pressurized pipes at high temperature* remains largely underutilized, and is especially relevant to industry applications where creep takes place in the complex, multiaxial stress state of a pressurized pipe.

In a low-temperature reinforcement architecture optimization study of a brass-stainless steel system, designed for ease of fabrication and to negate oxidation issues, pipes were pressurized and creep rupture tested at 400°C. Even in an unoptimized state, braided reinforcement was observed to out-perform a simple

helical wrap by at least 22%, giving a 10-times life extension without rupture, and a reduction in creep rate in excess of 45-times for reinforcement oriented at a 50°.

A simple analytical model from reinforced pressure vessel theory predicts a neutral angle (θ_N) of 54.7°, at which point the reinforcement is oriented to act proportionally to the applied pressure stresses. An empirical model of effective creep rate with varying reinforcement angle was derived in the present study, and used to find that a braid angle of approximately 54.7±1.5° is optimal to minimize the effective multiaxial creep rate of a hybrid pipe under internal pressure, reducing it to the point of being negligible.

The braided reinforcement was observed to be constantly shifting towards the equilibrium point of θ_N, but only for initial angles below θ_N. This concept of braid reorientation is generally associated with rapid elastic deformation or static reinforcement of systems at room temperature, and the gradual shift towards θ_N facilitated by creep deformation has not been reported previously. A relationship for $\dot{\varepsilon}$-θ (i.e. creep rate for a given reinforcement angle) was derived, including the reduction in $\dot{\varepsilon}$ as θ tends to θ_N.

Findings of this optimization study were applied to a high temperature system which served as an acceleration of reformer furnace operating conditions: 253MA pipes were reinforced with tungsten wire and creep rupture tested at 1030-1040°C. Using braided reinforcement oriented at 52.6±1.4° a life extension in excess of 700x was observed, with no signs of bulk deformation after a 309x life extension. These high temperature results were considered in light of the intended industry application, with a balance of life extension, weight reduction and increased operating temperature preferred over outright life extension for the reformer furnace application.

TABLE OF CONTENTS

CHAPTER 1: INTRODUCTION 1

1.1.1 Potential applications 1

1.1.2 Methanol production 4

1.1.3 Tests performed 5

1.2 Project Motivations 5

1.3 Research Objectives 7

1.4 Layout of Thesis 8

1.5 Research Achievements 10

1.6 Novel Contributions 11

CHAPTER 2: BACKGROUND 17

2.1 Hybrid Tube Concept 17

2.1.1 Hybridization 17

2.1.2 Testing approach 19

2.1.3 Creep reinforcement 21

2.2 Methanol Production 22

2.3 Reformer Tubes 26

2.3.1 Stress analysis 27

2.3.2 Material overview 29

2.3.3 Damage mechanisms 33

CHAPTER 3: LITERATURE REVIEW 37

3.1 Architectured Materials 37

3.1.1 Materials design techniques 38

3.1.2 Performance indices for creep 40

3.2 Reinforced Pressure Vessels 43

3.2.1 High temperature pressure vessels 44

3.3 Neutral Angle 45

3.3.1 Neutral angle derivation 45

3.3.2 McKibben actuators 51

3.3.3 Biological systems 54

3.4 Structure-Property Relationships 57

3.4.1 Braid stiffness from classical lamination theory 58
3.4.2 Wrap stiffness from spring constant 62
3.5 Creep 64
3.5.1 Creep mechanisms 67
3.5.2 Creep in a complex stress state 70
3.5.3 Multiaxial creep testing 71
3.5.4 Solutions against creep at high temperature 73
3.6 Refractory Creep Reinforcement 74
3.6.1 High temperature performance 76
3.6.2 Intermetallic formation 82
3.6.3 Oxidation 84

CHAPTER 4: REINFORCEMENT ARCHITECTURE STUDY 93
4.1 Methodology 93
4.1.1 Life prediction of unreinforced materials 93
4.1.2 Model pipe material selection 95
4.1.3 Reinforcement Architecture 97
4.1.4 Longitudinal stiffness measurement 100
4.1.5 Pressurized pipe tests 102
4.2 Results and Discussion 106
4.2.1 Longitudinal stiffness measurement 106
4.2.2 Pressurized pipe tests 108
4.2.3 Stiffness analysis 116
4.2.4 Creep strain rate analysis 119
4.3 Conclusions 135

CHAPTER 5: IN-SITU LONGITUDINAL CREEP STRAIN MEASUREMENT 139
5.1 Expected Trends 140
5.2 Methodology 143
5.2.1 Apparatus 143
5.2.2 Pressurized pipe tests 147
5.3 Results and Discussion 150
5.3.1 Control rupture life and total strain comparison 150
5.3.2 Steady state creep rate of the unreinforced pipes 152

5.3.3 Creep rate behaviour of the reinforced pipes 159
5.3.4 Reinforcement engagement theory 171
5.4 Conclusions 175

CHAPTER 6: HIGH TEMPERATURE HYBRID SYSTEM 179
6.1 Proof of Concept 179
6.2 Simple Tungsten Reinforcement 181
6.2.1 Design of experiment 182
6.2.2 Results and discussion 187
6.2.3 Preliminary conclusions from proof of concept testing 192
6.3 Braided Tungsten Reinforcement 193
6.4 Methodology 194
6.4.1 Life prediction of unreinforced materials 197
6.4.2 Materials selection 198
6.4.3 Hybrid pipe architecture 199
6.5 Results and Discussion 200
6.5.1 Life extension and damage analysis – unoptimized braid test 200
6.5.2 Life extension and damage analysis – optimized braid test 205
6.5.3 Microstructural analysis 212
6.5.4 Secondary damage mechanisms 217
6.6 Conclusions 226

CHAPTER 7: IMPLICATIONS FOR INDUSTRY 229
7.1 Balance Between Life and Temperature 229
7.2 Critical Flaw Size 232
7.3 Long-Term Effects in Reformer Application 232
7.4 Additional Stresses in Reformer Application 236
7.5 Thermal Conductivity 237
7.6 Comparison with Existing Technology 242
7.7 Conclusions 245

CHAPTER 8: SUMMARY AND CONCLUDING REMARKS 251
8.1 Summary of Achievements 251
8.1.1 Multiaxial strain measurement 251
8.1.2 Reinforcement architecture 252

8.1.3 Effective creep rate model 252
8.1.4 Change in braid angle 253
8.1.5 Effect of reinforcement 254
8.1.6 Industry implications 255
8.2 Concluding Remarks 256
8.3 Future Work 258
8.3.1 Tangential creep rate measurement 259
8.3.2 Suppression of intermetallic formation 259
8.3.3 Reformer furnace conditions 261
8.3.4 Reformer-sized braid 261
8.3.5 Counterweights 262
8.3.6 Additional creep tests 263
8.3.7 Modifications to creep testing apparatus 264

Appendix A: PUBLICATIONS 267

LIST OF FIGURES

Figure 2.1. Possibilities of hybridization. Adapted from Ashby [8]..... 18
Figure 2.2. Hybrid tube schematic. 19
Figure 2.3. Schematic of pipe rupture testing apparatus. 20
Figure 2.4. Principal uses of methanol. Adapted from [25-28]. 23
Figure 2.5. Simplified schematic of the methanol manufacturing process. Adapted from Methanex Corporation, 2011 [29]..... 24
Figure 2.6. Cylindrical coordinate system for tubular pressure vessel..... 28
Figure 2.7. Reformer tube stress state resulting from internal pressure, expressed as a function of position in wall from inner radius (r_i) = 50mm to outer radius (r_o) = 60mm..... 29
Figure 2.8. *Timeline of reformer tube material development [38].* 30
Figure 2.9. Stress-rupture plot for 100,000 hour rupture lives for various reformer alloys. Adapted from Beyer et al. [39] to include 253MA. 32
Figure 3.1. Resistivity and reciprocal of tensile strength for 1700 metals and alloys, seeking to find a material which minimizes both. Clear 'hole' in the property space, filled by copper-steel hybrid [11]. 39
Figure 3.2. Young's modulus plotted against density, identifying a hole in property space for low density materials with high stiffness. Adapted from [7]..... 40
Figure 3.3. Free body diagram for neutral angle derivation over a unit length of a filament-reinforced pressure vessel. 46
Figure 3.4. Longitudinal section of reinforced pressure vessel, allowing tangential stresses to be balanced against wire tensions in the tangential direction. 47
Figure 3.5. Circumferential section of reinforced pressure vessel, allowing longitudinal stresses to be balanced against wire tensions in longitudinal direction. 48
Figure 3.6. McKibben actuator – cylindrical flexible tube surrounded by a braided shell [21]. 51

Figure 3.7. Axial tension in a McKibben actuator as a function of braid angle. Note axial tension is zero at the neutral angle of 54.7°. 54
Figure 3.8. (a) Unit length of a cylindrical 'worm' bounded by a single turn of the geodesic fibre system (fibres running in the opposite sense have been omitted for clarity) (b) the same unit length of worm slit along the top and flattened out (c) curve representing the theoretical relationship between the volume contained by the fibre system and the inclination of the fibres to the longitudinal axis. Points of intersection, F and G, are the limiting positions of elongation and contraction for the particular species of worm. (d) effect of fibre angle on length of a helical fibre wrapping a constant volume cylinder. Adapted from [26, 27]. 56
Figure 3.9. Braid sectional schematic (a) Overall braid schematic for section in x' plane (b) yarn cross sectional shape with individual wire strands shown. 58
Figure 3.10. Schematic of single lamina coordinate systems, global (x-y) coordinates and local (1-2) coordinates 59
Figure 3.11. Simple schematic of 2-ply laminate 61
Figure 3.12. Axial spring schematic. 63
Figure 3.13. Projected sectional area of wire wrap in tension test. 64
Figure 3.14. Typical creep curve showing the three stages of creep. 65
Figure 3.15. Creep rupture plots for 253MA (a) secondary creep rate data (b) creep rupture life data [39] 66
Figure 3.16. Deformation mechanism map for type 316 stainless steel [40]. 68
Figure 3.17. Schematic of classical ring test [42]. 71
Figure 3.18. Schematic of optimized ring testing system and notched ring specimen [42]. 72
Figure 3.19. Larson-Miller parameter normalization for time to 1% creep for refractory metal alloys [74]. Note that Cb refers to Columbium, now more commonly referred to as Niobium (Nb). 78
Figure 3.20. 100 hour rupture strength versus homologous temperature for refractory metals in the recrystallized condition [75]. 79

Figure 3.21. Typical creep stress-rupture behaviour of tungsten wire 0.127mm in diameter, as-drawn [76]. 80
Figure 3.22. Tungsten-nickel phase diagram [85]. 83
Figure 3.23. Tungsten-iron phase diagram [89]. 84
Figure 4.1. Brass tube stress state as a function of position in wall from inner radius (r_i) = 11.48mm to outer radius (r_o) = 12.70mm. 95
Figure 4.2. Cu-Zn phase diagram [3]. 96
Figure 4.3. Creep rupture curve for 70-30 alpha-brass. Adapted from Evans and Wilshire [4]. 97
Figure 4.4. Reinforcement configurations tested (a) 0.4mm diameter wire wrap (b) C-65° (c) F-50° (d) F-42° (e) C-36° 98
Figure 4.5. Braid tensile sample, held in MTS by customized grips. 101
Figure 4.6. Partially disassembled braid grips. Braid pulls over tube and internal component of grip, which clamps to outer grip component via central bolt. Tension is then applied to braid without stressing the inner tube. 101
Figure 4.7. Temperature profile in tube furnace set to 400°C. 103
Figure 4.8. CMM probe positioned above tube sample. 105
Figure 4.9. Stress-strain curves for braids in tension. Longitudinal stiffness values determined for period where reinforcement is fully engaged (E_z)..... 107
Figure 4.10. Cracks and impressions present in pipes after rupture (reinforcement removed). (a) longitudinal crack in control pipe (b) circumferential crack in wrap-reinforced pipe and impression left by helical winding (c) midpoint of C-36° sample (d) superficial markings at end of C-36° sample. 110
Figure 4.11. Metallographic sample, sectioned from midspan of C-36° pipe. 111
Figure 4.12. Mean tangential creep rates. Error bars denote variation in repeated tests. 112
Figure 4.13. Mean longitudinal creep rates. Error bars denote variation in repeated tests. 112

Figure 4.14. Tangential and longitudinal strain measurements from periodically interrupted creep test on pipe with F-42° reinforcement architecture, plotted against test duration to form a pseudo creep curve. Test ended after 10-times life extension over control, rather than being tested to failure. 115
Figure 4.15. Observed longitudinal stiffness measurements are compared against the classical lamination theory model for two lamina of ±θ and varying transverse stiffness values (E_2 from 0.5 to 3.5 GPa). Horizontal error bars denote standard deviation in the reinforcement angle. Vertical error bars reflect measurement error in crosshead displacement method of strain measurement (some bars smaller than data points).....118
Figure 4.16. Linear least squares fit for tangential creep rate trend below θ_N.....125
Figure 4.17. Measured mean tangential, longitudinal and radial creep rates plotted against initial reinforcement angle (solid points) and final angle (unfilled points), with creep rate trends superimposed. Shaded bands cover range of predicted behaviour from initial angle (solid line) to final angle at t = 820 hours or failure (dashed line). Creep strain data from the interrupted F-42° test is superimposed, with ✖ and ✚ symbols, showing tangential and longitudinal creep rates, respectively. Some error bars smaller than data points. 126
Figure 4.18. Instantaneous creep strain data in the tangential and longitudinal directions, as measured during the interrupted F-42° test from time t = 0 hours to t = 820 hours. Some error bars smaller than data points.....128
Figure 4.19. Calculated mean effective creep rates plotted against initial reinforcement angle (solid points) and final angle (unfilled points). Shaded bands cover range of predicted behaviour from initial angle (lower band) to final angle at t = 820 hours or failure (upper band). 130
Figure 4.20. Measured and predicted radial creep rates, superimposed over radial creep rate trend line, predicted by the incompressibility condition. All rates plotted against initial reinforcement angle.....132

Figure 5.1. Hypothesized multiaxial creep rate behaviour over time for a reinforced sample with braid angle shifting to the neutral angle. 141
Figure 5.2. Representative figure of expected behaviour as braid orients itself to the neutral angle, θ_N. 142
Figure 5.3. Multiple pipe testing rig (a) rig assembly (b) sectional schematic (c) detailed view of strain measurement end (d) pressure fitting end. 144
Figure 5.4. Fans positioned to cool LVDTs at top end of creep rig. Inset: lower end of creep rig, with pressure lines connected to pipe samples. Bottom 50 mm of samples left uninsulated, with a second set of fans positioned to cool brazed joints. 145
Figure 5.5. Temperature profile in tube furnace with IFL, set to 400°C. Tube same within IFL highlighted in red. 146
Figure 5.6. Schematic of failure region in control pipes, with expansion shown in red and a representative crack shown in green (a) Chapter 4 tests without IFL (b) Chapter 5 tests with IFL and more evenly distributed deformation. 151
Figure 5.7. Representative creep curve for longitudinal direction, with trends superimposed for $\dot{\varepsilon}_{mean}$ and $\dot{\varepsilon}_{steady\ state}$. 153
Figure 5.8. Creep curve for representative control test, highlighting effect of smoothing algorithm. Mean and minimum creep rate trends superimposed. 154
Figure 5.9. Smoothed creep rate curve for representative control test. Minima from 40-60 hours indicating region of minimum (secondary) creep. 155
Figure 5.10 Smoothed control test results (a) creep curves (b) creep rate curves. 157
Figure 5.11. Predicted longitudinal creep rate trends for various reinforcement architectures (a) Predicted change in braid angle (b) Representative longitudinal creep rate trend from Figure 4.17 (c) Expected longitudinal creep rate trends for specific samples tested – i.e. C-36°, F-50° and C-65°, relative to an unreinforced sample. Not to scale. 160

Figure 5.12. Smoothed creep curves for reinforced samples, with the control behaviour of Figure 5.8 superimposed. 162
Figure 5.13. Smoothed creep rate curves for reinforced samples, with the control behaviour of Figure 5.9 superimposed. 163
Figure 5.14. Smoothed C-36° test result superimposed over control tests shown in Figure 5.10 (a) creep curves (b) creep rate curves. 168
Figure 5.15. Linear trend fitted to ε_z-t data for C-65° sample. 171
Figure 5.16. Initial 250 hours of Figure 5.12, truncated to allow for comparison between control and reinforced sample behaviour. 173
Figure 5.17. Steps in extension measurement resulting from irregular cycling of ambient temperature. 174
Figure 6.1. Failed plasma spray coating, with oxidized tungsten wire underneath [1] 181
Figure 6.2. Schematic of hybrid pipe geometry with solid sheath pipe acting as an oxidation barrier. 183
Figure 6.3. Dimensioned diagram of 253MA inner (liner) and outer (sheath) pipes with detailed section view for each design case (a) control, OD=48.7 mm (b) reinforced design 1 – thick sheath, OD=48.7 mm (c) reinforced design 2 – thin sheath, OD=43.9 mm. 184
Figure 6.4. Partial section of reinforced design 1 – thick sheath 185
Figure 6.5. Crimp bead in as-received condition, alongside bead crimped to hold wire loop fixed. 185
Figure 6.6. Schematic of unreinforced pipe, with photos of sections taken after rupture. Note the drastic increase in diameter and reduction in wall thickness. Liner and sheath pipe layers pressed together in region of maximum deformation 189
Figure 6.7. (a) control pipe prior to testing (b) control pipe after rupture caused by tangential creep (c) design 1 exhibiting notable snaking through its midsection (d) dramatic snaking in design 2 191
Figure 6.8. High temperature hybrid tube sectional schematic. Inset: 53° tungsten braid configuration. 195

Figure 6.9. 253MA creep rupture curve. Average stress to rupture in indicated times. Adapted from Rolled Alloys 253MA data sheet [2]. 198
Figure 6.10. Diameter-surface area coverage relationship for 38x7x0.4 tungsten braid [4] 199
Figure 6.11. Diameter-braid angle relationship for 38x7x0.4 tungsten braid [4]... 200
Figure 6.12. Defects present in unoptimized tungsten braid (W-46°) (a) pre-test, (b) post-test (different region) 201
Figure 6.13. Section of ruptured liner, reinforced with unoptimized tungsten braid (W-46°). Two creep blisters are present at defects in the braid, the leftmost of which led to the final failure of the liner. 202
Figure 6.14.Oxidation and embrittlement of tungsten braid around point of rupture. Oxidation occurred post-rupture while the furnace was cooling down. 203
Figure 6.15. Internal view of localised creep blister on W-46° sample. 204
Figure 6.16. Size and position of blister on inner surface, overlaid onto braid pattern on outer surface. Oxidation of the tungsten occurred post-rupture while the furnace was cooling down. Crumbling of the tungsten occurred while the sheath pipe was being removed. 205
Figure 6.17. Control pipe after rupture caused by tangential creep. 206
Figure 6.18. Point of rupture in control pipe – large longitudinal crack resulting from tangential expansion. 206
Figure 6.19. W-53 sample after 500 hours (309x life extension over control). Some superficial oxidation is present, but pipe dimensions have not changed measurably. 207
Figure 6.20. Break in braid at point of rupture. The braid itself has not crept, and failure is the result of tensile overload at a pre-existing defect. 208
Figure 6.21. Fragments of tungsten braid embedded in liner surface after W-53° test. 209
Figure 6.22. 253MA in as-received condition, etched with Kalling's No. 2 reagent. 213

Figure 6.23. Creep void formation in unreinforced control sample, etched with glyceregia. Material tip on left is necking at the point of rupture. 214
Figure 6.24. Creep void and carbide formation in unreinforced control sample, etched with glyceregia. 215
Figure 6.25. Large, aligned creep voids on grain boundaries in unreinforced control sample, etched with glyceregia.....215
Figure 6.26. W-53° sample. Tungsten wire, top, 253MA liner, bottom, with intermetallic layer in between. 216
Figure 6.27. W-53° sample. Section of wire bonded to outer surface of liner by intermetallic phase, formed over 570 hours at 1040°C. 218
Figure 6.28. W-53° sample. High magnification image of intermetallic phase between embedded tungsten wire and 253MA liner, formed over 570 hours at 1040°C. 219
Figure 6.29. W-53° sample. EDS map overlay of intermetallics formed at outer surface of liner after 570 hours at 1040°C. Major constituents coloured: tungsten (red), silicon (cyan), iron (blue) and chromium (green). 220
Figure 6.30. Individual maps for major constituents overlaid in Figure 6.29.....221
Figure 6.31. W-53° sample. SEM micrograph of chromium carbide formation at inner wall. 224
Figure 6.32. W-53° sample. EDS map of chromium carbide formation at inner wall over 570 hours at 1040°C. Major constituents coloured: iron (blue) and chromium (green). 225
Figure 7.1. Effect of 50°C temperature increase on 253MA creep rupture life when under typical reformer furnace conditions. Case (a) – matching stress and temperature conditions. Case (b) – matching life and temperature conditions. 230
Figure 7.2. Hybrid pipe schematic with diffusion barrier. 234
Figure 7.3. Hybrid pipe schematic with coextruded reinforcement. 235
Figure 7.4. Hybrid tube layer schematic, with thermal bridges. 238
Figure 7.5. Thermal resistor diagram for hybrid tube layer.....239

Figure 7.6. Effect of thermal bridge on total resistivity of pipe hybrid. 241
Figure 7.7. Stress-rupture plot for 100,000 hour tube lifetimes for various reformer tube materials. Adapted from Beyer et al. [13] to include 253MA with and without reinforcement. 244
Figure 8.1. Temperature profile during sample rupture. 264
Figure 8.2. Design for mechanical end cap to circumvent need for brazed joints. Schematic of mechanical sealing features. Inset: engineering drawing of end cap..... 265

LIST OF TABLES

Table 1.1. Potential applications for creep-resistant hybrid tubes. Adapted from [16-30]. 3
Table 2.1. Nominal composition of principal alloys used for reformer tubes, compared against 253MA..... 31
Table 3.1. Performance indices for resistance to creep in classical loading scenarios [12]. 43
Table 3.2. Creep exponents for various creep mechanisms [41]. 70
Table 3.3. Development of reinforcement for super alloy matrices [73]..... 76
Table 3.4. Summary of physical properties of drawn tungsten wire and 253MA at room temperature [78, 79]. 81
Table 4.1. Reinforcement architecture characterization. 99
Table 4.2. Creep rupture testing program. 106
Table 4.3. Measured longitudinal stiffness of stainless steel reinforcement. 107
Table 4.4. Comparison between final strains obtained with fixed and free and conditions. 113
Table 4.5. Post-test braid angle measurement. 120
Table 4.6. Form of trigonometric fits used for $\boldsymbol{\varepsilon - \theta}$ relationships in the tangential, longitudinal and radial directions. 124
Table 5.1. Reinforcement architectures selected for in-situ longitudinal strain measurement study. 148
Table 5.2. Creep rate analysis for samples with in-situ ε_z measurement..... 165
Table 6.1. Results of hybrid pipe tests with simple tungsten reinforcement. 188
Table 6.2. Comparison between reinforcement effectiveness in low and high temperature materials systems. 194
Table 6.3. Results of hybrid pipe tests. Braid-reinforced results shown in grey columns, compared to simple wrap-reinforcement case. 211
Table 6.4. Characterization of intermetallic phases formed at liner-reinforcement interface after 570 hours at 1040°C. 222
Table 7.1. Thermal properties used for hybrid tube heat transfer calculation. 241

CHAPTER 1: INTRODUCTION

From developments in iron and steel which led to the Industrial Revolution, to the creation of a high strength, lightweight aluminium alloy which fundamentally transformed the world of aviation, there is a historical precedent for breakthroughs in materials science being the key to the fundamental development of civilisation.

There is constant demand for improved materials that can perform at higher temperatures to increase efficiency and reliability of systems such as gas turbine engines and petrochemical facilities [1, 2]. Bulk materials have been continuously improved via alloying and manufacturing processes to obtain substantial gains in performance over the past few decades, e.g., in gas turbine engines [3, 4] steam reformer and steam cracker furnace tubes [5]. However, improvements are made in relatively small steps and it may be argued that such materials are reaching the limit of their potential. Furthermore, increases in turbine operating temperature since the 1970's have arisen more from improved cooling methods than from improved materials [6].

1.1.1 Potential applications

The present work seeks to utilize the design of "hybrid materials" as a pathway to obtain substantial performance improvements over bulk materials, and even composite materials, in high temperature piping applications. The simple hybrid design under consideration here involves externally reinforcing a pipe with an architectured layer of a material having substantially greater creep rupture life than the pipe material. Specifically, refractory metals are good candidates for achieving considerable gains in the creep rupture life of stainless steels and nickel-based superalloys [7-13]. This architectured reinforcement layer may be

comprised of filament windings or a braided sleeve. Unlike composite systems, the hybrid pipe geometry investigated here keeps the reinforcement layer separate from the pipe.

Gains in composites are limited by the rule of mixtures, where the arithmetic average of the properties of the components is weighted by their volume fractions [14]. Hybridization allows the most desirable properties to be extracted from each component and have them work together in parallel. Such a hybrid is predicted to have a substantial creep life extension, based on the concept that an external reinforcement layer will alter the stress state in a pressurized pipe such that tangential creep (driven by hoop stress) is circumvented as the primary mode of failure.

The present work is limited to tubular geometry, ruling more complex structures such as hypersonic airframes to be out of scope. However, this hybrid pipe technology still has potential use in a wide range of creep-limited high temperature applications where austenitic stainless steels and nickel-based superalloys are currently used. These applications include heat exchangers, furnace linings, boilers, jet engine burner liners, gas turbine exhaust systems and components in petrochemical furnaces [6, 15]. Table 1.1 outlines a wide range of creep-limited applications with tubular geometries, where nickel-based superalloys are commonly used at present, and large gains are possible via hybrid materials design which utilizes the creep strength of refractory metals. In addition to these superalloy-based applications, the excellent corrosion resistant and high melting point of zirconium mean that zirconium alloys are used in nuclear reactors – although these alloys are susceptible to hydrogen embrittlement and creep [16]. Lower-temperature metallic systems, such as aluminium heat exchanger tubes, may also benefit from hybrid pipe technology so long as thermal conductivity is not hindered significantly [17].

Table 1.1. *Potential applications for creep-resistant hybrid tubes. Adapted from [16-30].*

Application	Nominal Temperature (°C)	Approximate Stress (MPa)	Typical Mode of Failure
Steam methane reformer tubes (methanol and hydrogen production)	800-980	16-25	Longitudinal cracking driven by tangential creep from internal pressure stresses.
Ethylene pyrolysis tubes	750-1150	2-3	Circumferential cracking driven by longitudinal creep from self weight.
Gas turbines (combustion liner)	900-1600	15-27	Fatigue and creep crack growth. Creep driven by thermal stresses caused by large temperature gradients.
Nuclear reactors	300-1000	60-250	Creep of structural components in the reactor cores. Corrosive environment if using molten salt coolant.
Heat exchangers	350-1000	5-30	Longitudinal cracking driven by tangential creep from internal pressure stresses, exacerbated by thermal cycling.
Radiant tube burners	760-1130	14-70	Creep, driven by a combination of mechanical loading and thermally induced stresses from non-uniform temperature distribution and heat fluxes.
Ammonia cracking furnaces	900-1000	8-16	Longitudinal cracking driven by tangential creep from internal pressure stresses.
Fossil fuel-fired boilers	560-850	10-38	Decarburization, creep cracking driven by internal pressure. 30% of all tube failures in boilers are caused by creep.
Direct-reduced iron (DRI) reduction furnace tubes	900-1100	7-20	Carburization, metal dusting and longitudinal cracking driven by internal pressure stresses.

Steam methane reforming, integral to the production of methanol and hydrogen, will be considered as the model application for the hybrid pipe technology. This focus on a single application allows for test conditions to be set and financial implications to be explored in greater detail. It is believed that a dramatic

improvement in the performance of high-temperature materials will accommodate the growth in global demand for hydrogen and methanol.

1.1.2 Methanol production

By volume, methanol is one of the top five chemical commodities shipped around the world annually. The global methanol industry generates US$36 billion in economic activity each year, while creating over 100,000 jobs [31]. In 2013, global demand for methanol was 65 million metric tons, and is expected to exceed 90 million metric tons by 2016 [31, 32]. This dramatic growth is driven largely by the global housing market and the demand for cleaner energy.

Methanol is produced through the synthesis of methane, usually by heating it, adding steam, and using nickel-oxide as a catalyst. This synthesis process takes place under extraordinarily hostile conditions inside a large array of vertically oriented austenitic stainless steel tubes located in a reformer furnace.

Additionally, the hydrocarbon synthesis gas produced in the reformer furnace is a source of hydrogen. Globally, hydrogen production is an estimated NZ$130-200 billion industry [33, 34]. As of 2014, approximately 95% of hydrogen produced in the United States is made via steam-methane reforming. Approximately 45% of this hydrogen is then consumed on-site in oil refining, and in the production of ammonia and methanol [35, 36].

In order to drive the endothermic reaction, reformer tubes typically operate at approximately 950°C and an internal pressure of 3.5 MPa, which translates to a hoop stress of ~21 MPa. As a result of these operating conditions, creep is the dominant failure mechanism experienced in service.

1.1.3 Tests performed

In this investigation, a model system of pressurized tube samples of grade 253MA austenitic stainless steel, reinforced with tungsten wire, were creep tested to rupture. This pressurized tube testing replicated the complex stress state of reformer tubes under service conditions. Reinforcement in the form of helical winding and braided sleeves was tested. By changing the architecture of the reinforcement, tangential and longitudinal stresses on the tube were altered, thereby allowing multiaxial creep strains to be controlled.

To negate potential oxidation issues and allow a complete focus on optimizing the reinforcement architecture, a lower temperature model system of brass tubes reinforced with grade 316 or 304 austenitic stainless steel was also tested.

1.2 Project Motivations

Process efficiencies and rates of reaction in an endothermic environment such as a steam reforming furnace are intrinsically linked to operating temperature. Often this maximum operating temperature is dictated by the material and its susceptibility to environmental attack and creep at an elevated temperature.

Traditionally, nickel-based superalloys have been favoured for high temperature applications, particularly when operating temperatures exceed 800°C [37]. Since their emergence in the 1940's, the development of these superalloys through additional alloying, processing and grain boundary engineering has lead to significant improvements in maximum allowable temperature, creep life, tensile strength at high temperature, and oxidation and corrosion resistance. However, potential gains are rapidly diminishing as operating temperatures approach limits imposed by the constituent elements of the superalloys.

As the benefits from developing nickel-based superalloys reach a plateau, a paradigm shift is required. Specifically, refractory metals are seen as a good device for achieving considerable gains in the creep rupture life of stainless steels and nickel-based superalloys [7-13]. Substantial work has been performed on testing alloys and composite systems strengthened by refractory metals [8-13, 38, 39].

Effectively harnessing the potential for refractory metals in creep applications could result in improved process efficiencies, fewer shutdowns and reduced frequency of material replacement. The potential to operate at higher temperatures for longer durations without material replacement translates to significant economic incentive. Globally, there are approximately 2000 steam reforming plants, each with up to 1000 reformer tubes which cost approximately NZD$25,000 per tube. Each year, NZD$1.3-2.6 billion is spent on reformer tube replacement [34, 40, 41].

The loss in production associated with the sudden and unexpected failure of a reformer tube can cost NZD$0.5-4 million per day [40]. To mitigate this risk, entire sets of reformer tubes are periodically checked and replaced after approximately 11 years at a cost on the order of NZD$21 million for a typical plant (250-450 tubes) [40, 41]. While reformer efficiency is extremely complex and variable between sites, it can be roughly quantified that for a single plant, every 20°C increase in operating temperature correlates to approximately NZD$0.5 million per year in improved process efficiency [42].

1.3 Research Objectives

It is hypothesised that multiaxial creep strains can be controlled by changing the architecture of the reinforcement in a multi-layered hybrid pipe.

Desired outcomes of this investigation to optimize hybrid creep performance by tailoring reinforcement architecture to alter stress state (and thus control creep rate) included:

- The development of appropriate techniques and testing apparatus to assess the creep performance of a hybrid tube under internal pressure.
- A quantitative comparison between the creep life of hybrid and unreinforced tubes, and the effect the reinforcement layer has on the stress state as well as creep micro- and macromechanics.
- The determination of any correlation between reinforcement architecture and bulk mechanical properties, specifically reinforcement angle and multiaxial stiffness.
- The understanding of key failure mechanisms of the hybrid material under service conditions.
- The determination of optimal reinforcement architecture to minimize the effective creep rate of a tube under internal pressure.
- A contribution to the literature on the reinforcement of piping for creep reduction, and how to utilize the creep strength of refractory metals.

1.4 Layout of Thesis

This thesis is divided into 8 chapters, each detailing a separate section of the research. Each chapter is briefly summarised below.

Chapter 1 (current chapter) establishes the broader context of the research presented in the thesis. The background, motivations and objectives of the research are briefly discussed.

Chapter 2 outlines the hybrid tube concept and provides the reader with some background information regarding the methanol production process and issues faced by current-generation reformer technology. An overview of furnace operating conditions and a stress analysis of reformer tubes is provided in order to permit a creep life prediction for the unreinforced tubes.

Chapter 3 provides a comprehensive literature review of related work, including creep mechanics in a complex stress state, materials design techniques for hybridization, and previous work in the use of reinforcement for creep reduction in piping – particularly utilizing the creep strength of refractory metals. Previous work on relating reinforcement architecture to bulk material properties is also reviewed, including the use of classical lamination theory (CLT) to model stiffness properties of a balanced biaxial braid. Additionally, free body diagrams are used to derive a theoretical optimal reinforcement angle, the neutral angle (θ_N), where wire tensions act proportionally to internal pressure stresses. The oxidation properties of tungsten and its tendency to form intermetallics are also discussed.

Chapter 4 provides a study on the relationship between reinforcement architecture and multiaxial creep strain rate, as determined by the low temperature model system of brass tubes reinforced with austenitic stainless steel. The relationship between tangential and longitudinal creep in a pipe under internal pressure is addressed. A new model for evaluating creep reinforcement effectiveness is subsequently presented, and recommendations are made for an optimal reinforcement architecture for a given stress state.

Chapter 5 presents novel testing methodology utilised for in-situ measurement of the longitudinal creep strain in a pressurized pipe, thereby further exploring trends first revealed in Chapter 4. This in-situ strain measurement allows for the minimum creep rate to be compared to the mean creep rate approximation made in Chapter 4. Multiaxial creep behaviour is further investigated, and the mechanics of how the presence of a reinforcement layer brings about a reduction in creep rate is explored, with special consideration given to the dynamic nature of the reinforcement angle.

Chapter 6 is focused on applying the findings of the reinforcement architecture optimization study in Chapter 4 to a high temperature 253MA-tungsten hybrid tube. Unique failure mechanisms related to non-uniform longitudinal creep are discussed, as are issues with oxidation, intermetallic formation and damage tolerance.

Chapter 7 relates research achievements to the industry context, and addresses the hurdles between the present study and practical implementation of the hybrid pipe technology in industry. The hole in property space which has been filled by this novel technology is highlighted. Thermal conductivity is also considered, with the practical implications the hybrid tube may have on the endothermic reaction

outlined. An analysis of the trade-off between life extension and increased operating temperature for more efficient methanol production is also presented.

Chapter 8 provides a summary of the major achievements of this work, and contributions it has made to the literature. It also leaves the reader with some concluding remarks regarding the outcomes of the project in relation to the initial objectives. Further research which stems from this project is also explained, namely the issue of intermetallic formation consuming the refractory reinforcement. Steps towards implementing the hybrid tube technology in a practical industry environment are also outlined.

Appendix A contains a copy of the major journal article, "Hybrid Materials Design to Control Creep in Metallic Pipes", which has been published in Materials and Design.

1.5 Research Achievements

This research project has generated outputs, as listed below. Papers which have been published to date are included in the appendix of this thesis.

- **B.P. Reyngoud, C.M. Bishop and M.V. Kral,** "*Hybrid Materials Design to Control Creep in Metallic Pipes*", Materials and Design, vol. 84, pp. 25-35, 2015.

- **M.V. Kral, C.K.H. Dharan and B.P. Reyngoud** "*Improved Tubes For High Temperature Industrial Application And Methods For Producing Same*", NZ provisional patent application no. 624351, 2014.

- **M.V. Kral, B. Reyngoud, H. Dharan**, "*Hybrid Materials Design to Control Creep in Pipes*", presented at MS&T14 Annual Meeting, 12-16 October, 2014, Pittsburgh, PA, USA.

- **B.P. Reyngoud and M.V. Kral,** "*Materials by Design Approach to a Multi-Layer Pipe Hybrid*", presented at ArchiMat International School on Architectured Materials, 22-28 May, 2011, Grenoble, France.

- **B.P. Reyngoud and M.V. Kral,** "*Creep, Oxidation and Intermetallic Phase Formation: Assessing the High Temperature Performance of a Tungsten-Stainless Steel Hybrid*", presented at TMS Annual Meeting, 27 February – 3 March, 2011, San Diego, CA, USA.

1.6 Novel Contributions

Specific areas of the current project which are viewed as unique and novel contributions are briefly summarized below:

- A relationship was derived for ε-θ (i.e. creep strain for a given reinforcement angle), and an empirical model was produced for $\dot{\varepsilon} - \theta$.

- By observing the change in $\dot{\varepsilon}$ as θ tends to θ_N, $\dot{\theta}$ behaviour as a function of θ is able to be inferred.

- The braid was observed to shift to the neutral angle (θ_N). Previously, this has been reported for systems at room temperature, where the shift in θ is brought about by rapid elastic deformation upon pressurization. This is the first reported instance of creep being the mechanism whereby braided reinforcement gradually orients itself to θ_N, thereby identifying the neutral angle as a relevant concept for creep strengthening.

In addition to these novel contributions, the current project has utilized a number of uncommon approaches in order to expand the field of knowledge in the following areas:

- The creep testing of pressurized pipes, as opposed to uniaxial tensile samples, particularly when testing metallic systems at relatively high temperatures.

- The use of refractory reinforcement in braided form, specifically for creep reduction.

- Arranging the reinforcement in a hybrid layup with a purely mechanical interface, rather than embedding the reinforcement in a matrix material.

CHAPTER REFERENCES

[1] Z. Huda and P. Edi, "Materials selection in design of structures and engines of supersonic aircrafts: A review," *Materials and Design,* vol. 46, pp. 552-560, 2013.

[2] Q. Lu, W. Xu, and S. Van Der Zwaag, "Computational design of precipitation strengthened austenitic heat-resistant steels," *Philosophical Magazine,* vol. 93, pp. 3391-3412, 2013.

[3] J. A. Lemberg and R. O. Ritchie, "Mo-Si-B alloys for ultrahigh-temperature structural applications," *Advanced Materials,* vol. 24, pp. 3445-3480, 2012.

[4] R. A. MacKay, T. P. Gabb, A. Garg, R. B. Rogers, and M. V. Nathal, "Influence of composition on microstructural parameters of single crystal nickel-base superalloys," *Materials Characterization,* vol. 70, pp. 83-100, 2012.

[5] V. Javaheri, F. Shahri, M. Mohammadnezhad, M. Tamizifar, and M. Naseri, "The effect of Nb and Ti on structure and mechanical properties of 12Ni-25Cr-0.4C austenitic heat-resistant steel after aging at 900 °c for 1000 h," *Journal of Materials Engineering and Performance,* vol. 23, pp. 3558-3566, 2014.

[6] F. R. N. Nabarro and F. deVilliers, *Physics of Creep and Creep-Resistant Alloys*. London, UK: Taylor & Francis Ltd, 1995.

[7] B. A. Pint, J. R. DiStefano, and I. G. Wright, "Oxidation resistance: One barrier to moving beyond Ni-based superalloys," *Materials Science and Engineering A,* pp. 255-263, 2006.

[8] G. Frommeyer and R. Rablbauer, "High Temperature Materials Based on the Intermetallic Compound NiAl Reinforced by Refractory Metals for Advanced Energy Conversion Technologies," *Steel Research International,* vol. 79, pp. 507-513, 2008.

[9] T. Grobstein and H. M. Yun, "The Role of the Interface in Refractory Metal Alloy Composites," in *American Institute of Physics*, 1991, pp. 186-192.

[10] D. W. Petrasek and R. H. Titran, "Creep Behaviour of Tungsten/Niobium and Tungsten/Niobium-1 Percent Zirconium Composites," in *Fifth Symposium on Space Nuclear Power Systems*, Albuquerque, New Mexico, 1988.

[11] J. R. Stephens, D. W. Petrasek, and R. H. Titran, "Refractory Metal Alloys and Composites for Space Power Systems," in *Spring meetings of the Materials Research Society*, Reno, Nevada, 1988.

[12] T. L. Grobstein, "Creep Behaviour of Tunsten Fiber Reinforced Niobium Metal Matrix Composites," in *Sixth Symposium on Space Nuclear Power System*, Albuquerque, New Mexico, 1989.

[13] M. E. El-Dahshan, d. P. Whittle, and J. Stringer, "The Oxidation and Hot Corrosion Behaviour of Tungsten-Fiber Reinforced Composites," *Oxidation of Metals,* vol. 9, pp. 45-67, 1974.

[14] M. F. Ashby, *Materials Selection in Mechanical Design*, 4th ed.: Butterworth-Heinemann, 2010.

[15] R. C. Reed, *The Superalloys. Fundamentals and Applications*. Cambridge, UK: Cambridge University Press, 2006.

[16] D. G. Franklin, G. E. Lucas, and A. L. Bement, *Creep of Zirconium Alloys in Nuclear Reactors*. Baltimore, USA: American Society of Testing and Materials, 1983.

[17] S. Kahl, H.-E. Ekström, and J. Mendoza, "Tensile, Fatigue, and Creep Properties of Aluminum Heat Exchanger Tube Alloys for Temperatures from 293 K to 573 K (20 °C to 300 °C)," *Metallurgical and Materials Transactions A,* vol. 45, pp. 663-681, 2014.

[18] C. E. Baukal, *Industrial Burners Handbook*: CRC Press, 2004.

[19] G. Y. Yai, *High Temperature Corrosion and Materials Applications*: ASM International, 2007.

[20] M. Mirzaei and R. Karimi, "Stress Analysis and Life Assessment of a Gas Turbine Blade," in *10th International Congress on Fracture*, Honolulu, USA, 2001.

[21] H. Moon, K. M. Kim, Y. H. Jeon, S. Shin, J. S. Park, and H. H. Cho, "Effect of thermal stress on creep lifetime for a gas turbine combustion liner," *Engineering Failure Analysis,* vol. 47, pp. 34-40, 2015.

[22] ArvosGroup. Ethylene Pyrolysis Processes & Schmidtsche® Transfer Line Exchangers, http://www.shg-schack.com/products-and-services/products-vs-applications/heat-transfer-in-ethylene-production/ethylene-pyrolysis-process-transfer-line-exchanger/, [Accessed January 3rd 2015].

[23] I. Kucora and L. Radovanovic, "Pyrolysis Furnace Tube Damaging and Inspection," *Acta Technica Corviniensis,* vol. 3, 2014.

[24] G. Breitbach and J. Altes, "Stress and creep damage analysis for HTR heat exchangers at very high temperatures," *International Journal of Pressure Vessels and Piping,* vol. 20, pp. 275-287, 1985.

[25] D. French, *Metallurgical Failures in Fossil Fired Boilers*: John Wiley & Sons, 1993.

[26] D. R. H. Jones, "Creep failures of overheated boiler, superheater and reformer tubes," *Engineering Failure Analysis,* vol. 11, pp. 873-893, 2004.

[27] M. Irfan and W. Chapman, "Thermal stresses in radiant tubes: A comparison between recuperative and regenerative systems," *Applied Thermal Engineering,* vol. 29, pp. 1913-1920, 2009.

[28] M. H. Shariat, A. H. Faraji, A. Ashrafriahy, and M. M. Alipour, "In Advanced Creep Failure of H.P. Modified Reformer Tubes in an Ammonia Plant," *The Journal of Corrosion Science and Engineering,* vol. 6, 2003.

[29] D. Alessio, G. Gonzalez, V. F. Pirrone, L. Lurman, and L. Moro, "Variation of Creep Properties in HP Steel by Influence of Temperature," *Procedia Materials Science,* vol. 1, pp. 104-109, 2012.

[30] APEC. Introduction of Micro Alloying Elements in Centrifugally Cast Tubes for the Steel Industry, http://goo.gl/eRyIKe, [Accessed December 28th 2014].

[31] The Methanol Industry, http://www.methanol.org/Methanol-Basics/The-Methanol-Industry.aspx, [Accessed December 2013].

[32] D. Johnson. Global Methanol Market Review, http://www.ptq.pemex.com/productosyservicios/eventosdescargas/Documents/Foro%20PEMEX%20Petroqu%C3%ADmica/2012/PEMEX_DJohnson.pdf, [Accessed Decmber 2013].

[33] Z. Barlow. Breakthrough in hydrogen fuel production could revolutionize alternative energy market, http://www.vtnews.vt.edu/articles/2013/04/040413-cals-hydrogen.html?utm_campaign=Argyle%2BSocial-2013-04&utm_content=shaybar&utm_medium=Argyle%2BSocial&utm_source=twitter&utm_term=2013-04-04-08-30-00, [Accessed November 10th 2014].

[34] CarbonSciences. Carbon Sciences Targets $150 Billion Hydrogen Market, http://www.carbonsciences.com/view_news.php?id=118, [Accessed November 10th 2014].

[35] "The Impact of Increased use of Hydrogen on Petroleum Consumption and Carbon Dioxide Emissions", U.S. Energy Information Administration, R-OIAF-CNEAF/2008-04, 2008.

[36] M. S. Dresselhaus and M. V. Buchanan, "The Hydrogen Economy", 2004.

[37] R. C. Reed, *The Superalloys: Fundamentals and Applications*. Cambridge, UK: Cambridge University Press, 2006.

[38] V. Y. Ivanov, Y. P. Nechiporenko, L. N. Yefimenko, and M. I. Yurchenko, *High Temperature Oxidation Protection of Tungsten*. Moscow: Atom Press, 1968.

[39] J. H.E. McCoy, R. L. Stephenson, and J. J.R. Weir, "Mechanical Properties of some Refractory Metals and their Alloys", Oak Ridge National Laboratory, 1964.

[40] B. Fisher, Quest Integrity Group, (personal communication with M. Kral, 2009)

[41] M. Altenberg, Quest Integrity Group, (personal communication with M. Kral, 2009)

[42] P. Tait, Methanex Corporation, (personal communication with B. Reyngoud, June 19th, 2013)

CHAPTER 2: BACKGROUND

The aim of this chapter is to provide the reader with some pertinent background information which will be expanded upon in Chapter 3. The hybrid tube concept is summarized in relation to controlling the creep response of a pressure vessel. Additionally, the methanol production process is briefly outlined, including a brief analysis of the stress state of reformer tubes.

2.1 Hybrid Tube Concept

For tubular creep samples under internal pressure, the primary mode of failure is tangential creep, where cracks are oriented along the axis of the tube. Through a greater understanding of the complex stress state of a pressurized tube, it is believed that a significant creep life extension can be attained. This predicted life extension is based on the principle that an external reinforcement layer may be utilised to alter the stress state in a pressurized tube such that tangential creep is circumvented as the primary mode of failure.

2.1.1 Hybridization

Hybridization allows the most desirable properties to be extracted from each component and have them work together in parallel. By transferring creep strength requirements to the reinforcement layer, the liner tube only needs to provide enough structural strength to hold the internal pressure and support its own weight.

This requires a reinforcement that does not experience creep at the service temperature. Specifically, refractory metals are good candidates for achieving

considerable gains in the creep rupture life of stainless steels and nickel-based superalloys [1-7]. By changing the architecture of the reinforcement, tangential and longitudinal stresses on the tube are altered, thereby allowing multiaxial creep strains to be controlled.

Unlike composite systems, the hybrid tube geometry investigated here keeps the reinforcement layer separate from the tube. This allows the property space between rule of mixtures and 'greatest of both' scenarios (Figure 2.1) to be explored, utilizing the structural strength and chemical resistance of the tube and the creep strength of the reinforcement layer.

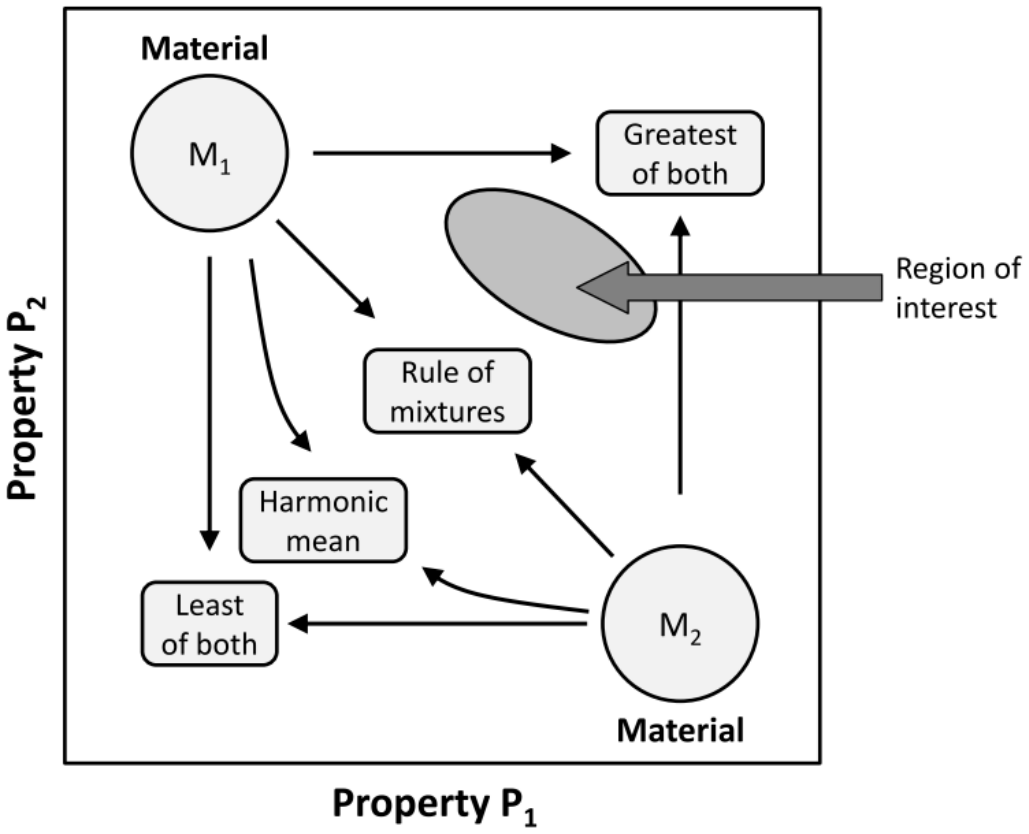

Figure 2.1. *Possibilities of hybridization. Adapted from Ashby [8].*

However, refractory metals are highly reactive and prone to aggressive oxidation at elevated temperatures. This necessitates the presence of a third, outer layer (hereafter known as the sheath) to shield the reinforcement layer from environmental attack. Figure 2.2 shows the relationship between the hybrid pipe layers in a simple schematic.

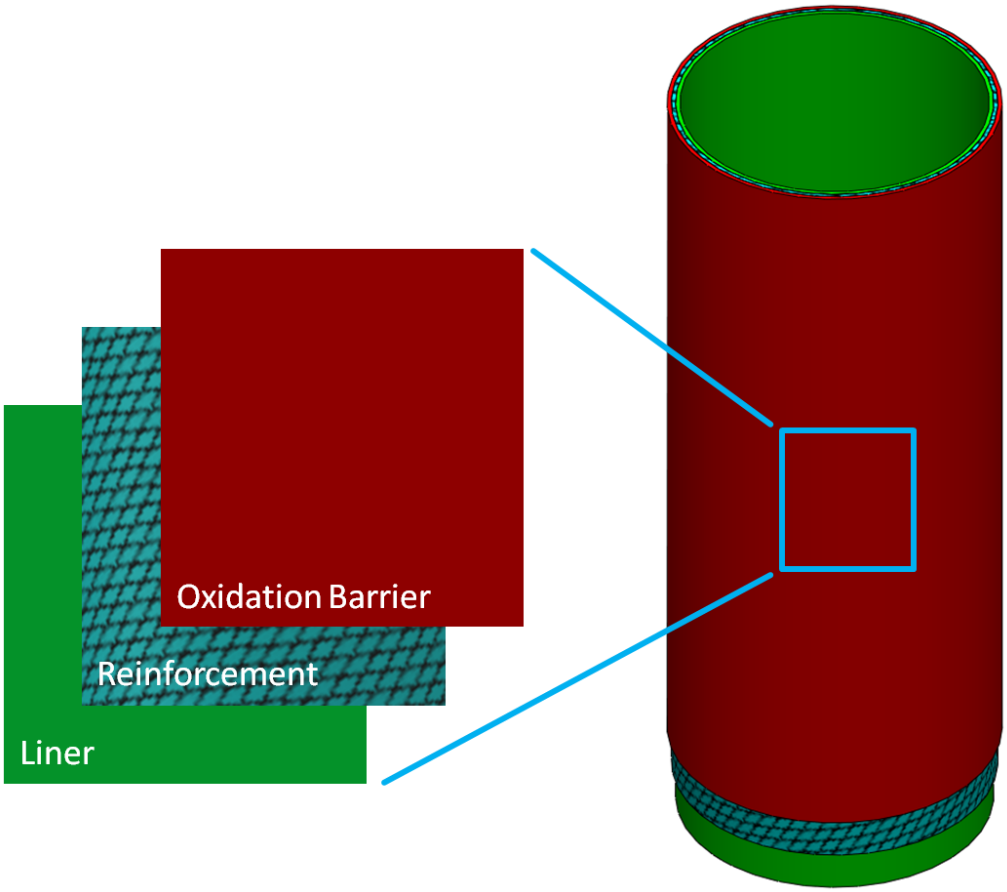

***Figure* 2.2.** *Hybrid tube schematic.*

2.1.2 Testing approach

Despite the prevalence of uniaxial creep testing, the majority of creep seen in industrial applications occurs in complex, multiaxial stress states. Because the loading on reformer tubes is primarily the result of internal pressure, one must consider the multiaxial mechanical properties. This becomes extremely important

when the material or structure is anisotropic or orthotropic, as is the case drawn for polymers, composites and hybrids [9].

In order to adequately reproduce the complex, multiaxial stress state seen by reformer tubes in service, creep tests were performed on entire pressurized pipes. This pipe testing apparatus is detailed in Figure 2.3. Note that this arrangement allows for pressure and temperature monitoring, as well as a measure of creep rupture life. However, unlike in conventional uniaxial creep tests and some more sophisticated multiaxial creep tests where strains may be measured in-situ [9-11], the multilayered nature of the hybrid pipe made in-situ strain measurement of the pipe problematic. Therefore, overall creep rupture time and final maximum strain in the tangential, longitudinal and radial directions were determined at failure.

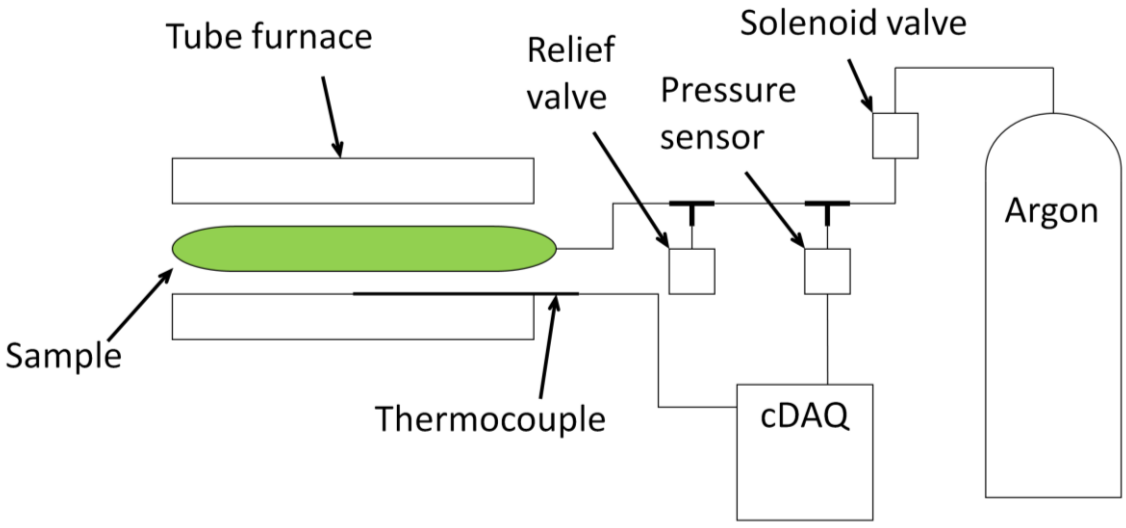

Figure 2.3. *Schematic of pipe rupture testing apparatus.*

While a similar approach to creep testing has been used for polymeric composites at low temperature [12, 13], the use of pressurized pipe tests to assess the creep rupture performance of metals at high temperature has only been considered in a few select cases [10, 14-16], and never for metallic composites or hybrids.

2.1.3 Creep reinforcement

Substantial work has been performed on testing alloys and composite systems strengthened by refractory metals [2-7, 17, 18]. However, the usefulness of refractories as high-temperature materials in air is limited by their poor oxidation resistance at service temperatures, meaning they can only be used in air when protected by suitable coating materials [17, 19]. As a result, most creep tests on refractory composite and alloy systems have been performed under vacuum with the intended application being high temperature components for use in space [3]. For some applications with shorter life requirements, it may be practical to minimize the rate of oxidation by alloying or coating materials such that they form a stable, dense surface oxide [1]. However, in order to form an effective oxide layer, a critical content of Cr, Si or Al is required in the alloy and such high levels of these alloying components cause brittle intermetallic phases to form in refractory metals [1, 20, 21].

At lower temperatures, creep reinforcement is a concept commonly associated with polymeric composites, where the reinforcement is often in the form of unidirectional fibres, randomly oriented chopped fibres, or particulates. As with refractory reinforcement under a vacuum, these reinforced polymers have shown a great deal of success in improving creep strength [22-24].

However, the gains in these composites are often limited by the rule of mixtures, where the arithmetic average of the properties of the components is weighted by their volume fractions [8]. The principles of hybridization, outlined in Section 2.3.1, free the hybrid tube from this limitation, allowing the best characteristics to be extracted from each component.

2.2 Methanol Production

As discussed in Chapter 1, there are a vast range of potential applications for a creep-resistant hybrid tube which is capable of operating at temperatures in excess of 1000°C. Of the range of operating temperatures and stresses outlined, steam methane reformer tubes are of particular interest to the present project due to the support the author has enjoyed from Methanex NZ. In order to fully appreciate this potential application and to grasp the operating conditions, essential for designing accelerated tests, it is useful to consider the methanol production process.

Methanol is one of the most versatile compounds on Earth. It is the basis for hundreds of chemicals and thousands of products which support our everyday lifestyles. Methanol is essential for the automotive, construction, pharmaceutical, electronic, fuel and textile sectors as well as for packaging, paints, insulation and solvents [25-28]. Figure 2.4 shows the primary chemicals derived from methanol and where these derivatives find use in many everyday products.

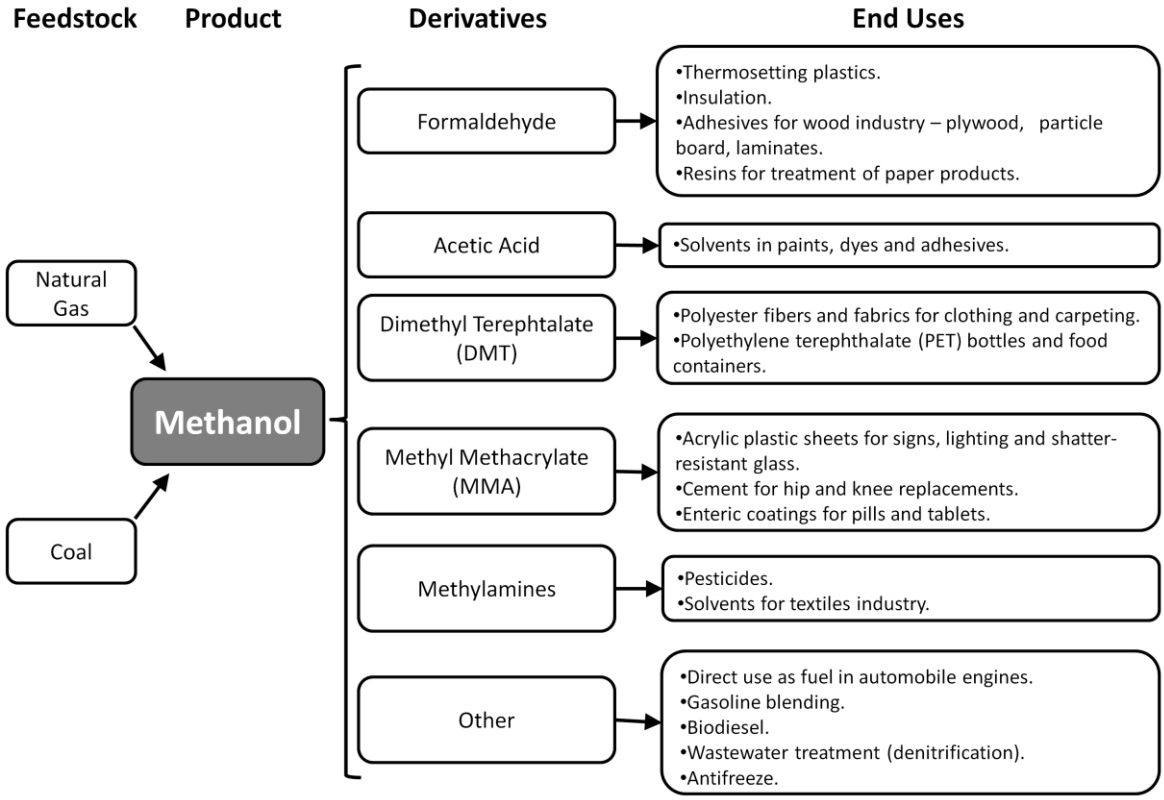

***Figure* 2.4.** *Principal uses of methanol. Adapted from [25-28].*

Feedstocks such as coal, biomass or natural gas may be used to produce methanol by utilizing a process known as steam reforming to produce the precursor to methanol, synthesis gas (syngas). Syngas is a mixture of carbon monoxide (CO), hydrogen (H_2) and carbon dioxide (CO_2).

The process of producing syngas from natural gas and converting to methanol can be broken into four key stages: desulphurization, reforming, conversion and distillation. For clarity, the schematic in Figure 2.5 neglects multiple preheating, compression, separation and recycling stages in order to focus on the four key stages of production.

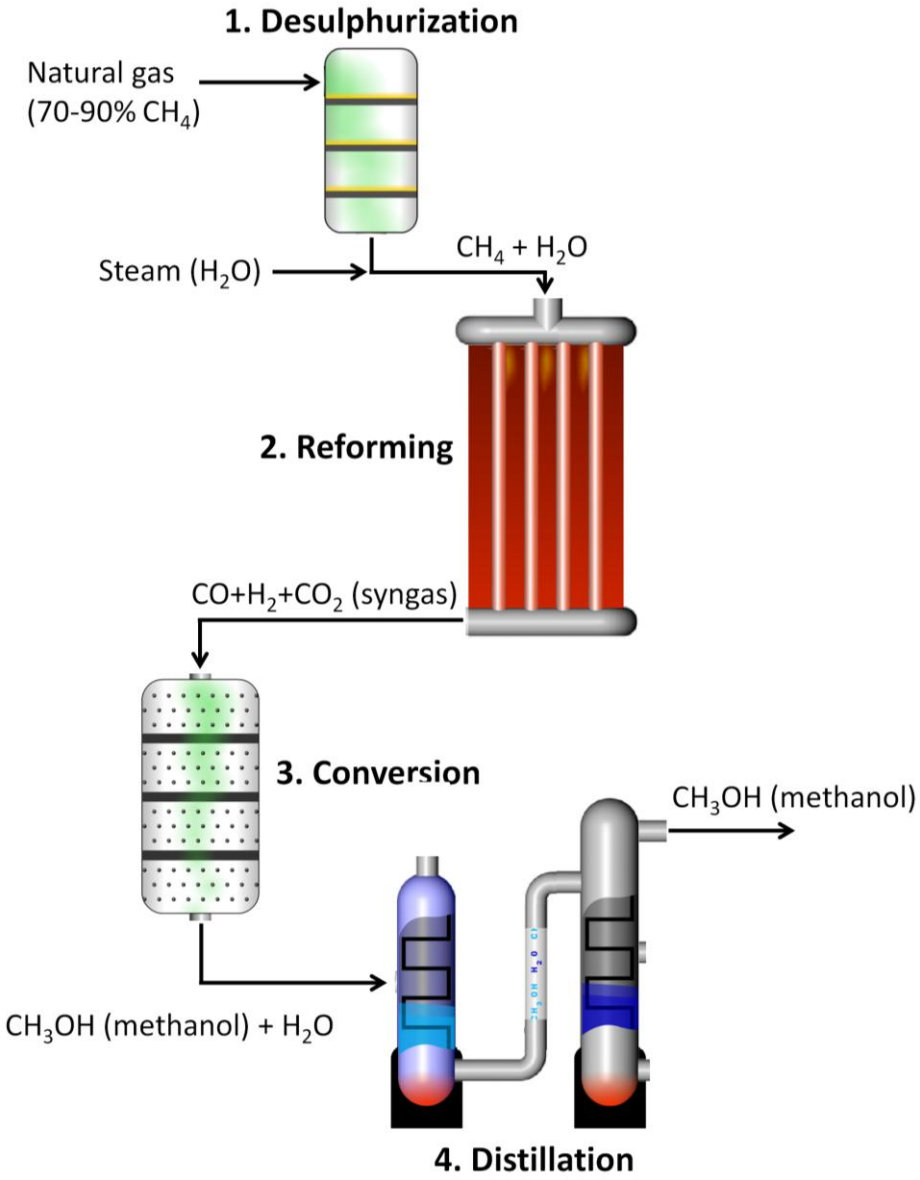

Figure 2.5. *Simplified schematic of the methanol manufacturing process. Adapted from Methanex Corporation, 2011 [29].*

Stage 1. Desulphurization

The presence of any sulphur in the natural gas prevents the reforming reaction from occurring. To remove sulphur, the gas is flowed through a bed of zinc oxide (ZnO) pellets. ZnO reacts with sulphur compounds present in the natural gas to form zinc sulphide.

Stage 2. Reforming

In the reformer, the natural gas and steam mixture moves through a series of vertical tubes heated in excess of 900°C by a series of burners. Each tube is packed with a nickel oxide (NiO) catalyst. The presence of the catalyst and this elevated temperature drives an endothermic reforming reaction that produces syngas. Supplementary steam is supplied in a water-gas shift reaction to produce additional hydrogen at the expense of carbon monoxide. This stage of the production process is the primary concern of the present project.

Reforming reaction: $CH_4 + H_2O \leftrightarrow CO + 3H_2$

Water-gas shift reaction: $CO + H_2O \leftrightarrow CO_2 + H_2$

Net reaction: $CH_4 + 2H_2O \leftrightarrow CO_2 + 4H_2$

Stage 3. Conversion

In the conversion reaction, syngas flows through a series of permeable beds holding pellets of copper (Cu) catalyst. The Cu promotes the reaction which forms methanol and water. Leftover, unreacted gas is recovered and re-processed.

Conversion reaction: $CO + 2H_2 \leftrightarrow CH_3OH$

Water-gas shift reaction: $CO_2 + H_2 \leftrightarrow CO + H_2O$

Net reaction: $CO_2 + 3H_2 \leftrightarrow CH_3OH + H_2O$

Stage 4. Distillation

Following conversion, the product is a 75% methanol, 25% water mixture known as crude methanol. Trace impurities and water are removed during the distillation process, with byproducts often fed back into the production process. The resultant

high purity methanol (≥99.8%) is then transferred to large storage tanks and distributed via tuck, rail, ship, pipeline and barge.

2.3 Reformer Tubes

A typical steam reforming furnace consists of a series of 250-450 tubes, oriented vertically. These reformer tubes are centrifugally cast from nickel-based superalloys, most recently a series known as high performance (HP) alloys. While there is a great deal of variability from plant to plant, tubes are typically 10-15 m long with a 100-135 mm outer wall diameter (OD) and a wall thickness between 8 and 12 mm [30-33].

The working pressure in a reformer furnace is between 1 and 5 MPa and is essentially constant during operation [34]. Worldwide, steam reforming furnaces operate at temperatures ranging from 800-980°C. Methanex tends towards the upper end of this spectrum, with current furnaces running at 930-950°C. This combination of pressure and temperature, along with tube geometry, is generally selected such that the reformer tubes have an expected life of 100,000 hours (11.4 years of continuous operation).

Due to limited resource availability and the finite life of other components in the reforming plant, it is not necessarily ideal to increase creep life indefinitely. Instead, it is preferable to seek a balance of increased creep life and an elevated operating temperature, as increasing temperature improves plant efficiency and throughput by accelerating rates of reaction in the reformer. From a processing point of view, the only limit on maximum possible operating temperature is the burner temperature. However, from a metallurgical standpoint, practical limitations are imposed by components within the furnace. Assuming hybrid pipe

technology alters the reformer tubes such that concerns over their creeping is no longer a limiting factor, operating temperature is then restricted to approximately 1050°C by downstream components which are exposed to flue gases at the outlet of the reformer. If these downstream components were to be shielded, or the flue gas was actively cooled, then the maximum operating temperature would be limited by the NiO catalyst, which begins to melt and leach minerals at approximately 1100°C [35, 36].

2.3.1 Stress analysis

Reformer tubes are thick-walled pressure vessels. Shigley [37] states that a pressure vessel can be assumed to be thin-walled when the ratio of the wall thickness to inner radius (t/r_i) is < 0.05. For typical reformer tube dimensions of 120 mm OD and 10 mm wall thickness, t/r_i = 0.2, and the thin-walled assumption is not valid.

Equations 2.1-2.3 are Lamé's equations for stresses in a thick-walled pressure vessel, reduced for zero external pressure. Von Mises equation (Equation 2.4) is used to resolve these multiaxial stresses into an equivalent stress, σ_{VM}. Principal stresses in the cylindrical coordinate system in the radial, tangential and longitudinal directions (σ_r, σ_t and σ_z) are functions of radial distance from the axis of the tube, r, Figure 2.6. p_i is internal pressure and r_o and r_i are outer and inner radius, respectively.

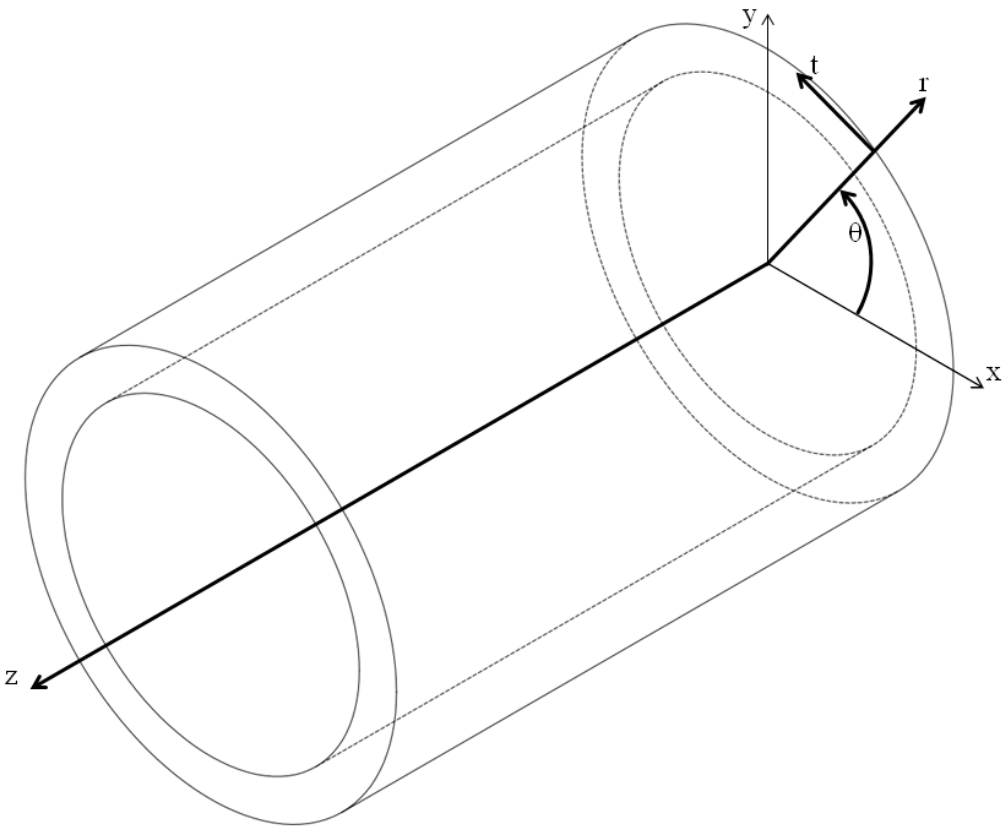

Figure 2.6. *Cylindrical coordinate system for tubular pressure vessel.*

$$\sigma_r = \frac{p_i r_i^2}{r_o^2 - r_i^2}\left[1 - \frac{r_o^2}{r^2}\right] \tag{2.1}$$

$$\sigma_t = \frac{p_i r_i^2}{r_o^2 - r_i^2}\left[1 + \frac{r_o^2}{r^2}\right] \tag{2.2}$$

$$\sigma_z = \frac{p_i r_i^2}{r_o^2 - r_i^2} \tag{2.3}$$

$$\sigma_{VM} = \sqrt{\frac{[(\sigma_r - \sigma_t)^2 + (\sigma_t - \sigma_z)^2 + (\sigma_r - \sigma_z)^2]}{2}} \tag{2.4}$$

Equations 2.1-2.4 can then be solved for typical reformer tube dimensions and operating conditions. Figure 2.7 is produced using an internal pressure of 3.5 MPa in a 120 mm OD pipe with a 10 mm wall thickness.

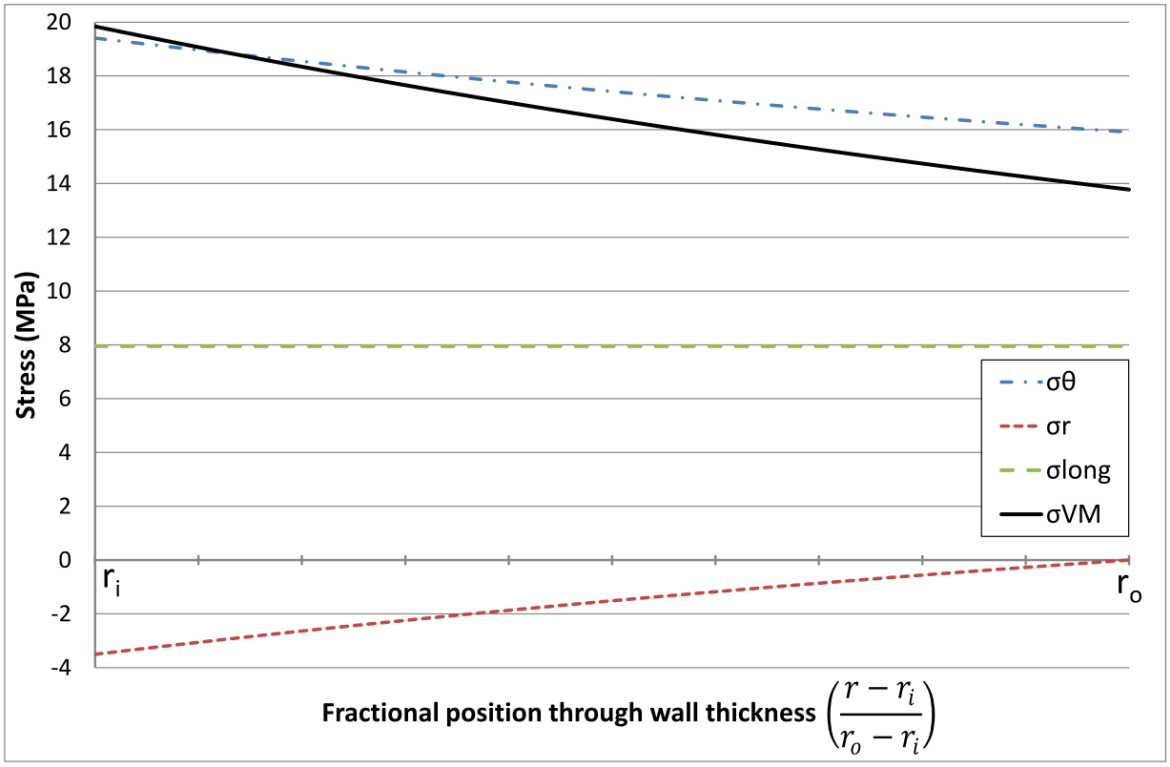

Figure 2.7. *Reformer tube stress state resulting from internal pressure, expressed as a function of position in wall from inner radius (r_i) = 50mm to outer radius (r_o) = 60mm.*

Averaging through the wall thickness, the von Mises effective stress is 16.5 MPa. Assuming a reformer tube length of 13 m and a typical HP alloy density of 7860 kg/m^3, self weight increases σ_z from 7.95 MPa to a maximum of 8.96 MPa. But this increase in σ_z has very little overall effect on the average σ_{VM} through the wall thickness, increasing it by 0.5% to 16.6 MPa

2.3.2 Material overview

Centrifugally cast materials are the preferred choice for reformer tubes. A 5-6 m long steel mould is spun at high speed by drive rollers while liquid alloy is poured into the mould. A hollow liquid tube is formed by centrifugal forces and gradually solidifies. These tube sections are then welded together to form a full length (10-15 m) reformer tube.

HK40 is an alloy containing 25wt% chromium (Cr) and 20wt% nickel (Ni), which was brought about through the development of wrought stainless steel. Since its introduction in the 1960's, it served the reforming industry reliably and became the "standard" material. The addition of niobium (Nb) and significantly more nickel in HP alloys raised reformer tube creep strength appreciably, though cost also increased and greater skill is required to produce the HP alloys.

A large number of HP alloy compositions, which contain a wide variety of modifying elements (e.g. niobium, titanium, tungsten, zirconium and yttrium), are currently used in service. Figure 2.8 outlines the history of materials development for reformer tubes, paying particular attention to the two most common HP-modified alloys currently found in service: HP Mod (also known as HP-Nb) and HP-NbTi (niobium and titanium modified, commonly known as HP-Micro or HP-MA).

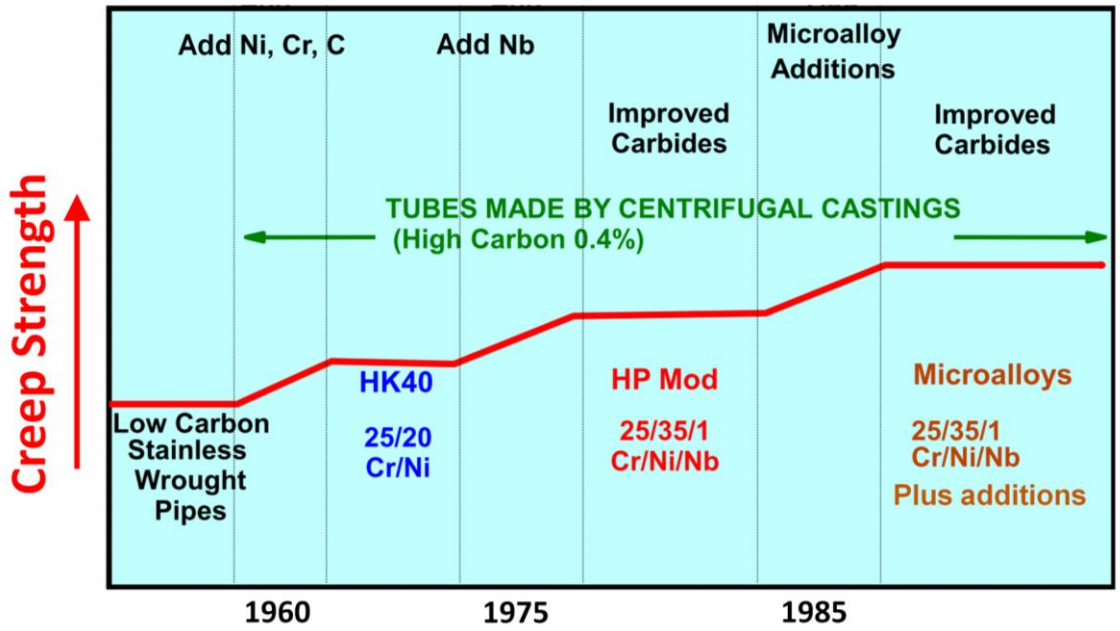

Figure 2.8. *Timeline of reformer tube material development [38].*

Logistically, it is impractical for performance testing purposes to match service conditions exactly, and allow individual creep tests to run for 100,000 hours.

Accelerated creep testing requires an increase in temperature and/or pressure from service conditions, ideally without altering the creep mechanism. 253MA is readily available in a range of sizes and is known to resist oxidation at temperatures up to 1150°C, making it an ideal candidate for testing the effectiveness of creep reinforcement at temperatures exceeding those seen in a reformer furnace. For this reason, the composition of 253MA is included alongside compositions for principal alloys used for reformer tubes, Table 2.1.

Table 2.1. *Nominal composition of principal alloys used for reformer tubes, compared against 253MA.*

	HK40	**HP-Nb**	**HP-MA**	**253MA**
Carbon (wt%)	0.35-0.45	0.4-0.5	0.4-0.5	0.05-0.1
Chromium (wt%)	23-27	24-28	25	20-22
Nickel (wt%)	19-22	34-37	35	10-12
Niobium (wt%)	-	0.6-1.5	1.5	-
Titanium (wt%)	-	-	0.02-0.1	-
Other	-	-	Micro-alloy additions	-
Iron (wt%)	Balance	Balance	Balance	Balance

These alloys are used not only for reformer furnaces, but for a wide range of industrial applications, outlined in Table 1.1, all of which would benefit from creep-resistant hybrid pipe technology. Without the benefit of refractory reinforcement, increasing nominal reformer operating temperatures from 950°C to 1050°C results in a dramatic loss of creep strength, illustrated as a stress-rupture plot in Figure 2.9. For example, a HP-MA component operating at 950°C reduces its allowable stress for a 100,000 hour creep life by 60% when temperature is increased to 1050°C.

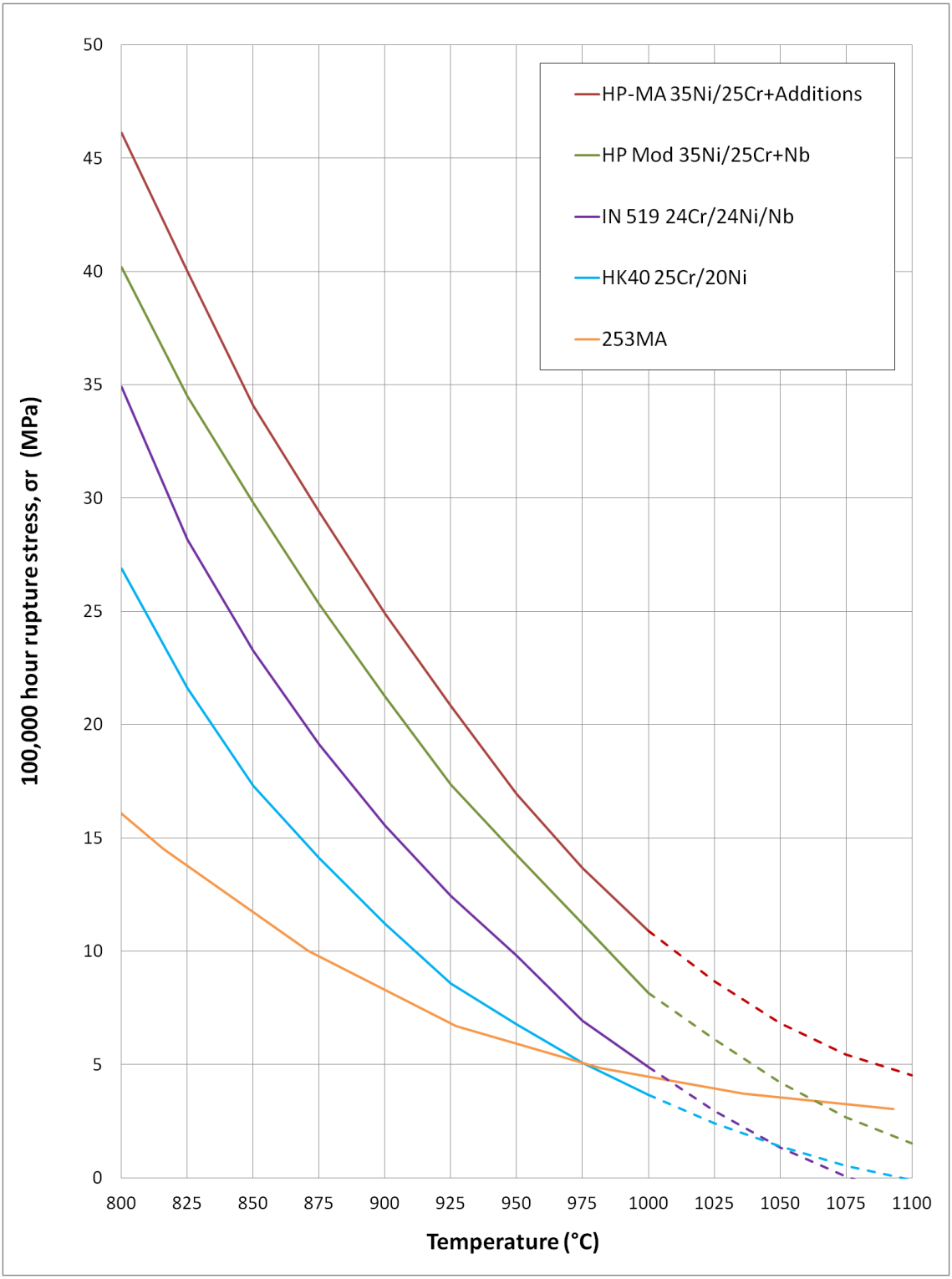

Figure 2.9. *Stress-rupture plot for 100,000 hour rupture lives for various reformer alloys. Adapted from Beyer et al. [39] to include 253MA.*

2.3.3 Damage mechanisms

Reformer tube material requirements include:

- Excellent creep strength.
- Good low-cycle fatigue strength.
- Oxidation resistance.
- Structural stability.

As reformer tubes operate at high temperatures and internal pressures, the primary cause of tube failure is tangential creep damage driven by the tangential (hoop) stress. The considerable self weight of the reformer tubes, in addition to internal pressure stresses, drives the continuous elongation of the tubes during operation. Reformer tubes are inspected regularly, and replaced periodically to avoid unexpected shutdowns due to tube failure. Weld regions are particularly susceptible to cracking. Due to the proprietary nature of HP alloys and reformer technology, deformation mechanism maps are not readily available.

However, reformer tubes are also subjected to other life-limiting mechanisms, such as overheating and thermal shock. During the life of a reformer tube, it will experience a significant number of full thermal and pressure cycles caused by plant start-ups and shut-downs. The cumulative effect of these cycles can be extremely damaging and lead to accelerated creep cracking.

A metal in a gaseous environment constitutes a complex chemical system. In comparison to the "mild" oxidizing environment of air at room temperature, the mixed environment and high temperature inside a reformer furnace is seen as "extremely severe" [40]. The elevated temperature increases rates of reaction exponentially by the Arrhenius equation, resulting in aggressive environmental attack. As a result, reformer alloys are designed to be highly oxidation resistant.

CHAPTER REFERENCES

[1] B. A. Pint, J. R. DiStefano, and I. G. Wright, "Oxidation resistance: One barrier to moving beyond Ni-based superalloys," *Materials Science and Engineering A,* pp. 255-263, 2006.

[2] G. Frommeyer and R. Rablbauer, "High Temperature Materials Based on the Intermetallic Compound NiAl Reinforced by Refractory Metals for Advanced Energy Conversion Technologies," *Steel Research International,* vol. 79, pp. 507-513, 2008.

[3] T. Grobstein and H. M. Yun, "The Role of the Interface in Refractory Metal Alloy Composites," in *American Institute of Physics*, 1991, pp. 186-192.

[4] D. W. Petrasek and R. H. Titran, "Creep Behaviour of Tungsten/Niobium and Tungsten/Niobium-1 Percent Zirconium Composites," in *Fifth Symposium on Space Nuclear Power Systems*, Albuquerque, New Mexico, 1988.

[5] J. R. Stephens, D. W. Petrasek, and R. H. Titran, "Refractory Metal Alloys and Composites for Space Power Systems," in *Spring meetings of the Materials Research Society*, Reno, Nevada, 1988.

[6] T. L. Grobstein, "Creep Behaviour of Tunsten Fiber Reinforced Niobium Metal Matrix Composites," in *Sixth Symposium on Space Nuclear Power System*, Albuquerque, New Mexico, 1989.

[7] M. E. El-Dahshan, d. P. Whittle, and J. Stringer, "The Oxidation and Hot Corrosion Behaviour of Tungsten-Fiber Reinforced Composites," *Oxidation of Metals,* vol. 9, pp. 45-67, 1974.

[8] M. F. Ashby, *Materials Selection in Mechanical Design*, 4th ed.: Butterworth-Heinemann, 2010.

[9] S. Arsene and J. Bai, "A New Approach to Measuring Transverse Properties of Structural Tubing by a Ring Test," *Journal of Testing and Evaluation,* vol. 24, pp. 386-391, 1996.

[10] S. McAllister, R. C. Hurst, and T. E. Chung, "Modelling the Multiaxial Creep Behaviour of Alloy 800H," *International Journal of Pressure Vessels and Piping,* vol. 47, pp. 355-370, 1991.

[11] J. Lee, R. C. Bradshaw, R. W. Hyers, J. R. Rogers, T. J. Rathz, J. J. Wall, *et al.*, "Non-contact measurement of creep resistance of ultra-high-temperature materials," *Materials Science and Engineering A,* vol. 463, pp. 185-196, 2007.

[12] U. Andersson, "Which Factors Control the Lifetime of Plastic Pipes and how the Lifetime can be Extrapolated," in *Plastic Pipes XII*, Munchen, Germany, 2001.

[13] Z. W. Guan and J. C. Boot, "Creep Analysis of Polymeric Pipes Under Internal Pressure," *Polymer Engineering and Science,* vol. 41, pp. 955-961, 2001.

[14] T. Mitsueda, K. Fujii, and S. Ohnuki, "Comparison of Creep Damage Appearances Among Low Alloy Steel Pipes," in *Creep and Fatigue and Elevated Temperatures 8*, San Antonio, Texas, 2007.

[15] R. J. Browne, "Creep Rupture Testing of Tubular Model Components," in *Techniques for Multiaxial Creep Testing*, D. J. G. e. al., Ed., ed: Elsevier Applied Science Publishers Ltd, 1986, pp. 311-332.

[16] S. N. Gundarev, A. F. Gurov, V. V. Dement'ev, A. S. Demidov, A. E. Rusanov, and A. A. Khomyakov, "High-Temperature Creep Tests on Specimens of Single Crystal Molybdenum with a Complex Stress State," 1990.

[17] V. Y. Ivanov, Y. P. Nechiporenko, L. N. Yefimenko, and M. I. Yurchenko, *High Temperature Oxidation Protection of Tungsten*. Moscow: Atom Press, 1968.

[18] J. H.E. McCoy, R. L. Stephenson, and J. J.R. Weir, "Mechanical Properties of some Refractory Metals and their Alloys", Oak Ridge National Laboratory, 1964.

[19] P. Schwarzkopf and R. Kieffer, *Refractory hard metals*: Macmillan, 1953.

[20] M. P. Brady and P. F. Tortorelli, "Alloy design of intermetallics for protective scale formation and for use as precursors for complex ceramic phase surfaces," *Intermetallics,* vol. 12, pp. 779-789, 2004.

[21] P. Kofstad, *High Temperature Corrosion*: Elsevier Applied Science Publishers Ltd, 1988.

[22] J. Li and G. J. Weng, "Effective Creep Behaviour and Complex Moduli of Fiber- and Ribbon-Reinforced Rolymer Matrix Composites," *Composites Science and Technology,* vol. 52, pp. 615-629, 1994.

[23] J. Raghavan and M. Meshii, "Creep of Polymer Composites," *Composites Science and Technology,* vol. 57, pp. 1673-1688, 1997.

[24] L. Srikanth and R. M. V. G. K. Rao, "Strength and stiffness behaviour of braided and filament wound glass epoxy composites - Simultaneous studies and comparison," *Journal of Composite Materials,* pp. 1-8, 2013.

[25] D. Johnson. Global Methanol Market Review, http://www.ptq.pemex.com/productosyservicios/eventosdescargas/Documents/Foro%20PEMEX%20Petroqu%C3%ADmica/2012/PEMEX_DJohnson.pdf, [Accessed Decmber 2013].

[26] B. Boyd. Methanol Industry Presentation, http://www.petroleum-economist.com/pdf/BradBoyd.pdf, [Accessed December 2013].

[27] Methanex. Methanol in our lives, http://www.methanol.org/Methanol-Basics/Resources/Methanol-Basics/Methanol-In-Our-Lives.aspx, [Accessed December 2013].

[28] Methanol Principle Uses, http://www.southernchemical.com/wp/products/methanol/principle-uses, [Accessed December 2013].

[29] MethanexCorporation, "Making Methanol," ed, 2011.

[30] M. H. Wesenberg, "Gas Heated Steam Reformer Modelling," Department of Chemical Engineering, Norwegian University of Science and Technology, 2006.

[31] J. Huber and D. Jakobi, "Centricast Materials for High-Temperature Service," presented at the Nitrogen + Syngas 2011 International Conference, Dusseldorf, Germany, 2011.

[32] A. A. Wahab and M. V. Kral, "3D analysis of creep voids in hydrogen reformer tubes," *Materials Science and Engineering A,* vol. 412, pp. 222-229, 2005.

[33] M. Strait, G. Allum, and N. Gidwani, "Synthesis Gas Reformers", Rice University, 1997.

[34] T. L. d. Silveira and I. L. May, "Reformer Furnaces: Materials, Damage Mechanisms and Assessment," *The Arabian Journal for Science and Engineering,* vol. 31, pp. 99-119, 2006.

[35] P. Tait and T. Pearce, Methanex Corporation, (personal communication with B. Reyngoud, 2014)

[36] P. Imizcoz, Schmidt+Clemens, (personal communication with B. Reyngoud, 2013)

[37] J. E. Shigley, *Mechanical Engineering Design*, 1st ed. Singapore: McGraw-Hill Inc, 1986.

[38] G. B. Hawkins, "Steam Reforming: Tube Design", GBH Enterprises Ltd., 2013.

[39] F. Beyer, J. Brightling, P. Farnell, and C. Foster, "Steam Reforming - 50 years of Development, and Challenges for the Next 50 years.", Uhde GmbH, Johnson Matthey Catalysts, 2005.

[40] U. K. Chatterjee, S. K. Bose, and S. K. Roy, *Environmental Degradation of Metals: Corrosion Technology*. New York, NY: Marcel Dekker, Inc., 2001.

CHAPTER 3: LITERATURE REVIEW

The purpose of this chapter is to provide a comprehensive literature review on the subjects of hybrid materials design and high temperature creep reinforcement, as well as the general usage of reinforcement in pressure vessels. A theoretical optimal reinforcement angle is derived, where wire tensions act proportionally to internal pressure stresses.

The subject of creep is briefly outlined, specifically as it pertains to this complex stress state of a heated pipe under internal pressure. For a broader overview on the general subject of creep, many excellent resources such as Dowling, Davis and Kassner [1-3] are available. Additionally, this chapter reviews solutions against creep at high temperature. The high temperature performance characteristics of tungsten are considered alongside other refractory metals. Additionally, issues with oxidation and intermetallic formation, commonly faced by tungsten at high temperature, are briefly addressed.

3.1 Architectured Materials

Materials scientists have thoroughly explored the possibility of "microstructure by design", tailoring properties by altering grain size, twin density, precipitation and polymer chain design. At the opposite end of the scale, structural engineers have developed a number of strategies, using the geometry of components, to meet design requirements without greatly changing the materials. Architectured materials sit at the intermediate scale: developing either geometries or microstructure gradients, at scales which are comparable to the scale of the component. The result of this evolution is that the classical distinction between "materials" and "structures" becomes blurred.

Architectured materials often require the provision of either a controlled spatial distribution of the constituent phases, or multiple length scales in the structure at both the microscopic and mesoscopic levels. Thus the development of architectured materials produces an important paradigm shift in materials engineering because it targets the development of tailored heterogeneous materials [4].

3.1.1 Materials design techniques

Focusing on a specific geometry and composition very early can severely limit potential for optimization. M. Ashby and Y. Bréchet promote a more general 'materials by design' technique which revolves around understanding the physics of the system and tailoring the macro/microstructure to suit. This 'materials by design' approach has been shown to be approximately 70% faster and 10-20% the cost of traditional methods for developing materials [5]. In theory, this approach allows for the potential of individual components to be maximised while also allowing for unit weight/cost to be minimized [6-10].

Ashby and Bréchet have built on Ashby's well-established methodology to explore ways of designing hybrid materials to allow for a superposition of their properties. Here, a hybrid material is defined as "a combination of two or more materials in a predetermined geometry and scale, optimally serving a specific engineering purpose" – paraphrased as "A + B + shape + scale". By treating the hybrid as a whole and selecting materials based on a criterion of excellence derived from the physics of the system, for example stiffness per unit mass, design solutions can be reached which are optimized for a desired property. The example in Figure 3.1 shows how this principle can be applied to design a hybrid material with high strength and high electrical conductivity. The hybrid material 'fills a hole' in the properties chart and is the optimal solution if strength and conductivity are weighted with equal importance.

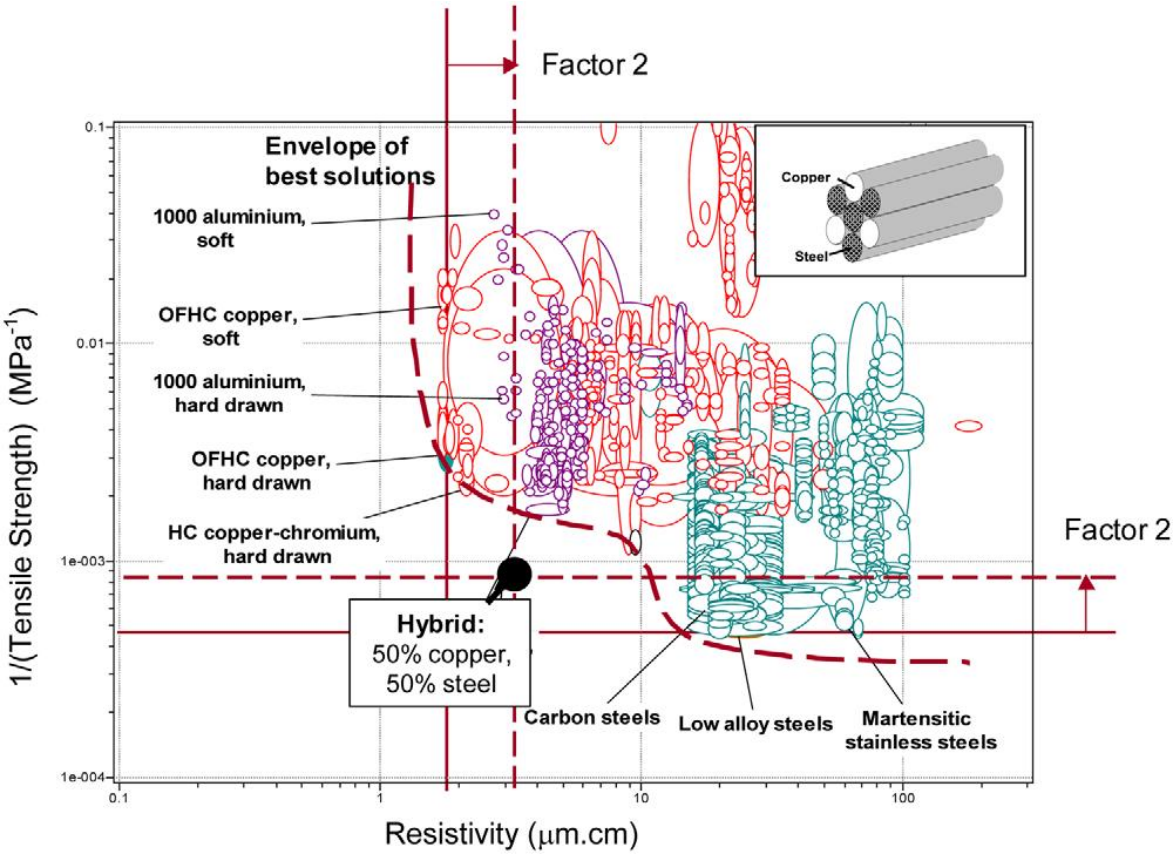

Figure 3.1. *Resistivity and reciprocal of tensile strength for 1700 metals and alloys, seeking to find a material which minimizes both. Clear 'hole' in the property space, filled by copper-steel hybrid [11].*

Low density materials with high stiffness are desirable for numerous applications including structural members of airframes. By plotting Young's modulus against density, Figure 3.2 highlights a hole in property space. With toughness limitations ruling out the use of technical ceramics for many applications, carbon-fibre-reinforced polymers (CFRP) and wood are attractive materials choices where applications call for high stiffness and low density. The development of aluminium foams somewhat begins to fill the hole identified in property space, bridging the gap between metals and polymer foams. Aluminium micro-lattices have the potential to extend even further into this hole in property space, as their structured porosity and interconnectivity can be better controlled to increase part stiffness without an appreciable change in density.

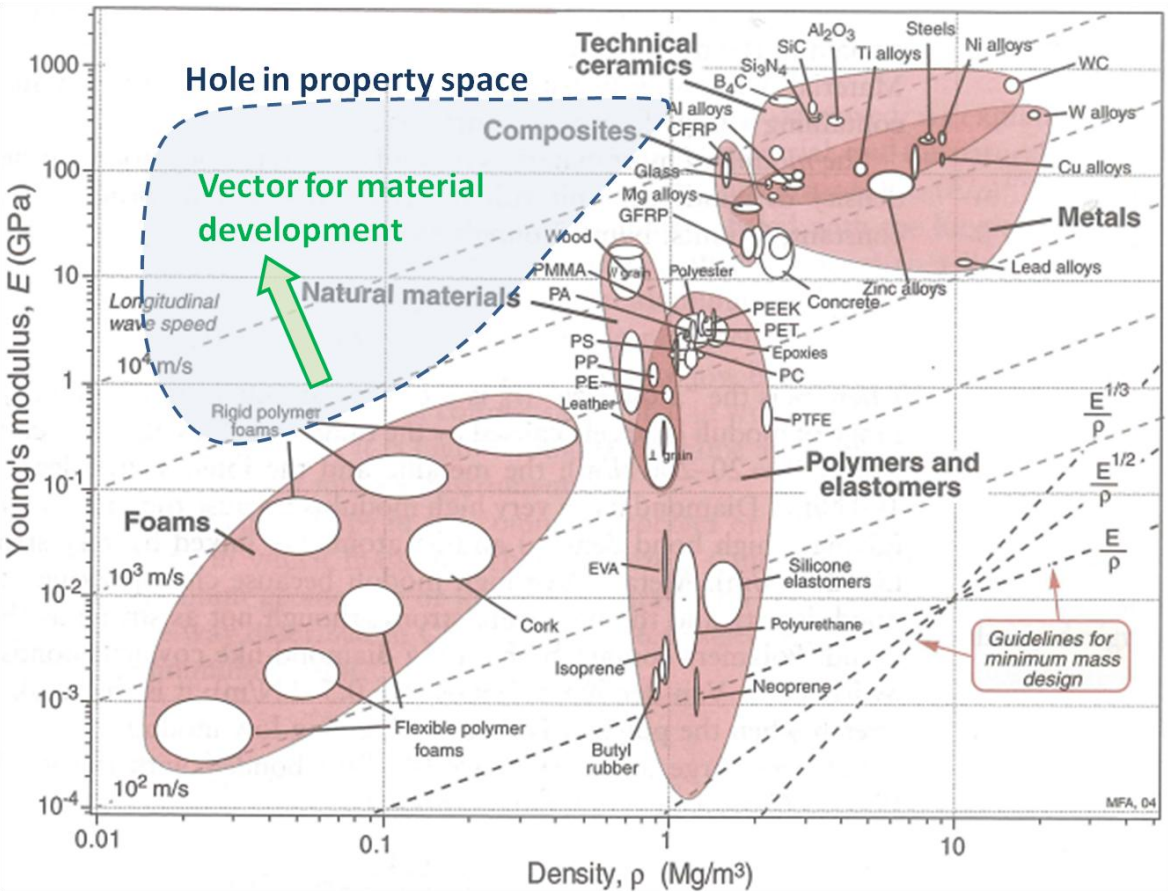

Figure 3.2. *Young's modulus plotted against density, identifying a hole in property space for low density materials with high stiffness. Adapted from [7]*

3.1.2 Performance indices for creep

Selecting an appropriate performance index for a component with a finite life is somewhat complicated. To achieve this, simple models are required to indicate the expected deterioration as a function of stress and environmental conditions. From these models of performance, indices are derived which include variables from the lifetime expected for the part.

To simplify the approach, it is assumed that the material is in steady state creep and follows the classic power law creep expression. First consider, for example, the simple case of a cantilever beam of length L with a load F at its end. Suppose mass is to be minimized and the deflection for a given running time, t_D, should not

exceed δ_D. Again for simplicity, suppose the beam has a square cross section with sides of length 'a' and that this dimension is the free variable while the length L of the beam is fixed. Assuming power law creep, the rate of deflection of the beam is given by:

$$\dot{\delta} = \frac{2}{n+2} A e^{\left(\frac{-Q}{RT}\right)} L^2 \left[\frac{2n+1}{2n} \frac{4FL}{\sigma_0} \frac{1}{a^{\left(\frac{3n+1}{n}\right)}}\right]^n \tag{3.1}$$

Where A and n are material constants, Q is the activation energy, R is the ideal gas constant, T is the absolute temperature and σ_0 is the applied stress.

This rate of decline should be less than δ_D/t_D, which imposes a minimum value for a. It can be shown that for n values commonly observed for metals and alloys, the mass of the beam must be greater than:

$$m = \rho L \left(\frac{4FL}{\sigma_D}\right)^{\frac{2}{3}} \tag{3.2}$$

where σ_D characterizes the magnitude of creep resistance of the material for the design conditions and operating time given. It is given by:

$$\sigma_D = \sigma_0 \left(\frac{n+2}{2} \frac{\delta_D / t_D}{LAe^{\left(\frac{-Q}{RT}\right)}} \right)^{\frac{1}{n}} = \sigma_0 \left(\frac{n+2}{2} \frac{\dot{\delta}}{L\dot{\varepsilon}_0} \right)^{\frac{1}{n}} \tag{3.3}$$

with

$$\dot{\varepsilon}_0 = Ae^{\left(\frac{-Q}{RT}\right)} \tag{3.4}$$

For the cantilever beam case, seeking to maximise specific creep resistance gives a performance index of:

$$I = \frac{\sigma_D^{\frac{2}{3}}}{\rho} \tag{3.5}$$

This general approach can be applied to other modes of loading to find performance indices, as shown in Table 3.1.

Table 3.1. *Performance indices for resistance to creep in classical loading scenarios [12].*

Type of loading	Geometry	Design strength	Performance index
Tension : axial loading 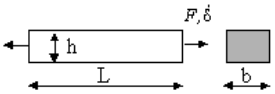	*b* and *h* free	$\sigma_D = \sigma_0 \left(\frac{\dot{\delta}}{L\dot{\varepsilon}_0} \right)^{\frac{1}{n}}$	$I = \frac{\sigma_D}{\rho}$
Bending 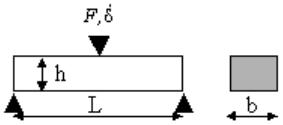	$b = \alpha h$	$\sigma_D = \sigma_0 \left(\frac{\dot{\delta}}{L\dot{\varepsilon}_0} \right)^{\frac{1}{n}}$	$I = \frac{\sigma_D^{2/3}}{\rho}$
	b fixed, *h* free		$I = \frac{\sigma_D^{1/2}}{\rho}$
	h fixed, *b* free		$I = \frac{\sigma_D}{\rho}$
Pipes and pressure cylinders 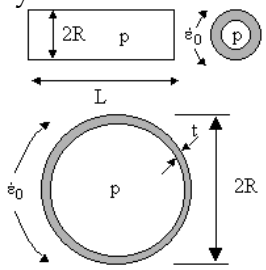	*R* fixed, *t* free	$\sigma_D = \sigma_0 \left(\frac{\dot{R}}{R\dot{\varepsilon}_0} \right)^{\frac{1}{n}}$	$I = \frac{\sigma_D}{\rho}$

3.2 Reinforced Pressure Vessels

Fibre reinforcement is a widely used means of increasing the burst strength of pressure vessels, also facilitating potential cost and weight reduction. Practical applications for this technology range from hydraulic hoses to aircraft fuselages. Most commonly, composite overwrapped pressure vessels are polymers reinforced with carbon or Kevlar® fibres [13].

A polyethylene pipe containing aramid fibres can permit operating pressures of around ten-times the capability of conventional polyethylene pipe. Unlike conventional long fibre reinforced pipe materials, this particular type of construction does not bind the fibres into the matrix, thus preserving the high flexibility of the polyethylene pipe and retaining the ability to coil the pipe [14].

Wire braid reinforcement is the most common reinforcement type used for hydraulic applications, because it provides the best service life/cost economics. At higher pressures, helical winding may be preferred because there are no cross-over points (as in braided constructions) and hence no localised regions of rubbing. [15]

Composite overwrapped pressure vessels are formed by wrapping a filament wound composite (such as carbon fibre set in a polymer matrix) around a metallic or ceramic liner. This liner may be designed to prevent leaking through matrix microcracks as well as protecting the vessel structure from chemical or environmental damage due to the contents of the vessel. The liner may also carry a significant portion of the pressure load [16, 17].

An alternate method of strengthening metallic pressure vessels, without resorting to reinforcement, is to induce an internal compressive residual stress during fabrication. By applying a large internal pressure, the vessels yields plastically and leaves an inner layer of compressively stressed metal once the pressure is released. This method of fabrication is known as autofrettage.

3.2.1 High temperature pressure vessels

While general strategies to strengthen or control the failure of pressure vessels remain largely unchanged with temperature, elevated temperatures limit the

range of suitable materials. The increased temperature also introduces a new range of potential failure mechanisms. Hydraulic systems are predominantly concerned with overpressurization, whereas creep and environmental attack become more of a factor at elevated temperatures, depending on the material systems in question.

While purely conceptual, a 1995 patent by Nobuyuki [18] proposed the use of helically wound reinforcement, welded in place over the external surface of a pipe to increase resistance to elongation deformation in a high temperature environment such as an ethylene pyrolysis furnace. Proposed materials for the pipe body include typical reformer tube materials HK40 and HP-alloy, and specified reinforcement candidates are Ni-based alloys. The present work seeks to improve on this base concept through the utilization of refractory reinforcement with an optimized braided architecture which is not permanently bonded to the pipe surface.

Following a general explanation of creep, Section 3.5.4 details numerous strategies specific to combating creep. The methods outlined are all applicable for the strengthening of high temperature pressure vessels.

3.3 Neutral Angle

3.3.1 Neutral angle derivation

The anisotropy of the reinforcement layer can be manipulated such that a cylindrical pressure vessel is twice as strong circumferentially as it is axially, effectively making it reinforced proportionally to the internal stresses. For fibre reinforcement oriented at an angle θ from the pipe axis, the theoretical angle at

which pressure stresses are balanced by the reinforcement is known as the neutral angle (θ_N), and is 54.7° regardless of factors such as pipe diameter [14, 15, 19].

Consider a cylindrical pressure vessel reinforced by fibres oriented at angle θ to the longitudinal axis. Figure 3.3 shows a free body diagram of a unit length in the longitudinal direction, where there are n fibres transmitting tension T. The circumferential distance cut by these n fibres is $tan\theta$. Tube wall thickness is denoted t.

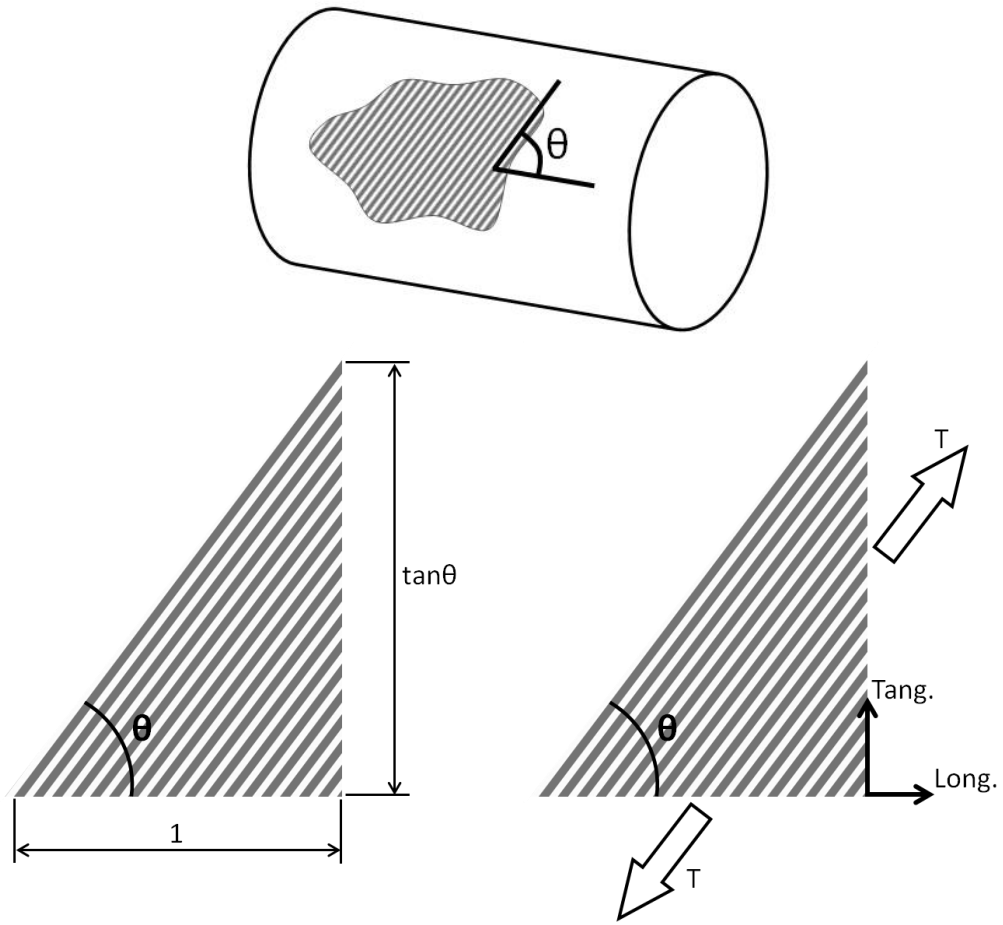

Figure 3.3. *Free body diagram for neutral angle derivation over a unit length of a filament-reinforced pressure vessel.*

The wire tension force is decomposed into the tangential and longitudinal directions, and those tension components are aligned to balance tangential (hoop) and longitudinal stresses. Figure 3.4 considers the loads applied along a longitudinal section of a reinforced pressure vessel.

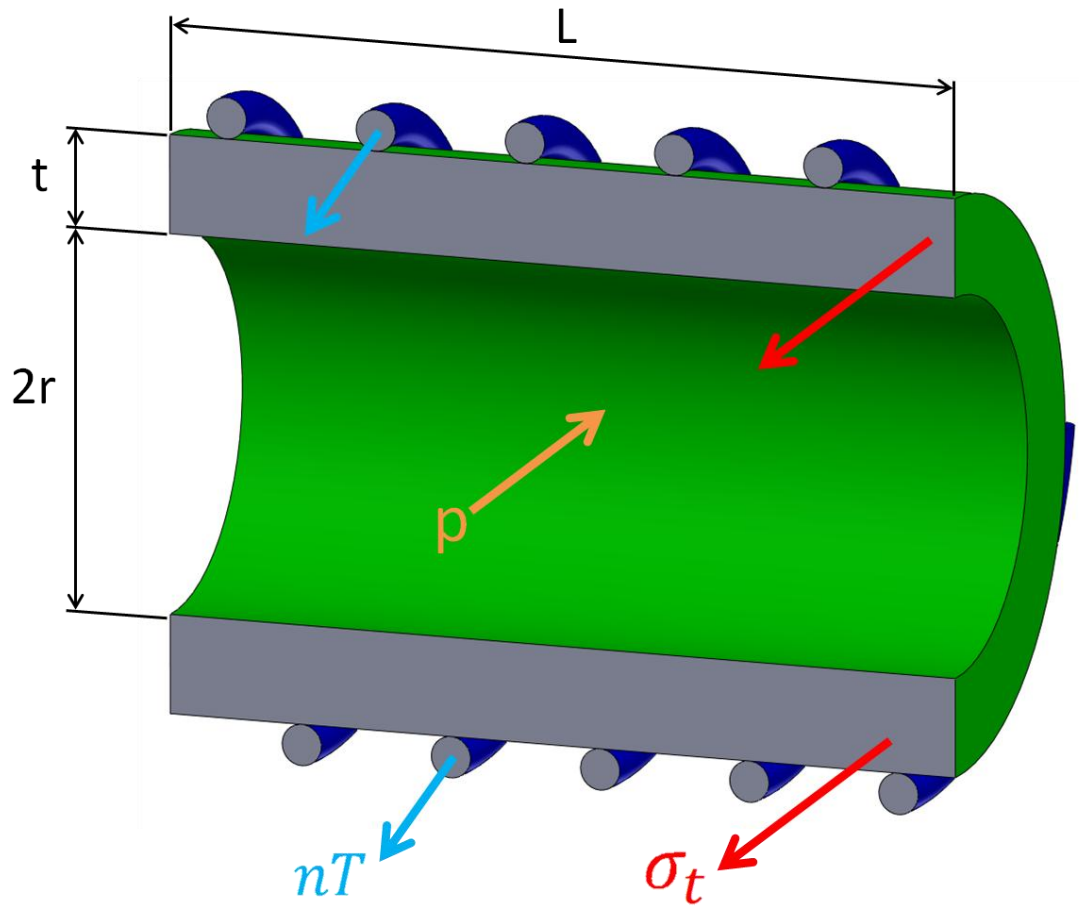

Figure 3.4. *Longitudinal section of reinforced pressure vessel, allowing tangential stresses to be balanced against wire tensions in the tangential direction.*

Translating tangential (hoop) stress and internal pressure into forces, and decomposing the tension force into the tangential direction (from Figure 3.3), a force balance in the direction of the tangential stress gives:

$$\sigma_t 2tL = p2rL - nTsin\theta 2L \tag{3.6}$$

$$\sigma_t = \frac{pr}{t} - \frac{nT}{t} sin\theta \tag{3.7}$$

Note that the pressure vessel has been assumed to be thin-walled. If the reinforcement were to be removed, Equation 3.7 reduces to the typical expression for tangential (hoop) stress in a thin-walled pressure vessel: $\sigma_t = pr/t$.

Letting $A = pr/t$ and $B = nT/t$, Equation 3.7 simplifies to:

$$\sigma_t = A - B\sin\theta \qquad (3.8)$$

Sectioning in a plane orthogonal to that considered in Figure 3.4 allows loads applied along the pressure vessel axis to be resolved, Figure 3.5.

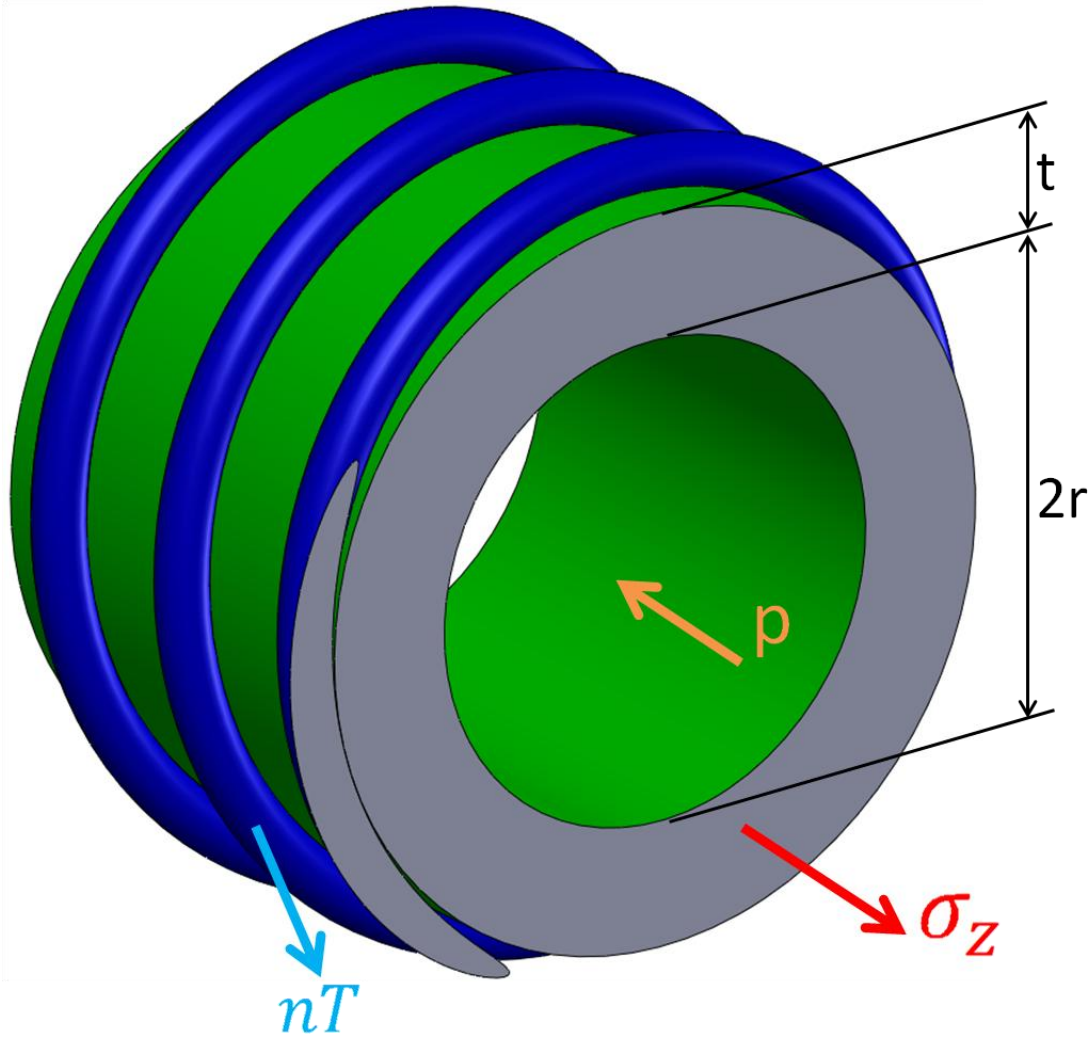

Figure 3.5. *Circumferential section of reinforced pressure vessel, allowing longitudinal stresses to be balanced against wire tensions in longitudinal direction.*

Translating longitudinal stress and internal pressure into forces, and decomposing the tension force into the longitudinal direction (from Figure 3.3), a force balance in the direction of the longitudinal stress gives:

$$\sigma_z 2\pi rt = p\pi r^2 - \frac{nTcos\theta}{tan\theta} 2\pi r \tag{3.9}$$

$$\sigma_z = \frac{pr}{2t} - \frac{nTcos\theta}{t * tan\theta} \tag{3.10}$$

$$\sigma_z = \frac{A}{2} - B\frac{cos\theta}{tan\theta} \tag{3.11}$$

At θ_N, the reinforcement is oriented to act proportionally to the applied stresses, i.e. σ_t/σ_z = 2 for a thin-walled pressure vessel. Using Equations 3.8 and 3.11 to set σ_t= 2 σ_z gives:

$$A - Bsin\theta = 2\left(\frac{A}{2} - B\frac{cos\theta}{tan\theta}\right) \tag{3.12}$$

$$sin\theta = 2\frac{cos\theta}{tan\theta}$$

$$tan^2\theta = 2$$

$$\theta = 54.7°$$

Note that from the derivation of this state of equilibrium, net tangential and longitudinal stresses are not necessarily zero. From Equation 3.8, tangential stress is zero when $B = A/sin\theta$, implying there exists a specific wire tension, T, where net stress in the tangential direction is zero, assuming $A = pr/t$ is constant and recalling that $B = nT/t$. Similarly, Equation 3.11 reveals that longitudinal stress is zero when $B = Atan\theta/2cos\theta$. Equating these two expressions for B to find a point where both net tangential and longitudinal stresses are zero, gives:

$$B = \frac{Atan\theta}{2cos\theta} = \frac{A}{sin\theta} \tag{3.13}$$

$$\frac{1}{2} = \frac{cos\theta}{sin\theta tan\theta}$$

$$tan^2\theta = 2$$

$$\theta = 54.7°$$

That is, in theory, orienting reinforcement at θ_N does in fact reduce the net multiaxial stress resulting from internal pressure to zero. This observation is fitting with the observations of Safford, Hunt, Vaughan and Evans [14, 15, 19]. At the neutral angle of 54.7°, reinforcing fibres can carry virtually all the pressure generated stresses without any plastic strain on the containing walls. The pipe strength is then determined by the fibre strength. When the reinforcement is oriented at this angle and internal pressure is applied, it has been demonstrated that there is no plastic strain of the pipe in any direction, assuming no elongation of the reinforcement [14, 15, 19].

In the case of reinforcement embedded in the matrix of the pipe, and assuming there is sufficient plasticity in the pipe, the reinforcement will shift and seek to orient itself at the equilibrium position of the neutral angle. i.e. when the reinforcement angle is higher than θ_N: the pipe will increase in length, and its diameter will decrease. When the reinforcement angle is lower than θ_N: the pipe will shorten in length, and its diameter will increase [19].

It is particularly important for fire hoses to be reinforced at θ_N, to avoid the nozzle jumping forward or backward as the fibres try to align themselves to the neutral angle [20]. Pneumatic artificial muscles use this phenomenon to their advantage, deliberately setting the reinforcement angle different to the θ_N to produce a known magnitude of extension/contraction when pressurized.

3.3.2 McKibben actuators

As alluded to in the previous section, there are specific design applications where a controllable elongation/contraction is required for a given applied pressure. The phenomenon whereby braided reinforcement shifts to seek the equilibrium position of the neutral angle is utilized in pneumatic artificial muscles. When considering the creep reinforcement application intended for the current project, performance is expected to be optimal when the braid is oriented at θ_N. However, studies of McKibben actuators offer useful insight into the dynamics of how the reinforcement shifts towards this optimal point of equilibrium.

The most frequently used and researched pneumatic muscle is the McKibben actuator [21], an internally pressurized elastic cylinder, or membrane, covered by a shell braided with rigid fibres woven at $\pm\theta$ to the longitudinal axis, Figure 3.6. Typical materials used are latex or silicone rubber and nylon fibres for the membrane and braid, respectively.

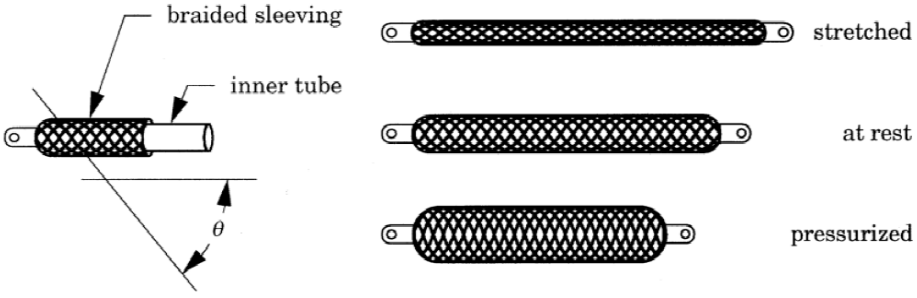

Figure 3.6. *McKibben actuator – cylindrical flexible tube surrounded by a braided shell [21].*

Analytical results of McKibben actuator tests show that the deformed fibre angle approaches 54.7° at infinite pressure. The actuator elongates and contracts for initial angles above and below 54.7°, respectively [22]. Typically, these actuators

are designed for a reinforcement angle of 60° for the maximum inflation state, and 20° for the fully stretched state [23].

Chou and Hannaford [24] considered the conservation of energy in a McKibben actuator in order to derive an expression for net axial tension as a function of braid angle, θ. In doing so, they provided an alternate derivation for the neutral angle which showed that axial tension is zero when θ = 54.7°.

Input work (W_{in}) is done when gas pushes the inner membrane surface:

$$dW_{in} = \int_{S_i} (P - P_0) dl_i \cdot ds_i = (P - P_0) \int_{S_i} dl_i \cdot ds_i = P' dV \tag{3.14}$$

where P is the absolute internal pressure, P_0 is the environment pressure (1 atm), P' denotes the relative pressure, S_i, the total inner surface, ds_i, the area vector, dl_i, the inner surface displacement, and dV, the volume change. Output work (W_{out}) is associated with the volume change when the actuator shortens:

$$dW_{out} = -FdL \tag{3.15}$$

where F and dL are axial tension and axial displacement, respectively. Assuming an idealized system without losses or energy storage, conservation of energy dictates that:

$$dW_{out} = dW_{in} \tag{3.16}$$

$$-FdL = P'dV$$

$$F = -P' \frac{dV}{dL} \tag{3.17}$$

To estimate dV/dL, it is assumed that the reinforcement shell is rigid in the tangential direction, so the actuator volume depends only on length. Additionally,

the middle portion of the actuator is treated as a perfect cylinder of length L with zero wall thickness. As in Figure 3.6, θ is the angle between the helically wound reinforcement threads of which the braid is comprised, and the longitudinal axis of the cylinder. D is the diameter of the cylinder, n the number of turns and b is the length of the helically wound thread. Geometrically, L and D can be expressed as functions of θ, n and b.

$$L = b\cos\theta \tag{3.18}$$

$$D = \frac{b\sin\theta}{n\pi} \tag{3.19}$$

The cylinder volume is:

$$V = \frac{1}{4}\pi D^2 L = \frac{b^3}{4\pi n^2}\sin^2\theta\cos\theta \tag{3.20}$$

Therefore from Equation 3.17, F can be expressed as a function of P' and θ:

$$F = -P'\frac{dV}{dL} = -P'\frac{dV/d\theta}{dL/d\theta} \tag{3.21}$$

$$= \frac{P'b^2(3\cos^2\theta - 1)}{4\pi n^2}$$

$$\rightarrow F = \frac{\pi D_0^2 P'}{4}(3\cos^2\theta - 1) \tag{3.22}$$

Where $D_0 = b/n\pi$, is the diameter when θ = 90°. Equation 3.22 shows that tension is linearly proportional to pressure, and is a monotonic function of the braid angle for 0° < θ < 90°. Maximal shortening of the actuator is achieved when $F = 0$ i.e. when $3\cos^2\theta - 1 = 0$, $\theta = \cos^{-1}\left(\sqrt{1/3}\right)$ = 54.7°. The tension-braid angle relationship of Equation 3.22 is plotted in Figure 3.7 using nominal dimensions of D_0 = 25.4 mm and P' = 4 MPa.

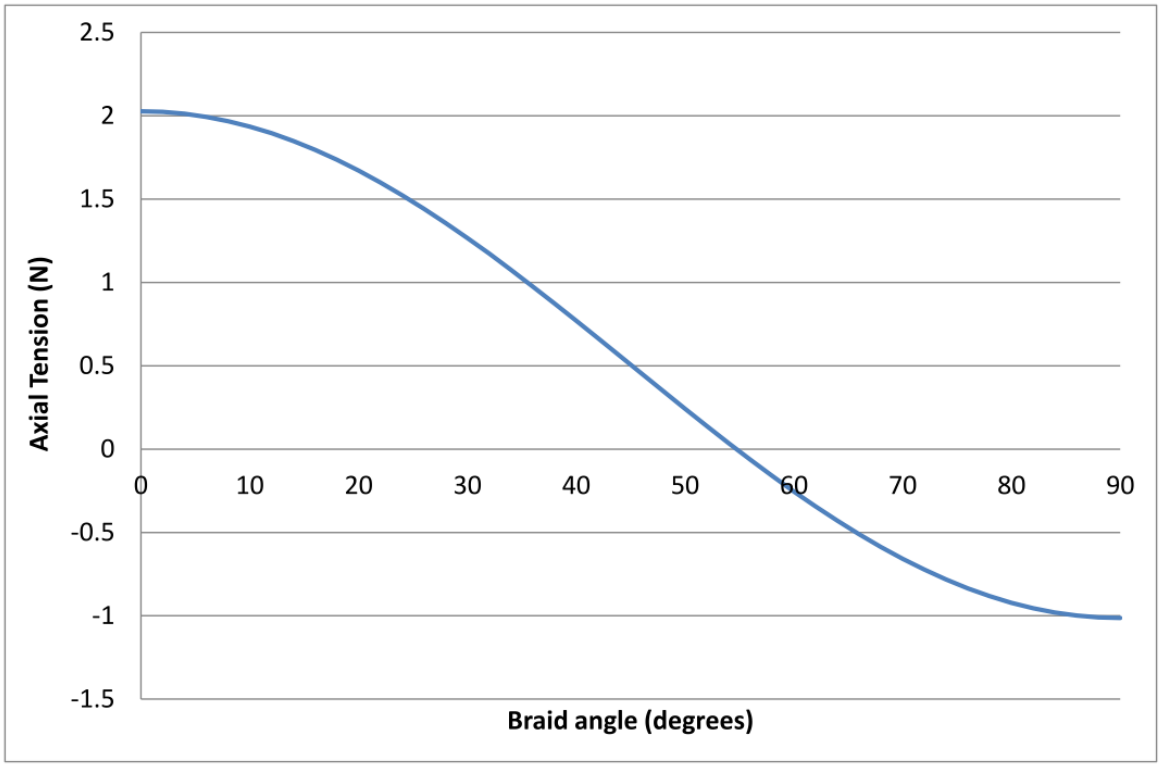

Figure 3.7. *Axial tension in a McKibben actuator as a function of braid angle. Note axial tension is zero at the neutral angle of 54.7°.*

3.3.3 Biological systems

In a similar capacity to McKibben actuators, biologists have found crossed fibre reinforcement structures in a range of biological systems where rapid contraction or elongation is required for a given change in pressure. These structures have been found in animals as diverse as squids and worms [25, 26]. When capturing prey, the muscular stalks of the two tentacles of a squid (as opposed to the eight legs) rapidly elongate – approximately 70% over 30 ms. This rapid forward motion is, in part, facilitated by layers of helical muscle fibres in the tentacular stalk [25].

It has been observed that for a small fibre angle relative to the longitudinal axis, the structures contract when pressurized e.g. lizard tongues [27]. At an angle of 54.7°, the tangential and longitudinal stresses balance and increase volume tensions the fibres without causing either contraction or elongation. This angle

also provides the maximum enclosed volume for a given fibre length and produces the strongest structure [22]. For reinforcement angles above 54.7° (e.g. starfish tube feet [28]), the structure elongates under pressure.

Work by Clark and Cowey [26] into the change in shape of specific group of worms revealed a structure of inextensible fibres arranged in alternate left- and right-handed geodesic helices running around the body of the animal, Figure 3.8(a). Investigation into factors controlling this observed change in worm shape reveals further information on the general behaviour of braided and helical reinforcement as it seeks the equilibrium point of the neutral angle. Although the fibres themselves are inextensible, changes of length of the body, or parts of the body, of the worm are permitted by a change in the angle between intersecting elements in the lattice formed by the fibres.

As the inclination of the fibres changes, so does the total volume the system can contain. Assuming a circular cross-section throughout, the volume varies as:

$$V = \frac{D^3 sin^2\theta cos\theta}{4\pi} \tag{3.23}$$

Where D is the length of a single turn of the geodesic fibre bounding the system and θ is the angle between the fibre and the longitudinal axis, Figure 3.8(b). Alternatively, assuming constant volume, Equation 3.23 can be rearranged to express helical fibre length, D, in terms of θ, as can be seen in Figure 3.8(d).

$$D = \sqrt[3]{4\pi V / sin^2\theta cos\theta} \tag{3.24}$$

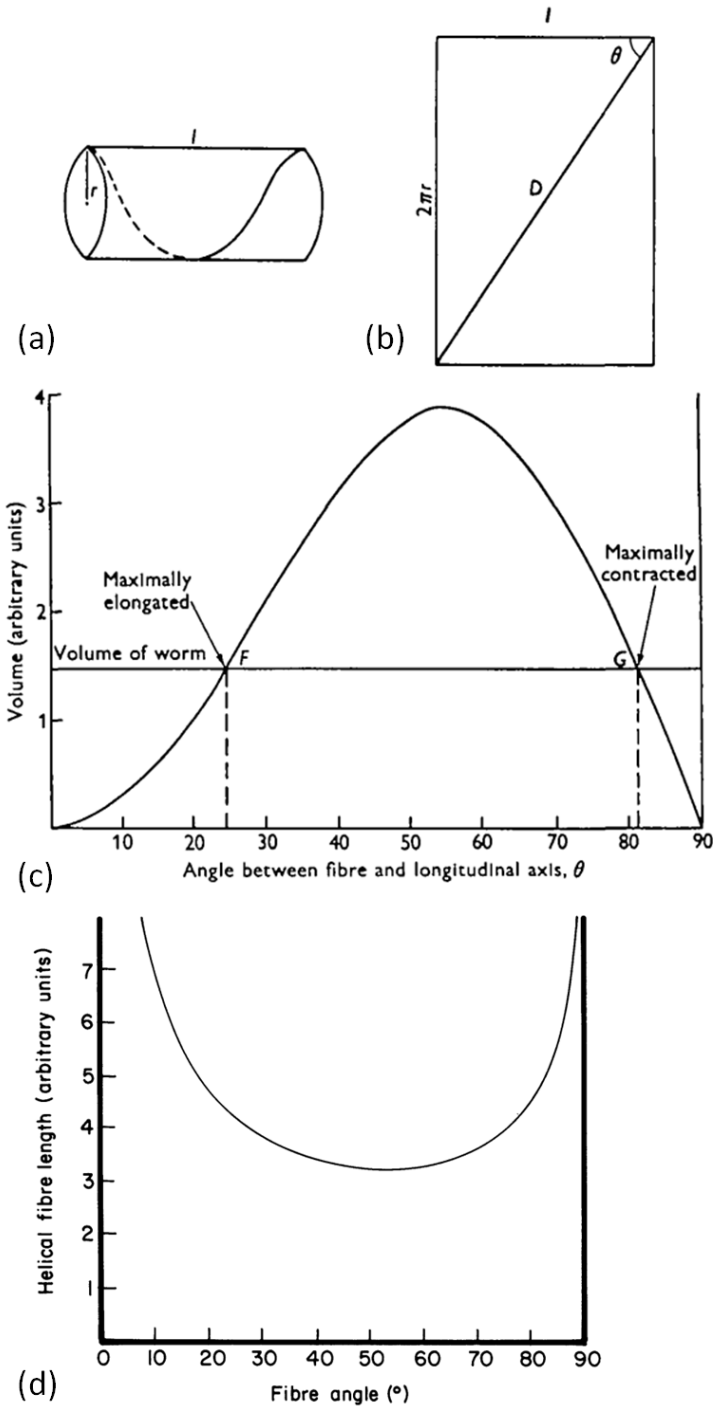

Figure 3.8. *(a) Unit length of a cylindrical 'worm' bounded by a single turn of the geodesic fibre system (fibres running in the opposite sense have been omitted for clarity) (b) the same unit length of worm slit along the top and flattened out (c) curve representing the theoretical relationship between the volume contained by the fibre system and the inclination of the fibres to the longitudinal axis. Points of intersection, F and G, are the limiting positions of elongation and contraction for the particular species of worm. (d) effect of fibre angle on length of a helical fibre wrapping a constant volume cylinder. Adapted from [26, 27].*

Figure 3.8(c) reveals that volume approaches zero as θ tends to 0° and the system elongates to become a long, thin thread and the length approaches D. The other limit, where the volume again approaches zero is when θ tends to 90° and the system is reduced to a thin disk of a circumference equal to D. At an intermediate point where θ = 54.7°, the volume contained by the system is at a maximum. Alternatively, Figure 3.8(d) shows that for a constant volume cylinder, the helical fibre length D is minimized when θ = 54.7°. Both Figures 3.8(c) and (d) clearly illustrate the state of equilibrium which is reached at θ_N, where maximum volume or minimum fibre length can both be viewed as 'lowest energy states' for a given internal pressure.

3.4 Structure-Property Relationships

Commonly employed modelling approaches such as those used in [29-32] to calculate hybrid mechanical properties of braided composite material were not applicable here due to the absence of a matrix. However, the methodology used to develop a stiffness model for a triaxial braid in [29, 33] does reveal that overall braid stiffness is a function of braid angle (θ), wire diameter (d_w), packing fraction (κ), yarn sectional area (A_y), and length (L_c) and angle of undulation (crimp angle) (ϕ) through the thickness of the braid, Figure 3.9.

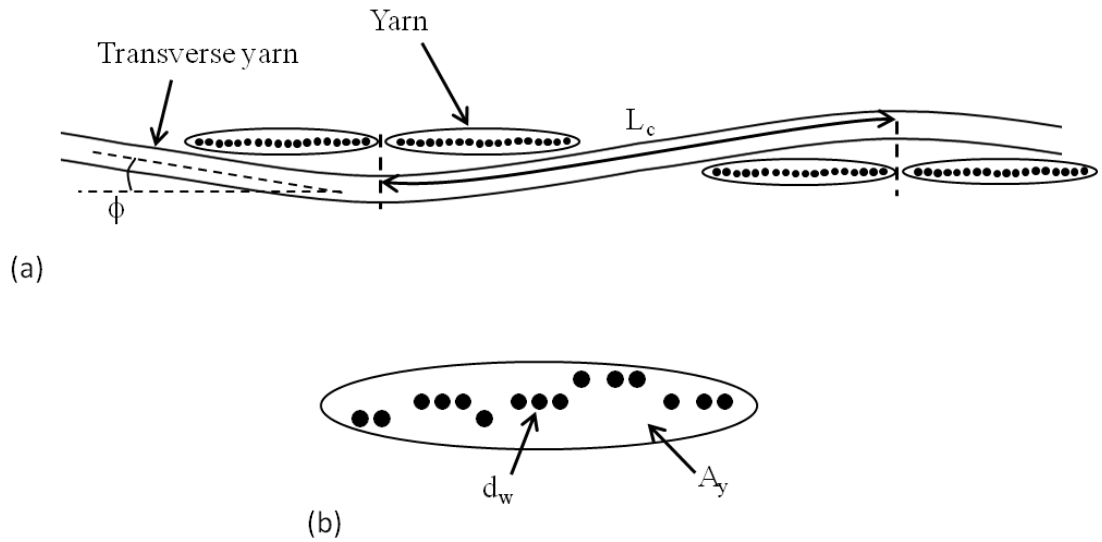

Figure 3.9. *Braid sectional schematic (a) Overall braid schematic for section in x′ plane (b) yarn cross sectional shape with individual wire strands shown.*

Where n_w is number of wires in a single yarn and therefore the packing fraction is $\kappa = n_w\pi(d_w/2)^2/A_y$.

Therefore, it can be deduced that an experimentally measured stiffness encapsulates the collective effect of these architectural features. Stiffness is also a property which can be determined theoretically, using means such as classical lamination theory.

3.4.1 Braid stiffness from classical lamination theory

Braided composite stiffness properties are strongly influenced by braid angle. As a simple model, the braid geometry may be thought of as a laminate of two lamina oriented at $\pm\theta$. Using Cartesian coordinates, this permits classical lamination theory (CLT) to be used to determine the braid stiffness characteristics in the global (x-y) coordinate system [34]. A schematic of the coordinate system for a single lamina is shown in Figure 3.10. However, it should be noted that the constitutive micromechanical laws for unidirectional plies do not account for undulations, and work by Birkefeld et al [35] has shown that CLT consistently

overestimates E_x and E_y when compared to proprietary modeling software packages WiseTex and LamTex.

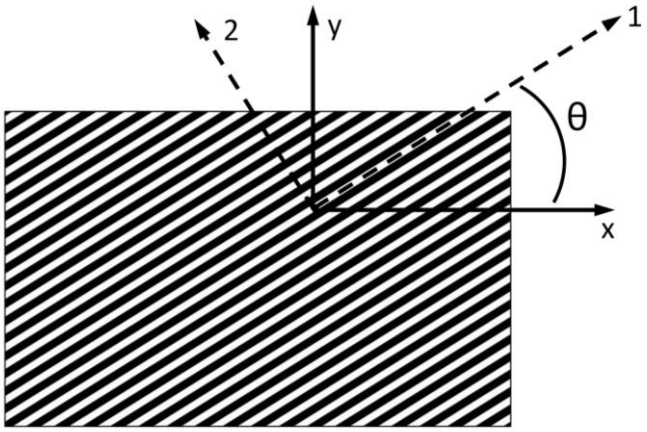

Figure 3.10. *Schematic of single lamina coordinate systems, global (x-y) coordinates and local (1-2) coordinates.*

The primary differences between the ideal laminate considered by CLT and a braided tubular structure are the lack of matrix material in the braid to bond the fibres together and fix the reinforcement angle, and also the cylindrical geometry of the braided reinforcement. However, stiffness perpendicular to the fibre direction (E_2) is still nonzero in the case of the braided reinforcement due to frictional interactions between strands and the overlapping, interlocking nature of the basket weave structure.

In terms of tensor strains, the 2D lamina stiffness relation can be expressed as:

$$\begin{Bmatrix}\sigma_{11}\\ \sigma_{22}\\ \tau_{12}\end{Bmatrix} = \begin{bmatrix}Q_{11} & Q_{12} & 0\\ Q_{21} & Q_{22} & 0\\ 0 & 0 & 2Q_{66}\end{bmatrix}\begin{Bmatrix}\varepsilon_{11}\\ \varepsilon_{22}\\ \varepsilon_{12}\end{Bmatrix} \tag{3.25}$$

Where σ is stress, τ is shear stress, [Q] is the lamina stiffness matrix and ε is strain. Note that these properties are defined in the local (*1-2*) coordinate system, with σ_{11}

denoting stress in the fibre direction, σ_{22} the stress perpendicular to the fibres, and τ_{12} the shear stress in the *1-2* plane. Terms in [Q] are defined as:

$$Q_{11} = \frac{E_1}{1 - v_{12}v_{21}}, \quad Q_{22} = \frac{E_2}{1 - v_{12}v_{21}}, \quad Q_{12} = \frac{v_{12}E_2}{1 - v_{12}v_{21}},$$
$$Q_{21} = \frac{v_{21}E_1}{1 - v_{12}v_{21}}, \quad Q_{66} = G_{12} \tag{3.26}$$

Where ν_{12} and ν_{21} are the major and minor Poisson's ratios, respectively, ν_{12} is the ratio of strain caused in the transverse direction by a strain in the fibre direction. E_1 and E_2 are the moduli of elasticity in the fibre and transverse directions, respectively, and G_{12} is the shear modulus in the *1-2* plane. Note that for any linear elastic (Hookean) body, Maxwell's reciprocity theorem states that the stiffness matrix must be symmetrical [36, 37] and therefore $Q_{12} = Q_{21}$, giving $v_{21}E_1 = v_{12}E_2$.

[Q] is transformed from local (*1-2*) to global (*x-y*) coordinates by the operation:

$$[\bar{Q}] = [T]^{-1}[Q][T] \tag{3.27}$$

Where $[\bar{Q}]$ is the transformed lamina stiffness matrix and, letting $m=cos\theta$ and $n=sin\theta$, T is:

$$[T] = \begin{bmatrix} m^2 & n^2 & 2nm \\ n^2 & m^2 & -2nm \\ -nm & nm & m^2 - n^2 \end{bmatrix} \tag{3.28}$$

Repeating this process to obtain a second $[\bar{Q}]$ for the $-\theta$ lamina, CLT can then be used to combine the stiffness properties of the two layers.

For a simple 2-ply laminate, the height positions of the layer surfaces in the stack (relative to the mid-surface) are: $z_0 = -t/2$, $z_1 = 0$ and $z_2 = t/2$, where t is the overall laminate thickness, Figure 3.11.

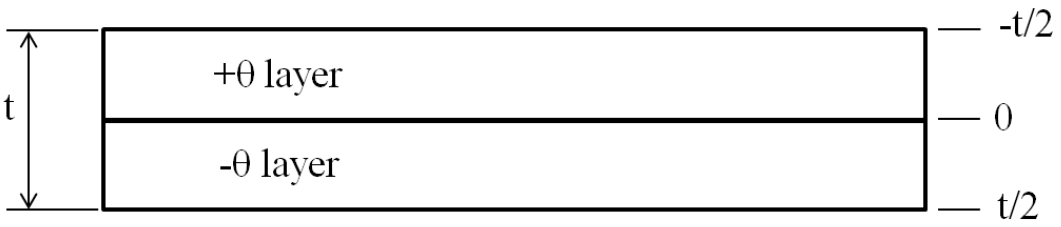

Figure 3.11. *Simple schematic of 2-ply laminate.*

[A], [B] and [D] are the extensional stiffness, coupling stiffness and bending stiffness matrices, respectively. For *N* lamina, they are expressed as:

$$A_{ij} = \int_{-t/2}^{t/2} \left(\bar{Q}_{ij}\right)_k dz = \sum_{k=1}^{N} \left(\bar{Q}_{ij}\right)_k (z_k - z_{k-1}) \tag{3.29}$$

$$B_{ij} = \frac{1}{2} \sum_{k=1}^{N} \left(\bar{Q}_{ij}\right)_k \left(z_k^2 - z_{k-1}^2\right) \tag{3.30}$$

$$D_{ij} = \frac{1}{3} \sum_{k=1}^{N} \left(\bar{Q}_{ij}\right)_k \left(z_k^3 - z_{k-1}^3\right) \tag{3.31}$$

These matrices relate force $\{N\}$ and moment $\{M\}$ resultants to mid-surface strains $\{\varepsilon_0\}$ and curvatures $\{\kappa\}$ by:

$$\begin{Bmatrix} N \\ M \end{Bmatrix} = \begin{bmatrix} A & B \\ B & D \end{bmatrix} \begin{Bmatrix} \varepsilon_0 \\ \kappa \end{Bmatrix} \tag{3.32}$$

Or inverting:

$$\begin{Bmatrix} \varepsilon_0 \\ \kappa \end{Bmatrix} = \begin{bmatrix} A' & B' \\ B' & D' \end{bmatrix} \begin{Bmatrix} N \\ M \end{Bmatrix} \tag{3.33}$$

where:

$$\begin{aligned} [A'] &= [A^*] - [B^*][D^*]^{-1}[C^*], & [B'] &= [B^*][D^*]^{-1} \\ [C'] &= -[D^*]^{-1}[C^*] = [B']^T = [B'], & [D'] &= [D^*]^{-1} \end{aligned} \tag{3.34}$$

and:

$$[A^*] = [A]^{-1}, \qquad [B^*] = -[A]^{-1}[B]$$
$$[C^*] = [B][A]^{-1}, \qquad [D^*] = [D] - [B][A]^{-1}[B] \tag{3.35}$$

The terms in the [A′] matrix represent compliances and can be associated with the material properties in the global (*x*-*y*) axes. Moduli of elasticity in the longitudinal and transverse directions are calculated as:

$$E_x = \frac{1}{tA'_{11}}, \quad E_y = \frac{1}{tA'_{22}} \tag{3.36}$$

3.4.2 Wrap stiffness from spring constant

To calculate the stiffness of simple helically wound reinforcement (commonly referred to as a wrap), it can be treated as an axial spring. A theoretical spring constant can be calculated from Equation 3.37 [38]. Where *G* is the shear modulus of rigidity, *d* is the wire diameter, *D* is the coil diameter and *N* is the number of active coils, Figure 3.12.

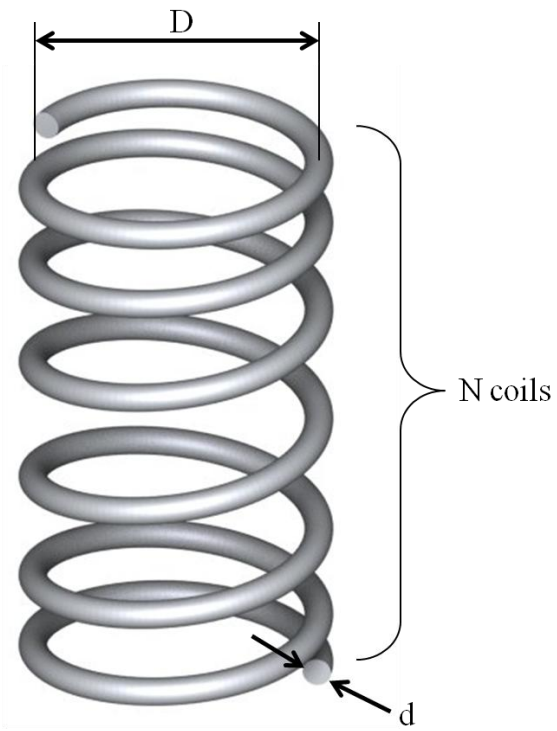

Figure 3.12. *Axial spring schematic.*

$$k = \frac{Gd}{8\left(\frac{D}{d}\right)^3 N} \tag{3.37}$$

In order to relate the theoretical spring constant to longitudinal stiffness, the sectional area of the wrap acting in the direction of applied load must be determined, Figure 3.13. Note that measurements of original length, L_0, and wrap angle, θ, are made under initial conditions, when the coil is hanging under self weight only.

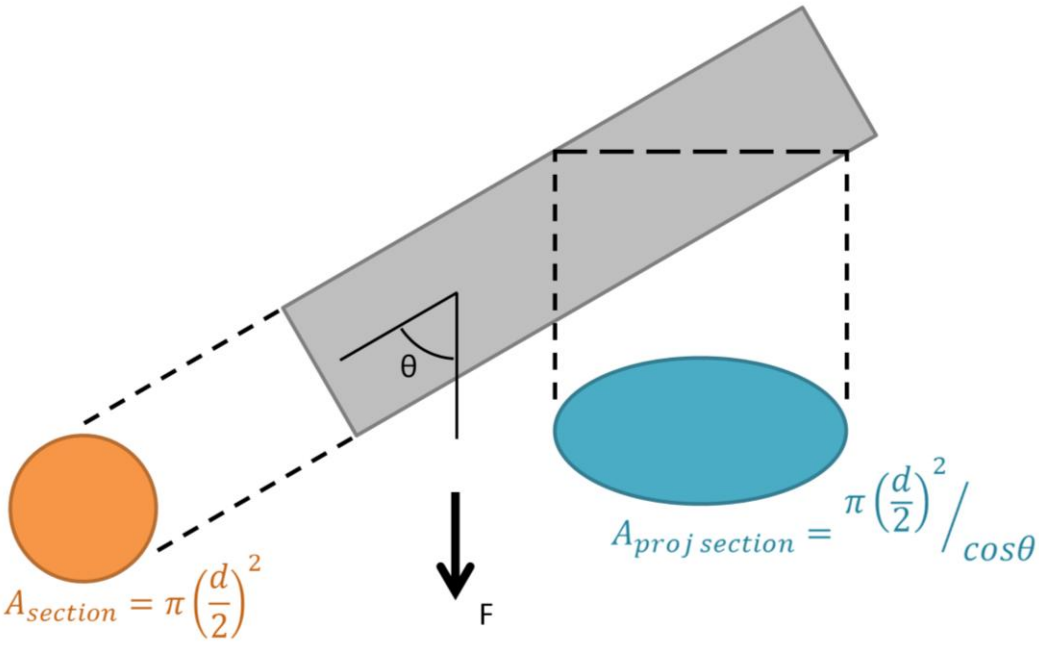

Figure 3.13. *Projected sectional area of wire wrap in tension test.*

The spring constant relates force to displacement. Therefore, longitudinal stiffness of the spring/wrap is given by:

$$E_{z,wrap} = \frac{F/A_{proj\ section}}{\Delta L/L_o} = \frac{kL_0}{A_{proj\ section}} = \frac{kL_0}{\pi\left(\frac{d}{2}\right)^2/cos\theta} \tag{3.38}$$

3.5 Creep

Creep is a mechanism of gradual, permanent deformation which takes place over an extended period of time in materials stressed at high temperature [1-3]. The rate of creep is governed by a combination of applied load, time and temperature. As opposed to plastic yielding, creep deformation is thermally activated and may occur at stress levels well below the yield point of the material (i.e. below the elastic limit).

In metals, creep deformation generally becomes a significant issue at temperatures in excess of 40% of the absolute melting temperature. Creep failure is said to have occurred when a component exhibits excessive deformation that interferes with its function, or when the component fractures as a result of the creep process (creep rupture). The typical deformation-time relationship for a constant-load test is shown in Figure 3.14.

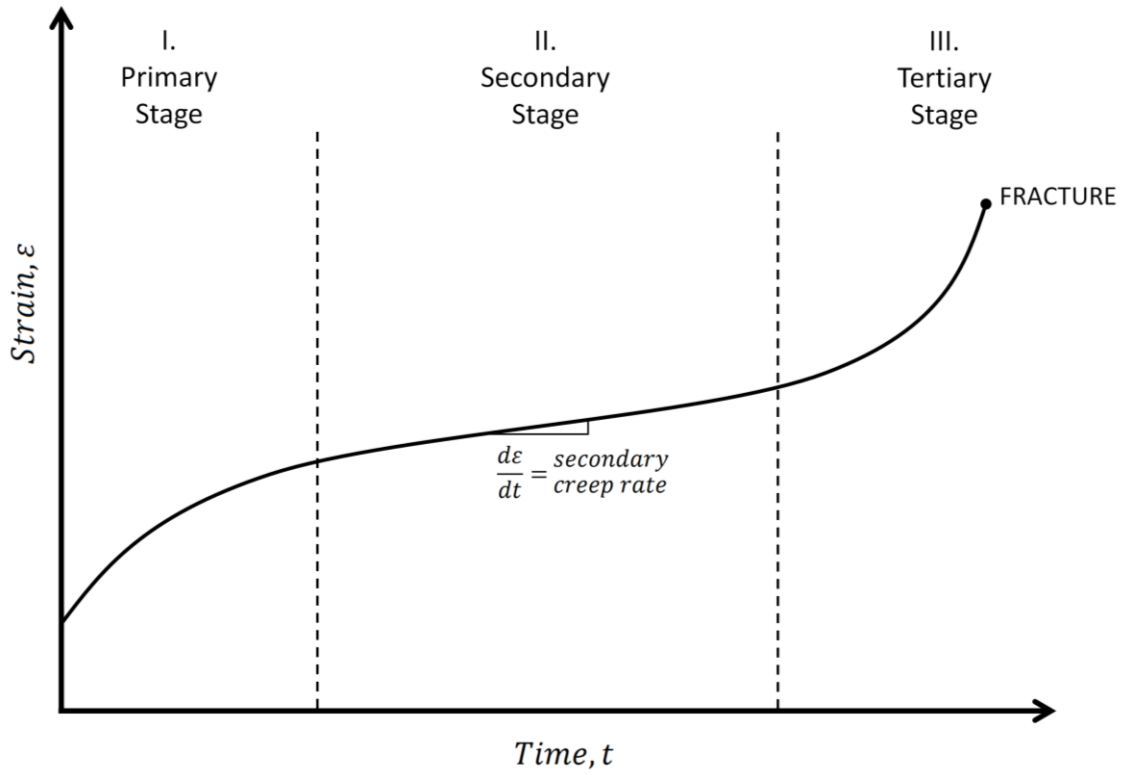

Figure 3.14. *Typical creep curve showing the three stages of creep.*

Creep data are generally presented as plots of secondary creep rate (also called steady state or minimum creep rate) versus stress for varying temperatures, as shown in Figure 3.15(a). Alternatively, the time to rupture may be plotted in a similar manner, such as in Figure 3.15(b).

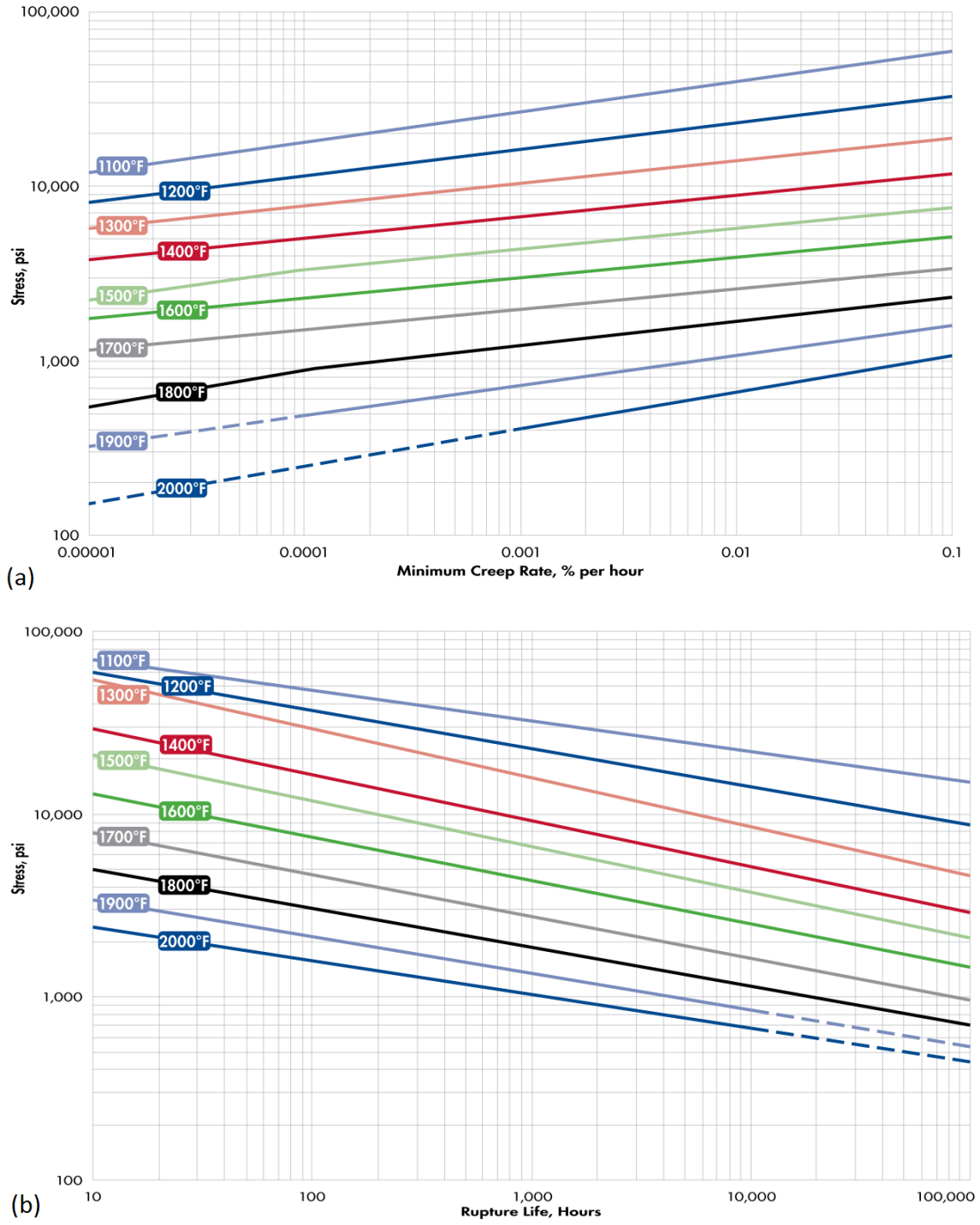

Figure 3.15. *Creep rupture plots for 253MA (a) secondary creep rate data (b) creep rupture life data [39].*

It is impractical for creep tests to be performed over several thousand hours. Instead, it is useful to relate short-term test data to long-term applications by time-temperature parameters such as the Shelby-Dorn and Larson-Miller parameters

[1]. The Larson-Miller parameter (P_{LM}) is the most commonly used approach for the design of reformer tubes. It is widely used to correlate stress versus rupture lifetime data over a wide range of temperatures, and is defined as: $P_{LM} = T(\log t_r + C)$, where T is the absolute temperature in degrees Kelvin, t_r is the rupture time in hours, and C is a constant specific to the material, typically on the order of 20. Through short-term creep testing, C is determined and P_{LM} is commonly presented as a plot against stress (known as a Larson-Miller diagram). With this data, P_{LM} for a given stress state can be determined, and therefore t_r can be estimated for a given temperature T.

3.5.1 Creep mechanisms

The general phenomenon of creep deformation can be attributed to several underlying microstructural and crystallographic characteristics of the subject material. However, since creep deformation can take place in a wide range of conditions from "high temperature – low stress", to "low temperature – high stress", there are a variety of creep mechanism regimes associated within a range of conditions that can be classified into various families. The competing deformation mechanisms were arranged into graphical form by Frost and Ashby [40]. An example of such a deformation mechanism map for 316 stainless steel is shown in Figure 3.16. No such maps exist for HP-alloy or 253MA.

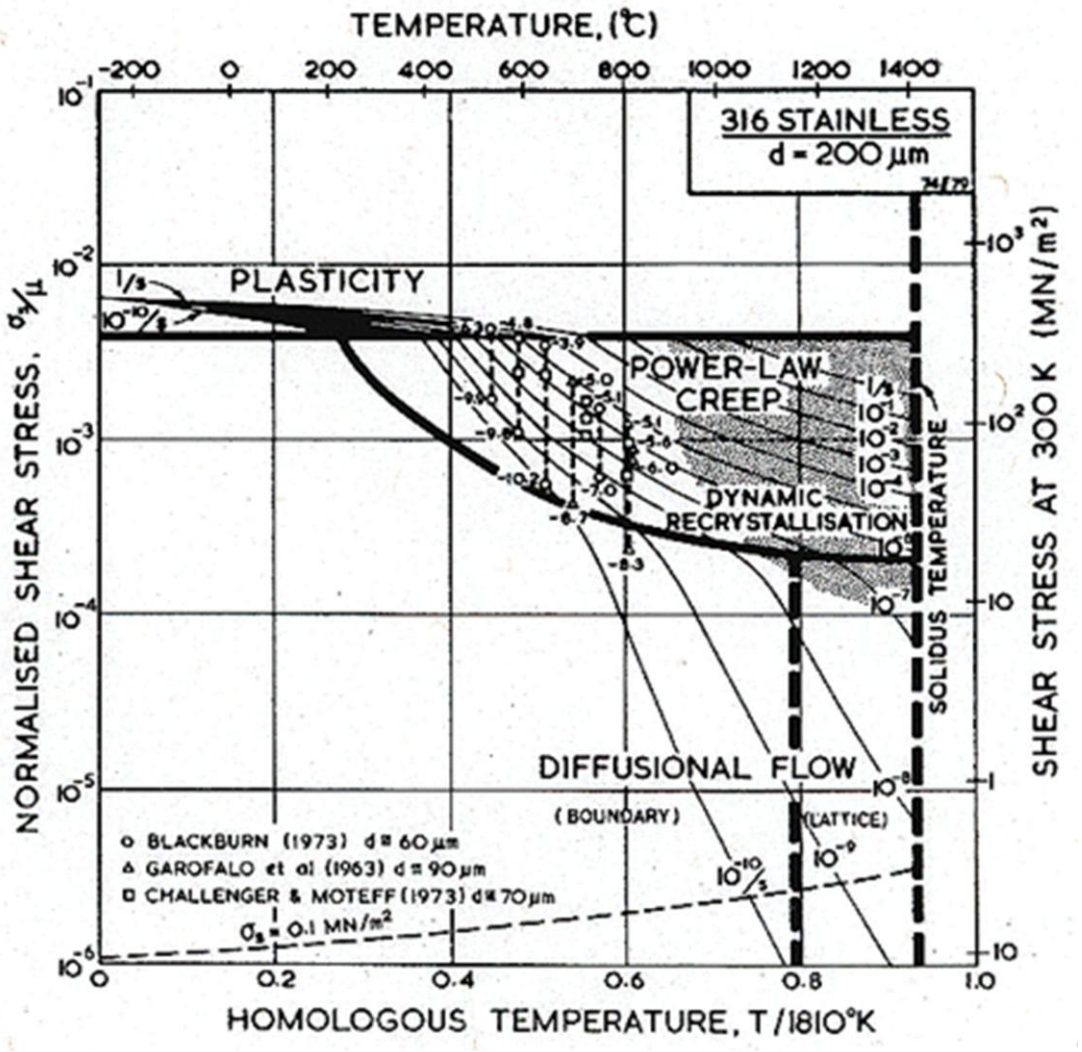

Figure 3.16. *Deformation mechanism map for type 316 stainless steel [40].*

The maps are unique to each alloy, and also dependent on grain size. They provide a means to predict both the strain rate and the dominant creep mechanism, based on the known temperature and stress. The accuracy of the maps reflects that of the experiments. Often different experimenters report strain-rates that differ by factors as large as 100 at a given σ_s and T, and it is necessary to judge which experiments more accurately reflect the true material behaviour. These judgments are to some extent subjective because of the large number of variables involved: composition, testing atmosphere, grain size, thermomechanical history, recrystallization effects, type of test and so forth.

Creep mechanisms occurring in metals are generally separated into two broad classes, termed 'diffusional flow' and 'dislocation creep'. Some authors also consider 'grain boundary sliding' to be a distinct mechanism. Diffusional flow creep occurs at relatively low stresses and high temperatures, and requires the motion of vacancies. This diffusion may take place through the crystal lattice (Nabarro-Herring creep), or along grain boundaries (Coble creep).

At high temperatures, dislocation motion acquires a new degree of freedom and can climb as well as glide. If a gliding dislocation is held up by discrete obstacles, a small climb may release it, allowing the dislocation to glide to the next set of obstacles where the process is repeated. This combined process of glide and climb is strain rate dependant, and is referred to as power law creep.

Equation 3.39 is the general form for the steady-state creep rate in a crystalline material. Strain rate, $\dot{\varepsilon}$, is affected by stress, σ, average grain diameter, d, and absolute temperature, T. The coefficient A_2, exponents m and q, and the activation energy Q have values that depend on the material and the particular creep mechanism that is acting. R is the universal gas constant. Values of m and q are summarized for various creep mechanisms in Table 3.2.

$$\dot{\varepsilon} = \frac{A_2 \sigma^m}{d^q T} e^{\frac{-Q}{RT}} \tag{3.39}$$

Table 3.2. *Creep exponents for various creep mechanisms [41].*

Creep Mechanism	m	q	Description
Diffusional flow (Nabarro-Herring creep)	1	2	Vacancy diffusion through the crystal lattice
Diffusional flow (Coble creep)	1	3	Vacancy diffusion along grain boundaries
Grain boundary sliding	2	2 or 3	Sliding accommodated by vacancy diffusion through the crystal lattice (q=2) or along grain boundaries (q=3)
Dislocation creep (power law creep)	3 to 8	0	Dislocation motion, with climb over microstructural obstacles

3.5.2 Creep in a complex stress state

As the bulk of creep literature is designed for unidirectional loading, it is useful to resolve multiaxial stress state into a single, equivalent stress. As seen when considering thick-walled pressure vessel stresses in Section 2.3.1, principal stresses are defined in the cylindrical coordinate system. Rather than using magnitude and direction of maximum principal stress, von Mises stress may be calculated to serve as the effective multiaxial stress.

Much like von Mises stress is used to determine effective stress in a multiaxial stress state, effective strain rate is given by Dowling [41] as:

$$\dot{\varepsilon}_{eff} = \frac{\sqrt{2}}{3}\sqrt{(\dot{\varepsilon}_t - \dot{\varepsilon}_r)^2 + (\dot{\varepsilon}_r - \dot{\varepsilon}_z)^2 + (\dot{\varepsilon}_z - \dot{\varepsilon}_t)^2} \tag{3.40}$$

In practice, experimental strain measurements may only be made in the tangential and longitudinal directions. But $\dot{\varepsilon}_r$, the radial strain rate, cannot be assumed to be zero as this imposes an unrealistic plane strain condition upon the system. Fortunately, incompressibility can be assumed which requires that volumetric strain be zero. Hence the volumetric strain rate is also zero, giving:

$$\dot{\varepsilon}_r = -(\dot{\varepsilon}_t + \dot{\varepsilon}_z) \tag{3.41}$$

3.5.3 Multiaxial creep testing

In order to determine the creep response of a material, a creep test is conducted. Generally, creep testing involves the application of a constant load to a tensile specimen, which is maintained at a constant temperature.

Despite the prevalence of this uniaxial method of creep testing, the majority of creep seen in industrial applications occurs in complex, multiaxial stress states. This implies that more complex creep testing methods are required to replicate the stress state seen in industry. Tangential creep properties (that is, in the direction of the tangential stress) can be investigated using three kinds of tests.

The first kind of multiaxial creep test is the ring test, which consists of applying an extension force from inside the ring by two cylinders or two half-cylinders, Figure 3.17. Its main shortcoming is that a bending moment develops in the two middle sections. Notched rings have also been used for the purpose of localizing deformation in the pre-set gauge length.

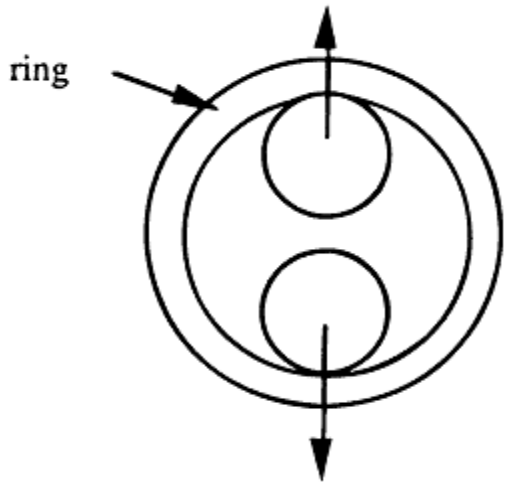

Figure 3.17. *Schematic of classical ring test [42].*

Additional modelling work by Arsene et al [42, 43] developed and experimentally verified a new design of holding device which creates a uniaxially stressed zone through gauge length *a* in a notched ring test specimen, Figure 3.18.

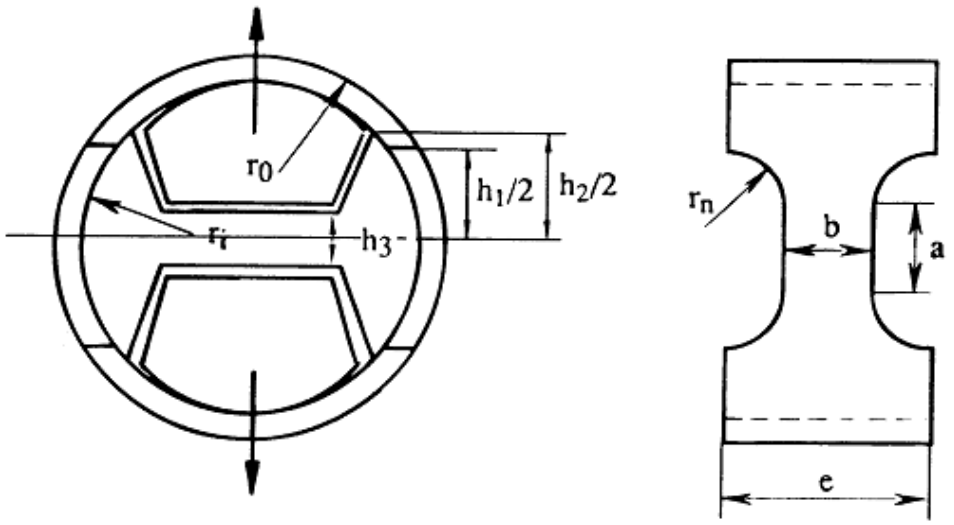

Figure 3.18. *Schematic of optimized ring testing system and notched ring specimen [42].*

Regardless of how optimized the ring testing apparatus is, problems arise when considering a hybrid, multi-layered specimen. In order for a deadweight to produce a reasonable stress, notch width, *b*, must be relatively small. However, this reduction somewhat trivialises the presence of the reinforcement, with an extremely small gauge length over which the reinforcement can act. In practice, it is also difficult to create a seal between layers to shield the reinforcement layer from oxidation. This effectively constrains testing to be performed under a vacuum.

The second kind of multiaxial creep test is a mandrel test. This test involves four or more mandrel parts placed within a section of the tube being pushed apart in the radial direction, thereby transmitting an expansion force to the ring. Although a more uniform stress field is created than in ring testing, the exact value of the force within the ring is difficult to measure.

The third kind of multiaxial creep test is the so-called burst, or pipe rupture, test – in which an internal pressure is applied. It requires special equipment and a relatively long tube specimen. Pipe rupture testing simultaneously assesses longitudinal and tangential creep strengths. While this approach to creep testing has been used for polymeric composites at low temperature [44, 45], the use of pressurized pipe tests to assess the creep rupture performance of metals at high temperature has only been considered in a few select cases [46-49], and never for metallic composites or hybrids prior to the present work.

During rupture testing, pressure and temperature may be monitored for stability, but strain measurement is less straightforward. Unlike in conventional uniaxial creep tests and some more sophisticated multiaxial creep tests where strains may be measured in-situ [42, 49, 50], the multilayered nature of the hybrid pipe makes in-situ strain measurement of the pipe problematic. Therefore, overall creep rupture time and final maximum strain in the tangential and longitudinal directions are most commonly determined upon failure.

Periodically interrupting pipe rupture tests to take regular strain measurements has also been used with some success on unreinforced metallic creep rupture specimens under internal pressure [46, 48], though to the author's knowledge it has never been used on composite or hybrid materials under a complex stress state. In the case of a hybrid tube, accurate strain measurement requires the removal of the reinforcement layer. This regular interruption and disassembly is likely to have some detrimental effect on the creep performance, particularly as thermal cycling is an inherent part of the interruptions.

3.5.4 Solutions against creep at high temperature

As creep is a stress-dependant process, one of the most effective means of reducing creep rate for a given applied load and material section is to utilize

reinforcement for stress shielding. The temperature-dependent nature of creep can also be exploited to minimize creep rate. Active cooling of critical components is a method frequently utilized in gas turbines, particularly at the turbine blades. Internal cooling involves passing air through passages internal to the blade, thereby reducing creep strain or allowing operating temperatures to increase to the range where an uncooled material would be susceptible to creep [51].

Dispersion strengthening is a method by which metals and alloys can be designed to withstand creep at high temperatures. Fine particles are evenly distributed throughout the matrix to impede dislocation motion [52]. A fine dispersion of hard precipitates such as carbides or intermetallics, e.g. VC and MO_2C in ferritic steels, and gamma prime in nickel-base alloys, obstruct the movement of dislocation climb and glide [53]. Molybdenum in solid solution reduces the creep rate of steel by slowing the coarsening (Ostwald ripening) of carbides during high-temperature service [54].

For creep mechanisms which are grain-size dependent, it is common for a minimum allowable grain size to specified. For example, Alloy 800H used in reformer furnace pigtails currently has a criterion which recommends an ASTM grain size of 5 or coarser [55]. As creep deformation occurs by the sliding of grain-boundaries, creep deformation is easier when there is a larger grain boundary area i.e. a smaller grain size.

3.6 Refractory Creep Reinforcement

Refractory metals are a class of metals that are extraordinarily resistant to heat and wear. While definitions vary, ASM International specifies a melting point greater than 2200°C to qualify as a refractory metal [56]. By this definition, the following

are considered to be refractory metals: niobium (Nb), molybdenum (Mo), tantalum (Ta), tungsten (W) and rhenium (Re). Fabricability is often used as a deciding factor in the selection of a specific refractory metal [57].

Substantial work has been performed on testing alloys and composite systems strengthened by refractory metals [58-65]. However, the usefulness of refractories as high-temperature materials in air is limited by their poor oxidation resistance at service temperatures, meaning they can only be used in air when protected by suitable coating materials which are typically based on silicides, borosilicides and aluminides [58, 66]. While these coatings have been used successfully to expose tungsten to temperatures as high as 2000°C, application of the coatings is expensive and time consuming, often relying on chemical vapour deposition. Additionally, welding or joining of components is not possible after coating [67-69].

As a result of this poor oxidation resistance, most creep tests on refractory composite and alloy systems have been performed under vacuum with the intended application being high temperature components for use in outer space [62]. For some applications with shorter life requirements, it may be practical to minimize the rate of oxidation by alloying or coating materials such that they form a stable, dense surface oxide (or scale) [70]. Al_2O_3, Cr_2O_3 and SiO_2 are the principal scale phases used for protection. However, in order to form an effective oxide layer, a critical content of Cr, Si or Al is required in the alloy and such high levels of these alloying components cause brittle intermetallic phases, such as Al_3Nb, Cr_2Ta and Si_2Ti, to form in refractory metals. Additionally, the formation of these intermetallic phases results in the depletion of Cr/Si/Al, which in turn reduces the ability for these elements to be used in the formation of a protective scale. For example, the reactive bases Nb, Ta, Ti and Zr are more thermodynamically stable with oxygen than Cr/Cr_2O_3. They also tend to form quite stable nitrides. These

factors can lead to difficulties in establishing a protective scale. [70-72]. Behaviour related to the formation of intermetallics and oxidation of tungsten are expounded upon in Sections 3.6.2 and 3.6.3, respectively.

3.6.1 High temperature performance

Due to their high melting point, as well as their ability to maintain tensile strength and stiffness at high temperature, refractory metals are particularly attractive options for creep reinforcement. While ceramics also fulfil these criteria, refractory metals are more durable and resistant to thermal cycling. Refractory metals are also more readily formed into wires, and have more desirable thermal conductivity properties for a reformer furnace application.

Of the reinforcement types developed for super alloy matrices, Table 3.3, ceramics are most commonly provided in the form of short, thin filaments (whiskers) or larger, discontinuous fibres. Additionally, they may also be present as particulates dispersed throughout the matrix.

Table 3.3. *Development of reinforcement for super alloy matrices [73].*

Form	Materials	Remarks
Whiskers	SiN, SiC, Al_2O_3	Loss of integrity Not technically and economically acceptable
Fibres	C, SiC, Al_2O_3	C, SiC - not stable above 900°C Al_2O_3 - poor thermal shock resistance
Wires	W, Ta, Mo, Nb, Re	Mo, Nb - form low temperature eutectic Nb, Ta, Re - cost constraints W - suitable for reinforcement

From Table 3.3, it can be seen that although ceramics may be produced in whisker and fibre form, they are uneconomical and have poor resistance to thermal shock. Whisker and fibre reinforcement architectures are also only functional when set in the matrix of a composite. For a layered hybrid material, the reinforcement must be supplied in the continuous form of a wire, or a solid tube. With this additional formability constraint, W, Ta, Mo, Nb and Re are the most suitable reinforcement candidates. Cost, availability and thermal stability all make tungsten the most suitable reinforcement option.

Considering creep strength in Figures 3.19 and 3.20, Ta- and W-based alloys have a distinct advantage over both Nb- and Mo-based alloys at temperatures above 2200°F (1204°C).

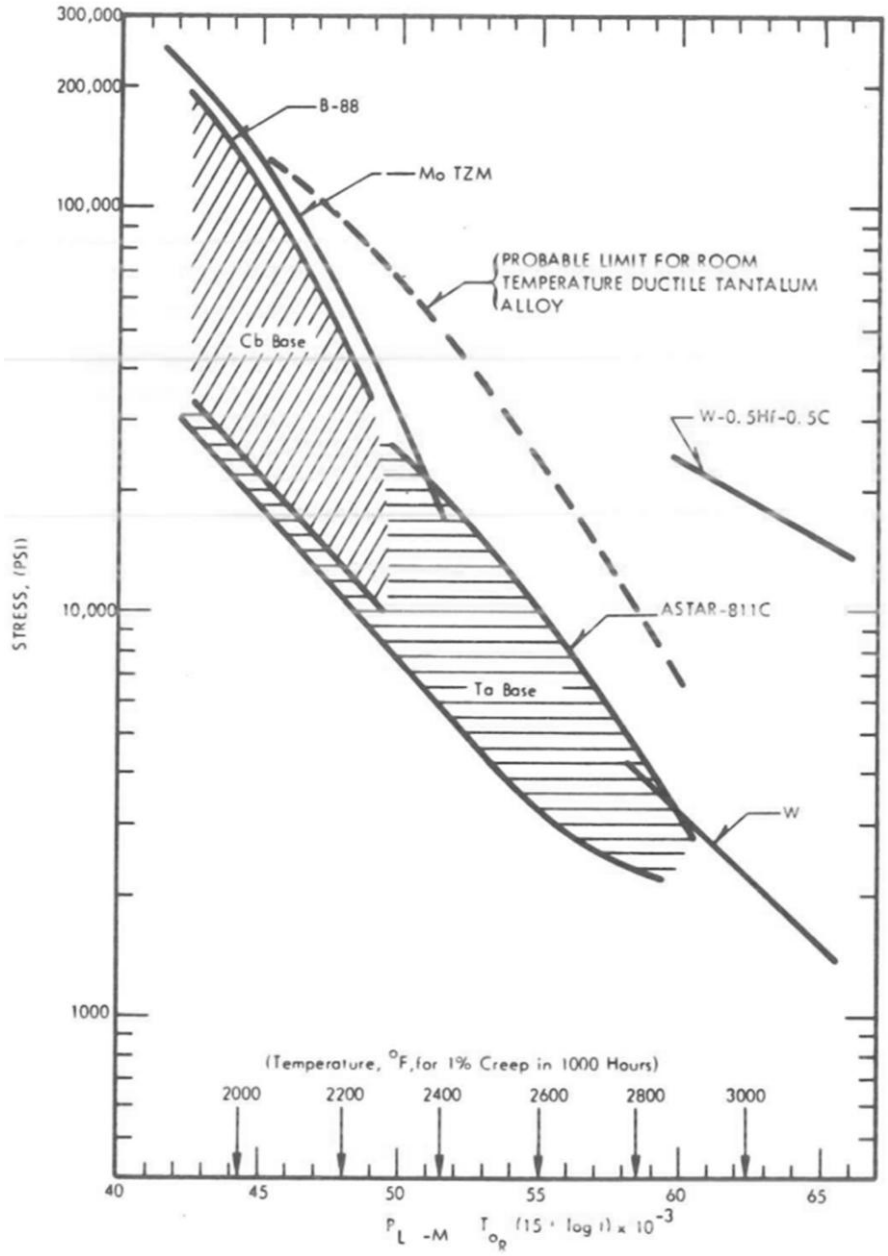

Figure 3.19. *Larson-Miller parameter normalization for time to 1% creep for refractory metal alloys [74]. Note that Cb refers to Columbium, now more commonly referred to as Niobium (Nb).*

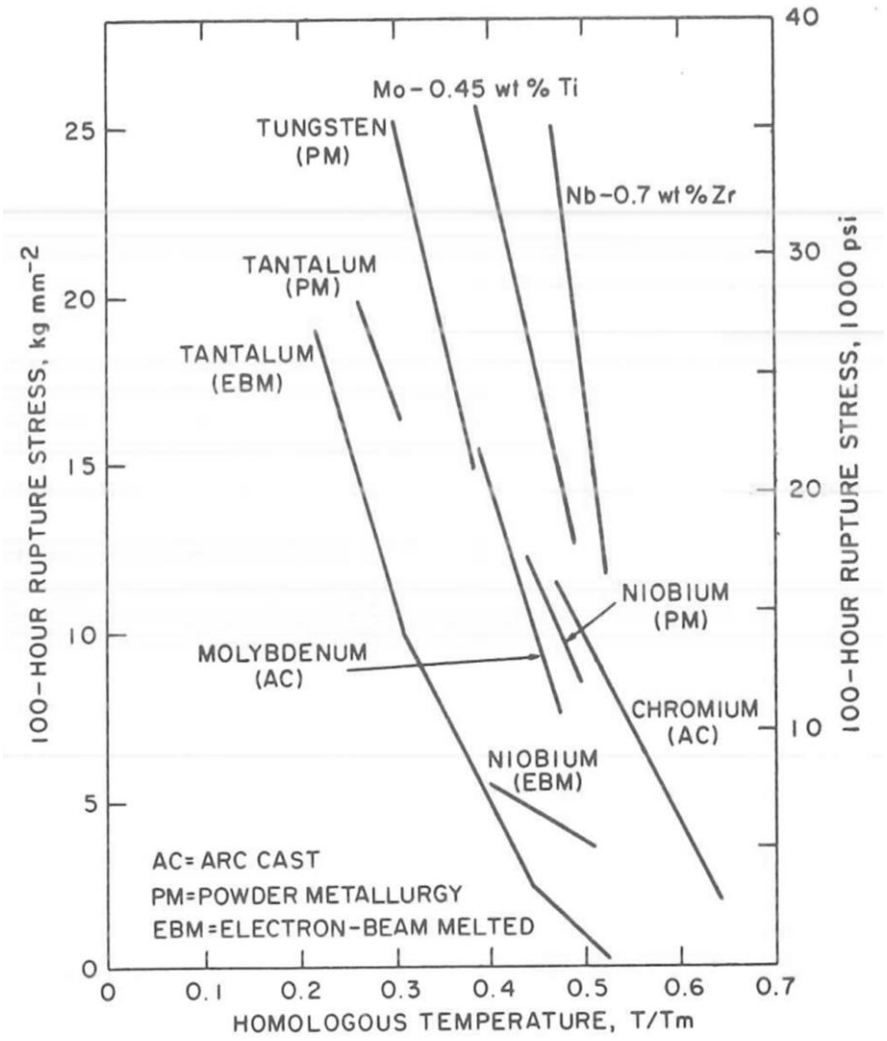

Figure 3.20. *100 hour rupture strength versus homologous temperature for refractory metals in the recrystallized condition [75].*

At approximately 950-1050°C, the temperature range under consideration in the present investigation, Figure 3.21 shows that stresses on the order of 500-750 MPa are required to cause tungsten to rupture via creep. As tangential stress is on the order of 20 MPa in a reformer tube, the tungsten wire reinforcement is essentially unaffected by creep under typical service conditions.

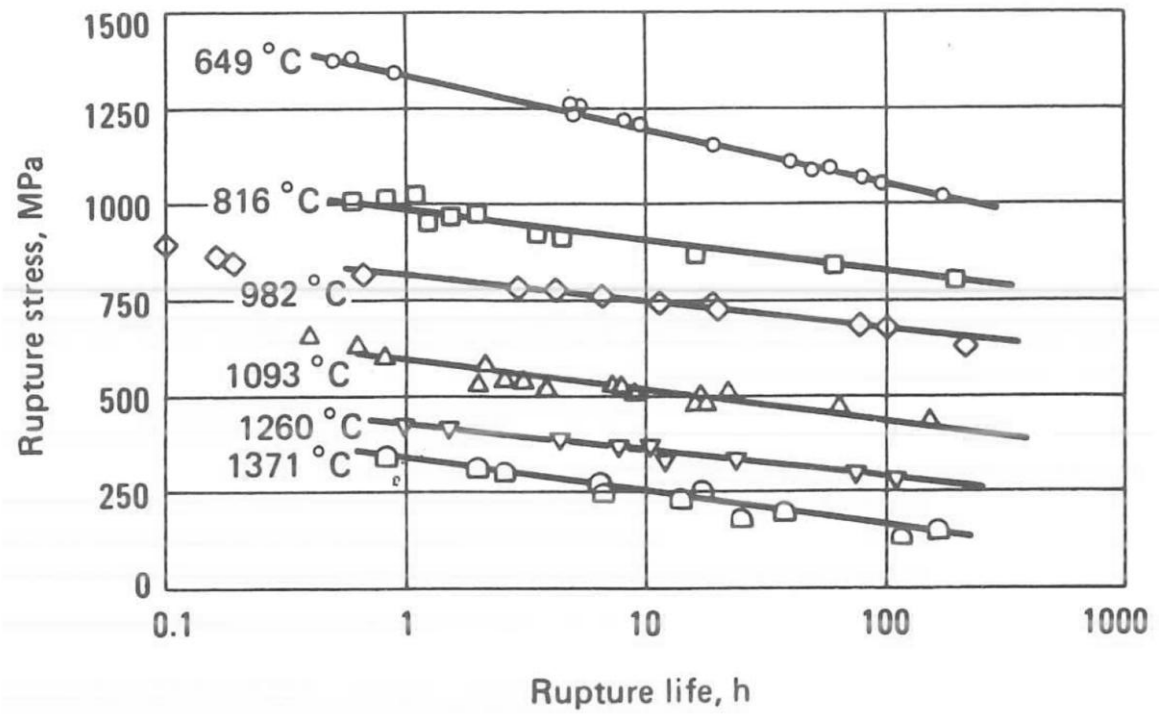

Figure 3.21. *Typical creep stress-rupture behaviour of tungsten wire 0.127mm in diameter, as-drawn [76].*

Most of the tungsten used thus far in aerospace applications has been in the unalloyed form, which is much easier and less expensive to produce and fabricate. While a decrease in strength is to be expected with increasing temperature, it has been found that, particularly at temperatures above 2200°C (~4000°F), the strengthening effects of many alloying agents decrease disproportionately [77].

Tungsten has high tensile strength and good creep resistance. However, its high density, poor low-temperature ductility, and strong reactivity in air limit its usefulness. Maximum service temperatures for tungsten range from 1925°C to 2500°C (3500°F to 4500°F), but surface protection is required for use in air at these temperatures. Room temperature physical properties for drawn tungsten wire are provided in Table 3.4 alongside properties for 253MA, an austenitic stainless steel.

Table 3.4. *Summary of physical properties of drawn tungsten wire and 253MA at room temperature [78, 79].*

	Tungsten wire	**253MA**
Density (g/cm^3)	19.3	7.80
Yield strength (MPa)	450	370
Elastic modulus (GPa)	400	200
Coefficient of thermal expansion (μm/m°C)	4.4	18.2
Melting point/solidus (°C)	3422	1360

The high melting point of tungsten means that it cannot be refined by traditional smelting. Instead, tungsten is extracted from ore through a series of chemical reactions, with the exact process varying depending on manufacturer and ore composition. The end product of this processing is tungsten oxide, which can then be roasted in a hydrogen atmosphere to create pure tungsten powder. Tungsten powder is the starting point of tungsten mill products, including wire. To produce wire, this powder is pressed into a bar and sintered by passing an electrical current through the bar. The heat generated causes the bar to densify to 85-95% of full density, and tungsten grains begin to form within the bar [80].

Malleability of the tungsten bar is increased by heating to 1200-1500°C and swaging. The swaging process involves passing the bar through a die which is designed to hammer the rod approximately 10,000 times per minute. Swaging elongates the tungsten grains, creating a fibrous structure. The tungsten rod is periodically reheated for stress relief, and swaging continues until the rod is 2.5-6.5 mm in diameter. At this point, swaged wire can be drawn through dies of tungsten carbide or diamond to further reduce the diameter. As wire is drawn,

fibres again elongate and tensile strength increases. It may be necessary to anneal the wire to allow further processing.

3.6.2 Intermetallic formation

The hybrid tube geometry avoids any liquid metal interaction and thus, there is no traditional wire-matrix diffusion interaction as seen in the manufacture of cast wire-reinforced composites. While diffusion over a mechanical interface is a largely unexplored field, it is theorized that the contact stresses at the liner-reinforcement interface are sufficient for an intermetallic layer to form at the interface. While this may not manifest as a serious problem in an accelerated creep test, long-term exposure to service conditions may lead to the embrittlement or complete dissolution of the reinforcement layer.

Studies on tungsten wire reinforced composite systems have revealed that reinforcement of superalloys with tungsten wires gives better short term strength, creep and thermal cycling properties [81]. It has also been shown that all matrices based on superalloys have a tendency to react with tungsten wire reinforcement at high temperatures (1000 to 1200°C) [82, 83]. In particular, nickel-base composites are more prone to wire-matrix interaction. The interaction results in the formation and growth of new reaction products in the interfacial region. This Ni/W based compound in the interfacial region is unstable at high temperature and decomposes to W and Ni solid solutions at around 1050°C (Figure 3.22), causing deterioration in the high temperature properties of the composite [84]. This interaction may cause dissolution of the wire, accelerated recrystallization, and embrittlement due to its reaction with the matrix.

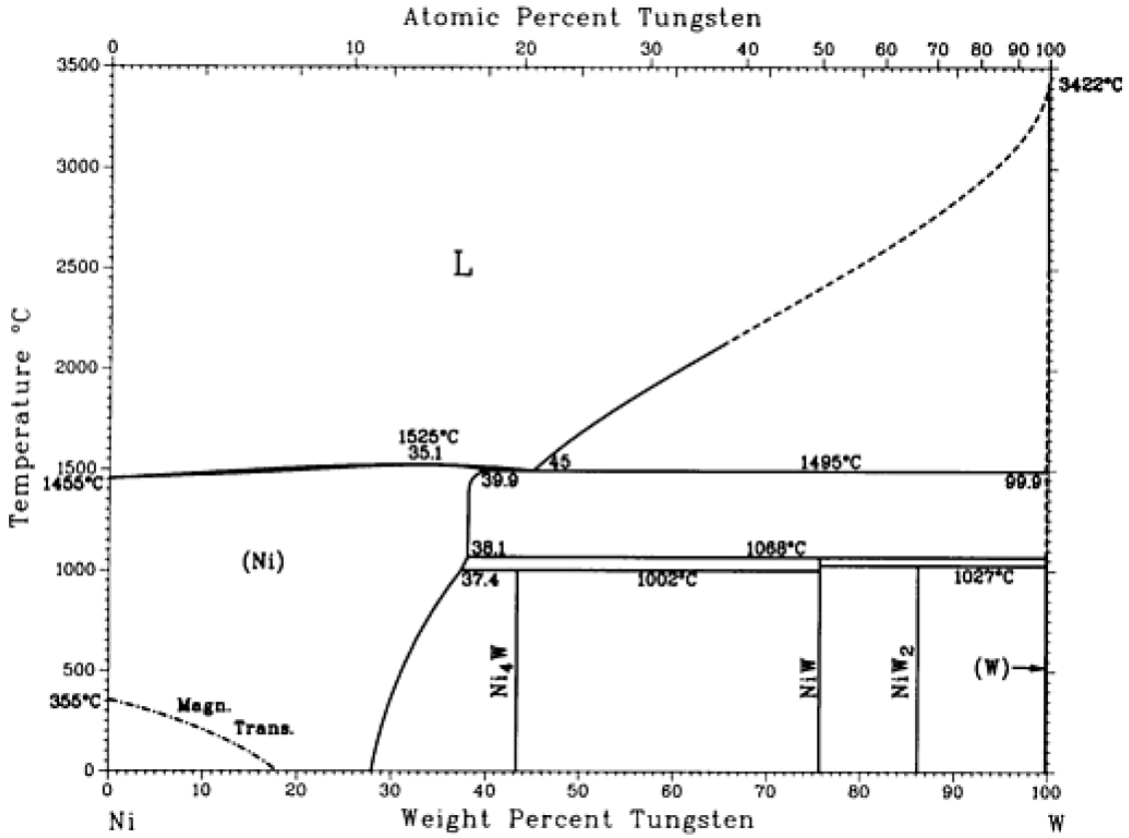

Figure 3.22. *Tungsten-nickel phase diagram [85].*

Iron-based matrices are reported to have shown the least interaction with tungsten wires [86]. This stability of tungsten in iron based matrices is attributed to the formation of comparatively stable Fe_7W_6 in the interfacial region [73]. The solubility of tungsten is much lower in iron than in nickel at 1000°C, and Fe_7W_6 can be stable up to 1640°C [87], Figure 3.23. At elevated temperatures (1000°C to 1200°C), growth of the interface takes place, resulting in the formation of the Fe_7W_6 compound. The reaction layer formed is brittle and acts as a barrier layer, giving long term high temperature compatibility to the wire-matrix combination [73, 88].

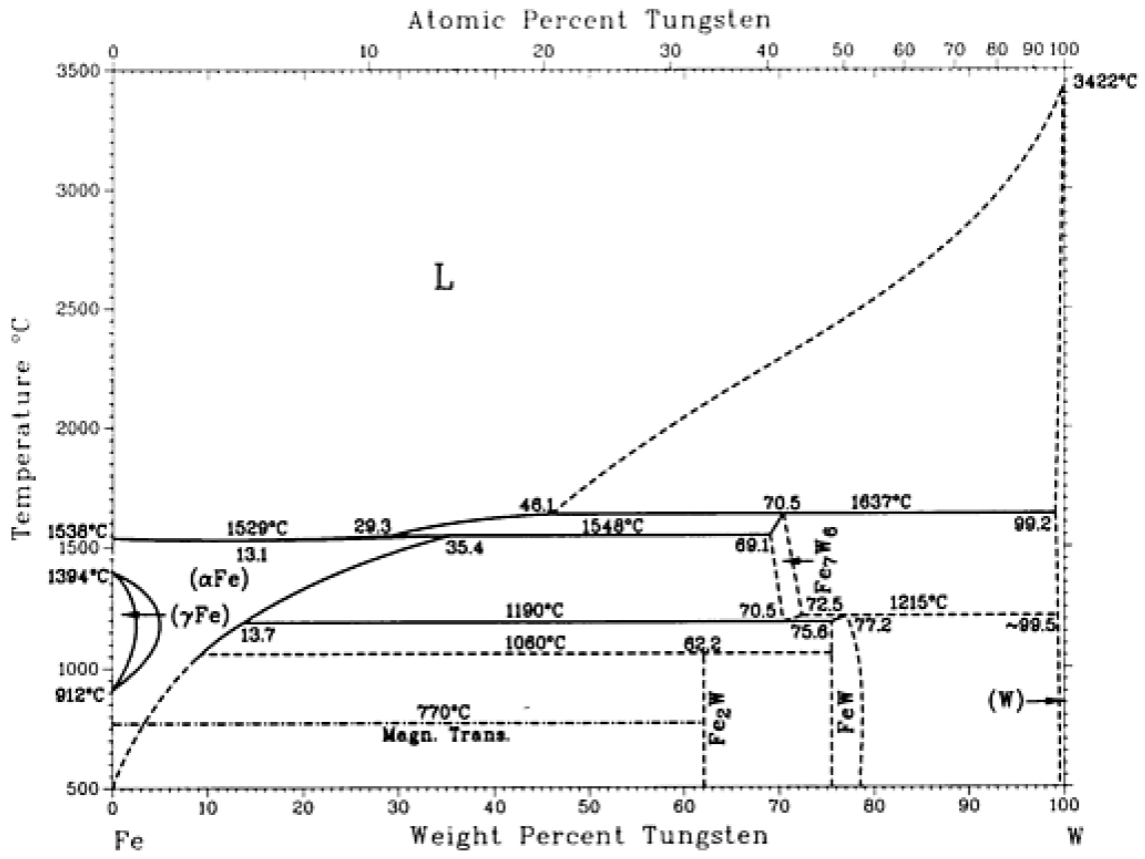

Figure 3.23. *Tungsten-iron phase diagram [89].*

In a study of reinforcement dissolution and intermetallic formation in a tungsten-stainless steel composite, Kumar [73] found that a Fe/Ni ratio of < 0.5 is required in the matrix material to suppress the formation of a tungsten intermetallic phase at the matrix-reinforcement interface. This knowledge may be used to formulate a nickel-based diffusion barrier between the reinforcement and liner pipe layers in the hybrid geometry in the future.

3.6.3 Oxidation

There is no practical strategy for completely *preventing* high-temperature oxidation (over 550°C). In the best case scenario, oxygen barriers still allow some oxygen diffusion and eventually crack, allowing oxygen ingress. The most practical long-term strategy is to *minimize* rate of oxidation by designing materials which form

and maintain a dense surface oxide (or scale) [70]. For long term (>1000 hour) use above 600°C, α-Al_2O_3, Cr_2O_3 and SiO_2 are the principal scale phases used for protection. When formed as continuous layers, the rates of metal and oxygen diffusion in them are sufficiently low that they grow at an acceptable rate [70, 71]. In combustion environments at 1200°C, these surface oxides have been shown to have parabolic rate constants of 10^{-9} to 10^{-13}, for a failure criteria of a 250 μm loss over 10,000 hours [70].

Pure tungsten forms volatile oxides which vaporize rather than forming a protective scale, allowing for extensive attack of the base metal. Above 1300°C the tungsten oxide evaporates as soon as it is formed, leaving the metal free of surface oxide during oxidation. In order to form an effective scale, a critical content of Cr, Si or Al is required in the alloy. However in general, such high levels of these alloying components are required that brittle intermetallic phases are formed in refractory metals [70-72].

CHAPTER REFERENCES

[1] N. E. Dowling, *Mechanical Behaviour of Materials: Engineering Methods for Deformation, Fracture and Fatigue.*, 3rd ed. Upper Saddle River, NJ: Prentice Hall, 2007.

[2] J. R. Davis, *Heat-Resistant Materials*. Materials Park, Ohio: ASM International, 1997.

[3] M. E. Kassner and M. Perez-Prado, *Fundamentals of Creep in Metals and Alloys*, 1st ed. Oxford, UK: Elsevier Ltd, 2004.

[4] Y. Brechet and J. D. Embury, "Architectured materials: Expanding materials space," *Scripta Materialia,* vol. 68, pp. 1-3, 2013.

[5] A. Misra, "Computational design of oxidation and creep-resistant ductile refractory alloys for high temperature applications.," in *TMS*, San Diego, 2011.

[6] M. F. Ashby, "Overview No. 92: Materials and Shape," *Acta Metallurgica et Materialia* vol. 39, pp. 1025-1039, 1991.

[7] M. F. Ashby, *Materials Selection in Mechanical Design*, 3rd ed. Oxford, UK: Butterworth-Heinemann, 2005.

[8] M. F. Ashby, Y. Bréchet, and D. Cebon, "Materials and process selection strategies," *Advanced Engineering Materials,* vol. 4, pp. 327-334, 2002.

[9] M. F. Ashby and Y. J. M. Bréchet, "Designing hybrid materials," *Acta Materialia,* vol. 51, pp. 5801-5821, 2003.

[10] Y. Bréchet, D. Bassetti, D. Landru, and L. Salvo, "Challenges in material and process selection," *Progress in Materials Science,* vol. 46, p. 407, 2001.

[11] M. F. Ashby and Y. J. M. Bréchet, "Designing hybrid materials," *Acta Materialia* vol. 51, pp. 5801-5821, 2003.

[12] M. F. Ashby, Y. Bréchet, and L. Salvo, *Selection des materiaux et des procedes de mise en oeuvre*. Lausanne, Switzerland: Presses polytechniques et universitaires romandes, 2001.

[13] B. C. Lung, "A Structural Health Monitoring system for Composite Pressure Vessels," Masters of Science, Mechanical Engineering, University of Saskatchewan, 2005.

[14] T. Safford, "Plastics in Pressure Pipes", Rapra Technology Ltd, Shropshire, UK1998.

[15] T. Hunt and N. Vaughan, *The Hydraulic Handbook*, 9th ed. Oxford, UK: Elsevier Advanced Technology, 1996.

[16] T. DeLay. Making a Metal-Lined Composite-Overwrapped Pressure Vessel, http://www.techbriefs.com/component/content/article/747, [Accessed January 8th 2015].

[17] R. M. Tapphorn and T. E. Roth. Protective Shells for Composite Overwrapped Pressure Vessels, http://www.techbriefs.com/component/content/article/5-ntb/tech-briefs/materials/6742, [Accessed January 8th 2015].

[18] S. Nobuyuki, "Heat-resistive alloy tube having excellent resistance to elongate deformation," Japan Patent no 1995-233886, 1995.

[19] C. W. Evans, *Hose Technology*, 2nd ed. London, UK: Applied Science Publishers Ltd, 1979.

[20] D. K. Roylance, "Netting Analysis for Filament-Wound Pressure Vessels", Army Materials and Mechanics Research Center TN 76-3, 1976.

[21] F. Daerden and D. Lefeber, "Pneumatic Artificial Muscles: actuators for robotics and automation," *European Journal of Mechanical and Environmental Engineering,* vol. 47, pp. 10-21, 2002.

[22] W. Liu and C. R. Rahn, "Fiber-Reinforced Membrane Models of McKibben Actuators," *Journal of Applied Mechanics,* vol. 70, pp. 853-859, 2003.

[23] D. G. Caldwell, G. A. Medrano-Cerda, and M. J. Goodwin, "Control of Pneumatic Muscle Actuators," *IEEE Control Systems Magazine,* vol. 15, pp. 40-48, 1995.

[24] C.-P. Chou and B. Hannaford, "Measurement and Modeling of McKibben Pneumatic Artificial Muscles," *IEEE Trasactions on Robotics and Automation,* vol. 12, pp. 90-102, 1996.

[25] J. L. VanLeeuwen and W. M. Kier, "Functional design of tentacles in squid: linking sarcomere ultrastructure to gross morphological dynamics," *Phil. Trans. R. Soc. Long. B,* vol. 352, pp. 551-571, 1997.

[26] R. B. Clark and J. B. Cowey, "Factors Controlling the Change of Shape of Certain Nemertean and Turbellarian Worms," *Journal of Experimental Biology,* vol. 35, pp. 731-748, 1958.

[27] W. M. Kier and K. K. Smith, "Tongues, tentacles and trunks: the biomechanics of movement in muscular-hydrostats," *Zoological Journal of the Lineean Society,* vol. 83, pp. 307-324, 1984.

[28] R. S. McCurley and W. M. Kier, "The Functional Morphology of starfish Tube Feet: The Role of a Crossed-Fiber Helical Array in Movement," *The Biological Bulletin,* vol. 188, pp. 197-209, 1995.

[29] J. Byun, "The analytical characterization of 2-D braided textile composites," *Composites Science and Technology,* vol. 60, pp. 705-716, 2000.

[30] J. E. Masters, R. L. Foye, C. M. Pastore, and Y. A. Gowayed, "Mechanical Properties of Triaxially Bradied Composites: Experimental and Analytical Results," *Journal of Composites Technology and Research,* vol. 15, pp. 112-122, 1993.

[31] R. A. Naik, P. G. Ifju, and J. E. Masters, "Effect of Fiber Architecture Parameters on Deformation Fields and Elastic Moduli of 2-D Braided Composites," *Journal of Composite Materials,* vol. 28, pp. 656-681, 1994.

[32] S. R. Kalidindi and A. Abusafieh, "Longitudinal and Transverse Moduli and Strengths of Low Angle 3-D Braided Composites," *Journal of Composite Materials,* vol. 30, pp. 885-905, 1996.

[33] J. Byun, "Stiffness Modelling of Triaxially Braided Textile Composites," in *ICCM12*, Paris, France, 1999.

[34] W. Haisler. Effective Moduli of a Continuous Fiber-Reinforced Lamina, http://aeweb.tamu.edu/haisler/aero405/, [Accessed 2013].

[35] K. Birkefeld, M. Roder, T. v. Reden, M. Bulat, and K. Drechsler, "Charcterization of Biaxial and Triaxial Braids: Fiber Architecture and Mechanical Properties," *Applied Composite Materials,* vol. 19, pp. 259-273, 2012.

[36] C. G. Daley. Stiffness Matrix and Maxwell's Riciprocal Theorem, http://www.engr.mun.ca/~cdaley/6002/Lect11_6002.pdf, [Accessed October 31st 2014].

[37] S. T. Mau, *Introduction to Structural Analysis: Displacement and Force Methods*: CRC Press, 2012.

[38] U. C. Jindal, *Machine Design*: Pearson Education India, 2010.

[39] RolledAlloys, "RA 253MA Data Sheet," ed, 2012.

[40] H. J. Frost and M. F. Ashby, *Deformation-mechanism maps: the plasticity and creep of metals and ceramics*, 1st ed. Oxford, UK: Pergamon Press, 1982.

[41] N. E. Dowling, *Mechanical Behaviour of Materials*: Pearson Prentice Hall, 2007.

[42] S. Arsene and J. Bai, "A new approach to measuring transverse properties of structural tubing by a ring test," *Journal of Testing and Evaluation,* vol. 24, pp. 386-391, 1996.

[43] S. Arsene and J. Bai, "A New Approach to Measuring Transverse Properties of Structural Tubing by a Ring Test - Experimental Investigation," *Journal of Testing and Evaluation,* vol. 26, pp. 26-30, 1998.

[44] U. Andersson, "Which Factors Control the Lifetime of Plastic Pipes and how the Lifetime can be Extrapolated," in *Plastic Pipes XII*, Munchen, Germany, 2001.

[45] Z. W. Guan and J. C. Boot, "Creep Analysis of Polymeric Pipes Under Internal Pressure," *Polymer Engineering and Science,* vol. 41, pp. 955-961, 2001.

[46] T. Mitsueda, K. Fujii, and S. Ohnuki, "Comparison of Creep Damage Appearances Among Low Alloy Steel Pipes," in *Creep and Fatigue and Elevated Temperatures 8*, San Antonio, Texas, 2007.

[47] R. J. Browne, "Creep Rupture Testing of Tubular Model Components," in *Techniques for Multiaxial Creep Testing*, D. J. Gooch, Ed., ed: Elsevier Applied Science Publishers Ltd, 1986, pp. 311-332.

[48] S. N. Gundarev, A. F. Gurov, V. V. Dement'ev, A. S. Demidov, A. E. Rusanov, and A. A. Khomyakov, "High-Temperature Creep Tests on Specimens of Single Crystal Molybdenum with a Complex Stress State," 1990.

[49] S. McAllister, R. C. Hurst, and T. E. Chung, "Modelling the Multiaxial Creep Behaviour of Alloy 800H," *International Journal of Pressure Vessels and Piping,* vol. 47, pp. 355-370, 1991.

[50] J. Lee, R. C. Bradshaw, R. W. Hyers, J. R. Rogers, T. J. Rathz, J. J. Wall*, et al.*, "Non-contact measurement of creep resistance of ultra-high-temperature materials," *Materials Science and Engineering A,* vol. 463, pp. 185-196, 2007.

[51] C. Wang, "Internal Cooling of Blades and Vanes on Gas Turbines", Lund University, 2013.

[52] M. Taneike, F. Abe, and K. Sawada, "Creep-strengthening of steel at high temperatures using nano-sized carbonitride dispersions," *Nature,* vol. 424, pp. 294-296, 2003.

[53] TWI. What determines the creep strength of an alloy?, http://www.twi-global.com/technical-knowledge/faqs/material-faqs/faq-what-determines-the-creep-strength-of-an-alloy/, [Accessed January 8th 2015].

[54] IMOA. High-temperature steel, http://www.imoa.info/molybdenum-uses/molybdenum-grade-alloy-steels-irons/high-temperature-steel.php, [Accessed January 8th 2015].

[55] B. Gardiner, "High temperature creep performance of alloy 800H," PhD, Mechanical Engineering, University of Canterbury, 2014.

[56] M. Bauccio, *Refractory Metals*, 1993.

[57] *ASM Metals Reference Book*, 3rd ed. Materials Park, OH: ASM International, 2005.

[58] V. Y. Ivanov, Y. P. Nechiporenko, L. N. Yefimenko, and M. I. Yurchenko, *High Temperature Oxidation Protection of Tungsten*. Moscow: Atom Press, 1968.

[59] J. H.E. McCoy, R. L. Stephenson, and J. J.R. Weir, "Mechanical Properties of some Refractory Metals and their Alloys", Oak Ridge National Laboratory, 1964.

[60] M. E. El-Dahshan, d. P. Whittle, and J. Stringer, "The Oxidation and Hot Corrosion Behaviour of Tungsten-Fiber Reinforced Composites," *Oxidation of Metals,* vol. 9, pp. 45-67, 1974.

[61] G. Frommeyer and R. Rablbauer, "High Temperature Materials Based on the Intermetallic Compound NiAl Reinforced by Refractory Metals for Advanced Energy Conversion Technologies," *Steel Research International,* vol. 79, pp. 507-513, 2008.

[62] T. Grobstein and H. M. Yun, "The Role of the Interface in Refractory Metal Alloy Composites," in *American Institute of Physics*, 1991, pp. 186-192.

[63] T. L. Grobstein, "Creep Behaviour of Tunsten Fiber Reinforced Niobium Metal Matrix Composites," in *Sixth Symposium on Space Nuclear Power System*, Albuquerque, New Mexico, 1989.

[64] D. W. Petrasek and R. H. Titran, "Creep Behaviour of Tungsten/Niobium and Tungsten/Niobium-1 Percent Zirconium Composites," in *Fifth Symposium on Space Nuclear Power Systems*, Albuquerque, New Mexico, 1988.

[65] J. R. Stephens, D. W. Petrasek, and R. H. Titran, "Refractory Metal Alloys and Composites for Space Power Systems," in *Spring meetings of the Materials Research Society*, Reno, Nevada, 1988.

[66] P. Schwarzkopf and R. Kieffer, *Refractory hard metals*: Macmillan, 1953.

[67] O. Lu-Steffes, R. Sakidja, and J. H. Perepezko, "Oxidation Resistant Mo-Si-B Coatings on Tungsten for Ultra High Temperature Environmental Protection," in *Materials Science and Technology*, Columbus, Ohio, 2011.

[68] K. Yoshimi, S.-H. Ha, K. Maruyama, N. Nomura, and S. Hanada, "Phase Formation and Oxidation Resistance of Mo-Si-B Alloys," in *Materials Science and Technology*, Columbus Ohio, 2011.

[69] M. Kathrein, M. Sulik, J. Januschewsky, H. Kestler, L. S. Sigil, H. Larcher, *et al.*, "Protective Coatings for Molybdenum – Industrial Processing and Applications," in *Materials Science and Technology*, Columbus, Ohio, 2011.

[70] B. A. Pint, J. R. DiStefano, and I. G. Wright, "Oxidation resistance: One barrier to moving beyond Ni-based superalloys," *Materials Science and Engineering A,* pp. 255-263, 2006.

[71] M. P. Brady and P. F. Tortorelli, "Alloy design of intermetallics for protective scale formation and for use as precursors for complex ceramic phase surfaces," *Intermetallics,* vol. 12, pp. 779-789, 2004.

[72] P. Kofstad, *High Temperature Corrosion*: Elsevier Applied Science Publishers Ltd, 1988.

[73] P. Kumar, "Studies of wire/matrix interactions in some tungsten wire reinforced stainless steels," PhD, Mechanical Engineering, University of Canterbury, 2014.

[74] J. R.W. Buckman and R. C. Goodspeed, "Considerations in the Developent of Tantalum Base Alloys," in *Refractory Metal Alloys*, Washington, D.C., 1968.

[75] W. D. Wilkinson, *Properties of Refractory Metals*. New York, NY: Gordon and Breach, 1969.

[76] MetalsHandbook, *Properties and Selection: Nonferrous Alloys and Pure Metals*, 9th ed. vol. 2. Metals Park, OH: American Society for Metals, 1979.

[77] TotalMateria. Refractory Metals: Tungsten and Tungsten alloys, http://www.keytometals.com/page.aspx?ID=CheckArticle&site=ktn&NM=110, [Accessed 2014].

[78] MatWeb. Tungsten, http://www.matweb.com/search/DataSheet.aspx?MatGUID=41e0851d2f3c417ba69ea0188fa570e3&ckck=1, [Accessed August 2nd 2014].

[79] MatWeb. Outokumpu 253MA® High Temperature Austenitic Stainless Steel, http://www.matweb.com/search/DataSheet.aspx?MatGUID=cde513f9b216440a8578764db8dada30, [Accessed August 2nd 2014].

[80] MidwestTungstsen. How Tungsten Wire is Made, http://www.tungsten.com/tungmade.html, [Accessed September 4th 2014].

[81] D. W. Petrasek and J. R. Stephens, "Fiber Reinforced Superalloys for Rocket Engines," *NASA Tech Memo 100880,* 1988.

[82] T. Caulfield and J. Tien, "High Temperature Reaction Zone Growth in Tungsten Fiber Reinforced Superalloy Composites: Part I. Application of the Movig Boundary Equations," *Metallurgical and Materials Transactions A,* vol. 20, pp. 255-266, 1989.

[83] J. Tien, T. Caulfield, and Y. Wu, "High Temperature Reaction Zone Growth in Tungsten Fiber Reinforced Superalloy Composites: Part II. Matrix Chemistry Effects," *Metallurgical and Materials Transactions A,* vol. 20, pp. 26-272, 1989.

[84] K. E. Poulsen, S. Rabaek, and E. W. Langer, *Scripta Met,* vol. 8, pp. 267-272, 1984.

[85] H. Okamoto, "Nickel - Tungsten Phase Diagram," in *ASM Metals HandBook, Volume 3: Alloy Phase Diagrams*, ed, 1991.

[86] R. Warren, L. O. Larsson, and C. H. Andersson, "Fibre/matrix Interactions in a Tungsten Alloy Wire-Reinforced Stainless Steel Composite," *Composites,* vol. 10, pp. 121-125, 1979.

[87] H. Baker, *ASM Handbook, Vol.3: Alloy Phase Diagrams*. Ohio: ASM International, 1992.

[88] L. O. K. Larsson and R. Warren, "Fiber Reinforc Metals in Turbine Blades, Transactions of the ASME," *Journal of Engineering for Power,* vol. 102, pp. 573-578, 1980.

[89] S. V. N. Naidu, A. M. Sriramamurthy, and P. R. Rao, "Iron-Tungsten Phase Diagram," in *ASM Metals Handbook, Volume 3: Alloy Phase Diagrams*, ed, 1992.

CHAPTER 4: REINFORCEMENT ARCHITECTURE STUDY

The aim of this chapter is to detail the relationship between reinforcement architecture and multiaxial creep strain rate. In order to circumvent potential oxidation issues, this reinforcement architecture study is performed with a low temperature model system of brass tubes reinforced with austenitic stainless steel. This model system is designed such that commercially available stainless steel braids are tested at a temperature where they are unaffected by creep, allowing them to control creep in brass pipes in a manner analogous to a higher temperature refractory-reinforced system.

Braid structure-property relationships are investigated and assessed in light of creep test performance. A new model for evaluating creep reinforcement effectiveness is subsequently presented, and recommendations are made for an optimal reinforcement architecture. An empirical model of multiaxial creep rate as a function of reinforcement angle is compared to a theoretical model which addresses the change in stress state as a function of reinforcement orientation.

4.1 Methodology

4.1.1 Life prediction of unreinforced materials

As seen in Section 2.3.1, a pressure vessel can be assumed to be thin-walled when the ratio of the wall thickness to inner radius (t/r_i) is < 0.05 [1]. The brass pipes used in this study had an OD of 25.4 mm and t = 1.22 mm, making this assumption invalid, as t/r_i = 0.106. Therefore, Lamé's equations for stresses in a thick-walled pressure vessel were reduced for zero external pressure (Equations

2.1-2.3). Von Mises equation (Equation 2.4) was used to resolve these multiaxial stresses into an equivalent stress, σ_{VM}. Principal stresses in a cylindrical coordinate system, σ_r, σ_t and σ_z, are functions radial distance at a given point (r), internal pressure internal pressure (p_i) and outer and inner radii (r_o and r_i) of the cylinder. Tangential and von Mises stresses are largest at the inner wall of the pipe.

Solving Equations 2.1-2.4 for typical test piece dimensions and an internal pressure of 2 MPa, Figure 4.1 shows these stress components plotted as a function of position in wall from the inner radius.

$$\sigma_r = \frac{p_i r_i^2}{r_o^2 - r_i^2}\left[1 - \frac{r_o^2}{r^2}\right] \tag{2.1}$$

$$\sigma_t = \frac{p_i r_i^2}{r_o^2 - r_i^2}\left[1 + \frac{r_o^2}{r^2}\right] \tag{2.2}$$

$$\sigma_z = \frac{p_i r_i^2}{r_o^2 - r_i^2} \tag{2.3}$$

$$\sigma_{VM} = \sqrt{\frac{[(\sigma_r - \sigma_t)^2 + (\sigma_t - \sigma_z)^2 + (\sigma_r - \sigma_z)^2]}{2}} \tag{2.4}$$

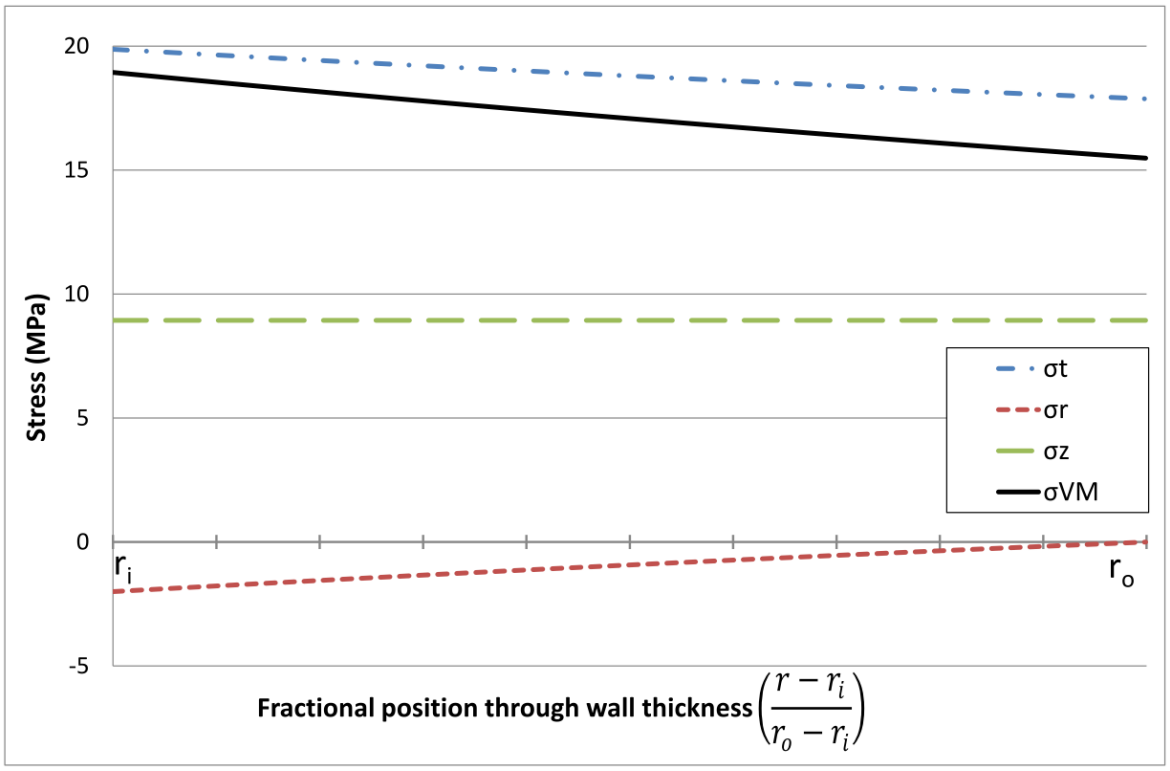

Figure 4.1. *Brass tube stress state as a function of position in wall from inner radius (r_i) = 11.48mm to outer radius (r_o) = 12.70mm.*

The average equivalent stress, σ_{VM}, through the wall thickness is 17.2 MPa and the peak equivalent stress at the inner wall is 18.9 MPa. This range of stresses was used for the life prediction of an unreinforced control pipe.

4.1.2 Model pipe material selection

The brass used in this study has a nominal composition of 65wt%Cu/35wt%Zn, with a copper composition typically in the range of 64-68.5% [2]. While some β' may exist in this composition at room temperature, it is in solution at 400°C and may be considered single phase α-brass during creep testing [3], Figure 4.2.

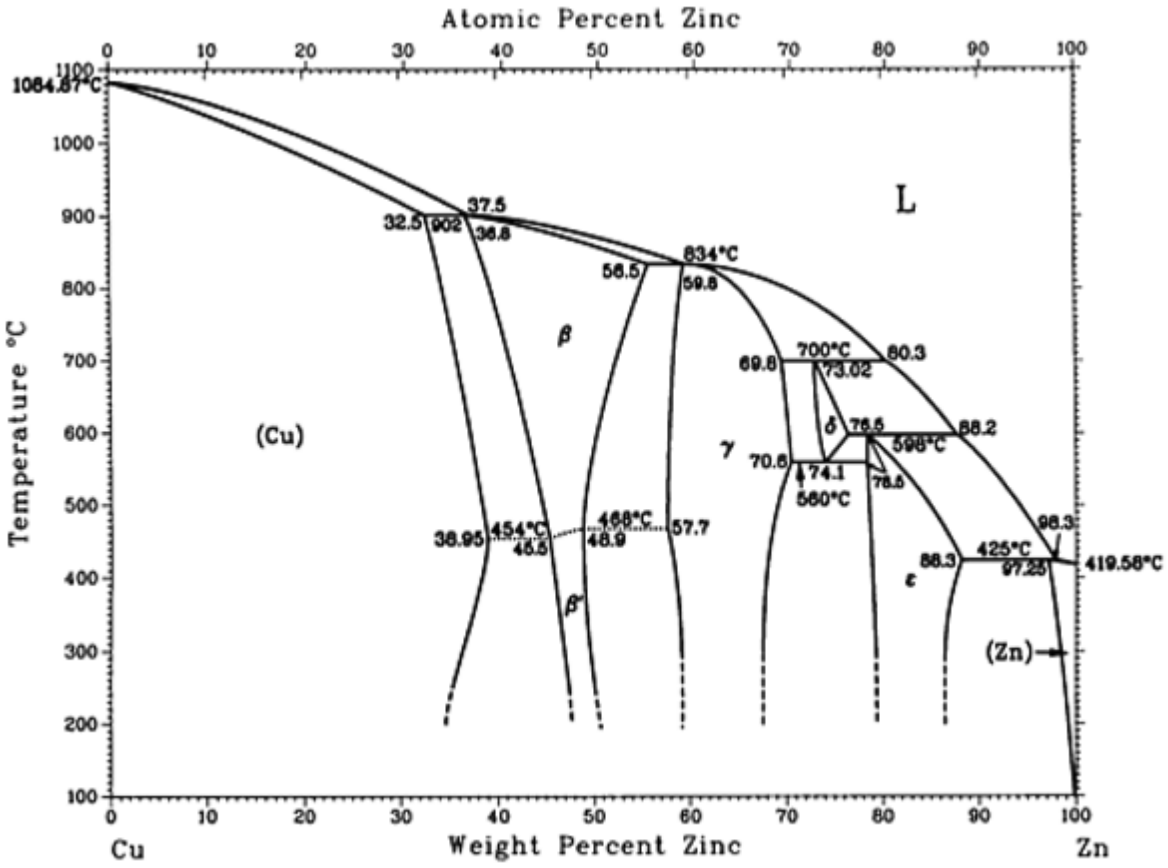

Figure 4.2. *Cu-Zn phase diagram [3].*

For a 400°C test temperature and a von Mises equivalent stress of 17.2-18.9 MPa, interpolating from the creep curve provided for 70-30 α-brass by Evans and Wilshire [4] gives an estimated creep rupture life of 84-130 hours for the unreinforced pipe, Figure 4.3.

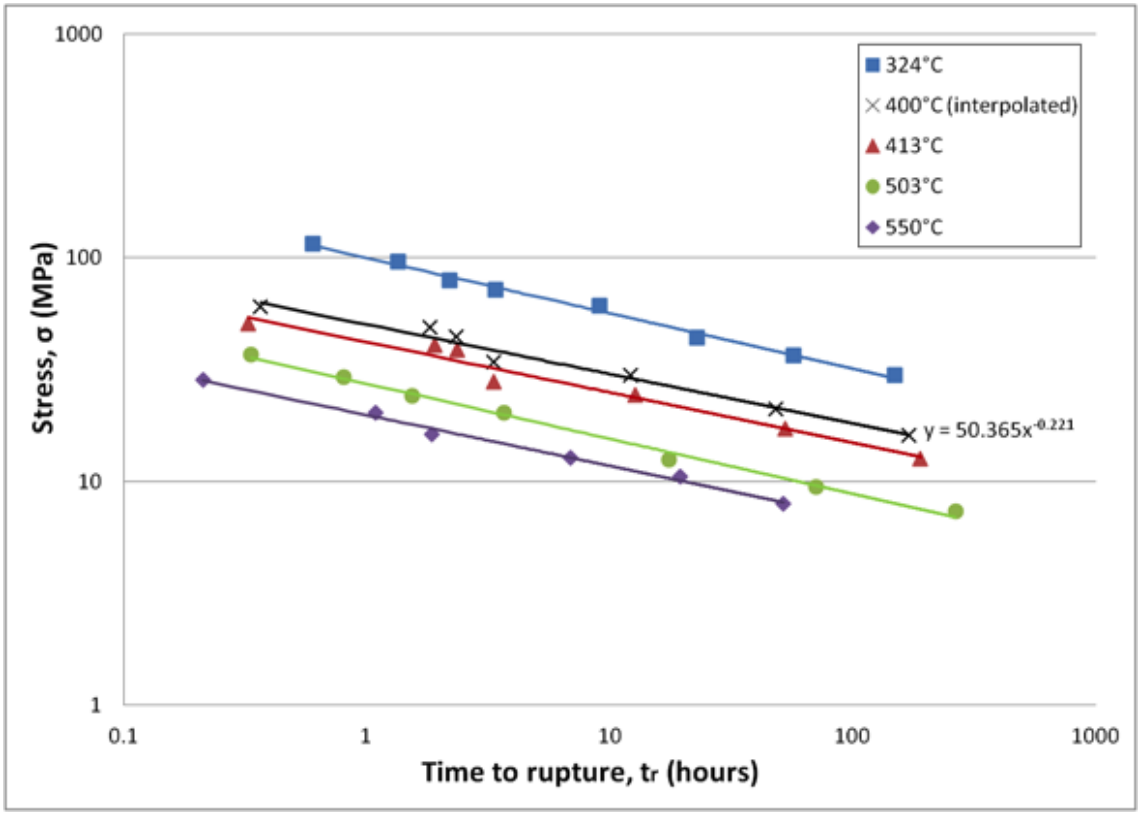

Figure 4.3. *Creep rupture curve for 70-30 alpha-brass. Adapted from Evans and Wilshire [4].*

4.1.3 Reinforcement Architecture

The 304 and 316L stainless steel reinforcement configurations tested were defined by parameters relating to their architecture. These include surface area coverage, braid/wrap angle, wire packing fraction, longitudinal stiffness, wire size, number of yarns and number of wires per yarn. Modelling [5, 6] outlined in Section 3.4 reveals that overall braid stiffness is a function of braid angle, wire diameter, packing fraction, yarn sectional area and length and angle of undulation (crimp angle) through the thickness of the braid.

These reinforcement configurations are shown in Figure 4.4, and their characteristics prior to testing are summarized in Table 4.1. Initial reinforcement angle, θ, was measured relative to the pipe axis (0°) and defined from $0° \leq \theta \leq 90°$. At least six measurements of θ were taken for each reinforcement type, with the mean

and standard deviation reported in Table 4.1. Using indentations left by the reinforcement on the pipe surface, this process was repeated to give measurements of θ in the post-test condition. Braid naming convention was selected based on the wire coarseness (C or F to denote 'coarse' or 'fine' wires, respectively) and nominal reinforcement angle.

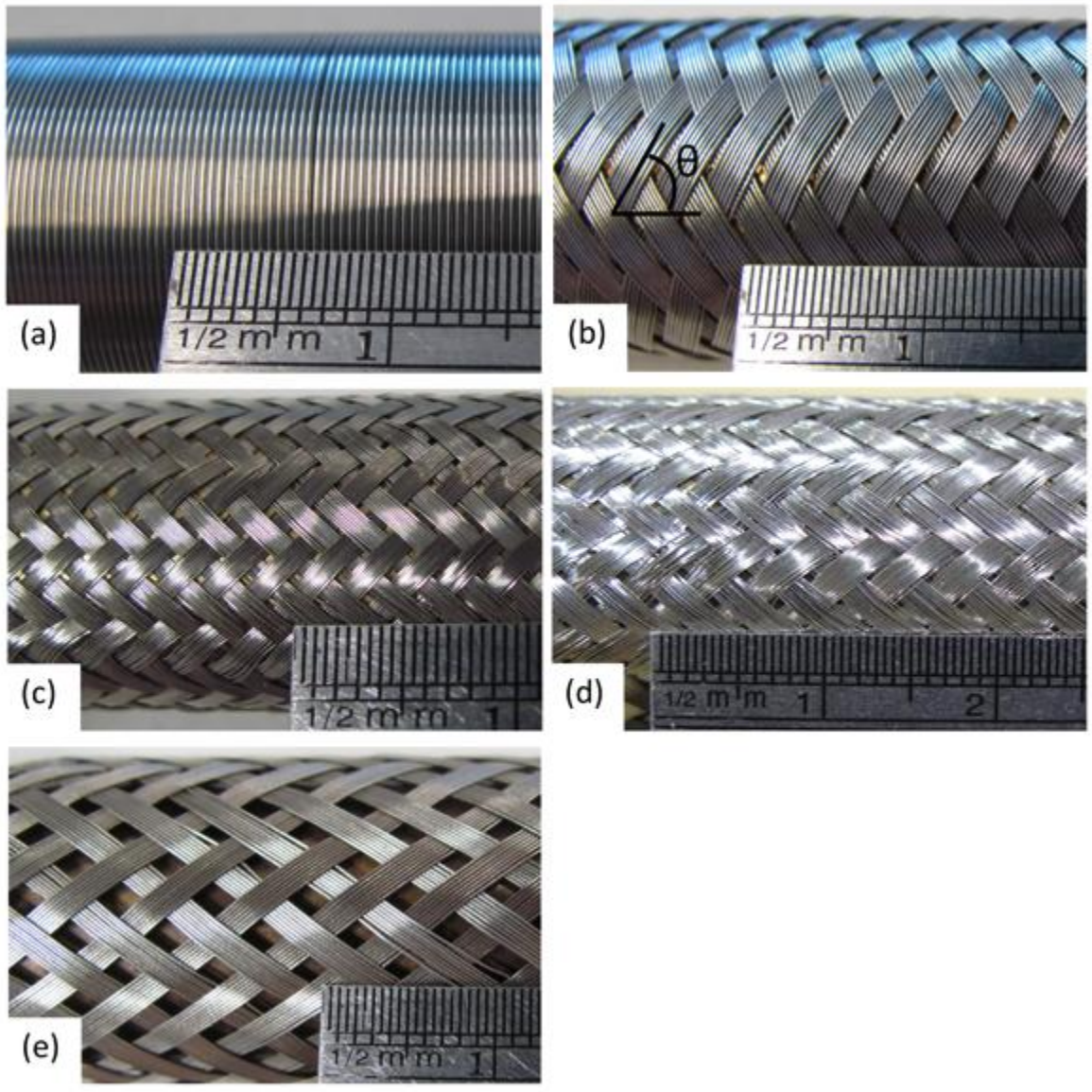

Figure 4.4. *Reinforcement configurations tested (a) 0.4mm diameter wire wrap (b) C-65° (c) F-50° (d) F-42° (e) C-36°*

Two pipe sizes were utilized to give a wider range of braid angles to be tested. The majority of pipes were 25.4 mm OD, while the F-50° architecture was achieved by

testing on a 19.05 mm OD pipe. All pipes had nominal 1.22 mm wall thickness. To keep effective stresses equivalent at 17.2 MPa, this smaller pipe size was pressurized to 2.75 MPa rather than 2 MPa.

Table 4.1. *Reinforcement architecture characterization.*

	Wrap	**C-65°**	**F-50°**	**F-42°**	**C-36°**
Material	316L SS	304 SS	304 SS	304 SS	304 SS
Wire diameter (mm)	0.4	0.254	0.127	0.127	0.254
~Wrap/ braid angle[a] (°)	86.2±0.8	65.3±1.1	49.5±2.4	41.5±1.0	36.2±1.2
Surface area coverage (%)	100	94	95	98	80
Yarns (strands)	1	24	48	48	36
Wires per yarn	1	8	11	15	8
Total wires	1	192	528	720	288

[a] mean ± standard deviation.

'C-65°' (Figure 4.4b) refers to a braided structure with an overall reinforcement layer thickness comparable to the 0.4mm wire wrap (Figure 4.4a). By comparison to C-65°, F-42° (Figure 4.4d) is comprised of many finer wires arranged in a tighter weave to give increased surface coverage.

While the helically wound wrap serves as an extremely effective means of restricting tangential expansion, it has low longitudinal stiffness and thus a very limited ability to control longitudinal expansion. By altering the reinforcement angle, the braided reinforcement sacrifices some of this tangential stiffness, but gains the ability to more effectively constrain the pipe in the longitudinal direction, particularly due to its interlocking nature. Note that the primary

difference between braids C-65° and C-36° is their braid angles, although they each used a different total number of wires.

4.1.4 Longitudinal stiffness measurement

As stated in Section 3.4, modelling employed in [5, 6] revealed that overall braid stiffness is a function of braid angle, wire diameter, packing fraction, yarn sectional area and length and angle of undulation (crimp angle) through the thickness of the braid. Therefore, it can be deduced that a measured stiffness encapsulates the collective effect of these architectural features.

Tensile testing was performed on the braid structures in an 810 Material Test System (MTS) using customized grips to hold the ends of the braid at the diameter of the brass pipe, Figures 4.5 and 4.6. In order to mimic geometric relationships seen in creep testing and limit the contraction of the braid, the samples consisted of a 140 mm length of 304 SS braid pulled over a 100 mm length of brass tube. With the tube left free in the middle of the braid sleeve, the excess braid was clamped at either end and elongated at 3 mm/min to produce a stress-strain curve. Strain was measured from crosshead displacement.

Figure 4.5. *Braid tensile sample, held in MTS by customized grips.*

Figure 4.6. *Partially disassembled braid grips. Braid pulls over tube and internal component of grip, which clamps to outer grip component via central bolt. Tension is then applied to braid without stressing the inner tube.*

Converting measured load into stress was achieved through knowledge of the wire diameter and the number of wires present in the braid. This sectional area was projected onto the direction of the applied load by dividing by $cos\theta$, as shown in Figure 3.13.

Treating the helical wrap reinforcement as a simple spring, a deadweight test was performed in order to measure the spring constant, a parameter closely related to longitudinal stiffness. This deadweight test involved hanging a 10 gram weight from the end of a length of coiled wire that contained 14 complete coils.

4.1.5 Pressurized pipe tests

1 meter lengths of 65wt%Cu/35wt%Zn brass pipe with a typical outer diameter of 25.4 mm and 1.22 mm wall thickness were brazed sealed and reinforced with austenitic stainless steel wire in the form of either a helical wrap (316L SS) or a braided sleeve (304 SS), as shown in Figure 4.4. The helical wrap reinforcement was held in place by hose clamps at either end of the sample. These tube samples were placed in a Labec HTF100/12 horizontal tube furnace at 400°C, pressurized to 2 MPa with argon and allowed to creep until rupture, or 820 hours had elapsed. This 2 MPa internal pressure was selected to give a von Mises equivalent stress of approximately 19 MPa, a slight acceleration from the 16-18 MPa seen in typical reformer furnace conditions. The present pressurized pipe tests are similar to previous methods [7-11]. ASTM E139-11 [12] outlines standard testing methods for creep testing of metallic materials, and was adhered to for heating, temperature measurement and post-mortem strain measurement guidelines.

The test temperature was selected such that the brass was subjected to creep conditions (approximately 42% of its melting point) while the stainless steel reinforcement was only exposed to approximately 30% of its melting point, leaving it unaffected by creep, which was confirmed by a lack of measurable

deformation and the absence of creep voids in post-test microstructural analysis. Therefore, the model materials serve as analogues of the behaviour of stainless steel (e.g., 253MA) pipe and refractory (e.g., tungsten) at high temperature (1313K). When set to 400°C and the ends insulated with Kaowool®, the full 650 mm length of the tube furnace had a temperature profile as shown in Figure 4.7.

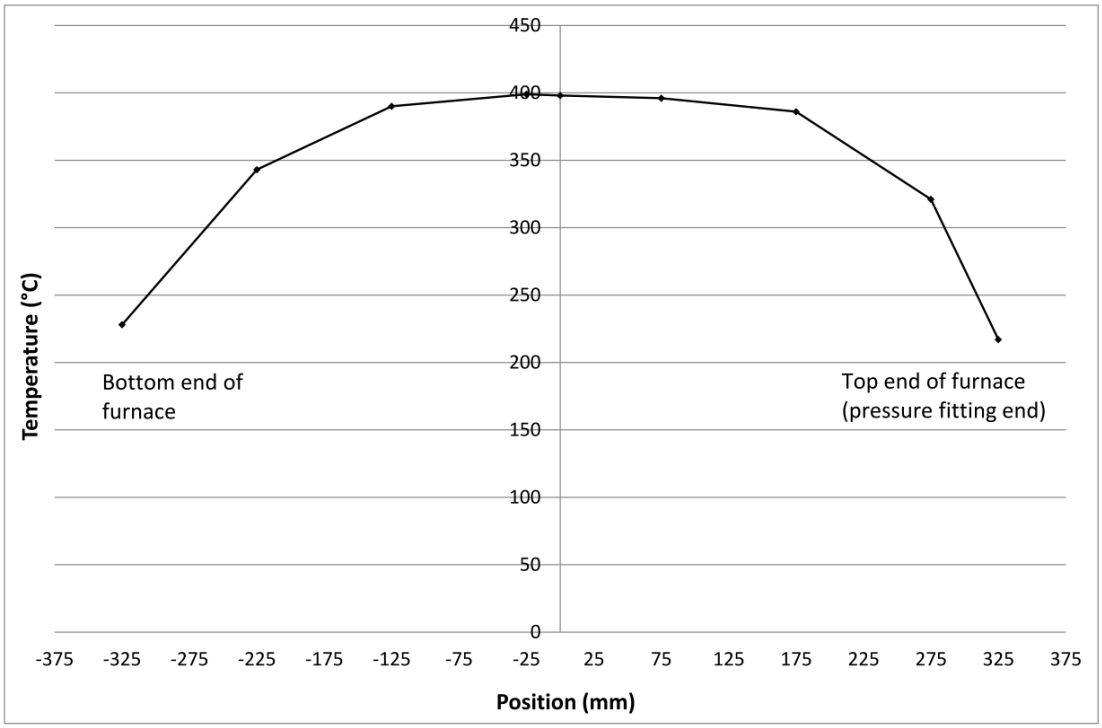

Figure 4.7. *Temperature profile in tube furnace set to 400°C.*

Internal pressure and temperature were logged every 60 seconds during all tests, and maintained stability to within ±0.2 MPa and ±1K. A sustained pressure drop indicated pipe rupture, in which case the test was ended. Unlike conventional uniaxial creep tests and some more sophisticated multiaxial creep tests where strains may be measured in-situ [10, 13, 14], the multilayered nature of the hybrid pipe made in-situ tangential strain measurement of the pipe problematic. Therefore, strain measurements were made during interruptions or after test completion.

Post-test longitudinal creep strain was measured at room temperature over a 50 mm gauge length across the midspan of the tube, positioned in the middle of the hot zone of the furnace. At least five measurements were made using digital callipers and the readings were averaged. Post-test measurements of the inside and outside diameter were made on a length of pipe sectioned from the midspan and positioned vertically in a 3-jaw chuck. A Giddings and Lewis Discovery D12 Cordax Series coordinate-measuring machine (CMM) with an Ø8 mm probe was used to take 12 diameter coordinate measurements to 1 µm resolution, Figure 4.8. These diameter measurements allowed tangential and radial creep strains to be determined.

In order to enhance understanding of strain behaviour during testing, an F-42° sample was interrupted periodically and the reinforcement was removed to enable strain measurements on the pipe. This method of periodic interruption to take strain measurements has been used previously on unreinforced metallic creep rupture specimens under internal pressure [7, 15]. To quantify the effect of this periodic interruption, two additional tests of F-42° samples were performed without interruption.

Figure 4.8. *CMM probe positioned above tube sample.*

Table 4.2 details the number and duration of creep rupture tests performed. A wide range of braid angles were tested in order to determine the effect on creep strain rate. All reinforced tests were ended either after rupture or after 820 hours had elapsed. Final strains in the tangential, longitudinal and radial directions were determined upon failure. Mean creep strain rates were determined by final strain divided by test duration.

Table 4.2. *Creep rupture testing program.*

Reinforcement designation	Number of tests performed	Average duration (hours)
Control (unreinforced)	3	83
Wrap-86°	1	647
C-65°	2	818*
F-50°	1	817*
F-42° (uninterrupted)	2	818*
F-42° (interrupted)	1	819*
C-36°	1	818*

* denotes tests which did not fail.

4.2 Results and Discussion

4.2.1 Longitudinal stiffness measurement

The stress-strain curves for the braided reinforcements are shown in Figure 4.9. Two extrema of curvature were identified on each curve. The region before the first extremum was attributed to a period of braid tightening, and was not used for further analysis involving longitudinal stiffness of the braids. The slope of the linear region between the two extrema, where the braid is fully engaged on the pipe, was denoted E_z and measured over a minimum of 100 data points well away from the extrema of curvature. Table 4.3 shows these measured longitudinal stiffnesses.

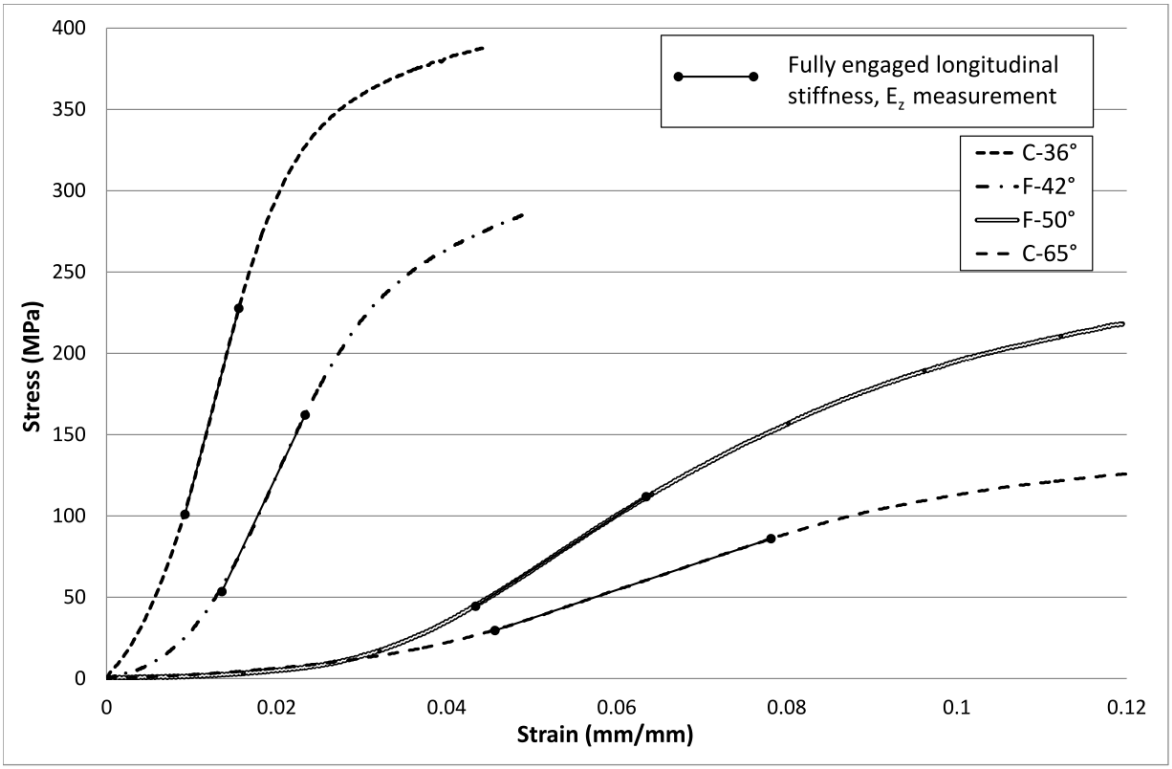

Figure 4.9. *Stress-strain curves for braids in tension. Longitudinal stiffness values determined for period where reinforcement is fully engaged (E_z).*

Table 4.3. *Measured longitudinal stiffness of stainless steel reinforcement.*

	Wrap	**C-65°**	**F-50°**	**F-42°**	**C-36°**
E_z (GPa)	1.05x10^{-4}	1.74	3.36	11.1	20.0

A simple deadweight test, involving hanging a 10 gram weight from the end of a length of coiled wire that contained 14 complete coils, gave a measured spring constant of 0.93 N/m. A theoretical spring constant was calculated from Equation 3.37, where *G* is the shear modulus of rigidity, *d* is the wire diameter, *D* is the coil diameter and *N* is the number of active coils [16]:

$$k = \frac{Gd}{8\left(\frac{D}{d}\right)^3 N} \tag{3.37}$$

Using a typical stainless steel modulus of rigidity of 70 GPa, a wire diameter of 0.40 mm, a coil diameter of 25.4 mm and 14 active coils, the theoretical spring constant was 0.98 N/m.

$$E_{long,wrap} = \frac{F/A_{proj\ section}}{\Delta L/L_o} = \frac{kL_0}{A_{proj\ section}} = \frac{kL_0}{\pi\left(\frac{d}{2}\right)^2/cos\theta} \quad (3.38)$$

Equation 3.38 was used to convert spring constants to longitudinal stiffnesses, with the initial length of the coil, L_0 = 55 mm and the initial reinforcement angle, θ = 75°. These measurements are made when the coil was hanging under self weight only. This gives a measured longitudinal stiffness of 105 kPa and a theoretical longitudinal stiffness of 111 kPa, four orders of magnitude lower than E_z of a typical braid.

4.2.2 Pressurized pipe tests

The average life of three creep rupture control tests was 83 ± 5 hours, which is at the lower end of the predicted life of 84-130 hours. This suggests that peak von Mises stress, rather than the average throughout the wall thickness, is a controlling factor. Additionally, the creep life prediction was made based on data for a slightly different alloy composition (70-30 rather than 65-35), and did not account for microstructural influences such as grain size. However any inconsistency is of little concern, as the purpose of these unreinforced control tests was to provide a creep rupture life baseline to which reinforced cases could be compared. A post-mortem average tangential expansion of 12.9% was observed at the midspan of the ruptured unreinforced pipes, with a corresponding average of 0.30% longitudinal expansion over the gauge length.

All of the braid-reinforced pipes achieved a 10-times life extension over the control pipe without rupturing, at which point testing was ended due to practicality. The helically wound reinforcement (Wrap-86°) failed after ~647 hours, a 7.8-times life extension over the control pipe, with a circumferential crack. A failed control pipe with a longitudinal crack is presented in Figure 4.10 alongside the failed wrap-reinforced pipe. This shift in the primary mode of failure between the control and wrap-reinforced pipe affirmed that tangential creep had effectively been arrested by the reinforcement, and identified longitudinal creep as a new failure mode for pipes exposed to internal pressure. Additionally, Figure 4.10 shows impressions left by C-36° reinforcement in the surface of an unruptured pipe.

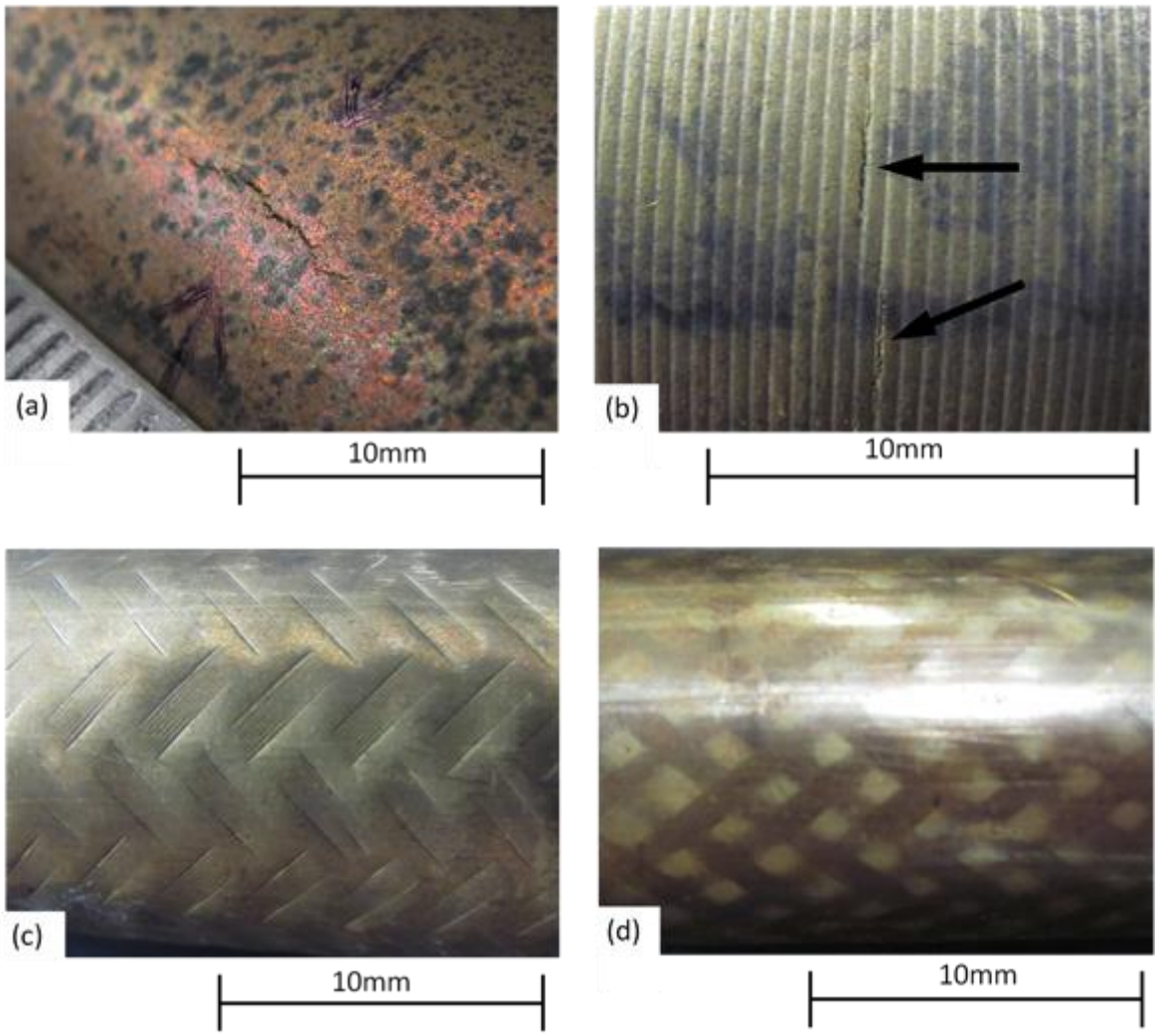

Figure 4.10. *Cracks and impressions present in pipes after rupture (reinforcement removed). (a) longitudinal crack in control pipe (b) circumferential crack in wrap-reinforced pipe and impression left by helical winding (c) midpoint of C-36° sample (d) superficial markings at end of C-36° sample.*

Figures 4.10(c) and (d) reveal that the depth and appearance of the impressions on the pipe vary with position in the furnace, with the elevated temperature in the midpoint of the furnace resulting in larger creep strains as well as increased thermal strains. To assess the appearance of the pipe surface at these impressions, metallographic samples were prepared and etched with a solution of 20mL NH_4OH and 10mL H_2O_2, Figure 4.11

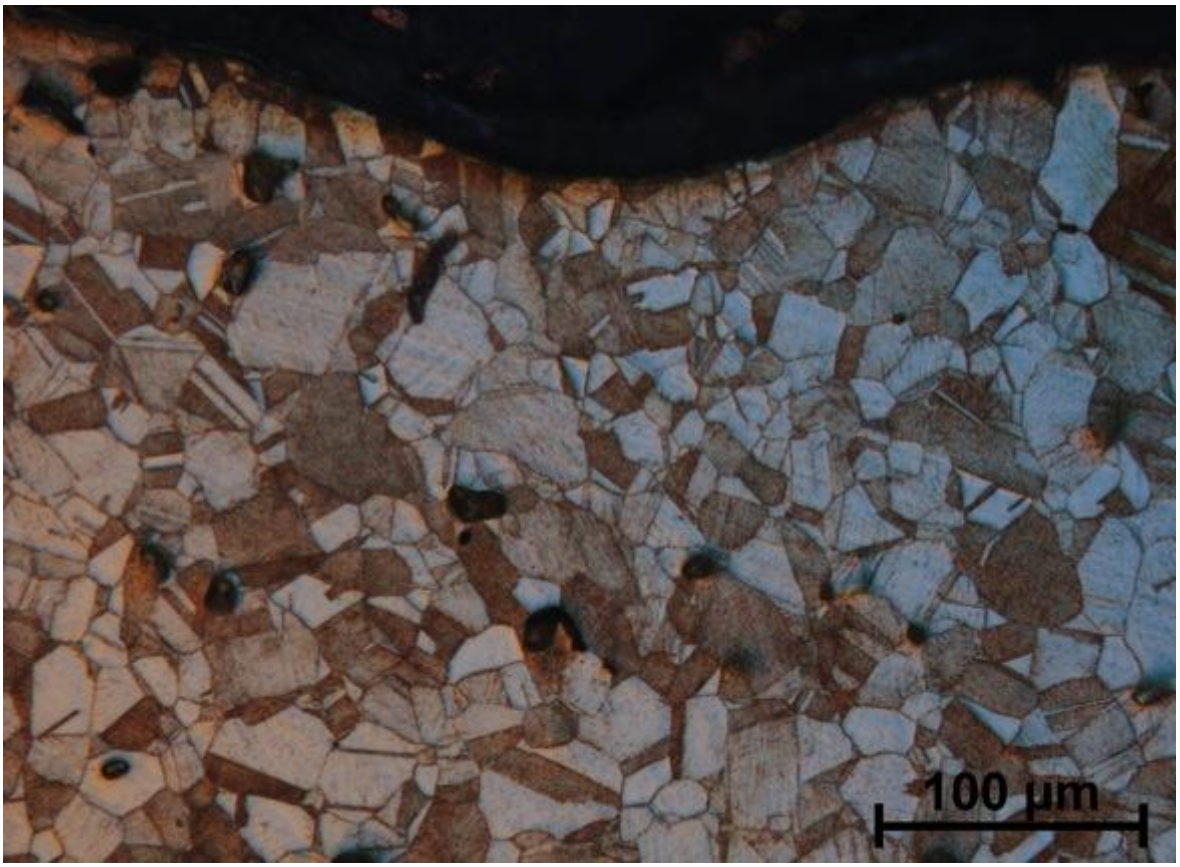

Figure 4.11. *Metallographic sample, sectioned from midspan of C-36° pipe.*

Figure 4.11 reveals these impressions left by the C-36° reinforcement have a depth on the order of 50-60 µm, or 20-25% of the wire diameter. The cross section shown in Figure 4.11 corresponds to a point of maximum tangential expansion in the pipe, and thus a region where indents are the deepest. Additionally, the C-36° sample showed the largest tangential expansion of all reinforced cases, though indent depth is also a dependant on initial tightness of the reinforcement.

Figures 4.12 and 4.13 show mean creep rates, $\dot{\varepsilon} = \frac{\varepsilon_{max}}{t_{max}}$, in the tangential and longitudinal directions, respectively, for each reinforcement type. Error bars denote variation in repeated tests.

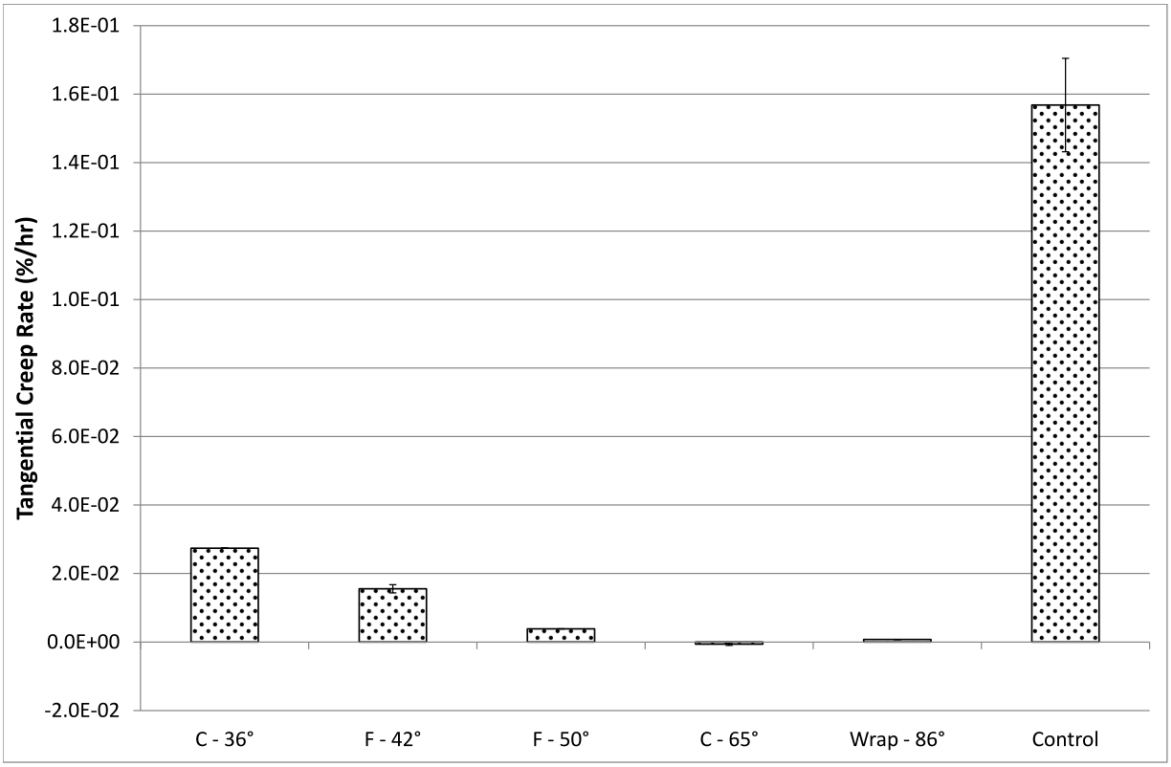

Figure 4.12. *Mean tangential creep rates. Error bars denote variation in repeated tests.*

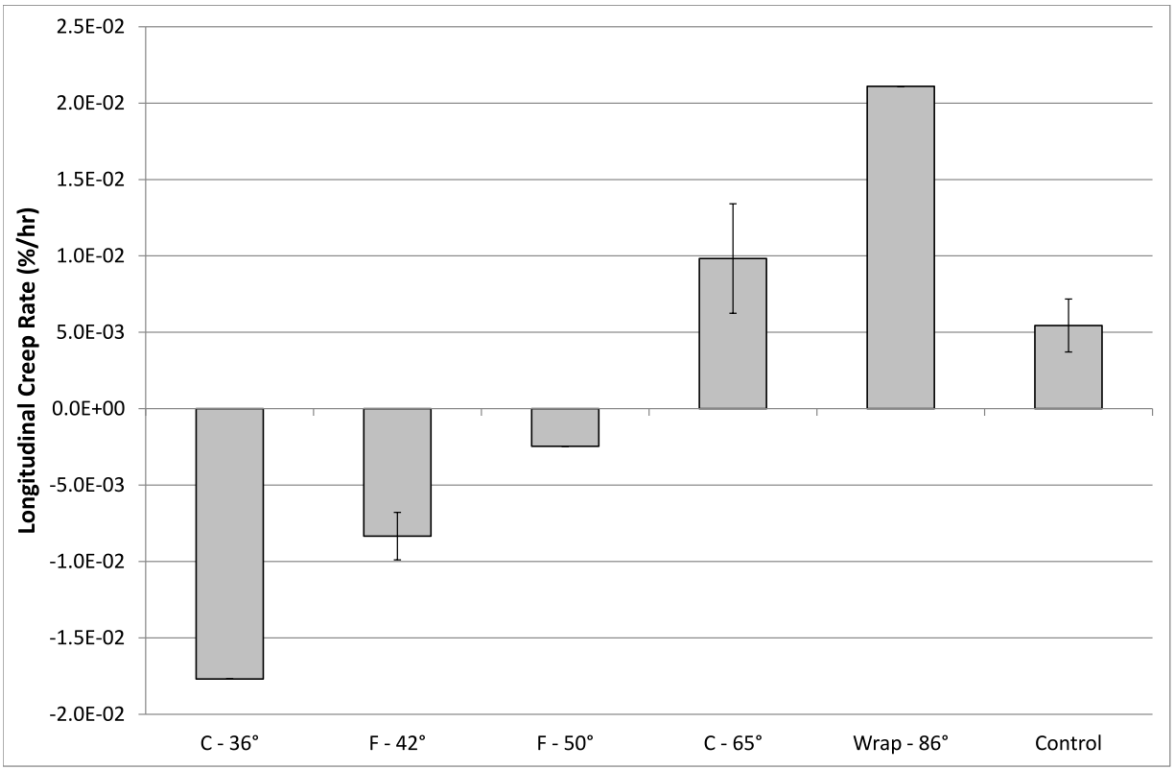

Figure 4.13. *Mean longitudinal creep rates. Error bars denote variation in repeated tests.*

The data shows that tangential creep rates decrease with increasing reinforcement angle, and that longitudinal creep rates increase with increasing reinforcement angle. Both tangential and longitudinal creep appear to be minimized between the 50° and 65° samples. The braid architecture parameters such as wire diameter, number of yarns and number of wires per yarn appear to have little effect on the observed trends, i.e., reinforcement angle appears to be dominant. In the case of the wrap and C-65° reinforcement, a substantial reduction in average tangential creep strain compared to the control pipe was observed, while the average longitudinal strain rate increased in these cases.

It was hypothesised that for some preliminary period prior to the engagement of the reinforcement, the reinforced samples would exhibit unrestrained creep behaviour matching that of the controls. In order to control initial tightness of the braid and minimise this period of unrestrained creep, the braid was pulled taut prior to testing and clamped at either end with hose clamps (termed 'fixed' end conditions). Table 4.4 quantifies the effect of pre-tightening the braid by comparing final strains for tests over 818 hours with fixed and free end conditions.

Table 4.4. *Comparison between final strains obtained with fixed and free and conditions.*

Reinforcement Designation	**End conditions**	**ε_t (%)**	**ε_z (%)**	**ε_r (%)**
C-65°	Fixed	-0.85	10.11	-6.10
	Free	-0.61	7.56	-6.40
F-42°	Fixed	11.75	-6.61	-1.90
	Free	13.53	-6.15	-1.58

Contrary to the previously stated hypothesis, the tests outlined in Table 4.4 give no clear evidence of fixed end conditions consistently reducing the magnitude of

creep strains. The variability in repeated tests, discussed further in Section 4.2.4, accounts for the range of final strains recorded with fixed and free end conditions. This observation suggests that either the C-65° and F-42° braids are close to fully engaged on the pipe in their initial state, or that the effect of end conditions on overall creep rate in these cases is sufficiently low so as not to be readily discernable from statistical variation. In extreme cases with a large radial clearance between the pipe and reinforcement layers, it is expected that an appreciable difference between fixed and free end conditions would be able to be discerned from the inherent variability in repeated tests.

As expected, Figures 4.12 and 4.13 show that for initial reinforcement angles below the neutral angle, the pipe expands tangentially and shortens longitudinally and vice versa for initial reinforcement angles above the neutral angle. In contrast to the near-instantaneous and largely elastic deformation observed in polymeric and elastomeric braid-reinforced pipes, this creep strain occurs gradually and is inelastic and non-recoverable.

The results of the periodically interrupted F-42° pressurized pipe test are shown in Figure 4.14 as a plot of tangential and longitudinal strain versus time. Power laws provide good fits for the strain and show that the magnitudes of the creep rates decrease with time compared to a linear trend over a 10-times control life test duration.

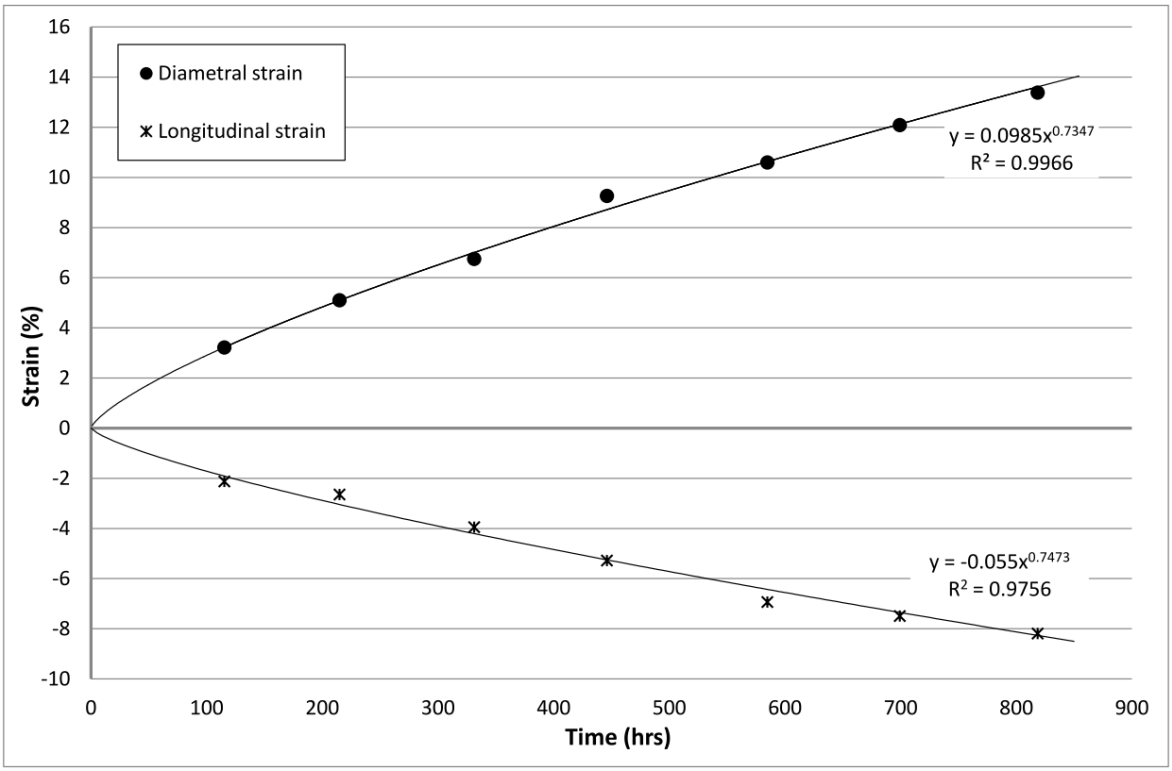

Figure 4.14. *Tangential and longitudinal strain measurements from periodically interrupted creep test on pipe with F-42° reinforcement architecture, plotted against test duration to form a pseudo creep curve. Test ended after 10-times life extension over control*, rather than being tested to failure.

This periodically interrupted test allows for an investigation of strain behaviour during testing, and a quantification of the effectiveness of the mean creep rate approximation. The instantaneous creep rate, calculated from the power law fits, differs by 8% at most from the mean creep rate approximation which consistently overestimates creep rate. This relatively small discrepancy supports the use of the mean creep rate in other tests.

At the end of the interrupted F-42° test, 13.4% tangential strain and -8.19% longitudinal strain were recorded. Comparatively, the two uninterrupted F-42° tests strained 11.7% to 13.5% in the tangential direction and -5.67% to -6.61% longitudinally, putting the tangential strain of the interrupted test within the range of observed tangential strains in the uninterrupted tests. The periodic

interruptions, involving regularly cooling the sample and removing the reinforcement layer to take strain measurements, appear to have caused a ratcheting effect which has enhanced strain in the longitudinal direction, causing an additional contraction on the order of 0.8 mm across the 50 mm gauge length when compared to equivalent uninterrupted tests.

4.2.3 Stiffness analysis

The control over tangential and longitudinal creep rates (demonstrated in Figures 4.12 and 4.13) is achieved by altering the relative tangential and longitudinal stiffnesses of the reinforcement. Naik et al [17] have previously suggested that braided composite stiffness properties are not a function of yarn size but are strongly influenced by braid angle and axial yarn content. However, those tests were performed on triaxially braided graphite fibres set in an epoxy resin matrix and tested as coupons under tension. While limited to braids of 30°, 45° and 55°, Birkefeld et al [18] have shown through predictive modelling and experimentation that stiffness varies non-linearly with braid angle in balanced biaxial materials.

Following the methodology outlined in Section 3.4.1, classical lamination theory (CLT) was used to model stiffness by treating the braid geometry as a laminate of two lamina oriented at $\pm\theta$. Properties were initially defined in the local (*1*-*2*) coordinate system using values typical of stainless steel, E_1 = 200 GPa and ν_{12} = 0.31, and an overall thickness of t = 3 mm. Note that the major Poisson's ratio (ν_{12}) is typically on the range of 0-0.5 for most materials. For triaxially braided graphite fibres set in an epoxy resin matrix and tested as coupons under tension, Naik et al. [17] showed that ν_{12} varies from approximately 0.25-0.45 for braid angles of 15-75°, suggesting that 0.31 is a reasonable first approximation for ν_{12} for the braided reinforcement.

As a simplifying approximation, G_{12} is set as equal to E_2. Recalling from Section 3.4.1 that Maxwell's reciprocity theorem requires a symmetrical stiffness matrix [19, 20] and therefore $Q_{12} = Q_{21}$, the minor Poisson's ratio (ν_{21}) was determined from the symmetry of the lamina stiffness matrix, [Q] where:

$$Q_{12} = \frac{\nu_{12}E_2}{1-\nu_{12}\nu_{21}} = \frac{\nu_{21}E_1}{1-\nu_{12}\nu_{21}} = Q_{21} \tag{4.1}$$

$$\rightarrow \nu_{21} = \frac{\nu_{12}E_2}{E_1} \tag{4.2}$$

To quantify the pseudo-matrix effect created by internal friction, E_2 was allowed to vary and the resultant 'fitted ideal laminate behaviour' was compared against measured longitudinal stiffness of braids, Figure 4.15 using a nonlinear least squares fit. Following the methodology outlined in Section 3.4.1, local *(1-2)* stiffness characteristics of a single lamina were related to the overall laminate properties in the global (*x-y*) coordinate system. E_x, bulk stiffness in the *x* direction, is analogous to braid longitudinal stiffness, E_z.

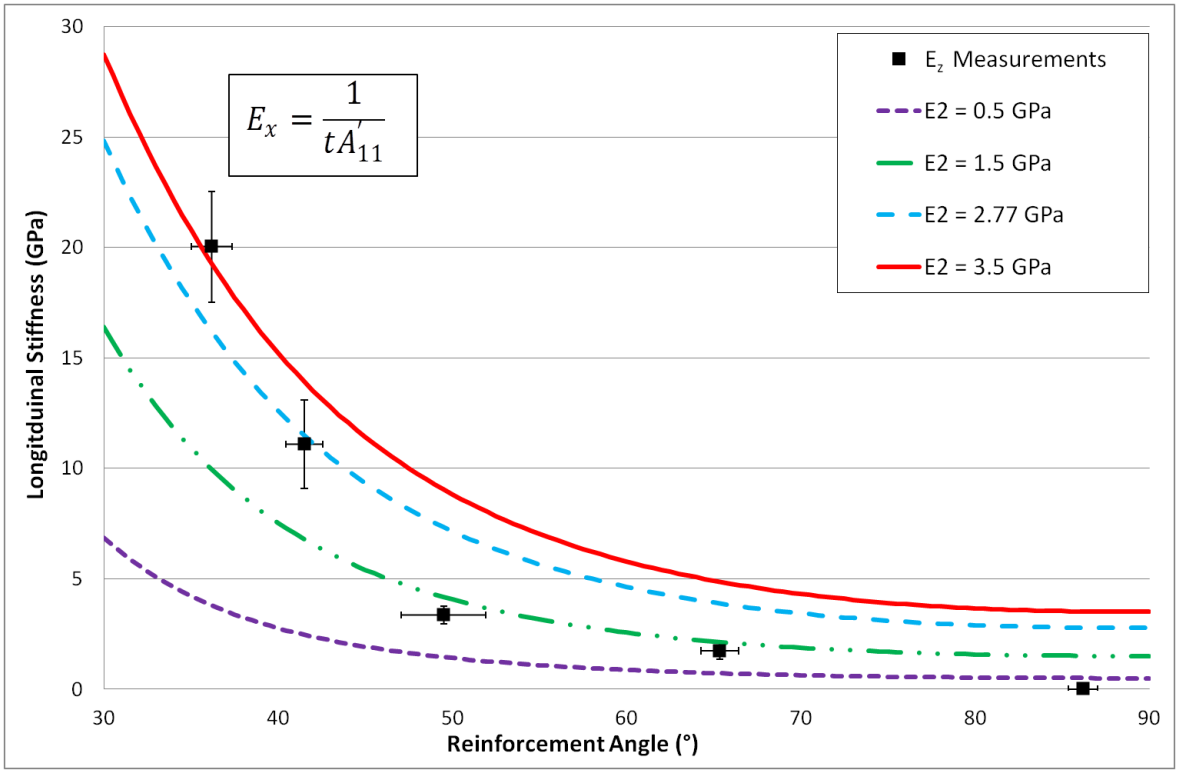

Figure 4.15. *Observed longitudinal stiffness measurements are compared against the classical lamination theory model for two lamina of ±θ and varying transverse stiffness values (E_2 from 0.5 to 3.5 GPa). Horizontal error bars denote standard deviation in the reinforcement angle. Vertical error bars reflect measurement error in crosshead displacement method of strain measurement (some bars smaller than data points).*

Figure 4.15 shows measured longitudinal stiffness E_x plotted against reinforcement angle, along with curves generated for various E_2 values. Higher values of E_2 (on the order of 3 GPa) better describe low-θ behaviour, but are less accurate than the lower E_2 values as θ tends to 90°. No single curve generated from the CLT model entirely captures the overall stiffness-reinforcement angle relationship seen when testing the braid. However, a nonlinear least squares fit shows that an E_2 value of 2.77 GPa is optimal, and the general trend observed in the E_x measurements in Figure 4.15 is not entirely dissimilar to what would be expected in an ideal 2-ply laminate. The vertical error bars in Figure 4.15 are reflective of measurement error associated with the crosshead displacement method, where strain of the crosshead is measured along with strain of the braid. While adequate for an order of magnitude comparison, this measurement could be

made to a higher degree of precision using non-contact strain measurement methods such as point tracking with a camera.

The curve fitting exercise in Figure 4.15 suggests that the frictional interaction responsible for E_2 varies as a function of reinforcement angle, and CLT does not account for this variability which thereby leads to a discrepancy between modeled behavior and empirical braid stiffness measurements. This variable internal friction is related to the braid-braid contact area, undulation through the thickness of the braid, and the braid-pipe contact area. As an order of magnitude approximation, the fitted E_2 value of 2.77 GPa, was used in Equation 3.31 to calculate tangential stiffness $E_y = \frac{1}{tA'_{22}}$.

4.2.4 Creep strain rate analysis

A major purpose of the present work is to determine the effect of braid architecture on creep strain rate. As mentioned previously, the neutral angle for internally pressurized, thin-walled pressure vessels with reinforcement in tension is $\theta_N^* = 54.7°$ [21-23], and systems with compliant matrices and stiff reinforcement deform elastically under pressure at low temperature so that the stiff reinforcement assumes this orientation [21]. In contrast to braid-reinforced polymeric and elastomeric tubes, the modulus of the pipe relative to the reinforcing material is comparatively large in the present study. As a result of this relatively large pipe stiffness, coupled with the high test temperature, creep deformation rather than elastic deformation is expected to be the mechanism for reorientation of the reinforcement in the present experiments. As the tube is not thin-walled (t/r_i>0.05), it is expected that a geometry dependent neutral angle (θ_N) will be obtained where $\theta_N \to \theta_N^*$ as $t/r_i \to 0.05$.

In the present case, indentations were left by the braid on the pipe surface (see Figure 4.10), so it was possible to ascertain whether reorientation of the

reinforcement is also observed in the hybrid pipe geometry deforming by creep. As indicated by Table 4.5, post-test braid angle measurements confirm that during testing, the braid angle shifts by $\Delta\theta$ toward some θ_N which is dependent on the particular tube geometry and the tangential/longitudinal stress ratio. However, the 50°, 65° and 86° samples all showed relatively small changes that are not significantly different from the range of measured braid angles in the as-manufactured condition. Predictably, $\Delta\theta$ is smaller in magnitude for initial angles around θ_N^*. The observation of small to negligible values of $\Delta\theta$ for initial angles greater than θ_N is related to the inability of this system to reduce the braid angle via a reduction in diameter due to the state of dynamic equilibrium that exists at the interface between the reinforcement and the liner, resulting in a requirement that $\dot{\varepsilon}_t \geq 0$. Tangential contraction would result in the reinforcement disengaging. If the reinforcement were to disengage, tangential creep would occur, and the pipe would begin to expand until the reinforcement was once again engaged. In order for a tangential contraction and concomitant reduction of larger braid angles towards θ_N to occur, the reinforcement would have to be bonded to the surface of the liner pipe or embedded within the pipe itself.

Table 4.5. *Post-test braid angle measurement.*

Reinforcement designation	**Pre-test reinforcement angle (°)**	**Post-test reinforcement angle (from indentations) (°)**	**Change in reinforcement angle (°)**
C-36°	36.2±1.2	47.8±1.4	**+11.6**
F-42°	41.5±1.0	50.0±2.6	**+8.5**
F-50°	49.5±2.4	50.7±1.9	**+1.2**
C-65°	65.3±1.1	63.8±1.5	**-1.5**
Wrap	86.2±0.8	86.6±0.7	**+0.4**

Rather than the near-instantaneous shift upon application of pressure seen with reinforced elastomeric or polymeric hoses [21], the shift in braid angle in reinforced metallic pipes occurs primarily through creep. All braid-reinforced brass pipe tests were interrupted prior to rupture after approximately 820 hours, so it is likely that all initial angles below θ_N would have continued to shift towards θ_N over time, limited only by the creep ductility of the brass.

Measured mean creep rates are plotted against initial reinforcement angle in Figure 4.17. Error bars for the mean reinforcement angle $\Delta_{mean} = \sqrt{\Delta_{pre}^2 + \Delta_{post}^2}$ were determined from standard deviations in the pre- and post-test angle measurements, Δ_{pre} and Δ_{post}, respectively. The fitted trendlines are based on an analysis of the stresses in a thin-walled pressure vessel at internal pressure p, reinforced with n fibres per unit length of pipe oriented at angle θ to the longitudinal axis and which transmit tension T. The radial stress in the pipe is zero. From force balances in the tangential and longitudinal directions, stresses in these respective directions are derived to be:

$$\sigma_t = \frac{pr_i}{t} - \frac{nT}{t} sin\theta$$
$$\sigma_z = \frac{pr_i}{2t} - \frac{nT}{t}\frac{cos\theta}{tan\theta} \quad (4.3)$$

and can be generalized to have the following dependences on θ:

$$\sigma_t = A - B sin\theta$$
$$\sigma_z = \frac{A}{2} - B\frac{cos\theta}{tan\theta} \quad (4.4)$$

Following Dowling [24], a time hardening model for multiaxial creep rates is used to associate multiaxial stress components to component strain rates:

$$\dot{\varepsilon}_t = \frac{1}{\eta}[\sigma_t - 0.5(\sigma_r + \sigma_z)]$$
$$\dot{\varepsilon}_z = \frac{1}{\eta}[\sigma_z - 0.5(\sigma_r + \sigma_t)] \quad (4.5)$$

Where η, the tensile viscosity, is the ratio of the effective creep rate to the von Mises stress and is, in general, a function of stress and time, given by:

$$\frac{1}{\eta} = \frac{\dot{\varepsilon}_{eff}}{\sigma_{VM}} = D_3 \emptyset \sigma_{VM}^{\delta-1} t^{\emptyset-1} \quad (4.6)$$

with D_3, $\emptyset$ and δ empirical constants related to creep data.

The effective creep rate is much like von Mises stress and is given by:

$$\dot{\varepsilon}_{eff} = \frac{\sqrt{2}}{3}\sqrt{(\dot{\varepsilon}_t - \dot{\varepsilon}_r)^2 + (\dot{\varepsilon}_r - \dot{\varepsilon}_z)^2 + (\dot{\varepsilon}_z - \dot{\varepsilon}_t)^2} \quad (4.7)$$

Substituting the expressions from Equations 7 into Equations 8 gives:

$$\dot{\varepsilon}_t = \frac{1}{\eta}\left[\frac{3A}{4} - B\left(sin\theta - \frac{cos\theta}{tan\theta}\right)\right]$$
$$\dot{\varepsilon}_z = \frac{1}{\eta}\left[B\left(\frac{sin\theta}{2} - \frac{cos\theta}{tan\theta}\right)\right] \quad (4.8)$$

Incompressibility requires that volumetric strain and therefore volumetric strain rate are zero [24] and gives:

$$\dot{\varepsilon}_r = -(\dot{\varepsilon}_t + \dot{\varepsilon}_z) \quad (4.9)$$

Equations 4.8 and 4.9 can then be used to generate a $\dot{\varepsilon}_r - \theta$ curve against which measured radial creep strains can be compared in order to validate the incompressibility assumption of Equation 4.9. Equations 4.8 and 4.9 suggest that this $\dot{\varepsilon}_r - \theta$ curve is of the form $-A + B\left(sin\theta + \frac{cos\theta}{tan\theta}\right)$.

A boundary condition has been applied such that the tangential fit for the tangential strain rate is terminated at the x-axis to ensure that $\dot{\varepsilon}_t \geq 0$. The reason for this boundary condition is that tangential contraction would result in the reinforcement disengaging. If the reinforcement were to disengage, tangential creep would occur, and the pipe would begin to expand until the reinforcement was once again engaged. Therefore, in this model the pipe is not allowed to contract tangentially. From Equation 8, the condition that $\dot{\varepsilon}_t = 0$ implies that $(\sigma_t - 0.5\sigma_z) = 0$. This modifies the longitudinal fit to be of the form $A - B\frac{cos\theta}{tan\theta}$, and the radial fit of the form $-A + B\frac{cos\theta}{tan\theta}$ for regions where the $\dot{\varepsilon}_t = 0$ boundary condition is applied.

Table 4.6 summarizes the form of the trigonometric fits used for the tangential, longitudinal and radial creep rates above and below θ_N. Justification for the form of these fits is given in Table 4.6, with reference to the $\dot{\varepsilon} - \sigma$ and $\dot{\varepsilon} - \theta$ relationships expressed in Equations 4.4 - 4.9.

Table 4.6. *Form of trigonometric fits used for* $\dot{\boldsymbol{\varepsilon}} - \boldsymbol{\theta}$ *relationships in the tangential, longitudinal and radial directions.*

		Below θ_N	**Above θ_N**
$\dot{\varepsilon}_t$	Justification for fit.	$\dot{\varepsilon}_t = \frac{1}{\eta}\left[\frac{3A}{4} - B\left(sin\theta - \frac{cos\theta}{tan\theta}\right)\right]$	$\dot{\varepsilon}_t = 0$
	Form of trigonometric fit.	$A - B\left(sin\theta - \frac{cos\theta}{tan\theta}\right)$	0
$\dot{\varepsilon}_z$	Justification for fit.	$\dot{\varepsilon}_z = \frac{1}{\eta}\left[B\left(\frac{sin\theta}{2} - \frac{cos\theta}{tan\theta}\right)\right]$	For $\dot{\varepsilon}_t = 0$, need $(\sigma_t - 0.5\sigma_z) = 0$ $\rightarrow \sigma_t = \frac{\sigma_z}{2}$ Know $\dot{\varepsilon}_z = \frac{1}{\eta}(\sigma_z - 0.5\sigma_t)$ $\therefore \dot{\varepsilon}_z = \frac{1}{\eta}\left(\frac{3}{4}\sigma_z\right)$ $\sigma_z = \frac{A}{2} - B\frac{cos\theta}{tan\theta}$ $\rightarrow \dot{\varepsilon}_z = \frac{3}{4\eta}\left[\left(\frac{A}{2} - B\frac{cos\theta}{tan\theta}\right)\right]$
	Form of trigonometric fit.	$B\left(\frac{sin\theta}{2} - \frac{cos\theta}{tan\theta}\right)$	$A - B\frac{cos\theta}{tan\theta}$
$\dot{\varepsilon}_r$	Justification for fit.	$\dot{\varepsilon}_r = -(\dot{\varepsilon}_t + \dot{\varepsilon}_z)$ $\dot{\varepsilon}_r = \frac{1}{2\eta}\left[\frac{-3A}{2} + B\left(sin\theta + \frac{cos\theta}{tan\theta}\right)\right]$	$\dot{\varepsilon}_r = -(\dot{\varepsilon}_t + \dot{\varepsilon}_z)$ $\dot{\varepsilon}_r = -\dot{\varepsilon}_z$
	Form of trigonometric fit.	$-A + B\left(sin\theta + \frac{cos\theta}{tan\theta}\right)$	$-A + B\frac{cos\theta}{tan\theta}$

Neglecting the stress- and time-dependency of η, least squares fits using the trigonometric relationships of Table 4.6 were used to fit the strain rate data and are shown on Figure 4.17, with curves generated at the initial angles (solid lines) and final angles at t = 820 hours (dashed lines), to create lower and upper bounds, respectively. To allow for goodness of fit to be assessed, as well as illustrating the transition made by individual samples from initial to final angle, measured mean

creep rates are plotted at both the initial angles (filled points) and final angles at t = 820 hours (unfilled points).

The method of least squares fitting involved plotting the trigonometric term against $\dot{\varepsilon}$, such that values for the constants A and B could be determined from the linear trend line formula $y = mx + c$. In fitting with the neutral angle theory outlined in Section 3.3.1, where it was shown that the neutral angle corresponds to a point where net stresses are zero for a simplified case where the only loading is from internal pressure, fits were constrained to zero creep rate at the neutral angle. Figure 4.16 gives an example of this fitting methodology, applied for the tangential rate curve below θ_N.

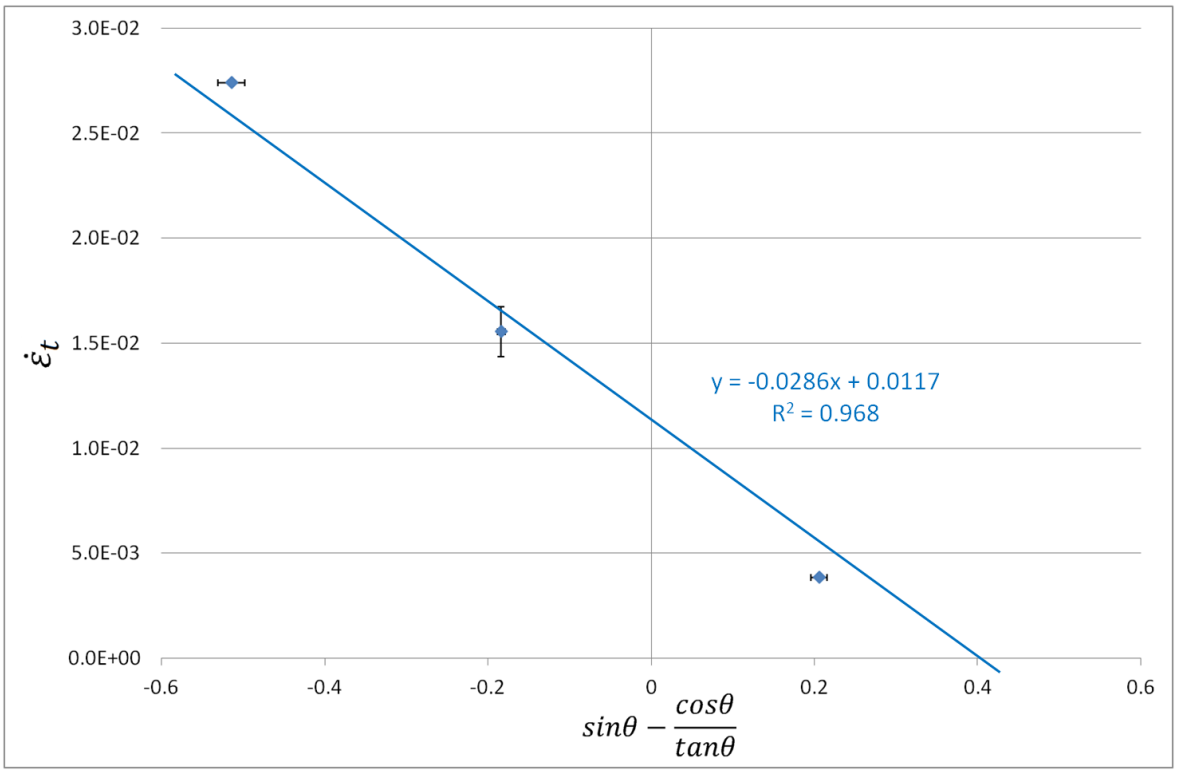

Figure 4.16. *Linear least squares fit for tangential creep rate trend below* θ_N.

Strain measurements taken during the periodically interrupted test shown in Figure 4.14 can be related to the instantaneous reinforcement angle geometrically.

This in turn allows the change in creep rate to be explored as the F-42° sample reinforcement reorients itself from 41.5° to 50.0°. The instantaneous creep rate and reinforcement angle are superimposed in Figure 4.17, showing the transition of the F-42° sample from the lower to the upper band.

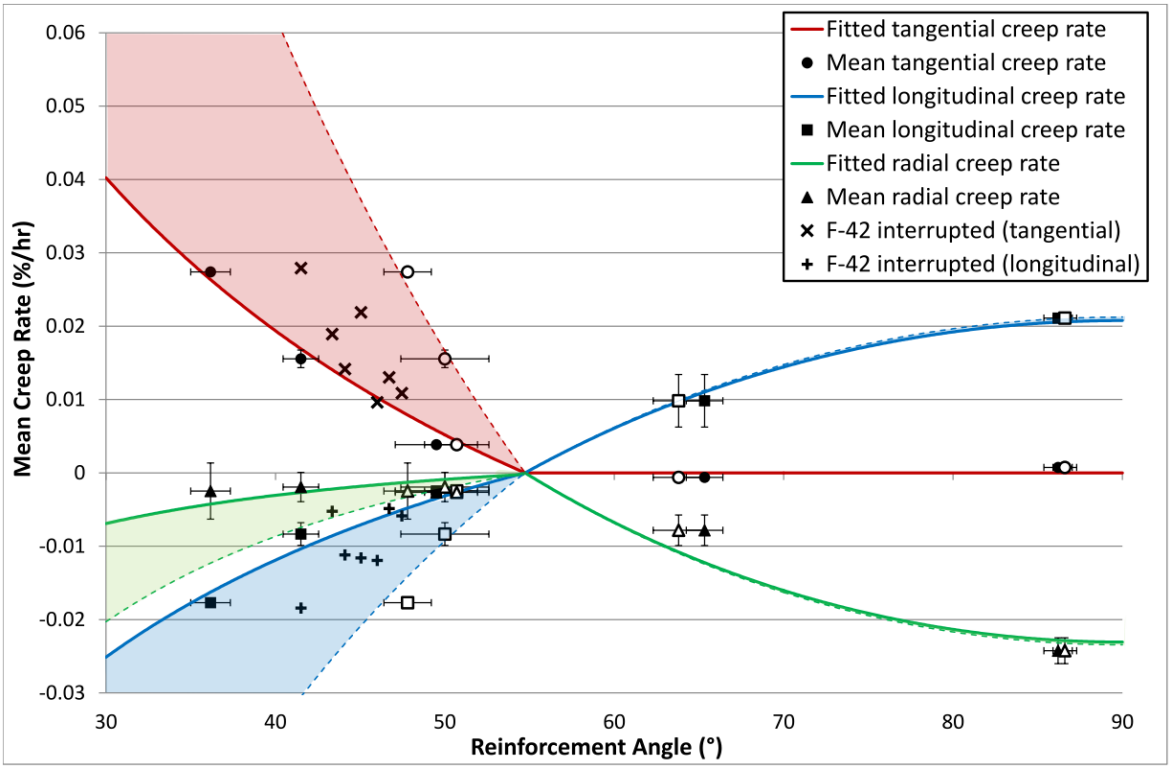

Figure 4.17. *Measured mean tangential, longitudinal and radial creep rates plotted against initial reinforcement angle (solid points) and final angle (unfilled points), with creep rate trends superimposed. Shaded bands cover range of predicted behaviour from initial angle (solid line) to final angle at t = 820 hours or failure (dashed line). Creep strain data from the interrupted F-42° test is superimposed, with ✕ and + symbols, showing tangential and longitudinal creep rates, respectively. Some error bars smaller than data points.*

Up to a value of $\theta \leq 54.7°$, the measured tangential creep rate varies with initial reinforcement angle as $\dot{\varepsilon}_t = 0.0117 - 0.0286\left(\sin\theta - \frac{\cos\theta}{\tan\theta}\right)$, as determined in the linear least squares fit of Figure 4.16, and has a coefficient of determination of R^2 = 0.968. At the least squares-fit generated using the final braid angle values, this R^2 value drops to 0.643.

The negligible shift observed in braid angle for initial angles above $\theta_N \approx \theta_N^*$ can be attributed to the lack of a driver for tangential contraction of the pipe, which is also responsible for the $\dot{\varepsilon}_t \geq 0$ boundary condition. As stated previously, to make tangential contraction (and reduction of larger braid angles toward θ_N) possible, the reinforcement would need to be bonded to the surface of the liner, or embedded within the pipe itself.

From Figure 4.17 it can be seen that for $\theta < \theta_N$ the measured longitudinal creep rate varies with initial braid angle as $\dot{\varepsilon}_z = 0.0319\left(\frac{\sin\theta}{2} - \frac{\cos\theta}{\tan\theta}\right)$, has an R^2 value of 0.939, and is zero at $\theta = 54.7°$. For $\theta > \theta_N$, this relationship is $\dot{\varepsilon}_z = 0.0204 - 0.0407\frac{\cos\theta}{\tan\theta}$ and has an R^2 value of 0.869. Note that the $\dot{\varepsilon}_z$ curve is negative for angles below θ_N. Unlike the tangential and radial trends, the $\dot{\varepsilon}_z$ curve exists both above and below the x-axis.

The measured values of radial creep rate conform to the general behaviour of the predicted radial creep rate trend, remaining negative and increasing in magnitude away from θ_N. For initial angles below θ_N, this radial creep rate trend is $\dot{\varepsilon}_r = -0.0104 + 0.0086\left(\sin\theta + \frac{\cos\theta}{\tan\theta}\right)$ and has an R^2 value of 0.734. Above θ_N, the $\dot{\varepsilon}_r - \theta$ trend is $\dot{\varepsilon}_r = -0.0228 + 0.0455\frac{\cos\theta}{\tan\theta}$ and has an R^2 value of 0.708.

Comparing the instantaneous creep rate from the periodically interrupted data with the mean creep rate for the F-42° sample, Figure 4.17 reveals that initial creep rate is on the order of 1.7-times greater than the mean rate, and decays to approximately 60% of the mean rate after 820 hours (i.e. at the final angle). Figure 4.18 reproduces these data points for the periodically interrupted test, highlighting the trend of maximum creep rate at the initial braid angle and a diminishing creep rate over the 820 hour duration of the F-42° test.

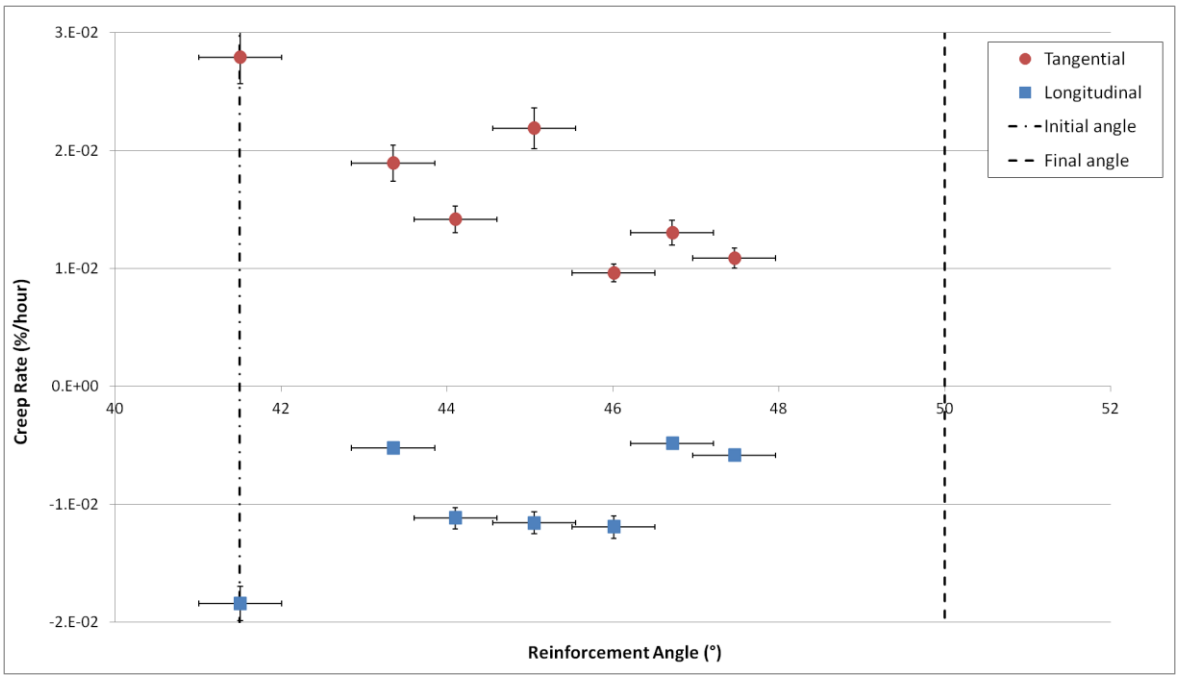

Figure 4.18. *Instantaneous creep strain data in the tangential and longitudinal directions, as measured during the interrupted F-42° test from time t = 0 hours to t = 820 hours. Some error bars smaller than data points.*

Scatter in creep rate measurements, apparent in Figure 4.18, makes it difficult to fit a trend to describe the change in creep rate in an individual sample as braid orientation and therefore stress state changes. Rather than repeating interrupted tests to reduce data scatter and make this trend more apparent, Chapter 5 explores the use of in-situ strain measurement in order to characterize changes in creep rate during testing. In-situ strain measurement also improves temporal resolution from approximately 100 hours to 60 seconds.

From measured strains, and knowledge of the initial angle, the geometric relationship between pipe size and braid orientation can be used to calculate a final braid angle of 47.5° for the F-42° sample (as shown in Figures 4.17 and 4.18). While lower than expected, this calculated final angle is within a single standard deviation of the measured final angle of 50.0 ± 2.6°. The geometric relationship between braid angle and pipe dimensions is based upon a single fibre in continuous contact with the pipe surface, and does not account for three-

dimensional effects of the reinforcement architecture such as curvature and undulation.

From Equation 4.8, it can be seen that the constant associated with the trigonometric terms in both the $\dot{\varepsilon}_t$ and $\dot{\varepsilon}_z$ expressions is B/η. The B/η terms at the initial reinforcement angle are 0.0286 and 0.0319 for the $\dot{\varepsilon}_t$ and $\dot{\varepsilon}_z$ trends, respectively – a difference of 11%.

The theoretical neutral angle (θ_N) is geometry and load-dependent, and is not necessarily θ_N^* = 54.7°, as derived for thin-walled pressure vessels. Effective strain rate, $\dot{\varepsilon}_{eff}$, is evaluated in order to consider the collective effect of the multiaxial strains presented in Figure 4.17. The optimum reinforcement angle (θ_{min}) is determined to be at the point where this effective strain rate is minimized, and is expected to approach θ_N^* as $t/r_i \rightarrow 0.05$.

Using Equation 4.7 to combine the fitted trigonometric functions from Figure 4.17, a plot of effective strain rate is generated, Figure 4.19, from which an optimum reinforcement angle can be predicted where multiaxial creep rates are minimized. Additionally, this plot reveals the nature of multiaxial strain behaviour away from the neutral angle, as described by Equation 4.10, which to the author's knowledge is previously unseen in the literature. Vertical error bars for the effective creep rate data are determined from propagation of uncertainty from each of the creep rate components, which are reflective of variation in repeated tests.

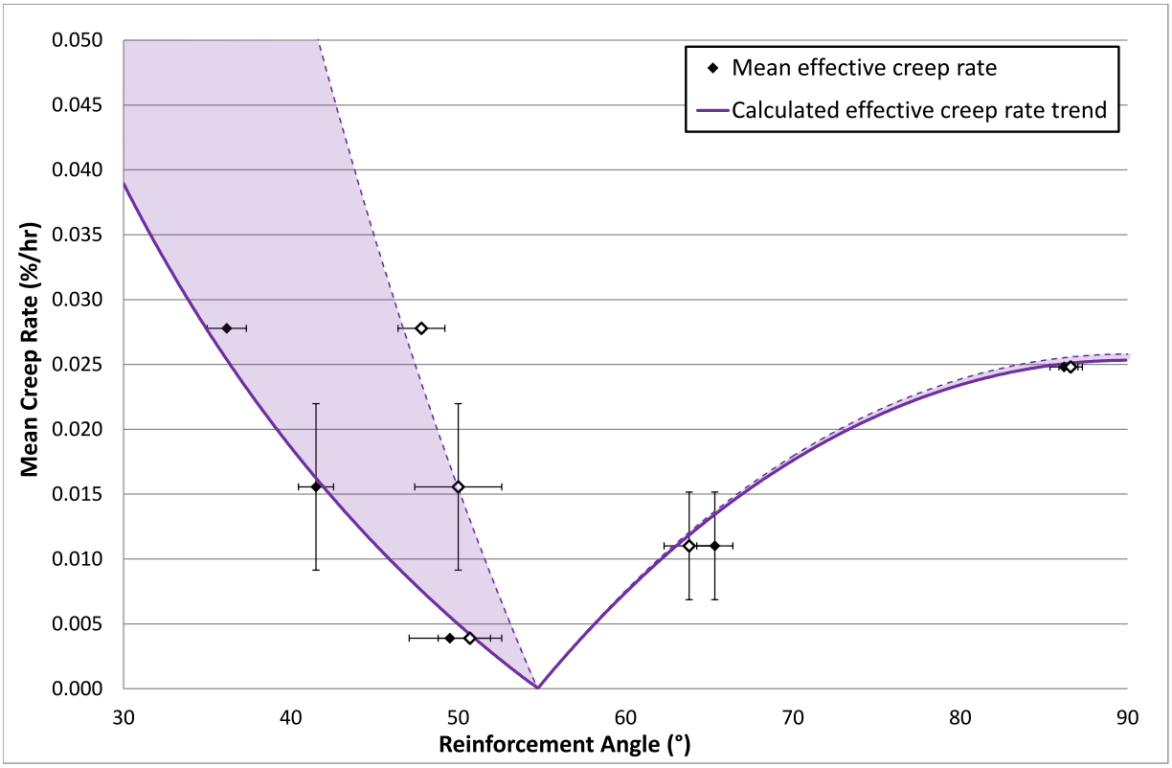

Figure 4.19. *Calculated mean effective creep rates plotted against initial reinforcement angle (solid points) and final angle (unfilled points). Shaded bands cover range of predicted behaviour from initial angle (lower band) to final angle at t = 820 hours or failure (upper band).*

Applying the trigonometric trendline formulae for the tangential and longitudinal fits to Equations 4.7 and 4.9 reveals the relationship between effective strain rate and reinforcement angle as:

$$\dot{\varepsilon}_{eff} = \begin{cases} \frac{\sqrt{2}}{3}\sqrt{0.0029sin^2\theta - 0.0025sin\theta - 0.0053cos^2\theta + 0.0036\frac{cos^2\theta}{tan^2\theta} + 0.0014\frac{cos\theta}{tan\theta} + 0.0007} & if\ \theta < 54.7° \\ \frac{\sqrt{2}}{3}\sqrt{0.0112\frac{cos^2\theta}{tan^2\theta} - 0.0112\frac{cos\theta}{tan\theta} + 0.0028} & if\ \theta \geq 54.7° \end{cases} \quad (4.10)$$

A minimum effective strain rate is found at a reinforcement angle of θ_{min} = 54.7±1.5°, with uncertainty based on typical variation in the measured braid angles. From observation of Figure 4.19, the location of this minima in the multiaxial curve is entirely expected as all three directional creep rate curves reach

zero strain at approximately θ = 54.7°. The final effective creep rate curve, generated by combining fitted trends, has a coefficient of determination of R^2 = 0.976 using initial angle values. In this instance, θ_{min} appears to be equal to θ_N^*, suggesting that the hybrid pipe behaves as a thin-walled pressure vessel despite not meeting the t/r_i < 0.05 criterion. As designed, the stress-bearing component of the hybrid pipe is the reinforcement layer and the pipe effectively acts as a shell, which transmits load to the reinforcement.

By magnitude, creep in the radial direction is the smallest contributor to the effective creep rate, particularly for $\theta < \theta_{min}$, where measurements of radial creep rate are an order of magnitude lower than those for the tangential and longitudinal directions. Referring to Figure 4.17, measured values of $\dot{\varepsilon}_r$ are consistently lower than expected for $\theta < \theta_{min}$. Because of the much smaller initial length scale, the error associated with radial strain measurement is proportionally much higher than the errors in the longitudinal and tangential directions. For the mean reinforcement angle trend, the absolute difference between measured and calculated strains in the radial direction lies in the range of 7-54 μm.

In the as-received condition, wall-thickness was found to only have a 0.4% standard deviation (on the order of 5 μm), suggesting it was not a significant contributor to variations in repeated tests. For diffusional creep, creep rate is proportional to $1/d^m$ where d is grain size and m is a constant typically between 2 and 3 [24]. Neglecting twin boundaries, the as-received grain size was determined to be 18.3 ± 3.2 μm, a variation of approximately 17%.

Utilizing the incompressibility assumption of Equation 4.9, predicted radial creep rates can be generated from measured creep rates in the tangential and longitudinal directions. In order to validate this assumption of incompressibility,

Figure 4.20 compares these predicted rates against the measured radial creep rate and the fitted radial creep rate trend, as was shown in Figure 4.17.

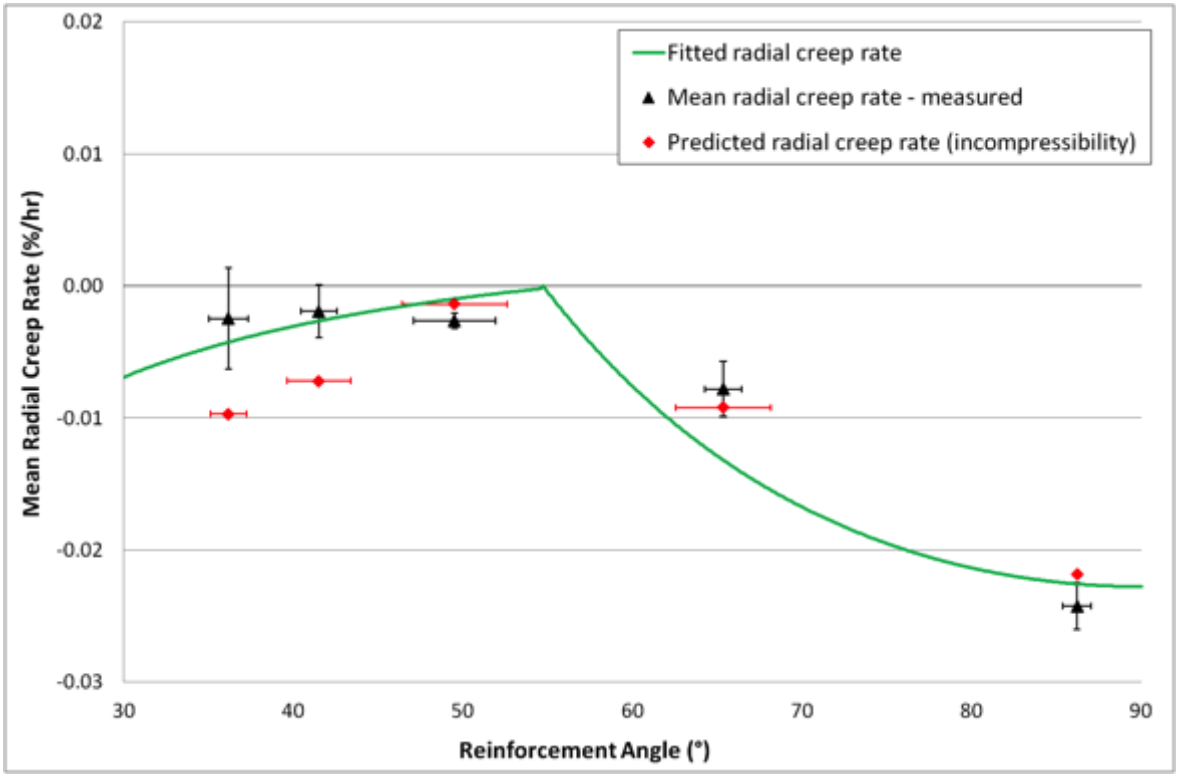

Figure 4.20. *Measured and predicted radial creep rates, superimposed over radial creep rate trend line, predicted by the incompressibility condition. All rates plotted against initial reinforcement angle.*

As the radial creep rate trend has been fitted to the measured radial creep rate data, it is unsurprising that the measured data is a better fit than the predicted creep rate values. The absolute difference between the measured and predicted radial strains is 4-54 μm.

The F-50° sample has an effective strain rate of $\dot{\varepsilon}_{eff}$ = 4.06 × 10^{-3} %/hour. By comparison, the average unreinforced control test has an effective strain rate of 0.190 %/hour, a reduction of creep rate by a factor of 47. The predicted effective strain rate at the optimum braid angle of θ_{min} is calculated to reduce creep rate by a

factor of over 3500, increasing the creep life from 83 hours to almost 300,000 hours and essentially negating creep as the primary mode of failure.

The effective creep rate modeled in Figure 4.19 changes significantly with deviation from the optimum angle. For example, a 2° deviation in the initial angle leads to a 40-60x increase in the effective creep rate. However, it should be noted that when the braid seeks to obtain this optimum angle, this elevated creep rate reduces as net stress is reduced and the braid approaches a position of force equilibrium.

The empirically derived neutral angle of θ_{min} = 54.7 ± 1.5° in the present case is consistent with the theoretical neutral angle of 54.7° for a thin-walled pressure vessel, predicted to give zero net stress and thus eliminate the driving force for creep deformation. The observed location and magnitude of this minimum is consistent with literature and modelling. The generated trends have a strong physical basis related to the trigonometric relationship between stress and reinforcement angle, and conform closely to the experimental data points. The shape of the $\dot{\varepsilon}_{eff} - \theta$ curve, as well as knowledge of the change in θ towards θ_N in creep applications, but only for $\theta < \theta_N$ when the reinforcement is unbonded, are unique observations with significant implications for industry when considering manufacturing guidelines and tolerances for braids. As seen in Tables *4.1* and *4.5*, the braid angle typically varies by 1-2.5°. Assuming a similar level of control during production, it would be advisable to produce a braid slightly below the neutral angle, so that it is able to tend to θ_N during service.

The focus of the present study was to explore the relationship between creep rate and braid angle over a wide range of braid angles. Measured mean creep rates in Figures 4.17 and 4.19 have been plotted against the mean braid angle. From Table 4.5, it can be seen that during testing, the braid orientation shifts towards the

optimum angle for initial angles below θ_N. Therefore, it is expected that the majority of creep deformation happens early in the test, while the braid angle is at its furthest from θ_{min}. As this deformation permits the shifting of the braid towards the optimum angle, it is theorized that the creep rate drops as the braid angle shifts. This theory is supported by instantaneous creep rate and reinforcement angle information collected during periodically interrupted testing, with a clear decrease in creep rate observed in Figures 4.17 and 4.20 as the F-42° sample tends to an angle of 50° after 820 hours. The time-dependent behaviour of the braid angle and its relationship with the creep rate is a concept that will be further explored in Chapter 5 via in-situ longitudinal strain measurement.

The present study has demonstrated that creep strains in both the tangential and longitudinal directions can be manipulated by exploiting the anisotropic nature of a braided reinforcement layer, particularly the coupling between its behaviour in the longitudinal and tangential directions. Furthermore, the reinforcement angle was identified as the key parameter of reinforcement architecture for controlling the creep response. Fitting with neutral angle theory, a braid angle of approximately 54.7 ± 1.5° is predicted empirically to be optimal to minimize the effective multiaxial creep rate of a hybrid pipe under internal pressure. In addition to this observation of the location of the minima, a full empirical model of creep rate as a function of reinforcement angle was derived to describe creep rate behaviour away from the neutral angle.

The braided reinforcement was observed to shift to the neutral angle (θ_N). Previously, this has been reported for systems at room temperature, where the shift in θ is brought about by rapid elastic deformation upon pressurization. This is the first reported instance of creep being the mechanism whereby braided reinforcement gradually orients itself to θ_N, thereby identifying the neutral angle as a relevant concept for creep strengthening.

4.3 Conclusions

A hybrid metallic pipe design was conceived to reduce or eliminate creep in high temperature applications (1173K and above). A model system (brass reinforced with austenitic stainless steel braid/wires) was selected to determine the effects of varying braid/wire angles.

Experimental methods have been developed to manufacture hybrid, reinforced pipes with a range of reinforcement architectures. Methods have been developed to subject the hybrid pipes to creep conditions, i.e., elevated temperatures and internal pressure, and to evaluate their response in terms of strain and rupture life.

Pipes reinforced with helical windings obtain approximately 7.6-times creep life extension compared to unreinforced pipes of the same dimensions. While pressurized unreinforced pipes normally fail through cracking in the longitudinal direction due to tangential stress, helical reinforcement shifts the failure mode to cracking in the tangential direction due to longitudinal stress.

As expected, unreinforced pipes fail through cracking in the longitudinal direction, due to hoop stress. When tangential creep is restricted by a helical reinforcement architecture, longitudinal creep is accelerated and the failure mode becomes cracking in the hoop direction due to longitudinal creep caused by longitudinal stress.

When a braided architecture in employed, creep strains in both the tangential and longitudinal directions can be controlled. A simple analytical model (Section 3.3) predicts a neutral angle of 54.7°, at which both tangential and longitudinal creep strain rates are zero in thin-walled pressure vessels. In the model material system,

an optimal braid angle was empirically determined to be 54.7 ± 1.5°. In the present case, for a model materials prototype with braid reinforcement angle of 50°, creep life extensions in excess of 10-times were observed without rupture, and a reduction in creep rate in excess of 45-times was measured. Understanding the effects of varying braid angle on performance in metallic pipes is critical, since the precise neutral angle will be difficult to achieve in industrial applications. Furthermore, hybrid architecture can be designed with specific braid angles to offset any combination of self-weight and internal pressure.

Effective creep rate is sensitive to braid angle, with a 2° deviation in the initial angle predicted to cause a 40-60x increase in the effective creep rate. However, it should be noted that the braid is constantly shifting to seek θ_N if the initial θ value is less than θ_N, and this elevated creep rate would be short lived as the braid approaches a position of force equilibrium and the rate of reduction of creep rate follows Equation 4.10, dropping rapidly for angles near θ_N.

Creep of the pipe facilitates this observed straining of the braid (both a change in angle and an increase in tension) up to the point where θ_N is reached. At θ_N, it is theorized that net stresses in the hoop and longitudinal directions are zero and there is no driving force for creep, as derived in Section 3.3.1. It is also notable that initial braid angles below θ_N appear to converge on θ_N faster than braids which start above θ_N. In fact, small to negligible values of $\Delta\theta$ were observed for initial angles greater than θ_N which was unexpected, and is theorized to be related to the interfacial interaction between the reinforcement and pipe. Chapter 5 explores this $\dot{\theta}$ behaviour as a function of θ, with a model in Section 5.2 specifically addressing theoretical behaviour, and how boundary conditions in the present system may have led to negligible $\Delta\theta$ for initial angles greater than θ_N.

CHAPTER REFERENCES

[1] J. E. Shigley, *Mechanical Engineering Design*, 1st ed. Singapore: McGraw-Hill Inc, 1986.

[2] AustralWrightMetals. Metal Alloys - Properties and Application of Brass and Brass Alloys, http://www.azom.com/article.aspx?ArticleID=4387, [Accessed 5 February 2014].

[3] A. P. Miodownik, "Phase Diagrams of Binary Copper Alloys," P. R. Subramanian and D. E. Laughlin, Eds., ed ASM International, 1994, pp. 487-496.

[4] W. J. Evans and B. Wilshire, "The High Temperature Creep and Fracture behaviour of 70-30 Alpha-Brass," *Metallurgical Transactions,* vol. 1, pp. 2133-2139, 1970.

[5] J. Byun, "Stiffness Modelling of Triaxially Braided Textile Composites," in *ICCM12*, Paris, France, 1999.

[6] J. Byun, "The analytical characterization of 2-D braided textile composites," *Composites Science and Technology,* vol. 60, pp. 705-716, 2000.

[7] T. Mitsueda, K. Fujii, and S. Ohnuki, "Comparison of Creep Damage Appearances Among Low Alloy Steel Pipes," in *Creep and Fatigue and Elevated Temperatures 8*, San Antonio, Texas, 2007.

[8] R. J. Browne, "Creep Rupture Testing of Tubular Model Components," in *Techniques for Multiaxial Creep Testing*, D. J. Gooch, Ed., ed: Elsevier Applied Science Publishers Ltd, 1986, pp. 311-332.

[9] S. N. Gundarev, A. F. Gurov, V. V. Dement'ev, A. S. Demidov, A. E. Rusanov, and A. A. Khomyakov, "High-Temperature Creep Tests on Specimens of Single Crystal Molybdenum with a Complex Stress State," *Problemy Prochnosti (Strength of Materials),* 1990.

[10] S. McAllister, R. C. Hurst, and T. E. Chung, "Modelling the Multiaxial Creep Behaviour of Alloy 800H," *International Journal of Pressure Vessels and Piping,* vol. 47, pp. 355-370, 1991.

[11] I. Nonaka, T. Ito, F. Takemasa, K. Saitou, Y. Miyachi, and A. Fujita, "Full size internal pressure creep test for welded P91 hot reheat elbow," *Internal Journal of Pressure Vessels and Piping,* vol. 84, pp. 97-103, 2007.

[12] ASTM E319-11: Standard Test Methods for Conducting Creep, Creep-Rupture, and Stress-Rupture Tests of Metallic Materials, 2011.

[13] S. Arsene and J. Bai, "A New Approach to Measuring Transverse Properties of Structural Tubing by a Ring Test," *Journal of Testing and Evaluation,* vol. 24, pp. 386-391, 1996.

[14] J. Lee, R. C. Bradshaw, R. W. Hyers, J. R. Rogers, T. J. Rathz, J. J. Wall, *et al.*, "Non-contact measurement of creep resistance of ultra-high-temperature materials," *Materials Science and Engineering A,* vol. 463, pp. 185-196, 2007.

[15] S. N. Gundarev, A. F. Gurov, V. V. Dement'ev, A. S. Demidov, A. E. Rusanov, and A. A. Khomyakov, "High-Temperature Creep Tests on Specimens of Single Crystal Molybdenum with a Complex Stress State," 1990.

[16] U. C. Jindal, *Machine Design*: Pearson Education India, 2010.

[17] R. A. Naik, P. G. Ifju, and J. E. Masters, "Effect of Fiber Architecture Parameters on Deformation Fields and Elastic Moduli of 2-D Braided Composites," *Journal of Composite Materials,* vol. 28, pp. 656-681, 1994.

[18] K. Birkefeld, M. Roder, T. v. Reden, M. Bulat, and K. Drechsler, "Charcterization of Biaxial and Triaxial Braids: Fiber Architecture and Mechanical Properties," *Applied Composite Materials,* vol. 19, pp. 259-273, 2012.

[19] C. G. Daley. Stiffness Matrix and Maxwell's Riciprocal Theorem, http://www.engr.mun.ca/~cdaley/6002/Lect11_6002.pdf, [Accessed October 31st 2014].

[20] S. T. Mau, *Introduction to Structural Analysis: Displacement and Force Methods*: CRC Press, 2012.

[21] C. W. Evans, *Hose Technology*, 2nd ed. London, UK: Applied Science Publishers Ltd, 1979.

[22] T. Hunt and N. Vaughan, *The Hydraulic Handbook*, 9th ed. Oxford, UK: Elsevier Advanced Technology, 1996.

[23] T. Safford, "Plastics in Pressure Pipes", Rapra Technology Ltd, Shropshire, UK1998.

[24] N. E. Dowling, *Mechanical Behaviour of Materials*, 3rd ed.: Person Prentice Hall, 2007.

CHAPTER 5: IN-SITU LONGITUDINAL CREEP STRAIN MEASUREMENT

This chapter explores creep rate trends revealed by the work in Chapter 4. Specifically, a specially designed test rig is utilized to measure longitudinal strain in-situ. This novel method of in-situ strain measurement allowed for the true steady state creep rate to be compared to the mean creep rate approximation made in Chapter 4.

Multiaxial creep behaviour is further investigated, and the mechanics of how the presence of a reinforcement layer brings about a reduction in creep rate is explored with special consideration given to the dynamic nature of the reinforcement angle.

Traditionally, in-situ strain measurement during multiaxial creep testing has been achieved via ring testing (detailed in Section 3.5.3) or non-contact strain measurement techniques [1-3]. However, the multilayered nature of the hybrid pipe rules out these methods.

In Chapter 4, strain measurements were made during interruptions or after test completion. This method of periodic interruption to take strain measurements has been used previously on unreinforced metallic creep rupture specimens under internal pressure [4, 5]. In order to gain a fuller understanding of the in-situ creep behaviour of the hybrid pipe, a specialised creep rig was devised which was capable of measuring longitudinal strain of the liner pipe via linear variable differential transformer (LVDTs). The design of this novel apparatus is outlined in Section 5.2.1.

5.1 Expected Trends

From the work in Chapter 4, the strain interaction between liner and reinforcement layers remains largely unexplored. It is important that the specific mechanics of the reinforcement interacting with the liner are well understood, particularly before translating the hybrid pipe technology to a high temperature material system and a larger scale.

Post-test braid angle measurements confirmed that during testing, creep deformation facilitates the shifting of the braided reinforcement from $\theta < \theta_N$ towards the equilibrium point of the neutral angle. Periodic interruption of a creep test revealed that, over the timeframe tested, creep is never completely halted, Figure 4.14. Additionally, no discontinuities or steps were observed, disproving the hypothesis that there is a clear point of engagement which results in an abrupt change in creep rate. This observation raises further questions about the nature of the engagement of the reinforcement onto the liner, and any significance of the initial tightness of the braid.

Note that the test shown in Figure 4.14 was ended before rupture, so tertiary creep was not expected. While periodic measurement gives insufficient resolution to conclusively determine the nature of the strain rate trend, power laws provided good fits for the strain and showed that the magnitudes of the creep rates decrease with time compared to a linear trend over a 10-times control life test duration.

The periodically interrupted test shown in Figure 4.14 also allowed for an investigation of strain behaviour during testing, and a quantification of the effectiveness of the mean creep rate approximation. The instantaneous creep rate,

calculated from the power law fits, was seen to differ by 8% at most from the mean creep rate approximation, which consistently overestimates creep rate.

In a conventional creep test of an unreinforced sample, it is known that the initial creep rate is relatively high during a period of primary creep. As shown in Figure 5.1, this creep rate decreases to a minimum, the steady state creep rate, before accelerating once more into tertiary creep [6-8]. On this same plot, the hypothesized multiaxial creep behaviour of a reinforced sample is shown, based on a shift in reinforcement orientation towards the neutral angle during testing.

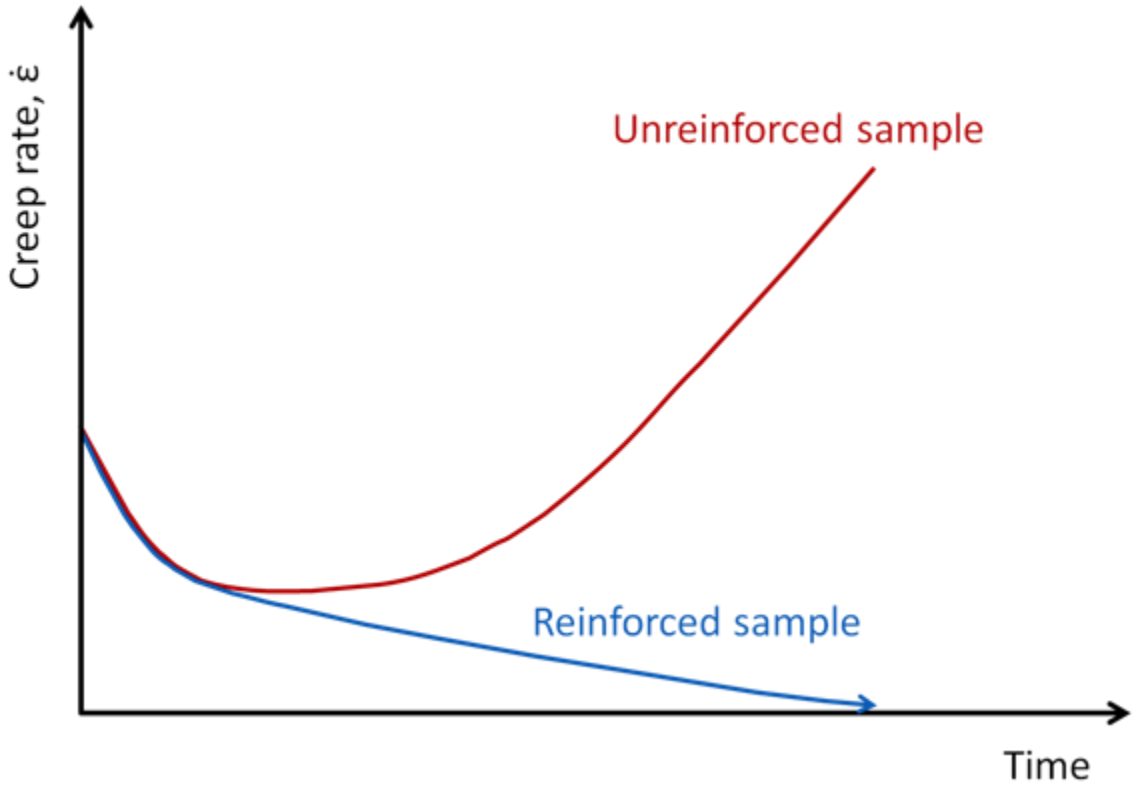

Figure 5.1. *Hypothesized multiaxial creep rate behaviour over time for a reinforced sample with braid angle shifting to the neutral angle.*

The in-situ strain measurement of a reinforced sample is expected to reveal a continually decreasing creep rate after an initial period of primary creep. Given

sufficient time and creep ductility, it is expected that the creep rate will reach zero when the braid is oriented at the neutral angle. However, the driving force for creep will decay as $\theta \rightarrow \theta_N$, thereby minimizing the mechanism for a change in braid angle [9-11]. This is expected to result in asymptotic behaviour, where $\dot{\varepsilon}$ approaches zero without reaching it. Taking a pragmatic approach to in-situ strain measurement of a multi-layered hybrid pipe, longitudinal strain is the most readily measured strain component as the presence of the reinforcement inhibits access to the pipe surface, required for tangential strain measurement. Therefore LVDTs are oriented to measure longitudinal strain. From the model presented in Section 4.2.4, observed changes in ε_z can be related to ε_t, ε_r and $\varepsilon_{eff.}$

Hypotheses related to the change in braid angle, which will be tested in the current chapter, can be summarized as:

- For $\theta < \theta_N$: as $t \rightarrow \infty$, $\theta \rightarrow \theta_N$ and $\dot{\varepsilon}_z \rightarrow 0$ (or some asymptotic decrease in $\dot{\varepsilon}_z$).
- $\dot{\theta}$ is zero for $\theta > \theta_N$.
- For $\theta < \theta_N$, $\dot{\theta}$ is greater for values of θ further from θ_N.
- $t_{\dot{\varepsilon}=0}$ is lower for initial values of θ closer to θ_N (for $\theta < \theta_N$).

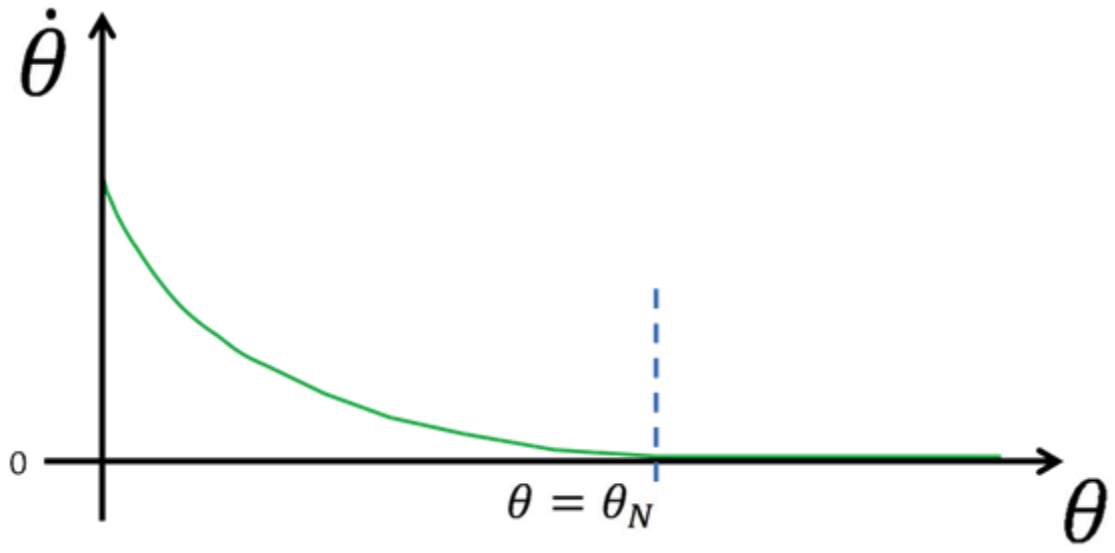

Figure 5.2. *Representative figure of expected behaviour as braid orients itself to the neutral angle, θ_N.*

By testing braids with initial angles of 36°, 50° and 65°, and looking at the rate of change of $\dot{\varepsilon}_z$ as well as the time taken to reach $\dot{\varepsilon}_z = 0$, the aforementioned hypotheses can be assessed.

It should also be noted that in the control tests, final strains in both the tangential and longitudinal directions were positive (i.e. the pipe elongated and expanded tangentially). However, final strains in the reinforced cases were most often different signs, Figures 4.12 and 4.13, i.e. if a tangential expansion was recorded, the length of the pipe was reduced and vice versa. It was also observed in Chapter 4 that reducing creep in the tangential direction causes creep in the longitudinal direction to accelerate. This phenomenon was most pronounced in the wrap-reinforced case, where the mean longitudinal creep rate was 3.9-times greater than was observed in the average control test.

5.2 Methodology

5.2.1 Apparatus

In order to permit in-situ longitudinal strain measurement and verify results from the single pipe testing rig, a new creep rig was devised, Figure 5.3. Additionally, this new rig was equipped with a potassium-filled isothermal furnace liner (IFL) for improved temperature uniformity. The IFL manufacturer, 1-ACT, claims an isothermal length to within ±0.1°C for operating temperatures between 400°C and 800°C [12]. Four parallel gas lines give this new apparatus the capability to test up to four pipes simultaneously, completely independent of one another.

In-situ longitudinal strain measurement is achieved by fixing vertical tube samples to a base plate alongside a control rod, which serves as a reference point,

Figures 5.3(b) and (c). The top end of each tube sample is free to elongate or contract, with a linear variable differential transformer (LVDT) core fitted to this free end to record longitudinal strain during testing. The LVDT tubes are fixed to the control rod via a boss. The end cap at the pressurized end of the sample is threaded, and screws directly into the base plate.

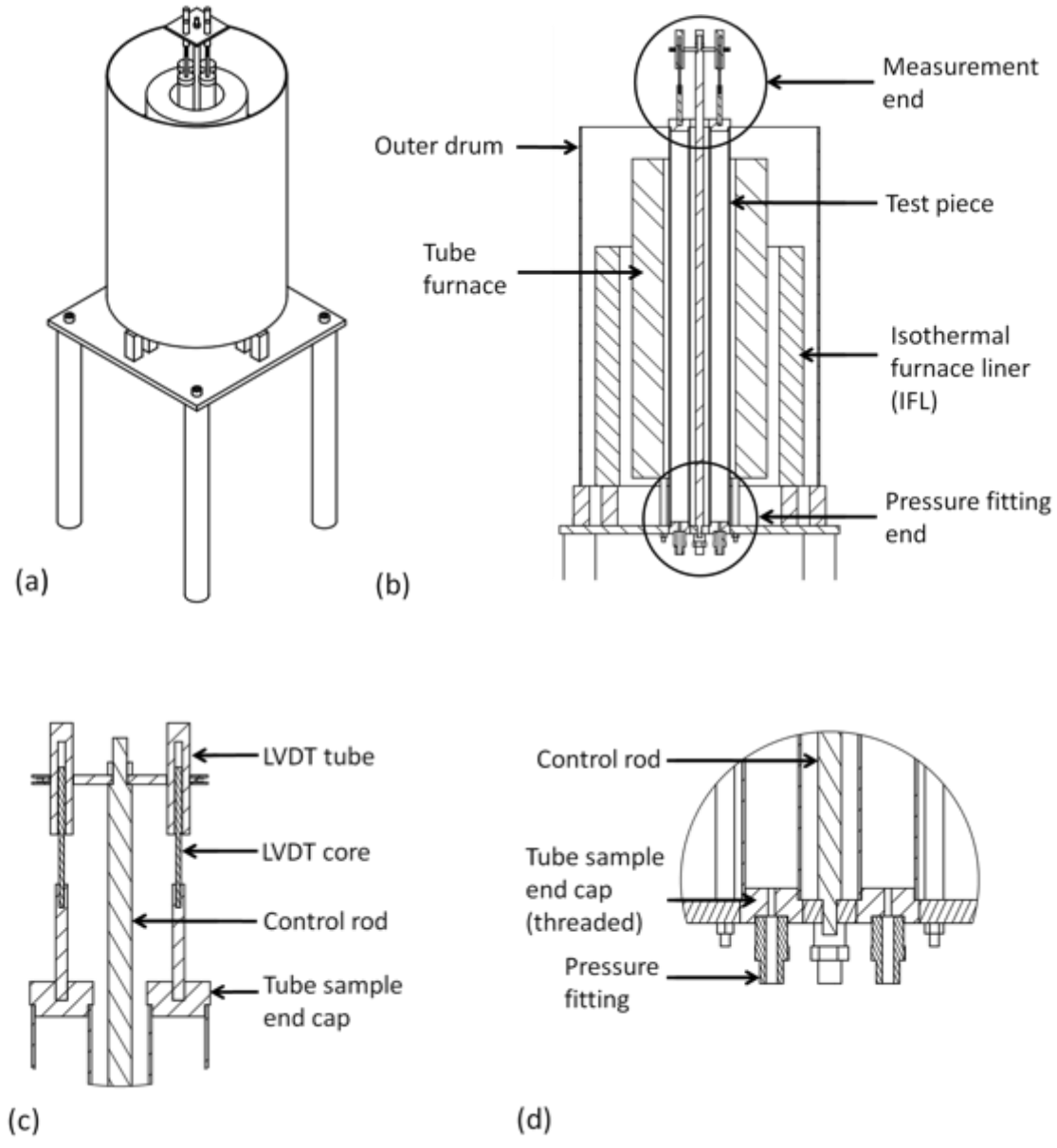

Figure 5.3. *Multiple pipe testing rig (a) rig assembly (b) sectional schematic (c) detailed view of strain measurement end (d) pressure fitting end.*

The LVDTs are not suitable for use over approximately 100°C, and the braze filler used to seal the end caps in place is not rated for continuous exposure at temperatures over 200°C. However, it is desirable to heat as much of the tube sample as possible. To achieve maximum temperature uniformity over the length of the sample, but not overheat the LVDTs or braze, a series of fans were positioned at either end of the outer drum to provide active cooling for critical components, Figure 5.4.

Figure 5.4. *Fans positioned to cool LVDTs at top end of creep rig. Inset: lower end of creep rig, with pressure lines connected to pipe samples. Bottom 50 mm of samples left uninsulated, with a second set of fans positioned to cool brazed joints.*

The cavity between the furnace and outer drum was packed with Kaowool®, as was either end of the IFL. Additionally, a 25 mm thick annulus of Fiberfrax® board was placed over the top end of the IFL, completely filling the space between the tube samples and the outer drum. The full 600 mm length from the LVDTs to the base plate has a temperature profile as shown in Figure 5.5, with the x-axis set relative to the centre of the tube sample.

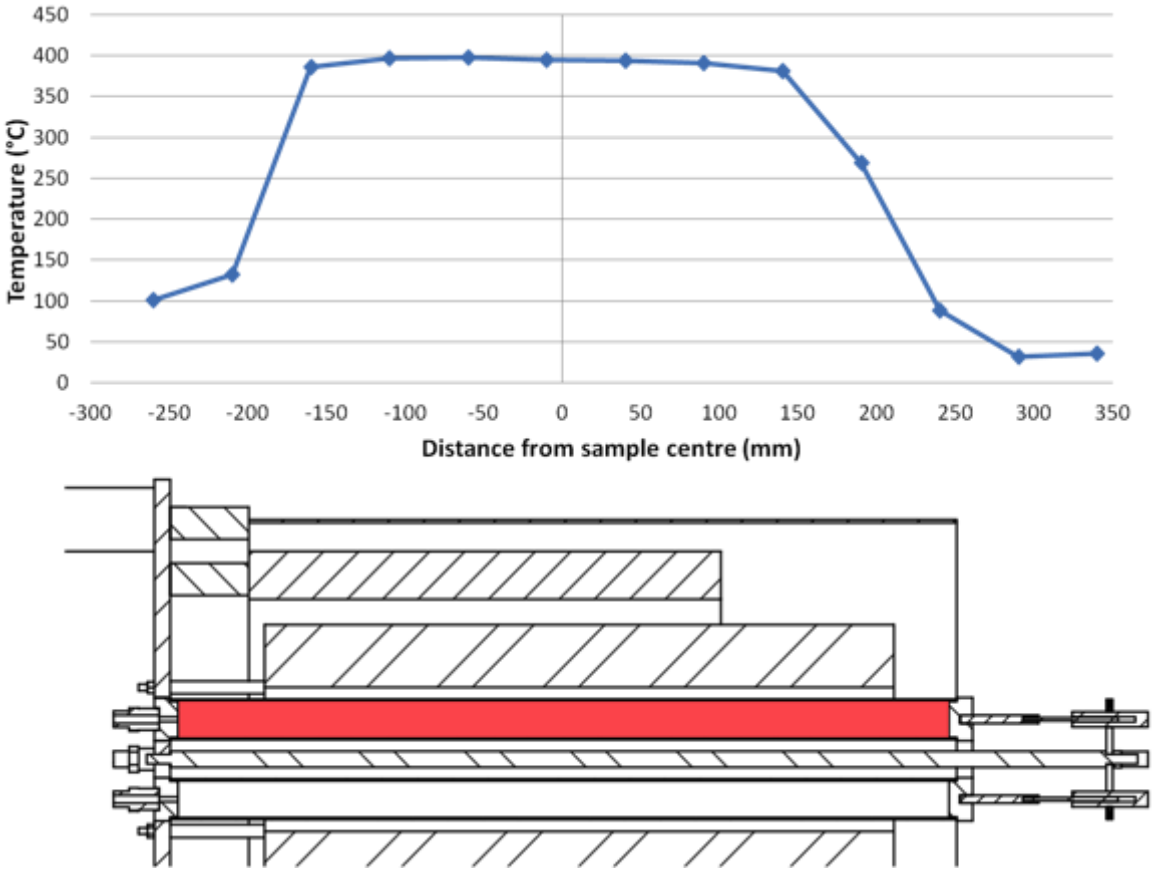

Figure 5.5. *Temperature profile in tube furnace with IFL, set to 400°C. Tube same within IFL highlighted in red.*

Without an IFL, the furnace used in Chapter 4 had a span of approximately 150 mm of the 1 m sample length (15%) where the temperature was maintained between 395°C and 400°C, Figure 4.7. With the IFL and shorter samples (500 mm),

the new creep rig has a span of approximately 220 mm (44%) where the temperature is maintained between 395°C and 400°C, Figure 5.5.

5.2.2 Pressurized pipe tests

Identical materials and reinforcement architectures to those outlined in Chapter 4 were used. The primary differences in sample geometry for this study was the reduction in sample length from 1 m to 500 mm, and the change in orientation from horizontal to vertical.

These tube samples were placed in a custom-built Argus vertical tube furnace at 400°C. Ø25.4 mm samples were pressurized to 2 MPa with argon, and Ø19.05 mm samples pressurized to 2.7 MPa to give an equivalent stresses of 17.2-18.9 MPa in both cases. These are identical conditions to the tests performed in Chapter 4, and so the predicted control life remains at 84-130 hours. To validate this prediction in the new test rig, two control tests were performed for each pipe size.

From Chapter 4, reductions in creep rate on the order of 45-times were observed when testing reinforced samples. Therefore, it was deemed impractical to allow reinforced tests here to run until rupture. Rather than selecting an arbitrary life extension over the control, as 10-times was used in Chapter 4, the in-situ strain measurement instead allowed for tests to be ended manually once the sample was observed to be in the secondary stage of creep, and a measure of the minimum creep rate can be made. For practicality, it was necessary to select an end condition for the reinforced samples in the event that these pipes did not rupture. The observation of a clear minimum creep rate, or a point where the braid shifted towards to the neutral angle such that strain rate reached a specified threshold creep rate of 0.5×10^{-4} %/hour were selected as conditions where creep testing could be terminated. This cutoff point was selected based on time constraints on the test regime.

Following heating and pressurization of the samples, LVDTs were zeroed such that measured longitudinal strain was solely the result of creep. Internal pressure, temperature and longitudinal strain were logged every 60 seconds during all tests, and maintained stability to within ±0.2 MPa, ±2°C and ±3 μm, respectively. A sustained pressure drop indicated pipe rupture, in which case the test was ended.

Using the same reinforcement architectures as those defined in Chapter 4, C-36°, C-65° and F-50° samples were selected for in-situ ε_z measurement, Table 5.1. Selecting samples with initial reinforcement angles furthest from the neutral angle gave the best opportunity to observe dramatic changes in creep rate while θ is reoriented during testing. Additionally, these samples allowed for creep characteristics of samples with initial braid angles *below* θ_N to be compared against those with initial braid angles *above* θ_N. The testing of a sample very near the neutral angle also presents the opportunity to test the hypothesis that $t_{\dot{\varepsilon}=0}$ is lower for initial values of θ closer to θ_N. It would be expected that the F-50° sample would show a minimal shift in braid angle during testing and therefore reach the point of zero creep rate sooner, but have lower magnitude of $\ddot{\varepsilon}_z$.

Table 5.1. *Reinforcement architectures selected for in-situ longitudinal strain measurement study.*

Reinforcement designation	**Pipe OD (mm)**	**p (MPa)**	**T (°C)**	**Initial braid angle (θ_i) (°)**
F-50°	19.05	2.75	400	49.5±2.4°
C-65°	25.4	2	400	65.3±1.1°
C-36°	25.4	2	400	36.2±1.2°

While Table 5.1 shows samples being tested at different internal pressures, the different pipe sizes means that the resultant equivalent stress is 17.2 MPa for all samples.

In addition to longitudinal strain being measured in-situ via linear variable differential transformers (LVDTs) over the entire 500 mm sample length, a 50 mm gauge length was marked at the midspan of each sample and used to take a second measurement of final longitudinal strain. Six measurements of pipe diameter were made over this 50 mm gauge length, with the measurement process repeated post-test to determine overall tangential strain.

Raw creep data was processed in MATLAB, using the inbuilt smoothing function and a 'LOWESS' (locally weighted scatter plot smooth) model which uses a locally weighted linear regression to smooth data over a specified span of 30 points (that is, 30 minutes). LOWESS is a non-parametric locally weighted smoothing function, which applies 1st or 2nd order polynomial fits over a local span, which shifts as is seen in a moving average smoothing function [13, 14].

Using the inbuilt 'gradient' function in MATLAB, this strain versus time data was then translated to a plot of strain rate versus time. This strain rate curve was utilized to identify the period of time where creep rate is a minimum, which was then approximated to be the steady state creep rate in the longitudinal direction i.e. $\dot{\varepsilon}_{min} \approx \dot{\varepsilon}_{SS}$.

5.3 Results and Discussion

5.3.1 Control rupture life and total strain comparison

The average life of the control pipes over four tests was 170 hours, and the standard deviation was 37 hours. While significantly more than the average life of 83 hours for the control pipes in Chapter 4, these results are consistent with the 84-130 hour window for the predicted creep rupture life of unreinforced α-brass tested at 400°C and a von Mises equivalent stress of 17.2-18.9 MPa, Section 4.1.2.

Although the IFL dramatically reduced the temperature gradient within the furnace, the temperature did not reach the ±0.1°C stability anticipated by the manufacturer. Temperature fluctuations on the order of ±2°C were attributed to the vertical sample orientation and relocation of the furnace to a room with more windows and an automated ventilation system, which led to the rig being more vulnerable to ambient temperature variations. The vertical orientation meant that air currents were drawn up through the furnace cavity, despite effort being made to pack Kaowool® in and around either end of the samples. Additionally, the 400°C testing temperature is at the lower end of the range at which the potassium IFL-filler is effective.

Comparing the appearance and rupture life of control pipes from the present series of tests to those conducted in Chapter 4, the improved temperature uniformity brought about by the IFL has resulted in longer rupture lives and more evenly distributed deformation, Figure 5.6.

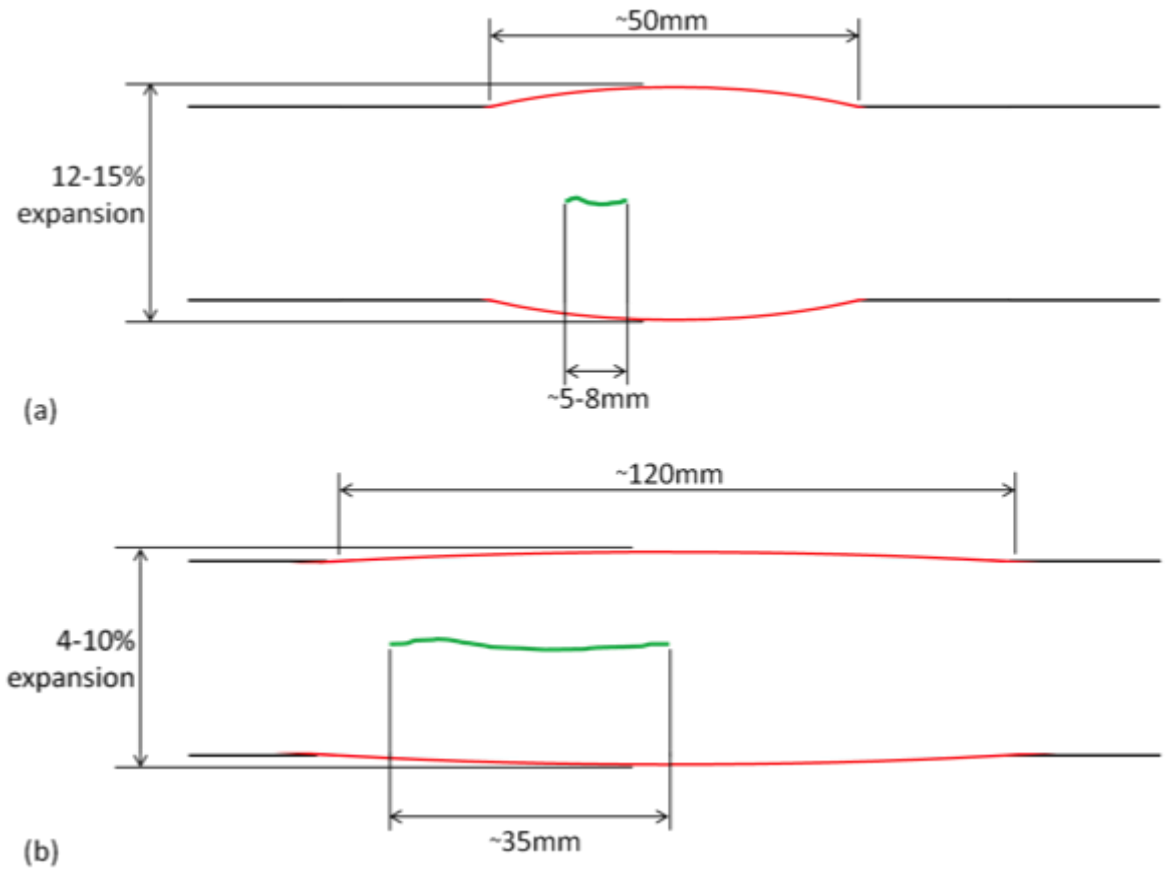

Figure 5.6. *Schematic of failure region in control pipes, with expansion shown in red and a representative crack shown in green (a) Chapter 4 tests without IFL (b) Chapter 5 tests with IFL and more evenly distributed deformation.*

In Chapter 4, the brass control samples had an average rupture life of 83 hours. As shown in Figure 5.6(a), these control pipes had a maximum 12-15% tangential expansion over a ~50 mm span, and final failure in the form of a 5-8 mm long crack that ran parallel to the longitudinal axis. In contrast, across the four control tests in the current investigation an average 4-10% tangential expansion was observed over a ~120 mm span, producing a longitudinal crack approximately 35 mm long, Figure 5.6(b). As the temperature and internal pressure are identical in both studies, this change is purely a result of the IFL providing more uniform heating, and a larger percentage of the sample length being heated – 44% with the smaller sample in the IFL, as opposed to 15% with the longer sample without an IFL.

As a single uniaxial strain gives an incomplete picture of the overall creep response and reasons for the ultimate rupture of the pipe, the concept of multiaxial creep strain becomes particularly important when strain in a single direction is being measured in-situ. For cylindrical polar coordinates, the von Mises equivalent (or effective) strain, ε_{eff}, is given by Dowling [15] as:

$$\varepsilon_{eff} = \frac{\sqrt{2}}{3}[(\varepsilon_t - \varepsilon_r)^2 + (\varepsilon_r - \varepsilon_z)^2 + (\varepsilon_z - \varepsilon_t)^2] \quad (5.1)$$

It is important to make the distinction between this von Mises strain at failure, and what is commonly referred to as creep ductility. While closely related, these terms are not interchangeable. Von Mises strain at failure is linearly proportional to creep ductility, related by a scalar referred to as the cavity growth factor (CGF). The CGF is determined experimentally, and is unknown in the present case. As a result, the von Mises strain at failure is the best available measure of overall deformation [15, 16]. Using directional strains measured over the four control tests, Equation 5.1 reveals that von Mises strain at failure ranges from 3-7% in the control tests.

5.3.2 Steady state creep rate of the unreinforced pipes

The in-situ measurement of ε_z presents an opportunity to quantify the impact of the $\dot{\varepsilon}_{mean}$ approximation used in Chapter 4. That is, a 'true' steady state creep rate in the longitudinal direction can be compared to a mean creep rate approximation based on the final longitudinal strain measurement, Figure 5.7.

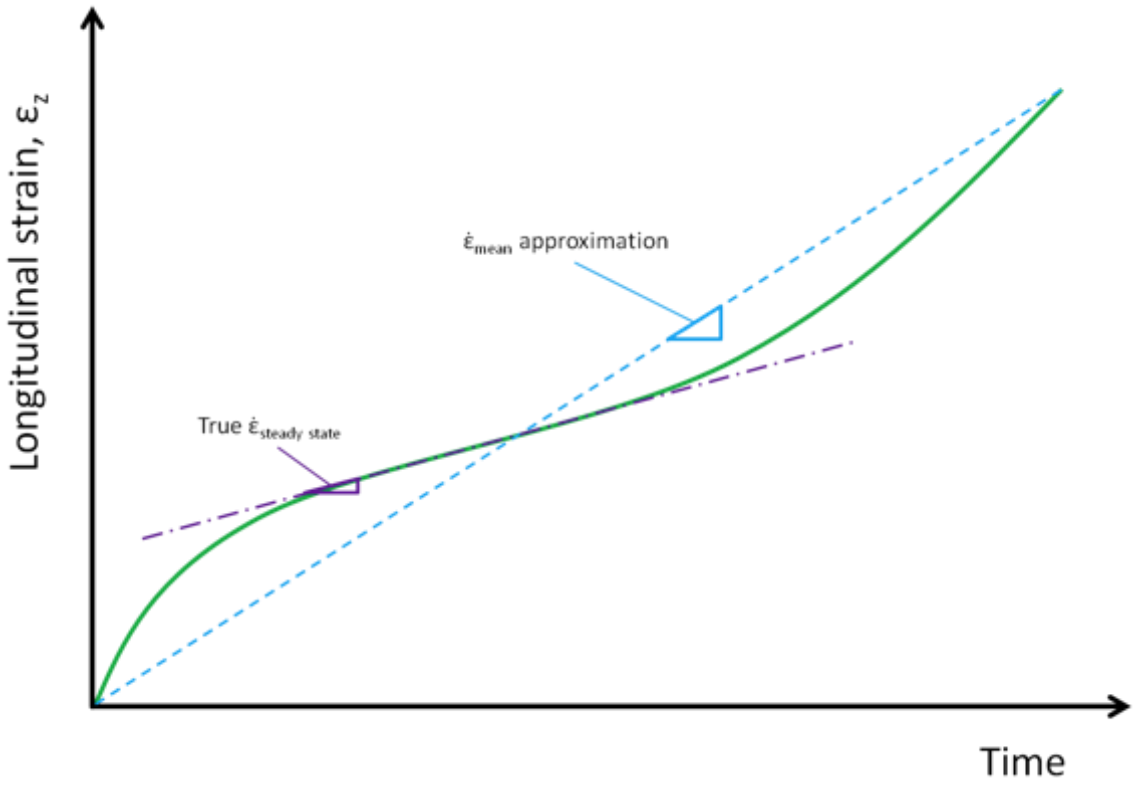

Figure 5.7. *Representative creep curve for longitudinal direction, with trends superimposed for* $\dot{\boldsymbol{\varepsilon}}_{\boldsymbol{mean}}$ *and* $\dot{\boldsymbol{\varepsilon}}_{\boldsymbol{steady\ state}}$.

Figure 5.8 uses real creep data from a representative control test to produce the trends that were represented schematically in Figure 5.7. Raw and smoothed data are superimposed in Figure 5.8 to show the effect of the MATLAB 'LOWESS' smoothing algorithm with a span of 30 data points (that is, 30 minutes).

Using the inbuilt 'gradient' function in MATLAB, this strain versus time data can be translated to a plot of strain rate versus time, Figure 5.9. This strain rate curve makes the region of minimum creep more easily identifiable, and was used to position the $\dot{\varepsilon}_{min}$ trend in Figure 5.8. Real, experimentally obtained creep data is not as smooth as that shown in the representative creep curve in Figure 5.7. Logistically, it is often more feasible to report the minimum (or secondary) creep rate, $\dot{\varepsilon}_{min}$, rather than the steady state creep rate. The mean creep rate is

determined from the total strain and superimposed onto Figure 5.8, allowing for a comparison between $\dot{\varepsilon}_{min}$ and $\dot{\varepsilon}_{mean}$.

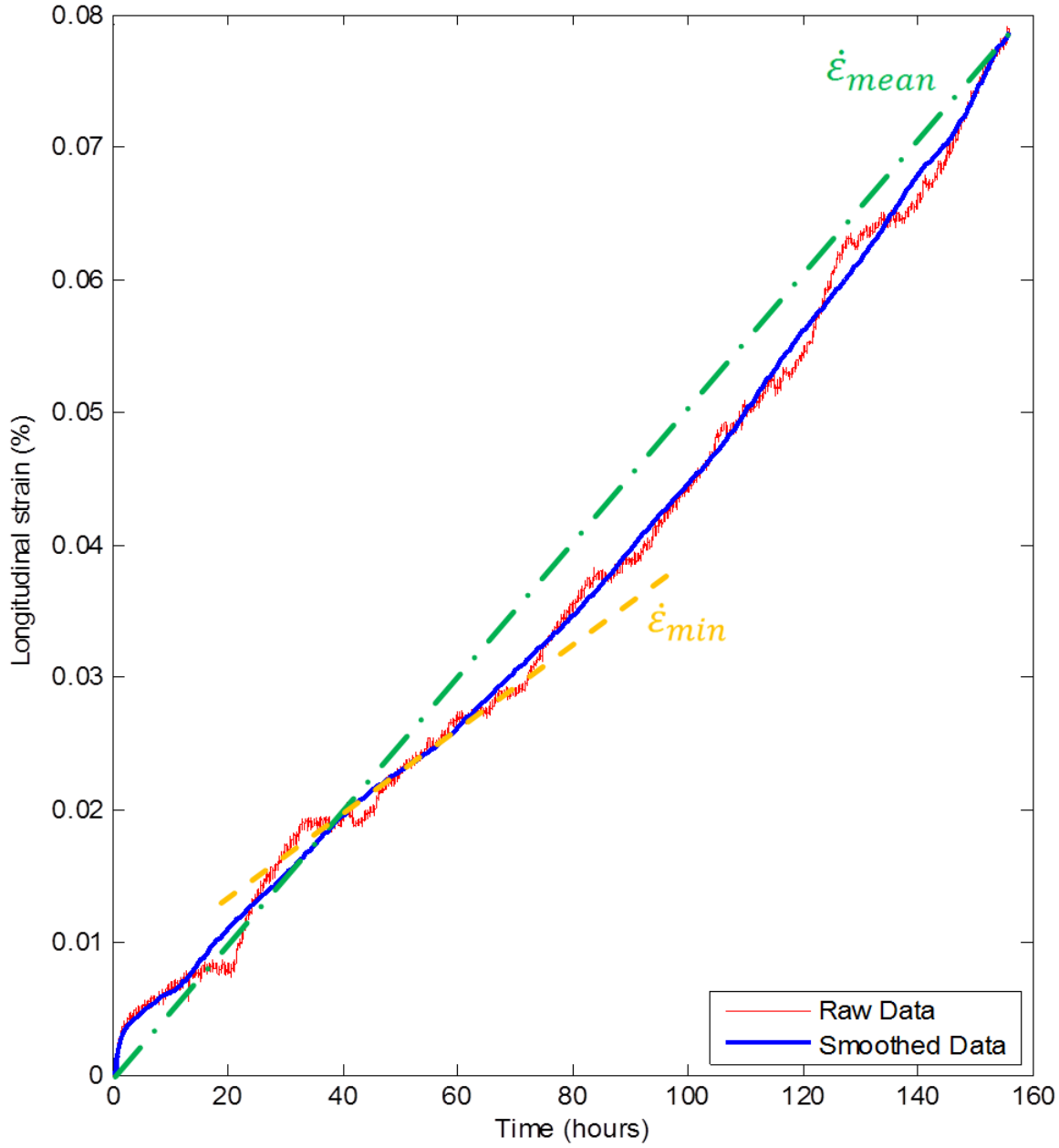

Figure 5.8. *Creep curve for representative control test, highlighting effect of smoothing algorithm. Mean and minimum creep rate trends superimposed.*

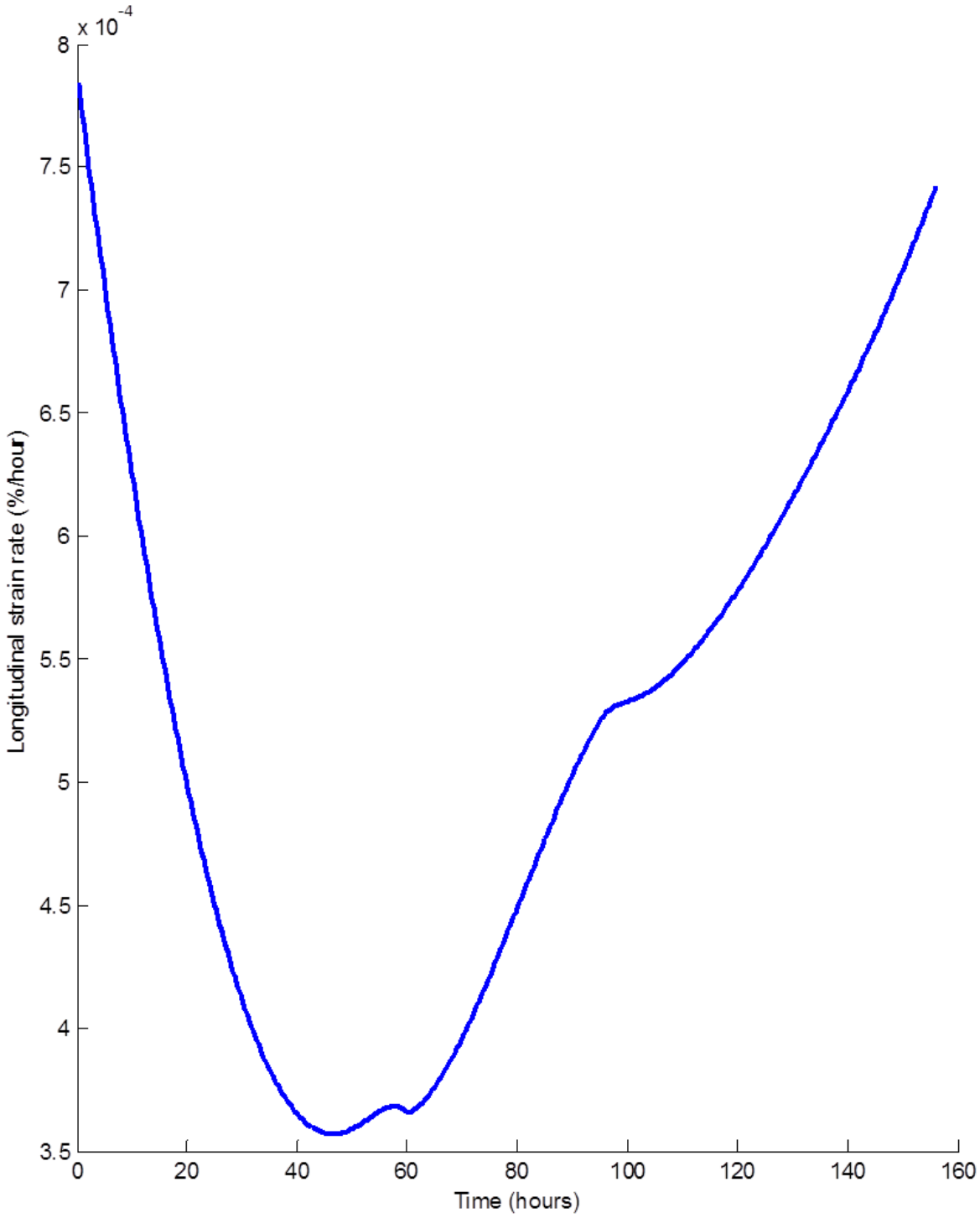

Figure 5.9. *Smoothed creep rate curve for representative control test. Minima from 40-60 hours indicating region of minimum (secondary) creep.*

From Figure 5.9, it can be seen that, similar to uniaxial creep testing, the strain rate in the control test approaches a minimum value, which is sustained for a period of time (secondary creep) before the sample accelerates into tertiary creep. For the

representative control sample shown in Figure 5.9, this stage of secondary creep takes place 40 hours to 60 hours into the test, and $\dot{\varepsilon}_{min}$ is approximately 3.6×10^{-4} %/hour. The mean creep rate in the longitudinal direction is 5.06×10^{-4} %/hour, 40% higher than the minimum creep rate. Repeating the process of graphically determining $\dot{\varepsilon}_{min}$ and $\dot{\varepsilon}_{mean}$ in the longitudinal direction reveals significant variation among the four control tests, Figure 5.10.

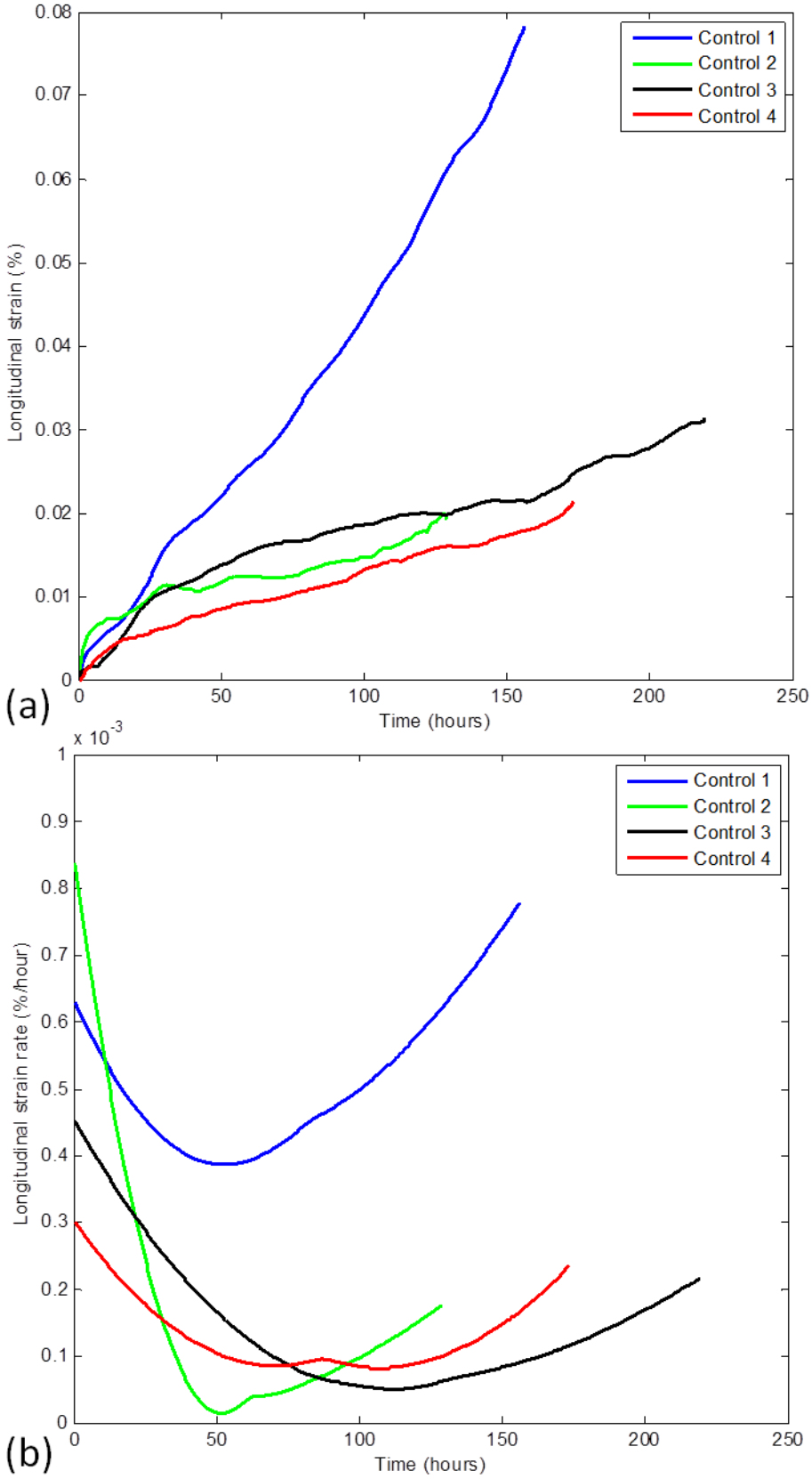

Figure 5.10 *Smoothed control test results (a) creep curves (b) creep rate curves.*

Using the minimum in the $\dot{\varepsilon} - t$ curve to determine the minimum creep rate, Figure 5.10(b) shows that $\dot{\varepsilon}_{min}$ in the longitudinal direction varies from 6.1x10^{-5} %/hour to 3.6x10^{-4} %/hour. Figure 5.10(a) reveals that strain at rupture in the longitudinal direction ranges from 0.017% to 0.079%. Comparing $\dot{\varepsilon}_{min}$ and $\dot{\varepsilon}_{mean}$ for each control test, it can be seen that for unreinforced samples tested to rupture, the mean creep rate approximation employed in Chapter 4 overestimates the minimum creep rate by 80 ± 40%.

Testing the samples to rupture represents a worst case scenario, as the region of tertiary creep is where $\dot{\varepsilon}_{min}$ and $\dot{\varepsilon}_{mean}$ deviate from one another most significantly. Thus, the 80 ± 40% discrepancy between $\dot{\varepsilon}_{min}$ and $\dot{\varepsilon}_{mean}$ is believed to be a consequence of the greater creep rates that occur during tertiary creep.

In a review of the sources of variation in creep testing, Loewenthal and Ellis [17] investigated the database of creep rupture behaviour of GRCop-84, an 8wt%Cu/4wt%Cr/88wt%Nb alloy developed by NASA for combustion chamber liners in reusable regeneratively cooled launch vehicle engines. Controlling processing variants and testing on the same creep frame reduced scatter in creep life from four orders of magnitude to two. It was unclear to Loewenthal and Ellis if this large variation was due to the test methods, the materials, or a combination of both. Using a simple lever arm machine with a vacuum chamber to assess creep rupture lives and rates, and taking precautions to control load, load train alignment and temperature, a 95% confidence interval for the creep life data was shown to span two orders of magnitude in a stress-life plot.

While the present study is for a different material system than that studied by Loewenthal and Ellis, their investigation is among a number of reviews which highlights the level of variation which is inherently associated with creep testing [17-20]. In light of this variation, the factor of six difference between measured

steady state creep rates in the longitudinal direction in the control tests (6.1×10^{-5} %/hour to 3.6×10^{-4} %/hour) in the present study is not unsurprising.

5.3.3 Creep rate behaviour of the reinforced pipes

During testing of reinforced pipes, any change in creep rate is intrinsically linked with changes in orientation of the reinforcement. Knowing that creep rate is zero at θ_N, and having previously investigated $\dot{\varepsilon} - \theta$ behaviour in Chapter 4, the change in braid angle as function of time can be inferred from the measured change in creep rate during testing. In Section 4.2.4, it was determined that with the reinforcement unbounded to the pipe, there is no driver for initial braid angles above θ_N to reduce to seek θ_N, Figure 5.11(a).

Therefore, the creep rate of the C-65° sample was not expected to reduce over time. In contrast to this, the C-36° and F-50° samples' creep rate was expected to decay as $t \to \infty$ and $\theta \to \theta_N$. Due to being closest to the neutral angle and having the lowest net stress, the F-50° sample was predicted to show the shallowest $\dot{\varepsilon}_z - t$ curve (lowest $|\ddot{\varepsilon}_{z,max}|$)and also the lowest $t_{\dot{\varepsilon}=0}$. In contrast to this, the C-36° sample was expected to show the most pronounced shift in θ and therefore the largest $|\ddot{\varepsilon}_{z,max}|$ and $t_{\dot{\varepsilon}=0}$, due to it starting furthest from the neutral angle and having the largest $\Delta\theta$ required to reach the equilibrium position of θ_N. Utilizing the $\dot{\varepsilon}_z - \theta$ trend derived experimentally in Chapter 4 in conjunction with this predicted $\dot{\theta}(\theta)$ behaviour, Figure 5.11(c) illustrates predicted longitudinal creep rate trends for various reinforcement architectures, accounting for their tendencies to shift orientation towards the neutral angle over time.

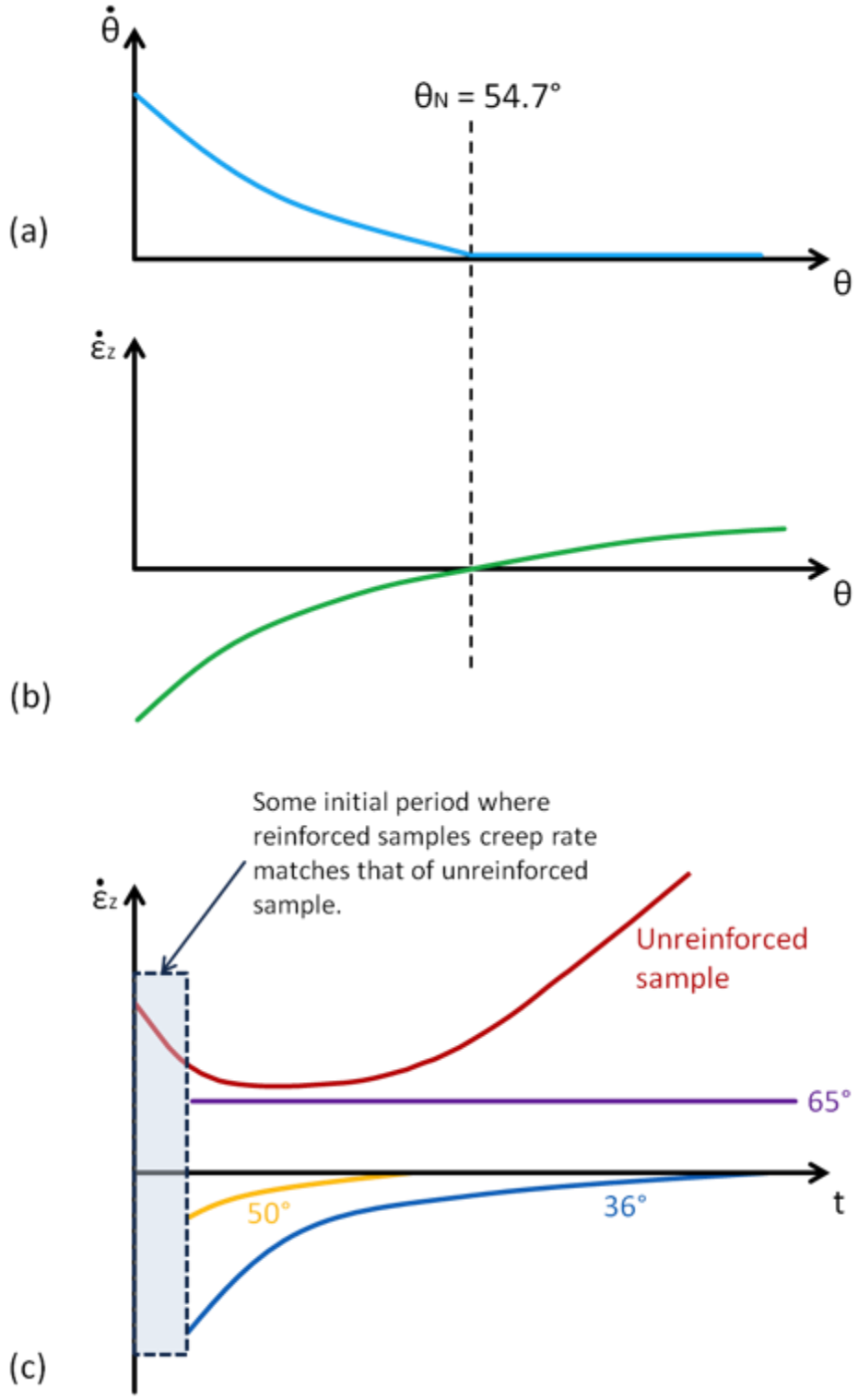

Figure 5.11. *Predicted longitudinal creep rate trends for various reinforcement architectures (a) Predicted change in braid angle (b) Representative longitudinal creep rate trend from Figure 4.17 (c) Expected longitudinal creep rate trends for specific samples tested – i.e. C-36°, F-50° and C-65°, relative to an unreinforced sample. Not to scale.*

Figure 5.11(c) also reveals that an initial region of unrestrained creep is expected in the reinforced samples. This behaviour was not captured in the periodically interrupted test shown in Figure 4.14, but its hypothesised existence is based on the initial tightness of the braid. That is, the length of time required for the reinforced creep curve to deviate from that of the unreinforced sample is predicted to be a function of the initial tightness of the reinforcement layer.

Figures 5.12 and 5.13 use smoothed creep data to show overall creep curves and the true $\dot{\varepsilon}_z - t$ behaviour for each reinforcement architecture, thereby allowing experimental creep rate trends to be compared to those predicted in Figure 5.11(c). Additionally, Figures 5.12 and 5.13 allow for $\dot{\varepsilon}_{min}$ to be determined and compared to $\dot{\varepsilon}_{mean}$ in the longitudinal direction.

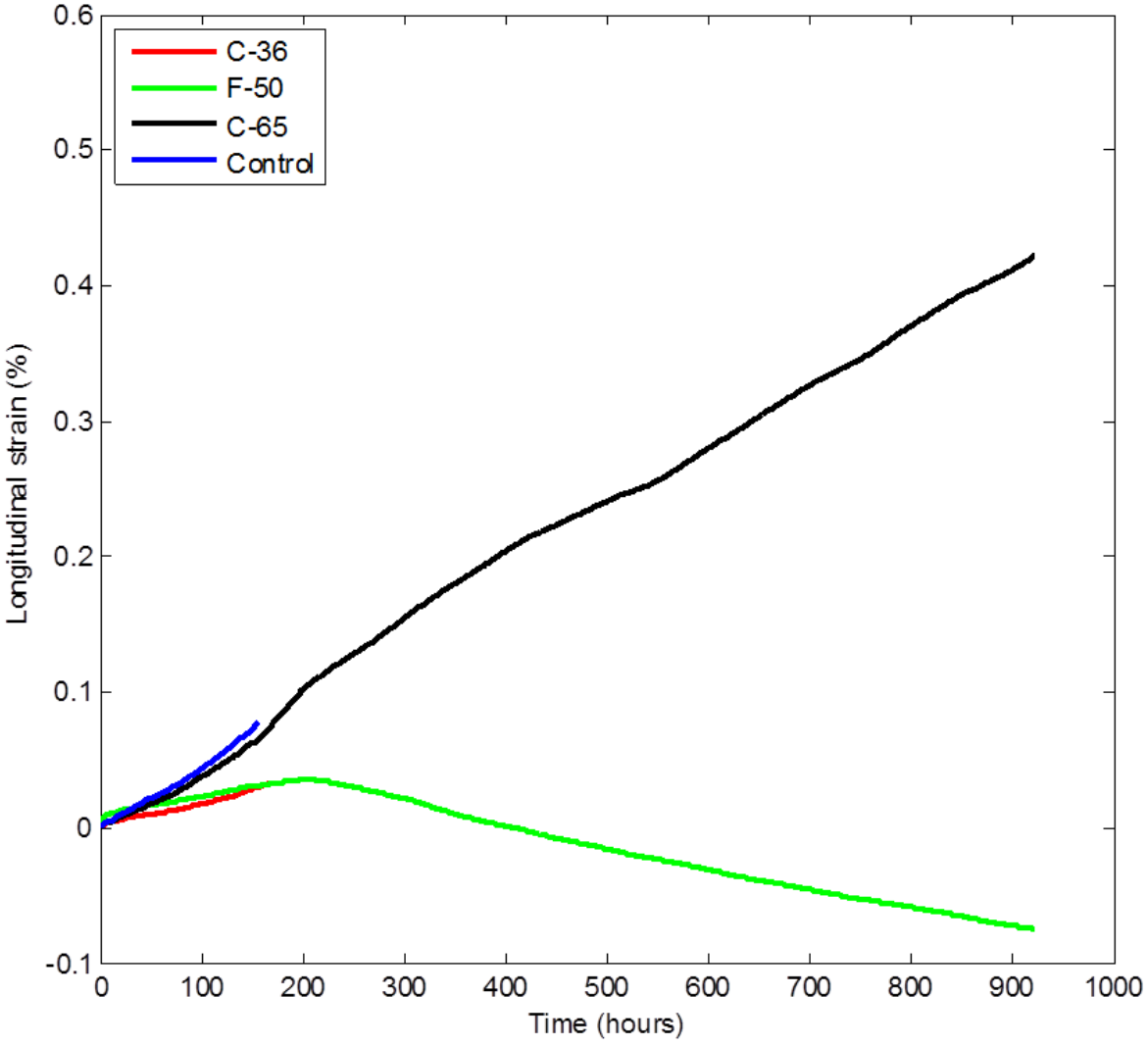

Figure 5.12. *Smoothed creep curves for reinforced samples, with the control behaviour of Figure 5.8 superimposed.*

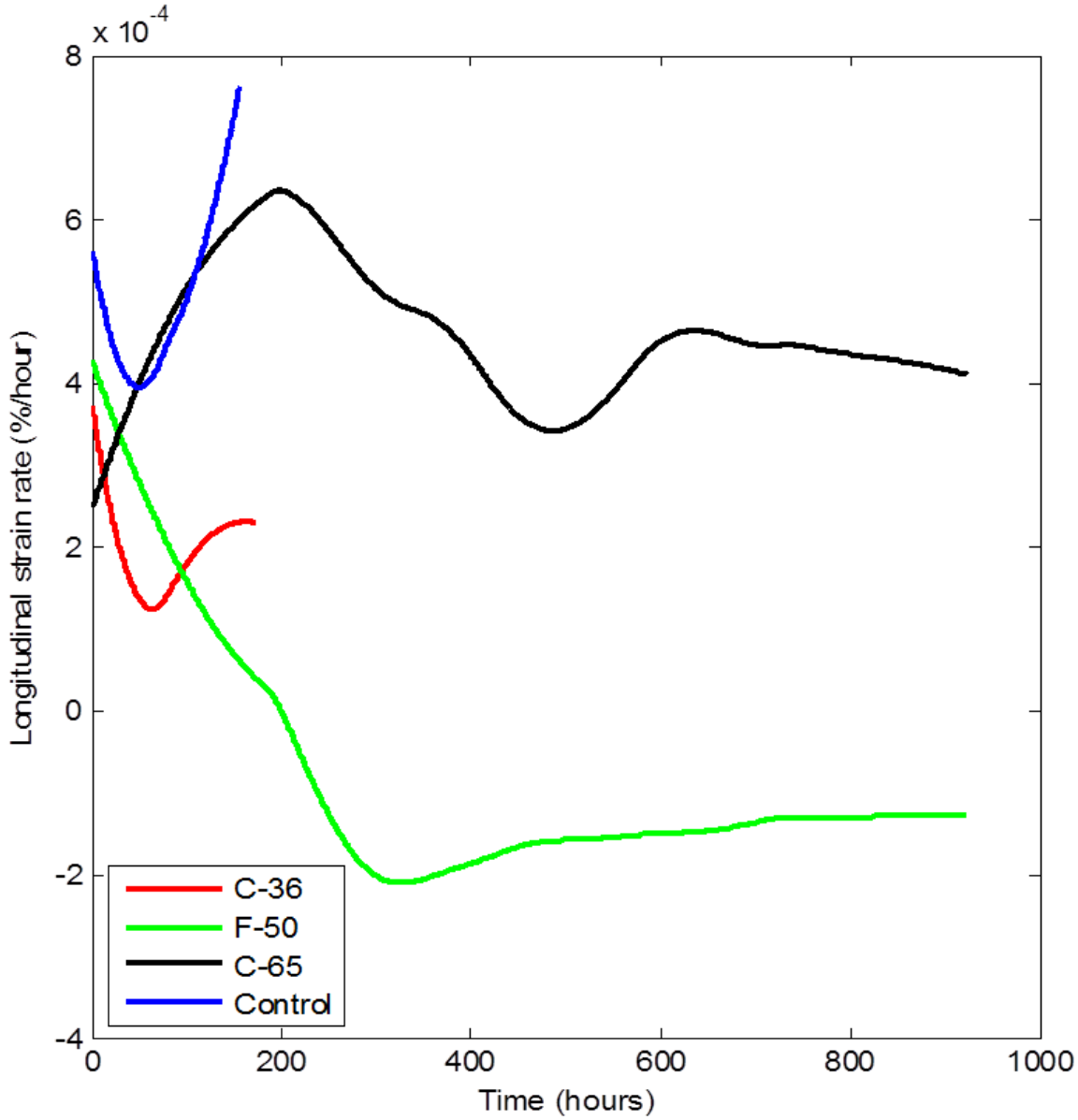

Figure 5.13. *Smoothed creep rate curves for reinforced samples, with the control behaviour of Figure 5.9 superimposed.*

Recall that the power law fits to the periodically interrupted test data shown in Figure 4.14, revealed that the mean creep rate approximation consistently overestimates the instantaneous creep rate. This difference was measured to be on the order of 8%. Due to the majority of the reinforced tests being stopped before failure, an absence of tertiary creep is expected. Tertiary creep is the predominant source for $\dot{\varepsilon}_{mean}$ overestimating $\dot{\varepsilon}_{min}$, and therefore smaller differences between

$\dot{\varepsilon}_{mean}$ and $\dot{\varepsilon}_{min}$ are expected for reinforced samples than was observed for the control tests.

From Figures 5.12 and 5.13, it can be seen that $\dot{\varepsilon}_{min}$ and $\dot{\varepsilon}_{mean}$ deviate from one another by 55 ± 8% in the reinforced tests. While lower than the 80 ± 40% overestimation $\dot{\varepsilon}_{mean}$ was shown to be over $\dot{\varepsilon}_{min}$ in the case of the control tests, this 55 ± 8% is still a significant overestimation. Minimum and mean creep rates for each reinforced sample are summarized in Table 5.2.

The LVDTs measured longitudinal strain over the entire sample length. However, longitudinal strain can also be measured from the 50mm gauge length marked at the midspan of the sample. While less precise than the LVDT measurement, this measure of strain at the midspan is a useful validation of the overall strain measurement. Table 5.2 presents a comparison between mean and minimum creep rates, as well as a measure of the rate of decrease in creep rate for the reinforced cases and the time to zero creep rate. Additionally, overall longitudinal strain is compared to that measured at the gauge length in the midspan of the sample.

Table 5.2. *Creep rate analysis for samples with in-situ ε_z measurement.*

	Control[a]	**C-36°**	**F-50°**	**C-65°**
Longitudinal $\dot{\varepsilon}_{mean}$ (%/hr)	$2.26 \times 10^{-4} \pm 1.87 \times 10^{-4}$	1.95×10^{-4}	-8.10×10^{-5}	4.57×10^{-4}
Longitudinal $\dot{\varepsilon}_{min}$ (%/hr)	$1.43 \times 10^{-4} \pm 1.45 \times 10^{-4}$	1.24×10^{-4}	-2.12×10^{-4}	3.12×10^{-4}
Difference between $\dot{\varepsilon}_{mean}$ and $\dot{\varepsilon}_{min}$ (%)	80 ± 40	57	62	47
$\lvert\ddot{\varepsilon}_{max}\rvert$ (%/(hour)²)[b]	$1.24 \times 10^{-5} \pm 1.07 \times 10^{-5}$ [c]	8.15×10^{-6}	6.51×10^{-6}	inconclusive
Max long strain from GL (%)	0.15 ± 0.05	0.08	-0.18	0.60
Max long strain from LVDTs (%)	0.04 ± 0.03	0.03	-0.08	0.42

[a] mean ± standard deviation for four tests.

[b] considered over the region where creep rate is decreasing.

[c] neglecting control 2 test reduces scatter significantly, altering this to $7.04 \times 10^{-6} \pm 1.10 \times 10^{-6}$.

Despite improved temperature uniformity, gauge length measurement pre- and post-test revealed that creep rate in the midspan of pipe is up to 2.5-times faster than the overall strain as measured by the LVDTs. Although, the LVDTs give a more precise elongation measurement, down to 0.1 μm, the lower accuracy in the gauge length measurement does not explain this significant difference in strain rates.

It is important to make the distinction that gauge length strain measurements were made at room temperature, whereas the strain recording performed by the LVDTs was on samples heated to 400°C and under internal pressure. As the LVDTs were zeroed once the samples were at test temperature and pressurized,

this discrepancy had no subsequent effect on the analysis of strain rate. However, the effects of heating and pressurization cause a difference in the in-situ and post-test strain measurement, seen when comparing measured strain at the gauge length to that recorded by the LVDTs. Analysis of the magnitude of thermal strains reveals that at 400°C, tangential expansion solely as a result of heating is on the order of 180 μm, or 5-10% of the creep strain in the tangential direction. Due to the larger length scale in the longitudinal direction (i.e. gauge length is approximately twice the diameter of the pipe), longitudinal thermal expansion is on the order of 360 μm. Over a gauge length of 500 mm, this translates to a 0.07% strain, which Figure 5.10(a) reveals to be the same order of magnitude as the overall longitudinal creep strain in the control pipes. From Figure 5.12 and Table 5.2, it can be seen that a 0.07% thermal strain in the longitudinal direction is the same order of magnitude as the longitudinal creep strain for the F-50° sample, and approximately 15% of the longitudinal creep strain for the C-65° sample.

The need for the braze joints and LVDTs to be cooled meant that an estimated span of 220 mm of the total 500 mm sample length is heated to between 395°C and 400°C, Figure 5.5. Figure 5.5 also reveals the dramatic reduction in temperature at the sample ends was caused by the active cooling system, necessitated by the limited braze and LVDT rated service temperatures. In order to quantify this effect, it is necessary to compare post-test longitudinal strains across the gauge length and overall length, as this negates previously discussed issues related to elastic strains resulting from thermal expansion and application of load. Comparing final longitudinal strains, the gauge length consistently strains more than the overall length by a factor of 2.2 ± 0.6. As the effect is uniform across all samples, the relative comparisons made between samples in Table 5.2 still stand. However, the observed behaviour is not necessarily representative of brass held at 400°C, as reported for uniaxial creep tests where the entire sample is heated uniformly.

Upon inspection, the longitudinal creep rate curves in Figure 5.13 appear to differ significantly from the hypothesized trends shown in Figure 5.11(c). The creep behaviour of each of the three reinforced samples is assessed in light of the predicted $\dot{\theta} - \theta$ and $\dot{\varepsilon}_z - t$ relationships.

Analysis of C-36° specimen behaviour

The C-36° sample ruptured after 175 hours, consistent with the control life of 170 ± 37 hours. An absence of impressions left by the reinforcement onto the pipe surface suggests that the reinforcement did not engage at any point, and the C-36° sample exhibited the same creep behaviour as a control pipe. It is theorized that the C-36° sample exhausted the creep ductility of the brass before any significant engagement had occurred. As mentioned previously, the presence of the IFL resulted in more uniform heating across the length of the sample, which in turn resulted in a smaller, less pronounced bulge at the point of rupture (i.e. the creep deformation was spread over a larger span), Figure 5.6.

The relatively low stiffness of the reinforcement layers in the longitudinal direction makes then particularly susceptible to changes in diameter when small longitudinal loading is applied. As a result, radial clearance between the pipe and braid is difficult to quantify, particularly as it is likely to have changed during the act of packing Kaowool® insulation around the tops of the samples. The F-50° and C-65° braids were reasonably tight fits on the pipes, with radial clearances on the order of 0.1-1 mm. The C-36° was comparatively loose on the pipe, with a radial clearance on the order of 2-3 mm. Therefore, this lack of pronounced tangential creep deformation inhibited the ability of the C-36° braid to engage onto the pipe surface. Due to the wide range of creep ductility exhibited by the brass in the as-received condition, this may not always be the case in repeated C-36° tests. Figure 5.14 compares the C-36° test with the full range of control test behaviour shown previously in Figure 5.10.

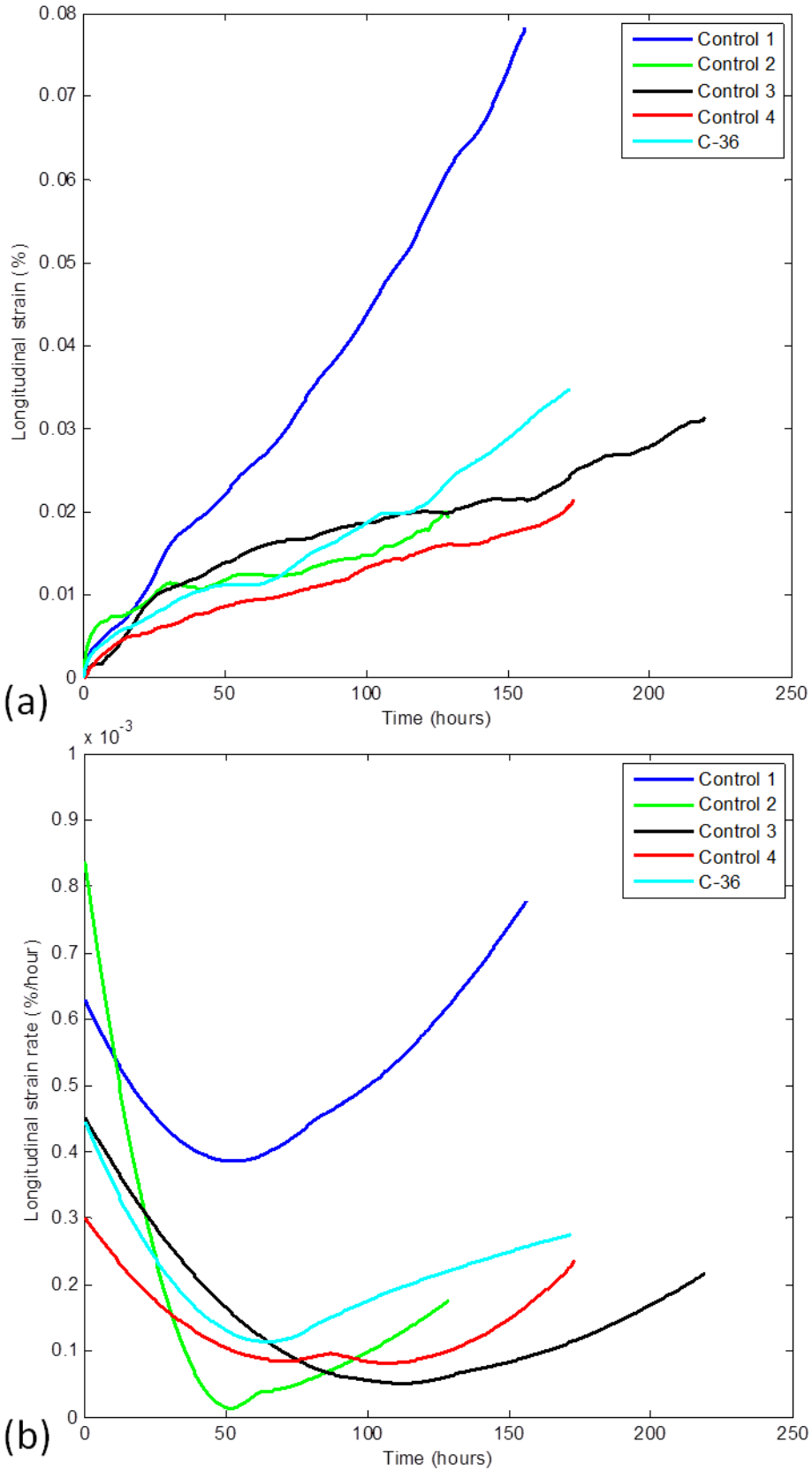

Figure 5.14. *Smoothed C-36° test result superimposed over control tests shown in Figure 5.10 (a) creep curves (b) creep rate curves.*

Figure 5.14 confirms that the C-36° test lies within the range of observed control behaviour. Following the minimum in Figure 5.14(b), which indicates the region of secondary creep, there is a region of acceleration which is indicative of tertiary creep. The onset and duration of both of these periods of creep are consistent with the behaviour observed for the unreinforced control tests.

Analysis of F-50° specimen behaviour

The test of the F-50° sample was ended without rupture after 922 hours. From Figure 5.13, it can be seen that the first 200 hours of the $\dot{\varepsilon}_z - \theta$ curve involve creep in the opposite direction to that required to bring about a shift towards the neutral angle (i.e. longitudinal contraction and tangential expansion). While $|\dot{\varepsilon}_z|$ decreases over this period, it is still positive – indicating longitudinal expansion. Knowing that the C-36° test was shown in Figure 5.14 to behave as a control test, Figure 5.13 reveals that the F-50° test closely follows expected control test behaviour for at least the first 100 hours. While less clear than the first 100 hours, the span from 100-170 hours during the F-50° test could also be within the range of control behaviour shown in Figure 5.10. This initial control-like behaviour, as well as the point at which the reinforcement takes effect and the F-50° curve deviates from the behaviour of a control test is expounded on in Section 5.3.4

Due to having an initial angle closest to the neutral angle and thus having the lowest net stress of all samples tested, the F-50° sample was predicted to show the shallowest $\dot{\varepsilon} - t$ curve (lowest $|\ddot{\varepsilon}_{max}|$), but also the lowest $t_{\dot{\varepsilon}=0}$. Referring to Figure 5.13, the sign of the longitudinal strain rate changes after approximately 200 hours. This longitudinal contraction is projected to allow the F-50° braid to approach the neutral angle, particularly if coupled with tangential expansion. As the braid tends to the neutral angle, it is expected that the longitudinal creep rate would tend to zero.

Although Figure 5.13 reveals that the $\dot{\varepsilon}_z$ curve for the F-50° sample exhibits asymptotic behaviour, it appears to be approaching approximately -1x10^{-4} %/hour. It is notable that this test was ended before rupture, and given another 1000 hours $\dot{\varepsilon}_z$ may very well tend to zero as θ tends to θ_N. Because of the lack of a bond at the interface between the braid and the pipe, it is feasible that an interfacial slip mechanism would facilitate the continual longitudinal creep of the pipe, regardless of the orientation of the reinforcement. As a result of the premature failure of the C-36° sample, the rate of change of $\dot{\varepsilon}_z$ as $\theta \rightarrow \theta_N$ could not be compared to that observed for the F-50° sample.

Analysis of C-65° specimen behaviour

As expected, Figure 5.13 reveals that creep rate decreases over time for initial braid angles below θ_N. Additionally, the C-65° sample shows no clear drop in creep rate over the duration of the test. This observation is attributed to the lack of a driver for tangential contraction necessary for a shift in this C-65° braid towards the neutral angle. While the experimental creep rate trend for C-65° shows far more fluctuation than the completely linear prediction made in Figure 5.11(c), Figure 5.12 still reveals this ε_z - t trend for the C-65° sample to be approximately linear (i.e. constant $\dot{\varepsilon}_z$), with a linear regression model (Figure 5.15) giving an R^2 value of 0.995.

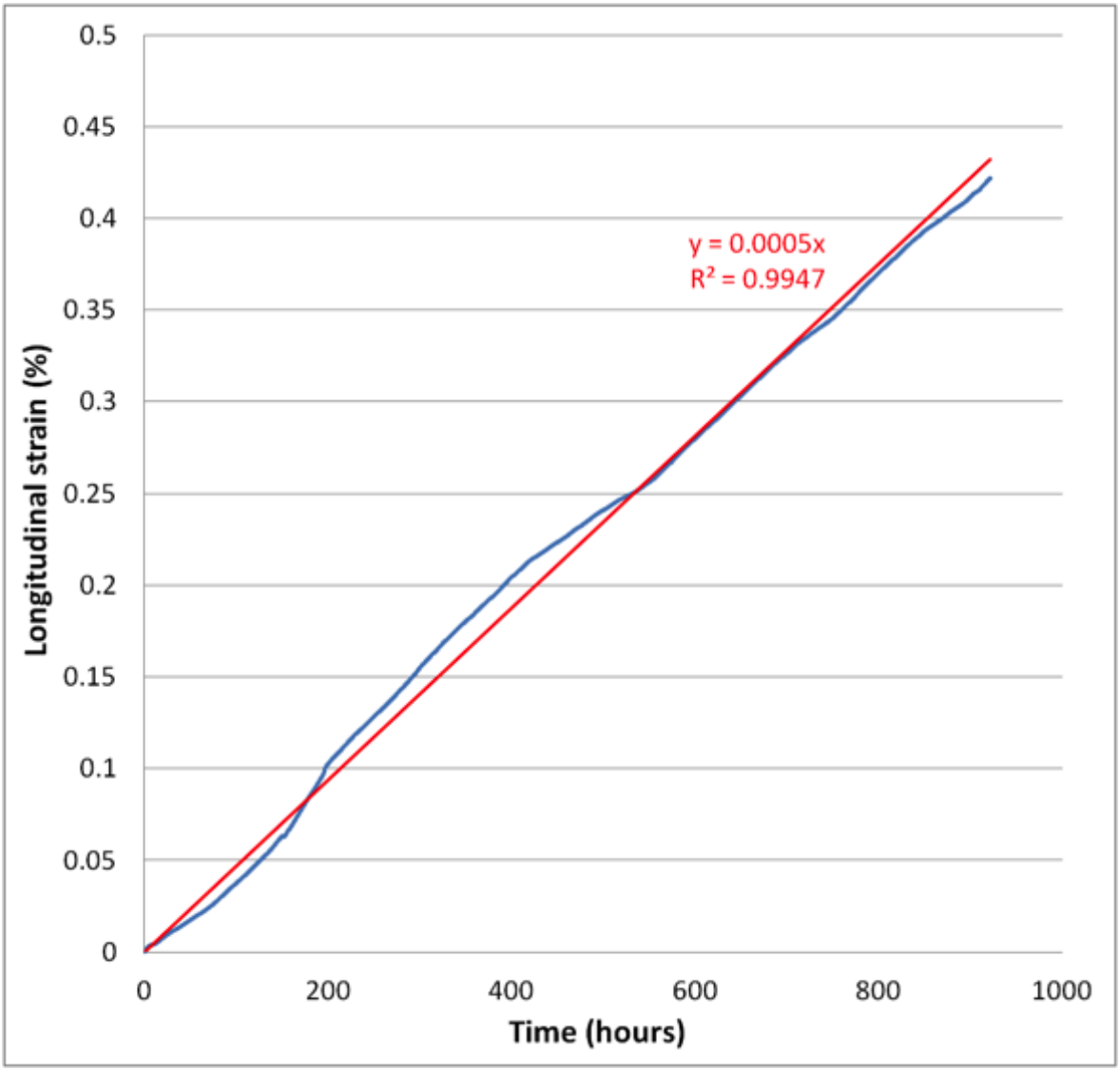

Figure 5.15. *Linear trend fitted to ε_z-t data for C-65° sample.*

5.3.4 Reinforcement engagement theory

As alluded to in Figure 5.11, there is expected to be some initial period of testing where the creep rate behaviour of the reinforced samples closely matches that of the unreinforced tests. This is because the initial tightness of the braid on the pipe is uncontrolled, and in theory the pipe is unrestrained for some period at the start of the test until the reinforcement engages. When investigating reinforcement architecture parameters in the tests performed in Chapter 4, it was thought that pulling the braid taut and clamping either end with hose clamps prior to testing would minimize this period of unrestrained creep and thus reduce mean creep

rate. Table 4.4 quantified the effect of fixed and free end conditions on final strain. Contrary to the previously stated hypothesis, the tests outlined in Table 4.4 gave no clear evidence of fixed end conditions consistently reducing the magnitude of creep strains. However, this data relies on final strain measurements, and does not fully characterize creep deformation behaviour during testing. With the added benefit of in-situ longitudinal strain measurement, Figure 5.12, reveals that the F-50° reinforcement architecture brings about a complete reversal in the direction of longitudinal creep, partway through the test.

Given the range of behaviour seen in the control tests, it is difficult to discern the point at which reinforced behaviour deviates from that of the control. Figure 5.16 shows the initial 250 hours of $\dot{\varepsilon}_z - t$ behaviour for the reinforced and unreinforced samples.

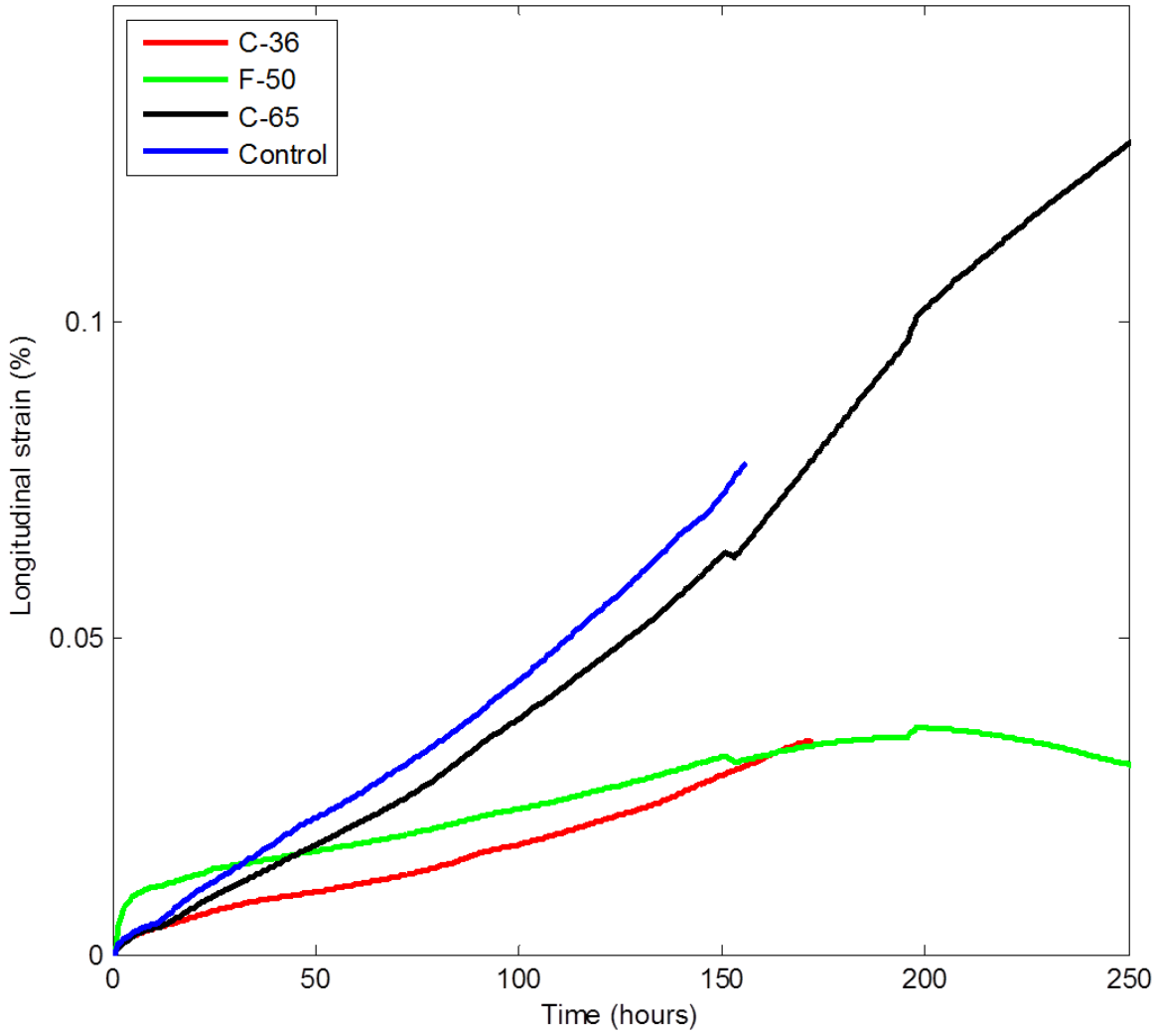

Figure 5.16. *Initial 250 hours of Figure 5.12, truncated to allow for comparison between control and reinforced sample behaviour.*

Due to the range of control behaviour, it is difficult to discern the point at which the behaviour of the reinforced samples deviates from that of the control tests. Considering the C-36° was shown in Figure 5.14 to lie within the range of control test behaviour, Figure 5.16 reveals that both the C-65° and F-50° curves closely conform to expected control behaviour. These reinforced tests fail to show behaviour atypical of unreinforced controls, until approximately 170 hours when the controls tend to rupture and reinforced samples exhibit a significant extension in ductility.

This lack of clear deviation from control behaviour is symptomatic of previously discussed scatter in control tests results. As a result, a clear point of engagement of the reinforcement cannot be discerned from the current study.

During creep testing, room temperature was observed to cycle by as much as ±15°C, driven by both weather effects and the automated switching on and off of heating and ventilation systems. The effect of this irregular thermal cycling on strain measurement is shown in Figure 5.17. Conducting future creep tests in a temperature-controlled room would significantly reduce noise in both furnace temperature and sample strain recordings.

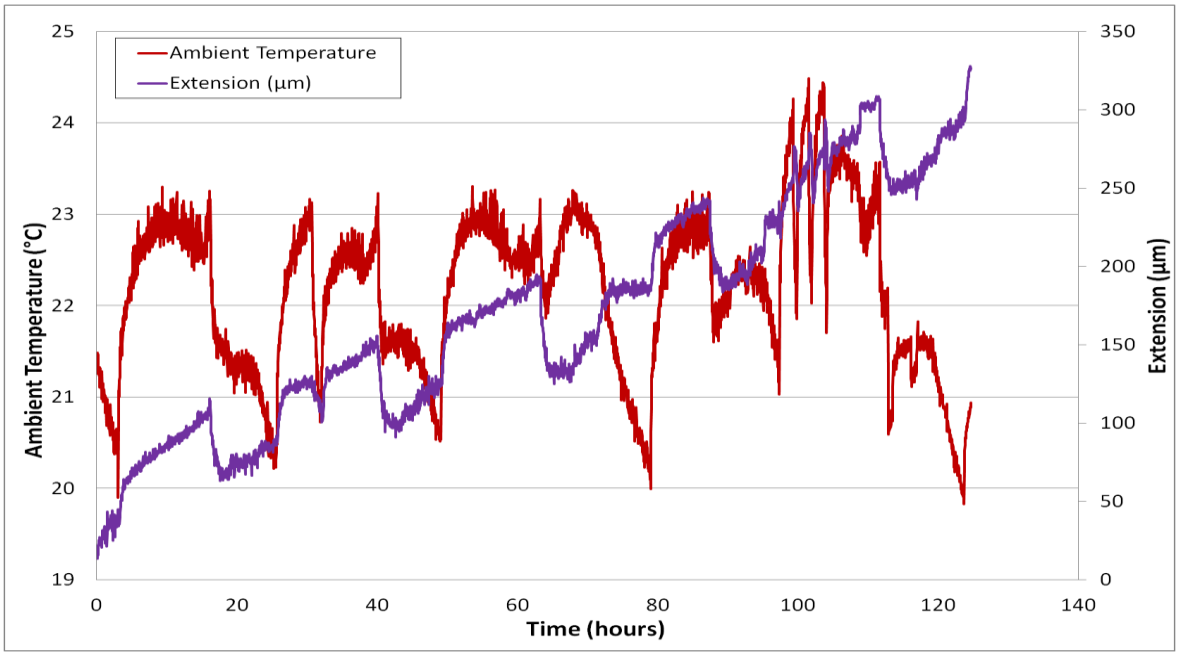

Figure 5.17. *Steps in extension measurement resulting from irregular cycling of ambient temperature.*

The present study utilised a novel creep rig design to provide the first documented instance of in-situ creep strain measurement of a multi-layered pipe sample under multiaxial loading. Successfully devising a means of measuring creep strain under this complex stress state is a step towards furthering the

understanding of creep behaviour of pressurized tubular components in industry. It has also been shown that by measuring the longitudinal strain component, overall multiaxial strain behaviour can be inferred alongside monitoring any changes in orientation of the reinforcement layer. Further utilization of this test apparatus is integral to a deepened understanding of $\dot{\varepsilon}_z - \theta - t$ relationships, particularly assessing rates of change of creep rate and reinforcement angle over a longer test duration.

5.4 Conclusions

As hypothesized, the observation that $\theta \rightarrow \theta_N$ is only true for initial braid angles less than θ_N, and in fact $\dot{\theta} = 0$ for $\theta > \theta_N$. This is evidenced by an approximately constant $\dot{\varepsilon}_z$ throughout the C-65° test, with a linear fit to the ε-t curve having an R^2 value of 0.995.

The premature failure of the C-36° sample meant that hypotheses related to $\ddot{\varepsilon}_z$ as $\theta \rightarrow \theta_N$ and $t_{\dot{\varepsilon}=0}$ for different initial angles could not be tested. Under the given conditions, reaching θ_N from an initial angle of 50° takes longer than 920 hours, and further testing is required to investigate the asymptotic behaviour of $\dot{\varepsilon} \rightarrow 0$ as $\theta \rightarrow \theta_N$.

For α-brass at 400°C, the mean creep rate approximation (as used in Chapter 4) was shown to overestimate the minimum creep rate by 80 ± 40%, as observed in unreinforced samples which were tested to rupture and experienced tertiary creep. For reinforced tests ended before tertiary creep and rupture, the difference between the mean creep rate approximation and the minimum creep rate is 55 ± 8% considering all reinforcement architectures, though this is a function of test duration.

CHAPTER REFERENCES

[1] S. Arsene and J. Bai, "A New Approach to Measuring Transverse Properties of Structural Tubing by a Ring Test," *Journal of Testing and Evaluation,* vol. 24, pp. 386-391, 1996.

[2] S. McAllister, R. C. Hurst, and T. E. Chung, "Modelling the Multiaxial Creep Behaviour of Alloy 800H," *International Journal of Pressure Vessels and Piping,* vol. 47, pp. 355-370, 1991.

[3] J. Lee, R. C. Bradshaw, R. W. Hyers, J. R. Rogers, T. J. Rathz, J. J. Wall, *et al.*, "Non-contact measurement of creep resistance of ultra-high-temperature materials," *Materials Science and Engineering A,* vol. 463, pp. 185-196, 2007.

[4] S. N. Gundarev, A. F. Gurov, V. V. Dement'ev, A. S. Demidov, A. E. Rusanov, and A. A. Khomyakov, "High-Temperature Creep Tests on Specimens of Single Crystal Molybdenum with a Complex Stress State," *Problemy Prochnosti (Strength of Materials),* 1990.

[5] T. Mitsueda, K. Fujii, and S. Ohnuki, "Comparison of Creep Damage Appearances Among Low Alloy Steel Pipes," in *Creep and Fatigue and Elevated Temperatures 8*, San Antonio, Texas, 2007.

[6] N. E. Dowling, *Mechanical Behaviour of Materials: Engineering Methods for Deformation, Fracture and Fatigue.*, 3rd ed. Upper Saddle River, NJ: Prentice Hall, 2007.

[7] J. R. Davis, *Heat-Resistant Materials*. Materials Park, Ohio: ASM International, 1997.

[8] M. E. Kassner and M. Perez-Prado, *Fundamentals of Creep in Metals and Alloys*, 1st ed. Oxford, UK: Elsevier Ltd, 2004.

[9] T. Safford, "Plastics in Pressure Pipes", Rapra Technology Ltd, Shropshire, UK1998.

[10] C. W. Evans, *Hose Technology*, 2nd ed. London, UK: Applied Science Publishers Ltd, 1979.

[11] T. Hunt and N. Vaughan, *The Hydraulic Handbook*, 9th ed. Oxford, UK: Elsevier Advanced Technology, 1996.

[12] Advanced Cooling Technologies Inc. (ACT). IFL Systems for Materials Processing, http://www.1-act.com/products/isothermal-furnace-liner/ifl-systems-for-materials-processing/, [Accessed Nov 28 2014].

[13] W. S. Cleveland and S. J. Devlin, "Locally Weighted Regression: An Approach to Regression Analysis by Local Fitting," *Journal of the American Statistical Association,* vol. 83, pp. 596-610, 1988.

[14] W. N. Venables and B. D. Ripley, "Smooth Regression," in *Modern Applied Statistics with S-PLUS*. vol. 3rd, ed: Springer New York, 1999, pp. 281-302.

[15] N. E. Dowling, *Mechanical Behaviour of Materials*, 3rd ed.: Person Prentice Hall, 2007.

[16] M. W. Spindler, "The multiaxial and uniaxial creep ductility of Type 304 steel as a function of stress and strain rate," *Materials at High Temperature,* vol. 21, pp. 47-54, 2004.

[17] W. S. Loewenthal and D. L. Ellis, "Sources of Variation in Creep Testing", NASA Glenn Research Center, Cleveland, Ohio, Technical Memorandum NASA/TM-2011-215493, 2011.

[18] C. Jeong, S. Bae, D. Ki, K. Watanabe, and B. Lim, "Creep rupture life and variation of microstructure according to aging time and creep test methods," *Materials Science and Engineering A,* vol. 449, pp. 155-158, 2007.

[19] T. Murakumo, T. Kobayashi, Y. Koizumi, and H. Harada, "Creep behaviour of Ni-based single-crystal superalloys with various γ′ volume fraction," *Acta Materialia,* vol. 52, pp. 3737-3744, 2004.

[20] J. K. Lai and A. Wickens, "Microstructural changes and variations in creep ductility of 3 casts of type 316 stainless steel," *Acta Metallurgica,* vol. 27, pp. 217-230, 1979.

CHAPTER 6: HIGH TEMPERATURE HYBRID SYSTEM

The focus of this chapter is to apply the findings of the reinforcement architecture optimization study in Chapters 4 and 5 to a high temperature system consisting of stainless steel reinforced with tungsten. This high temperature study is seen as a closer analogue to what would likely be applicable to the reformer furnace industrial application.

Preliminary, proof-of-concept tests are outlined and discussed, with early results presented for simple helically wound reinforcement architectures. Unique failure mechanisms which were not observed in the low temperature brass-stainless steel system are addressed. Specifically, methods devised to negate oxidation issues and the emergence of a non-uniform longitudinal creep phenomenon referred to as 'snaking' are outlined.

The performance of a tungsten braid produced at an 'optimal' architecture, as determined by the investigation in Chapter 4, is assessed in terms of its ability to assist 253MA to resist creep deformation. Issues with oxidation, intermetallic formation and damage tolerance of the reinforcement layer are discussed.

6.1 Proof of Concept

The scope of the work presented in Chapters 4 and 5 was limited to optimizing the architecture of the reinforcement, and the model brass-stainless steel system was selected to circumvent failure via oxidation. However, for this high temperature

system, oxidation protection is necessary. In this application, there are various means to isolate refractory metals from the atmosphere, such as coatings or a metallic sleeve.

Despite the vulnerability of refractory metals to oxidation, a proof-of-concept schedule 160 alloy 800H pipe was reinforced using helically wound Ø0.38 mm tungsten wires. The reinforced pipe was coated with 1-2 mm of a plasma sprayed 79E nickel-based alloy to act as an oxidation barrier. This proof-of-concept test showed at least a 4-times life extension over a monolithic pipe of equal dimensions in an accelerated test of ~2720 hours at 1030°C and internally pressurized to 3.5 MPa with argon. Although the prototype pipe did not rupture, there were signs of oxidation in the tungsten reinforcement, which was considered the life-limiting factor [1]. Upon ending the test, the plasma sprayed 79E layer was breached at either end of the wrapped section, and extensive oxidation of the underlying tungsten reinforcement was observed, Figure 6.1.

Figure 6.1. *Failed plasma spray coating, with oxidized tungsten wire underneath [1].*

6.2 Simple Tungsten Reinforcement

After trials with metallic arc-spray and brazed coatings, a solid metallic sheathing pipe was selected as the preferred method for protecting the tungsten reinforcement layer from oxidation. For these preliminary tests, a simple wrap reinforcement (helically wound at approximately 90° to the pipe axis) was used due to the wide availability and low cost of tungsten wire relative to more complex reinforced architectures such as braids.

Rather than deliberately negating oxidation through the use of a vacuum furnace, this system was seen as a step towards the intended industrial end-use. In practice, oxidation must be considered as one of many potential failure mechanisms acting in unison.

6.2.1 Design of experiment

Two pipes were oriented concentrically, with the inner pipe referred to as liner, designed solely to hold pressure load. The tungsten wire reinforcement layer was wound over the outside of this liner, with the intention of allowing the stresses driving tangential creep in the liner to be transferred to the reinforcement. Over both of these layers, an external pipe referred to as a sheath was welded in place. This sheath pipe was intended to have no structural role, and was purely to isolate the tungsten reinforcement from the oxidising environment, Figure 6.2.

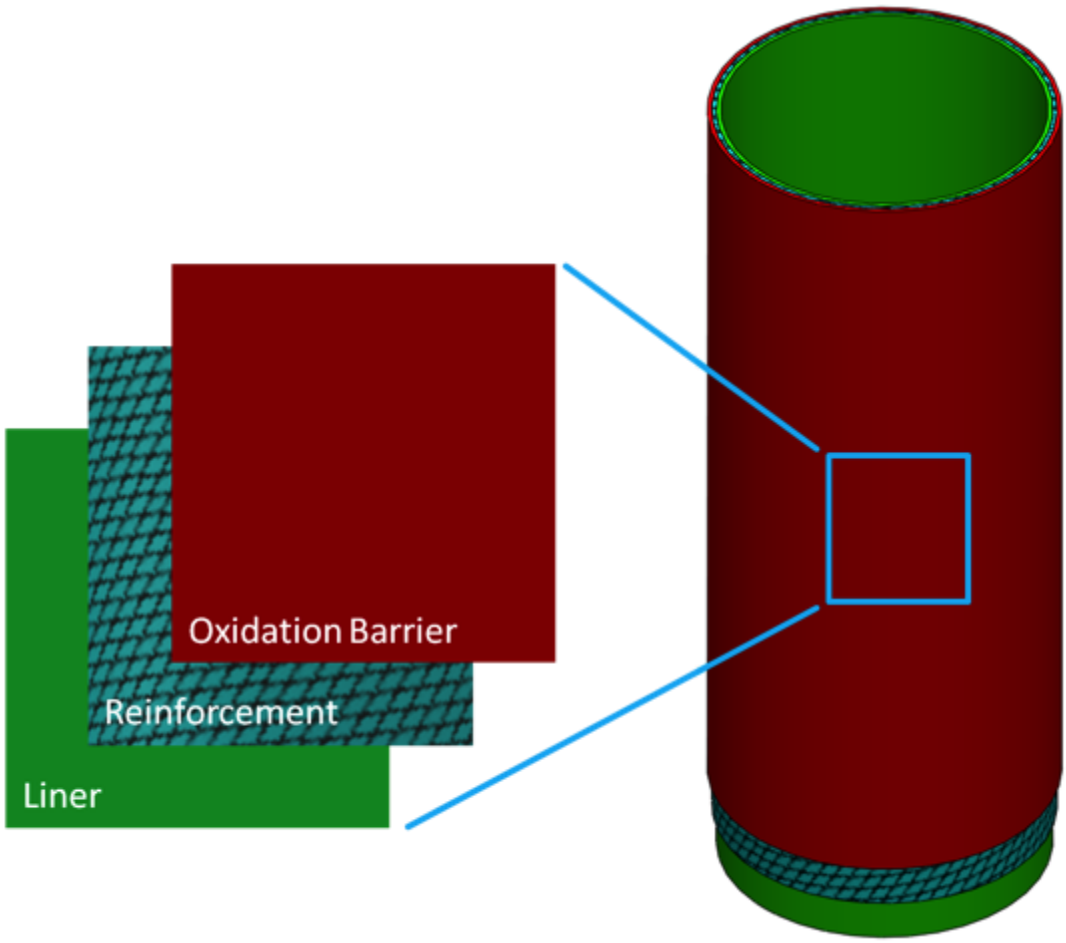

Figure 6.2. *Schematic of hybrid pipe geometry with solid sheath pipe acting as an oxidation barrier.*

As detailed in Section 2.3.2, 253MA is readily available in pipe form in a large range of sizes, and is known to resist oxidation at temperatures up to 1150°C. For these reasons, 253MA was chosen as the stainless steel component of the hybrid pipe, and was used for both the sheath and liner pipes.

Figures 6.3(a)-(c) give schematics of the three different high temperature hybrid pipe designs which were subjected to pressurised rupture testing in a horizontal Labec HTF100/12 tube furnace at 1030°C and pressurized with argon to 4 MPa. The hybrid pipes were composed of a 253MA stainless steel inner tube reinforced with tungsten wire. The additional outer sheath was also constructed of 253MA. Figure 6.4 shows a hybrid pipe sectioned to reveal all three layers.

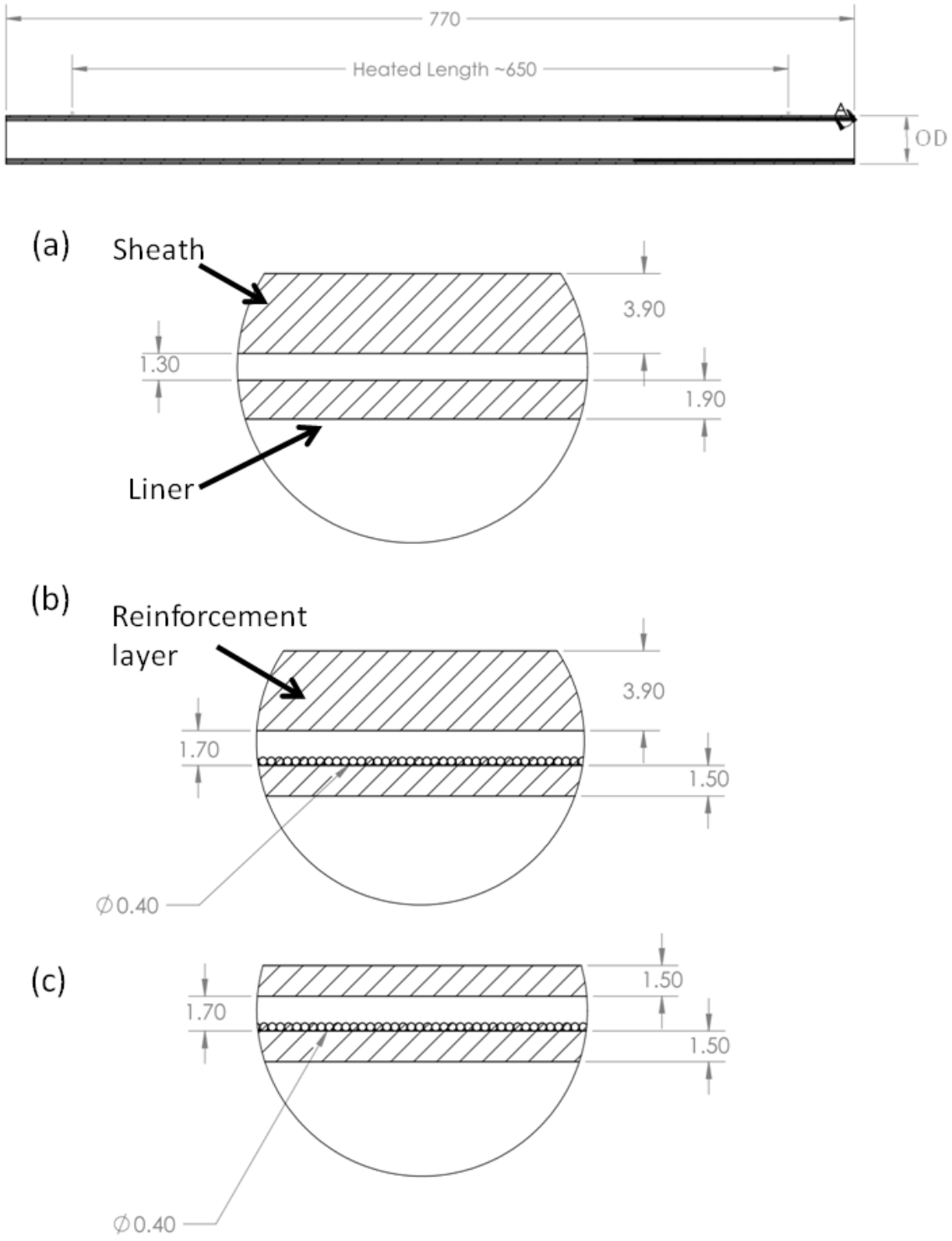

Figure 6.3. *Dimensioned diagram of 253MA inner (liner) and outer (sheath) pipes with detailed section view for each design case (a) control, OD=48.7 mm (b) reinforced design 1 – thick sheath, OD=48.7 mm (c) reinforced design 2 – thin sheath, OD=43.9 mm.*

Figure 6.4. *Partial section of reinforced design 1 – thick sheath.*

Unlike in Chapter 4, the elevated temperature and addition of the sheath layer meant that hose clamps could no longer be used to fix the ends of the wrap. Instead, a 316 stainless steel crimp bead was used to hold the wire ends in place. As shown in Figure 6.5, looping the wire back on itself through a crimp bead, before pressing the bead flat, fixes the first loop and holds the wrap in place.

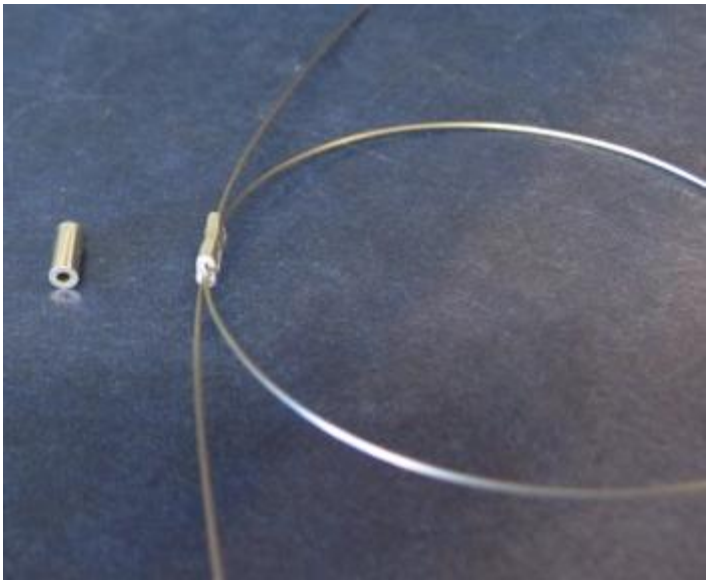

Figure 6.5. *Crimp bead in as-received condition, alongside bead crimped to hold wire loop fixed.*

As in the low-temperature investigation in Chapter 4, tangential and longitudinal strains were measured post-mortem. Tests were performed on three unreinforced control pipes, a wrap-reinforced pipe with standard pipe size 'thick' sheath (~3.2 mm) and a weight reduced design with machined 'thin' sheath (~1.5 mm), Figure 6.3.

Internal pressure and temperature were logged every 60 seconds during all tests, and maintained stability to within ±0.2 MPa and ±5°C. A sustained pressure drop indicated pipe rupture, in which case the test was ended.

In the unreinforced case, the large creep ductility of 253MA permits the liner pipe to creep until it comes into contact with the sheath pipe. From this point, both inner and outer pipe layers creep simultaneously until rupture. This effectively gives variable pipe dimensions, and makes it difficult to apply Equations 2.1-2.3 to determine principal stresses. Inner and outer radial distances, r_o and r_i, were simplified to include sheath and liner thicknesses, but not the air gap in between i.e. the true inner radius was used for the stress calculation and r_o was adjusted to subtract the air gap.

$$\sigma_r = \frac{p_i r_i^2}{r_o^2 - r_i^2}\left[1 - \frac{r_o^2}{r^2}\right] \quad (2.1)$$

$$\sigma_t = \frac{p_i r_i^2}{r_o^2 - r_i^2}\left[1 + \frac{r_o^2}{r^2}\right] \quad (2.2)$$

$$\sigma_z = \frac{p_i r_i^2}{r_o^2 - r_i^2} \quad (2.3)$$

$$\sigma_{VM} = \sqrt{\frac{[(\sigma_r - \sigma_t)^2 + (\sigma_t - \sigma_z)^2 + (\sigma_r - \sigma_z)^2]}{2}} \quad (2.4)$$

Chapter 4 revealed that the peak von Mises stress is a controlling factor in creep life, rather than the average von Mises stress through the wall thickness. By Equations 2.1-2.4 for thick-walled pressure vessels, a 4 MPa internal pressure gives

a maximum von Mises equivalent stress of 15.7 MPa in the thick sheath configuration and 25.3 MPa in the thin sheath design. Extrapolating from 1,000, 10,000 and 100,000 hour creep rupture data for 253MA, a control creep rupture life of 91 hours is predicted in the thick sheath configuration and 9 hours in the thin sheath configuration [2].

Unlike the brass-stainless steel system (Chapters 4 and 5), where the reinforcement was simply removed, the presence of the sheath layer makes a meaningful measurement of tangential strain difficult post-test. The nature of the creep deformation often makes it impossible to separate the liner from the sheath post-test. As a result, strain measurements are based on dimensions of the sheath.

6.2.2 Results and discussion

With simple, unoptimized tungsten reinforcement architecture, the preliminary results presented in Table 6.1 show that the fundamental creep reinforcement concept investigated in Chapters 4 and 5 are applicable to the high temperature tungsten-stainless steel system, and an order of magnitude life extension is achievable.

Table 6.1. *Results of hybrid pipe tests with simple tungsten reinforcement.*

	Average control	**Wrap – thick sheath (design 1)**	**Wrap – thin sheath (design 2)**
Calculated control life (hrs)	91	91	9
Measured life (hrs)	70	857[a]	118
Life extension compared to control[b]	-	12.2x	13.1x
Maximum tangential change (%)	53	-5.3	-8.0
$\dot{\varepsilon}_t^{\,c}$ **(%/hr)**	0.74	-6.8×10^{-3}	-6.8×10^{-2}
Overall longitudinal change (%)	Unknown	4.6	27
$\dot{\varepsilon}_z^{\,c}$ **(%/hr)**	Unknown	5.3×10^{-3}	0.23
Mode of failure	Tangential creep	**Test ended before failure.** Tangential creep effectively halted, revealed longitudinal creep as next path of least resistance.	Longitudinal creep – dramatically accelerated from design 1.

[a] test ended by power outage before rupture.

[b] compared to measured control life when applicable. In the case of the design 2 configuration, no control test was performed and life extension is compared against calculated control life.

[c] rates averaged over entire life of test.

As mentioned previously, the nature of the creep deformation often makes it impossible to separate the liner from the sheath post-test. This can be seen in Figure 6.6, where the liner and sheath layers have been pressed together.

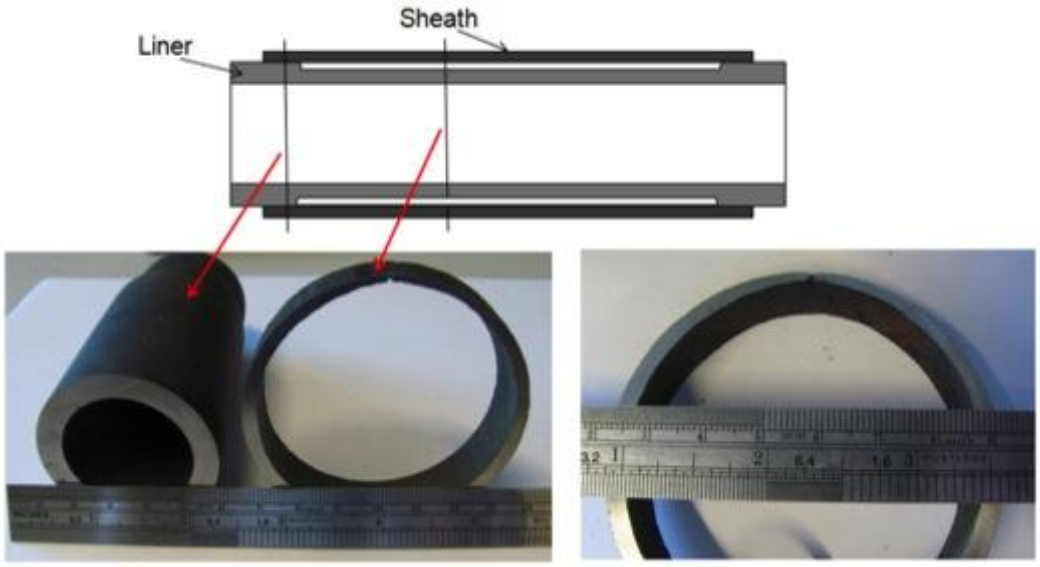

Figure 6.6. *Schematic of unreinforced pipe, with photos of sections taken after rupture. Note the drastic increase in diameter and reduction in wall thickness. Liner and sheath pipe layers pressed together in region of maximum deformation.*

The thick sheath test was abruptly ended by a power outage after 857 hours. Promisingly, this reinforced pipe had not ruptured, indicating a minimum 12-times extension in life over the control pipe tests under identical conditions. A 4.55% increase in length, 5.3% reduction in diameter and 22% reduction in wall thickness suggested that diametric creep had effectively been negated as the primary mode of failure.

However, a unique phenomenon was first observed in the unruptured tube, with the increase in length being particularly notable. From Figure 6.7(c) it can be seen that this elongation was not uniform, and is best described as 'snaking'. By transferring tangential stress from the liner pipe to the tungsten wire, longitudinal stress becomes the new path of least resistance and thus creep in this direction dominates. The snaking can partially be attributed to the horizontal orientation of the pipe during testing, with self weight causing the test piece to sag. However, this deformation can be observed in multiple planes rather than being uniform sagging. It is theorised that the non-uniformity of the longitudinal deformation is

primarily a result of hot spots in the furnace and not having the pipe positioned perfectly concentrically within the tube furnace, leading to one side of the tube sample being hotter than the other. This is turn would cause one side of the tube to creep faster than the other side. Notably, snaking was not observed in the tests in Chapter 5 where an IFL was used to improve temperature uniformity.

The reinforced pipe with a thin sheath ruptured after 118 hours due to longitudinal creep (a 13.1x extension in creep life compared to the calculated control life). It exhibited a significant degree of snaking, increasing in length by 27% and reducing in diameter by 8%. This reduced sheath thickness exacerbated the snaking phenomenon and made it far more pronounced (Figure 6.7(d)) as less material was available away from the neutral axis to resist bending moments. It can be seen from Figure 6.7(d) that the snaking eventually pushed the cooler side of the tube close enough to the wall of the tube furnace to change the direction of the snaking.

Figure 6.7. *(a) control pipe prior to testing (b) control pipe after rupture caused by tangential creep (c) design 1 exhibiting notable snaking through its midsection (d) dramatic snaking in design 2.*

In the extreme case shown in Figure 6.7(d), the 'snaked' pipe would not be functional in a reformer furnace up until the point of rupture. The reduction in diameter would crush the catalyst and snaking would cause interference with other pipes. As a general rule in reformer furnaces, lateral movement of tubes away from the original tube axis is not permitted beyond one tube diameter[1].

Despite the lack of an isothermal furnace liner and the horizontal sample orientation of the brass tests in Chapter 4, notable snaking was not observed. The lower testing temperature of 400°C was well within the operating range of the furnace, making hot spots less prevalent. The significantly smaller sample diameter and wall thickness resulted in reduced self weight and also placed the

[1] Personal communication with Peter Tait, Senior Reliability Engineer, Methanex, 2013

outer diameter of the tube samples further away from the heating elements in the furnace.

6.2.3 Preliminary conclusions from proof of concept testing

As in the low temperature brass-stainless steel tests of Chapters 4 and 5, it was demonstrated that creep in the longitudinal direction dominates when creep is halted in the tangential direction.

In these preliminary high temperature tests with a simple tungsten reinforcement architecture, this longitudinal creep manifested as 'snaking', a unique phenomenon driven by non-uniform creep due to hot spots in the furnace.

Despite the emergence of this failure mechanism, a number of important conclusions could be drawn from the preliminary testing:

- Sheathing is an effective means of isolating the tungsten reinforcement from oxidation.

- Through careful geometric application and design considerations, *overall* hybrid creep strength can be controlled by the creep strength of the refractory *reinforcement*.

- By utilizing the structural and oxidation resistant properties of the liner and sheath in conjunction with the creep properties of tungsten, *an increase in creep life in excess of 12-times is achievable in the high temperature application*.

6.3 Braided Tungsten Reinforcement

The sheathed tests in Section 6.2 confirmed tungsten reinforcement as an effective means of restricting 253MA from creeping, and proved sheathing as a viable means of protecting the tungsten from oxidation. While a potential life gain on the order of 12-times is a promising result, the presence of the snaking phenomenon highlighted the need for a more complex, structured reinforcement architecture, such as that considered in the reinforcement architecture optimization study conducted in Chapter 4.

By testing braided tungsten reinforcement with an optimized architecture, potential gains in the life extension are maximized. Additionally, these long-term high temperature tests can be used to identify secondary damage mechanisms and potentially problematic long-term phenomena such as grain growth and intermetallic phase formation.

Although the derivation of the theoretical neutral angle showed that θ_N is not a function of material properties, it is important to consider potential changes to the ideal reinforcement angle which may be brought about by the use of a different material system. In order to assess whether the brass/stainless steel material system is a good analogue for the high temperature 253MA/tungsten system, it is useful to compare stiffness (E), thermal expansion (α), test temperatures and melting points for each material system, Table 6.2. The single most important factor in the success of the reinforcement is its melting point relative to the test temperature. It is imperative that the reinforcement material does not undergo creep. In order to effectively restrain the pipe, it is also important that the reinforcement material has a relatively high stiffness compared to the pipe material. Thermal expansion characteristics are predicted to influence the nature by which the reinforcement first engages the pipe, and how rapidly creep strains

are halted. However, the stiffness and thermal expansion characteristics of the reinforcement layer are complicated by the braid geometry, which does not behave as a monolithic material.

Table 6.2. *Comparison between reinforcement effectiveness in low and high temperature materials systems.*

Material System	**Reinforcement/liner ratio**		$\mathbf{T_{test} / T_{M, reinf}}$
	E (GPa)	**α (μm/m °C)**	
SS/Brass	1.84	0.8-0.9	0.41
W/253MA	2.0	0.24	0.31

From Table 6.2, it can be seen that in both material systems the reinforcement layer is operating at a temperature approximately 30-40% of its melting point, suggesting there is negligible creep in the reinforcement layer in both cases. The tungsten reinforcement is slightly more rigid relative to the 253MA than the stainless steel is relative to brass. This suggests the tungsten may be slightly more effective in restricting creep. The thermal expansion differences suggest that there may be some subtle differences at the interface, where contact stresses alter the frictional interaction.

6.4 Methodology

A tungsten braid was produced commercially by Windhösel, and tested in two configurations – unoptimized and optimized. As in the tests in Section 6.2, ~800 mm long test pieces were tested horizontally inside a Labec HTF100/12 tube furnace. Samples were configured as shown in Figure 6.8, with a solid 253MA

sheath pipe welded in place over the liner and reinforcement layers, and internal pressure applied to the liner.

In the test of the unoptimized tungsten braid, pipe sizing and test conditions were kept identical to design 1 in the preliminary tests, Figure 6.3(a), as 4 MPa and 1030°C. Therefore, the measured control life of 70 hours (Table 6.1) still stands. From the study of the brass/stainless steel system in Chapter 4, the braided reinforcement would be expected to out-perform a simple helical wrap by at least 22%, in terms of life extension, even when the braided reinforcement is unoptimized.

For the optimized braid configuration, a larger liner pipe was used to alter the braid angle and bring it as close as possible to the optimal 54.7 ± 1.5°, predicted by the empirical model in Section 4.2.4. The liner pipe was turned down to an outer diameter of ø41.2 mm, and a wall thickness of 1.5 mm to produce a braid angle of 52.6 ± 1.4°. The sheath pipe had a nominal outer diameter of ø60.33 mm and a wall thickness of 3.91 mm.

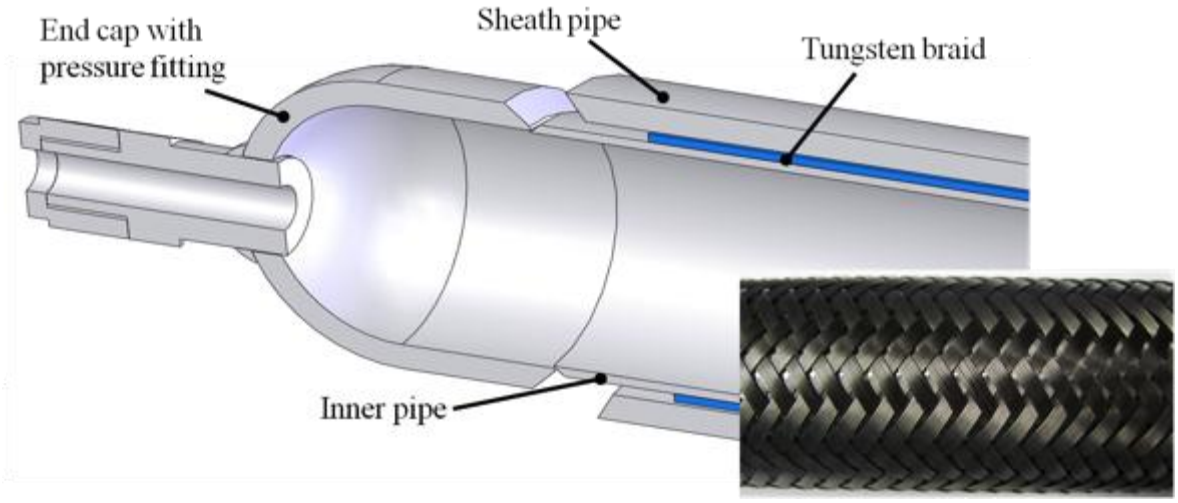

Figure 6.8. *High temperature hybrid tube sectional schematic. Inset: 53° tungsten braid configuration.*

In anticipation of the optimized braid test running for a considerable length of time, test pressure and temperature were increased to 5 MPa and 1040°C, this was dictated by the upper limit of the pressure transducer and the maximum furnace temperature. The change in pipe dimensions, as well as operating conditions, brought about the need for a new control test to be performed.

Internal pressure and temperature were logged every 60 seconds during all tests, and maintained stability to within ±0.2 MPa and ±5°C. A sustained pressure drop indicated pipe rupture, in which case the test was ended.

Recalling Section 3.5.3, strain measurement is difficult during rupture testing. While the method of periodically interrupting pipe rupture tests to take regular strain measurements was used with some success in Chapter 4, this necessitates the removal of the reinforcement layer. The presence of the external sheath, welded in place, makes periodic interruption for strain measurement of the liner impossible. Therefore, overall creep rupture time and final maximum strain in the tangential and longitudinal directions were determined upon failure.

In order to investigate for evidence of creep and microstructural changes, metallographic samples were prepared from as-received 253MA, as well as control and braid-reinforced samples post-test. Green bakelite powder was used to mount the samples, which were then ground sequentially with 180 to 600-grit silicon carbon pads, before being polished with 9 μm, 3 μm and 1 μm diamond suspension, and polished to a mirror finish with 0.06 μm colloidal silica.

For general-purpose revealing of the bulk microstructure, samples were etched with Kalling's No. 2 reagent (2g $CuCl_2$ (cupric chloride), 40 mL hydrochloric acid,

50 mL ethanol). Kalling's No. 2 is listed in ASTM E 407 as suitable for etching Ni-Cu, nickel-based superalloys, ferritic and martensitic stainless steels. The etchant darkens martensite, attacks ferrite readily, etches austenite slightly and does not attack carbides. In instances when the location and size of carbides was of particular interest, samples were etched with glyceregia (30 mL glycerol, 30 mL hydrochloric acid and 10 mL nitric acid) [3].

6.4.1 Life prediction of unreinforced materials

As previously mentioned, the measured control life of 70 hours is applicable in the case of the unreinforced tungsten braid.

In the unreinforced case, the large creep ductility of 253MA permits the liner pipe to creep until it comes into contact with the sheath pipe. From this point, both inner and outer pipe layers creep simultaneously until rupture. This effectively gives variable pipe dimensions, and makes it difficult to apply Equations 2.1-2.3 to determine principal stresses. Inner and outer radial distances, r_o and r_i, were simplified to include sheath and liner thicknesses, but not the air gap in between i.e. the true inner radius was used for the stress calculation and r_o was adjusted to subtract the air gap.

$$\sigma_r = \frac{p_i r_i^2}{r_o^2 - r_i^2}\left[1 - \frac{r_o^2}{r^2}\right] \tag{2.1}$$

$$\sigma_t = \frac{p_i r_i^2}{r_o^2 - r_i^2}\left[1 + \frac{r_o^2}{r^2}\right] \tag{2.2}$$

$$\sigma_z = \frac{p_i r_i^2}{r_o^2 - r_i^2} \tag{2.3}$$

$$\sigma_{VM} = \sqrt{\frac{[(\sigma_r - \sigma_t)^2 + (\sigma_t - \sigma_z)^2 + (\sigma_r - \sigma_z)^2]}{2}} \tag{2.4}$$

By Equations 2.1-2.4 for thick-walled pressure vessels, a 5 MPa internal pressure gives a von Mises equivalent stress of 22 MPa. Extrapolating from 1,000, 10,000

and 100,000 hour creep rupture data for 253MA, a control creep rupture life of 10 hours was predicted [2].

6.4.2 Materials selection

As introduced in Section 2.3.2, and alluded to in the design of the simple tungsten reinforcement tests (Section 6.2.1), the widespread availability and oxidation resistance of 253MA were primary reasons for its selection for the sheath and liner pipes.

Figure 6.9 is generated from creep rupture information provided in the Rolled Alloys 253MA data sheet [2], with stresses and temperatures converted to metric units for convenience. Linear interpolation was used to add trend lines for 1030°C and 1040°C. Note that data at 1,000, 10,000 and 100,000 hours were provided and plotted in [2], while trends were extrapolated to give points for 10 and 100 hour rupture times.

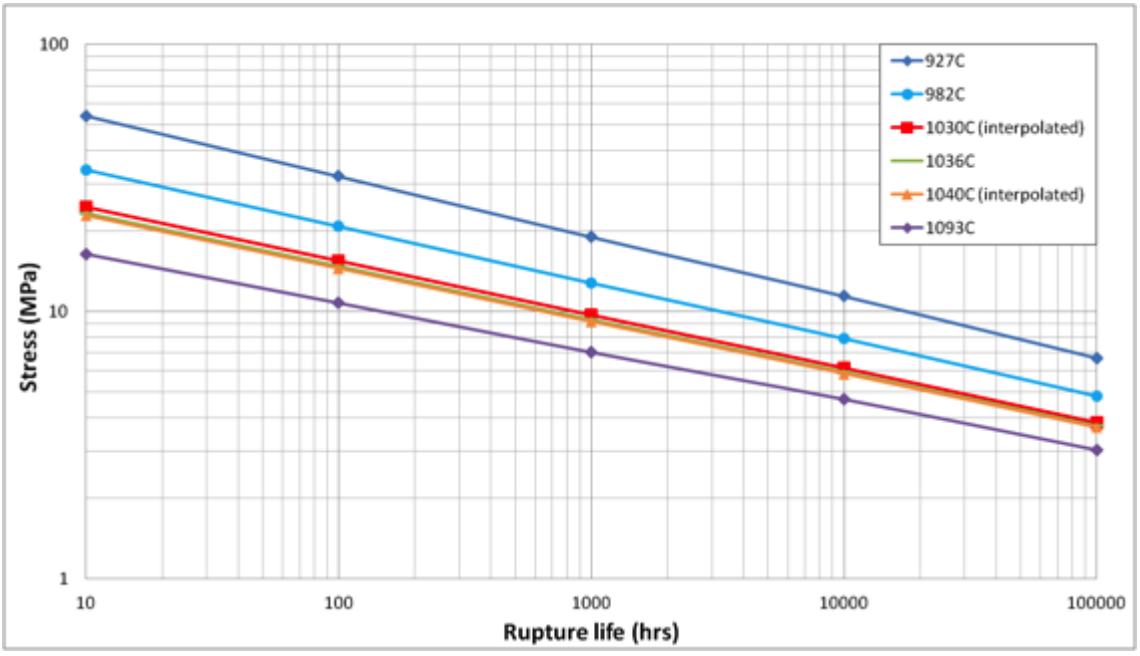

Figure 6.9. *253MA creep rupture curve. Average stress to rupture in indicated times. Adapted from Rolled Alloys 253MA data sheet [2].*

A power series fit of this 1030°C data predicts a stress-rupture life (σ-t_r) relationship governed by the equation: $\sigma = 39.006 t_r^{-0.201}$ or $t_r = \left(\frac{\sigma}{39.006}\right)^{-1/0.201}$.

At 1040°C, a σ-t_r relationship governed by: $\sigma = 36.132 t_r^{-0.198}$ or $t_r = \left(\frac{\sigma}{36.132}\right)^{-1/0.198}$ is predicted.

6.4.3 Hybrid pipe architecture

A tungsten braid was manufactured by Windhösel, a German company with 50 years braiding experience. This tungsten braid was produced with a 38x7x0.4 structure i.e. 38 strands, seven wires per strand and 0.4 mm wire diameter. While manufactured with a nominal braid angle of 38.3° on a Ø28.7 mm mandrel, a range of angles from approximately 32° to 70° could be achieved by expanding or contracting the braid. Relationships between nominal diameter, braid angle, and surface area coverage were provided in graphical form by the manufacturer, Windhösel [4], and are shown in Figures 6.10 and 6.11.

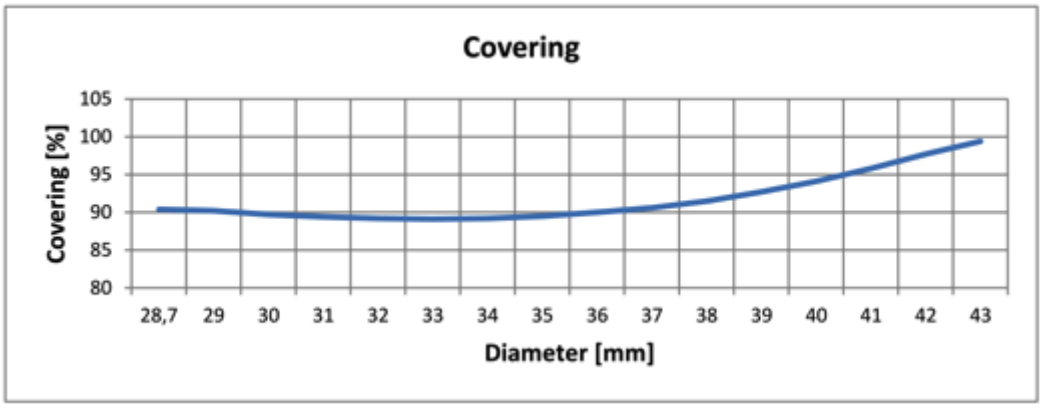

Figure 6.10. *Diameter-surface area coverage relationship for 38x7x0.4 tungsten braid [4]*

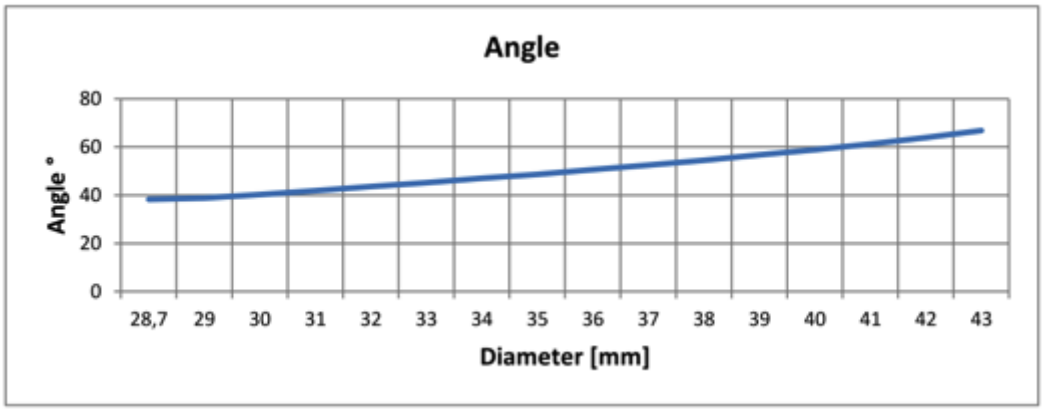

Figure 6.11. *Diameter-braid angle relationship for 38x7x0.4 tungsten braid [4]*

This tungsten braid was tested in two configurations – unoptimized and optimized. As mentioned in Section 6.4, the unoptimized braid test kept pipe sizing and test conditions identical to the preliminary tests (with thick sheath). The Ø37.5 mm liner produced a braid angle of θ = 45.8 ± 0.68° (± standard deviation) and a surface coverage of 90%. This unoptimized braid configuration was denoted W-46°.

For the optimized braid configuration, a larger liner pipe was used in order to alter the braid angle and bring it as close as possible to the optimal 54.7 ± 1.5°, predicted by the empirical model in Section 4.2.4. The liner pipe was turned down to an outer diameter of ø41.2 mm, which produced a braid angle of θ = 52.6 ± 1.4° and a surface coverage of 93%. This optimized braid configuration was denoted W-53°.

6.5 Results and Discussion

6.5.1 Life extension and damage analysis – unoptimized braid test

The unoptimized W-46° sample ruptured after 765 hours and exhibited a 26% increase in diameter in one isolated area, with no bulk deformation at the rest of

the liner tube. Despite this 765 hour rupture life being a 10.9x extension over the control, the failure was defined as premature.

As stated in Section 6.4, the braided reinforcement would be expected to out-perform a simple helical wrap by at least 22%, in terms of life extension, even when the braided reinforcement is unoptimized. However, the wrap-reinforced sample was shown in Section 6.2.2 to have given a 12.2x life extension without rupture. Unlike the wrap-reinforced case, the unoptimized braid test piece showed no sign of snaking (shown for a wrap-reinforced pipe of identical dimensions and test conditions in Figure 6.7).

Tungsten wire is stiff and brittle by nature, making it difficult to braid. The premature failure of the unoptimized W-46° sample was traced back to breaks in wire during the braiding process, which resulted in stress concentrations and areas of more sparse coverage, Figure 6.12. In subsequent tests, additional care was taken to avoid these regions of damage, at the expense of significant material wastage.

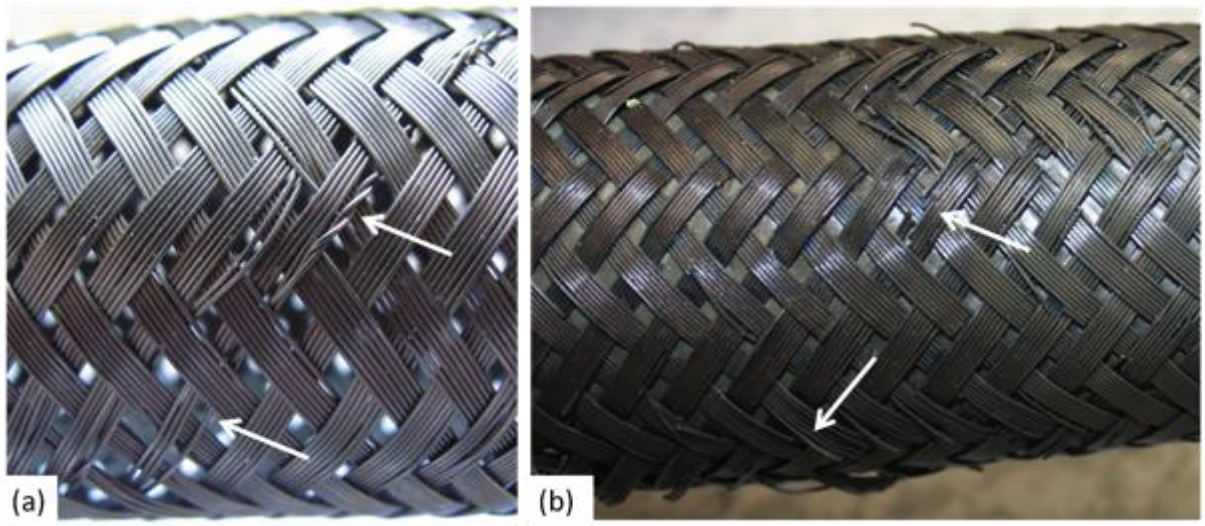

Figure 6.12. *Defects present in unoptimized tungsten braid (W-46°) (a) pre-test, (b) post-test (different region)*

In regions of particularly spare coverage, creep 'blisters' were observed to have formed. That is, highly localised creep deformation was seen to have occurred at defects in the braid. This localised region deformed heavily, eventually rupturing and leaking pressure to the external sheath pipe, which crept as normal to give a typical bulge in the midspan of the pipe. Post-rupture, the reinforcement oxidized heavily, causing yellowing of the tungsten around the point of rupture, Figures 6.13, 6.14 and 6.16. From Figure 6.13, note the lack of bulk deformation in unaffected regions of the liner, and the typical tangential creep expansion observed in the sheath pipe in the background.

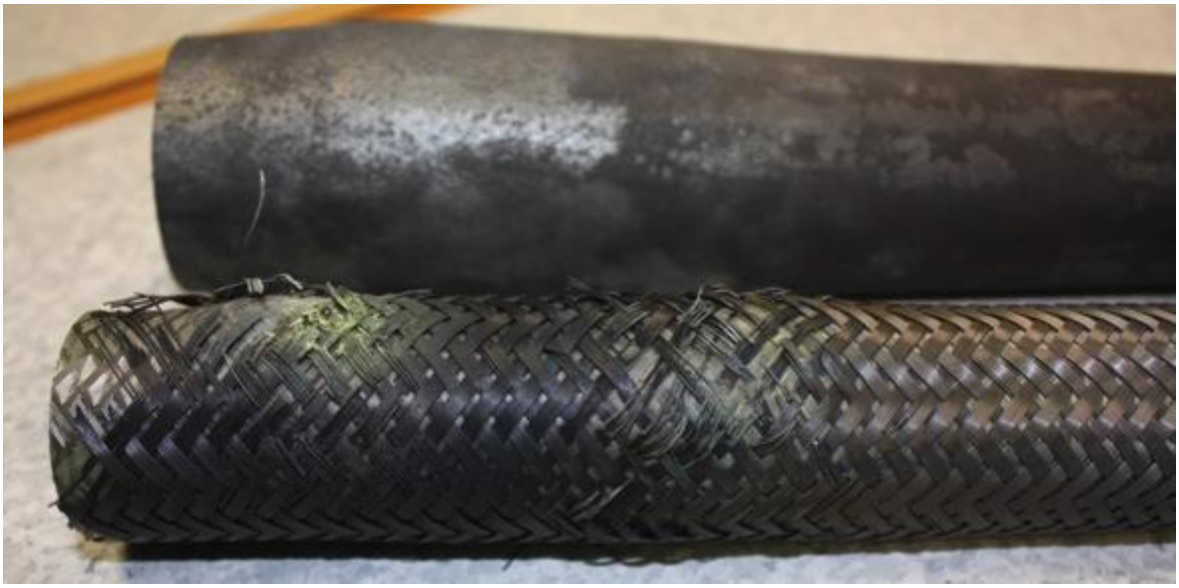

***Figure 6.13**. Section of ruptured liner, reinforced with unoptimized tungsten braid (W-46°). Two creep blisters are present at defects in the braid, the leftmost of which led to the final failure of the liner.*

Figure 6.14.*Oxidation and embrittlement of tungsten braid around point of rupture. Oxidation occurred post-rupture while the furnace was cooling down.*

Post-rupture damage to the braid makes it impossible to accurately determine the size of the defect prior to rupture. As an approximation, the dimensions of the dimple on the inside of the liner pipe, Figure 6.15, were used to judge the size of the unreinforced region.

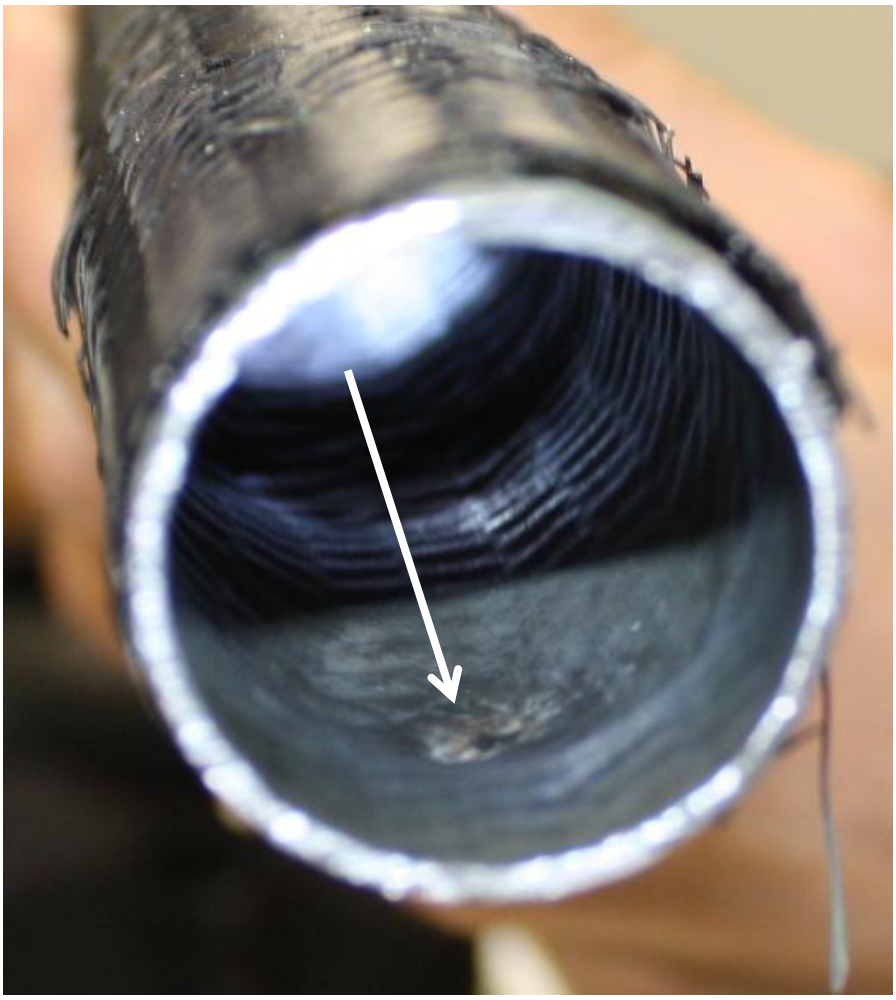

Figure 6.15. *Internal view of localised creep blister on W-46° sample.*

Using plasticine to take a casting of the inner surface, the internal dimple was estimated to be an ellipse aligned with the braid angle, 13 mm long on the major axis, and 7.5 mm long on the minor axis, Figure 6.16.

Figure 6.16. *Size and position of blister on inner surface, overlaid onto braid pattern on outer surface. Oxidation of the tungsten occurred post-rupture while the furnace was cooling down. Crumbling of the tungsten occurred while the sheath pipe was being removed.*

In subsequent tests, extra care was taken to select portions of the braid such that larger defects, on the order of 5 mm, were kept as far away from the hot zone as possible.

6.5.2 Life extension and damage analysis – optimized braid test

The additional acceleration used in the optimized braid test brought about the need for a new control pipe to be tested at 1040°C and 5 MPa internal pressure. Under these conditions, a control life of approximately 1.6 hours was observed. A maximum 45% tangential expansion was measured at the point of rupture along with a 0.31% increase in length. Figures 6.17 and 6.18 show the appearance of this control pipe after failure.

Figure 6.17. *Control pipe after rupture caused by tangential creep.*

Figure 6.18. *Point of rupture in control pipe – large longitudinal crack resulting from tangential expansion.*

This observed control life of 1.6 hours is significantly less than the 10 hour life predicted in Section 6.4.1. Creep data for 253MA is only available for 1,000-100,000 hour rupture lives, meaning that significant extrapolation was required for the 10 hour life prediction. It is suspected that this extrapolation is the cause of the discrepancy. However, the difference is of little consequence as long as the reinforced tests are conducted under identical conditions to the control.

The test of the W-53° (optimized tungsten braid) sample was stopped after 500 hours for measurement of the sheath pipe and repair of the furnace. With the

optimized reinforcement architecture, and braid defects minimized/avoided (particularly in the hot zone), the 500 hour break point already corresponds to a 309-times life extension over the control. No significant (measureable to 0.05 mm) bulk deformation was observed in either the tangential or longitudinal directions – i.e. deformation, if present at all, was smaller than natural variation in as-received pipe dimensions, Figure 6.19.

Figure 6.19. *W-53 sample after 500 hours (309x life extension over control). Some superficial oxidation is present, but pipe dimensions have not changed measurably.*

Following this stoppage for measurement of the W-53° sample and furnace repairs, the test was restarted under further accelerated conditions. During furnace repairs, pressure instrumentation was replaced to permit an increase in pressure from 5 MPa to 7.9 MPa. From the 253MA creep data sheet, this increase in internal pressure further accelerated creep in the W-53° test by a factor of 10 [2].

Upon this further acceleration of this W-53° sample, failure via tangential creep was observed after an equivalent total life extension of 724-times over the unreinforced control. However, this creep failure was brought about by a localised failure of the braid, Figure 6.20, resulting in a small region expanding 21% tangentially while adjacent regions of the liner strained 1.9% tangentially. In addition to the pre-existing braid defects discussed in Section 6.5.1, it is theorized that this localised break may be related to thermal cycling and the formation of a brittle intermetallic layer, discussed further in Section 6.5.4.

Figure 6.20. *Break in braid at point of rupture. The braid itself has not crept, and failure is the result of tensile overload at a pre-existing defect.*

It is conservative then to calculate mean effective strain rate from this maximum deformation, as it is measured from an isolated region where the braid has failed. 500 hours at 5 MPa followed by 67 hours at 7.9 MPa, providing an additional 10-times acceleration, is equivalent to a total 1172 hours at 5MPa. The 21% tangential expansion at the point of rupture and 0.26% overall longitudinal expansion over an equivalent of 1172 hours translates to a mean effective creep rate of 2.0×10^{-2} %/hour, 1,000-times times lower than the control test. Using strains recorded away from this anomalous region of localized creep, the mean effective creep rate is 2.0×10^{-3} %/hour, 10,000-times lower than the control test. This use of mean creep rate assumes linearity, seen in Chapter 5 to be an overestimate of the minimum creep rate by 80 ± 40% in the case of unreinforced pipes, and 55 ± 8% in the reinforced tests – with this reduction in the difference between $\dot{\varepsilon}_{min}$ and $\dot{\varepsilon}_{mean}$ attributed to an absence of tertiary creep in the reinforced tests which were stopped before failure.

The post-test braid angle was measured to be 54.4 ± 1.6° (compared to the initial braid angle of 52.6 ± 1.4°). This increase in braid angle suggests that, as

hypothesised in Chapters 4 and 5, the neutral angle is above 52.6° and creep deformation is the mechanism by which the reinforcement orients itself towards the neutral angle. A post-test braid angle of 54.4 ± 1.6° is consistent with the 54.7° neutral angle predicted both theoretically and empirically, suggesting that the behaviour of the high temperature 253MA/W system complies with the model derived in Chapter 4. From the $\dot{\varepsilon} - \theta$ explored in Chapter 5, it is predicted that zero creep occurred once the braid had shifted to θ_N, and the majority of this final recorded strain took place while the braid shifted to seek the neutral angle.

Upon removal of the W-53° braid to permit strain measurement of the liner, the embrittled tungsten braid broke apart. However, fragments of the braid remained embedded in the surface of the liner, apparently held in place by an intermetallic layer which had formed, Figure 6.21.

Figure 6.21. *Fragments of tungsten braid embedded in liner surface after W-53° test.*

Table 6.3 compares strain and overall life extension data for the unoptimized and optimized braid-reinforced cases against their respective control tests as well as the simple wrap-reinforcement case.

Table 6.3. *Results of hybrid pipe tests. Braid-reinforced results shown in grey columns, compared to simple wrap-reinforcement case.*

	Average control	Wrap – thick sheath (design 1)	Unoptimized tungsten braid (W-46°)	Control for W-53° test	Optimized tungsten braid (W-53°)
Calculated control life (hrs)	91	91	91	10	10
Measured life (hrs)	70	857[a]	765	1.62	567[b]
Life extension compared to control[c]	-	12.2x	10.9x	-	724x
Maximum tangential change (%)	53	-5.3	26	28	21
$\dot{\varepsilon}_t^{\,d}$ (%/hr)	0.74	-6.8x10^{-3}	3.5x10^{-2}	17	1.7x10^{-2}
Overall longitudinal change (%)	Unknown	4.6	-0.12	0.31	0.26
$\dot{\varepsilon}_z^{\,d}$ (%/hr)	Unknown	5.3x10^{-3}	-1.1x10^{-3}	0.19	2.2x10^{-4}
$\dot{\varepsilon}_{eff}^{\,d}$ (%/hr)	Unknown	7.15x10^{-3}	4.0x10^{-2}	20.1	2.0x10^{-3}
Mode of failure	Tangential creep	Test ended before failure.	Braid failure - localised creep.	Tangential creep	Braid failure – localised creep. No bulk deformation after 309-times life extension.

[a] test ended by power outage before rupture.

[b] 500 hours at 5 MPa, 67 hours at 7.9 MPa, equivalent to a total 1172 hours at 5 MPa.

[c] compared to measured control life when applicable.

[d] rates averaged over entire life of test.

After 500 hours, a breakdown of the furnace led to the optimized W-53° test being interrupted. This raises an interesting point which is of particular interest to industrial applications. When a single component of a system is strengthened dramatically, facilitating an increase in operating conditions, the weak link in the system often shifts and becomes the new limiting factor. In these 253MA/tungsten braid tests, it was seen that the testing apparatus itself was not fully equipped to deal with the conditions required to push the reinforced pipe to its full potential. Specifically, tripped circuit breakers and blown fuses were regular issues in the furnaces. Additionally, the pressure transducer was operating at its absolute upper limit, and was in danger of rupturing a diaphragm.

In the event that operating temperature is increased and/or service life is extended by an order of magnitude, a gas-fired reformer furnace would not necessarily need to contend with blown fuses or overloaded pressure transducers. However, there are plenty of other components in a complex reformer system which are in danger of failure if temperature is increased and expected service life is extended. The implications of the increased reformer tube life on the overall reforming plant performance will be explored further in Chapter 7.

6.5.3 Microstructural analysis

As well as investigating for signs of creep void formation in the W-53° reinforced sample, microstructural analysis allows for behaviour of the 253MA to be compared in the unreinforced and reinforced cases. That is, the effect the presence of the reinforcement has on factors such as carbide formation can be examined.

Figure 6.22 shows 253MA in the as-received condition, polished to a 0.06 μm finish and etched with Kalling's No. 2 reagent.

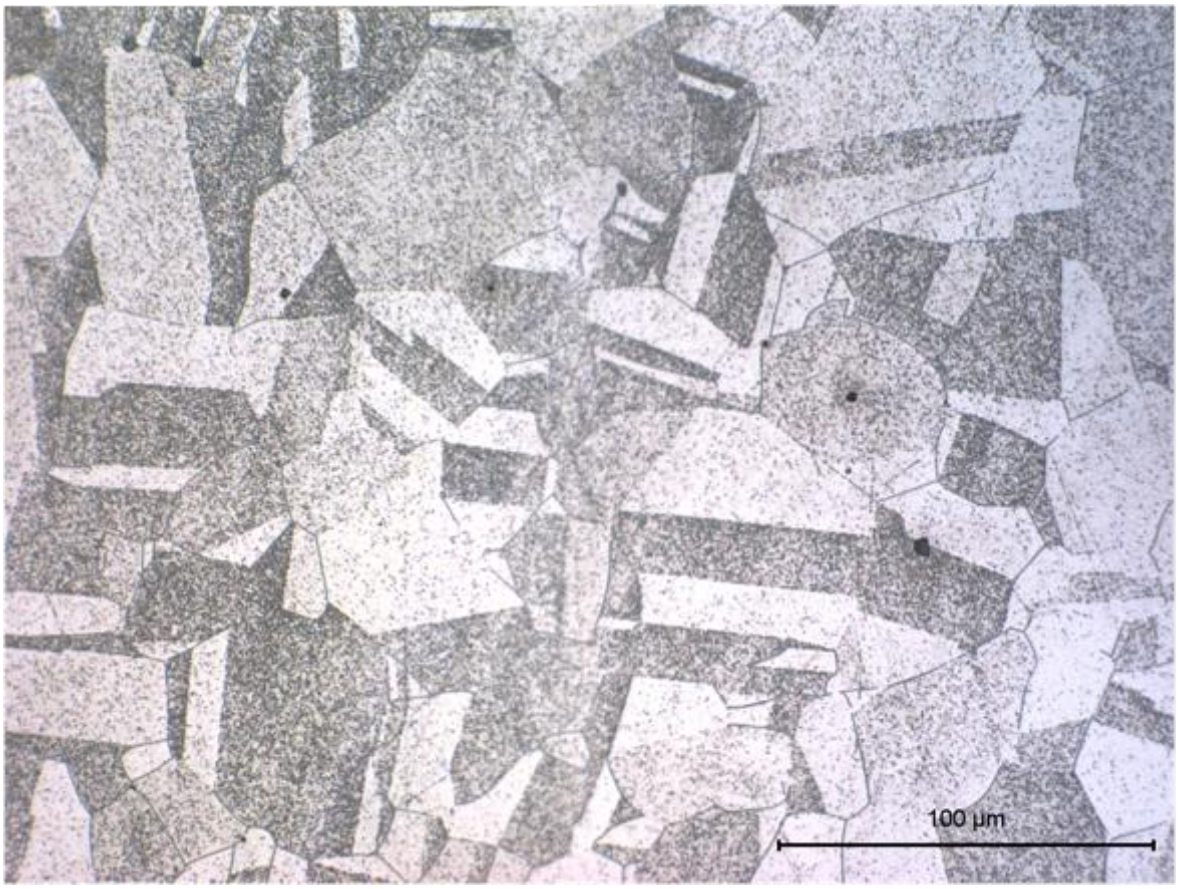

Figure 6.22. *253MA in as-received condition, etched with Kalling's No. 2 reagent.*

253MA typically has an ASTM grain size of 3-6 (45-127 µm) in the as-received condition [5]. The Kalling's No. 2 etch in Figure 6.22 reveals considerable twinning and an average grain size of approximately 48 µm, with a standard deviation of 15 µm in the grain size measurement.

In an investigation of the microstructural evolution of 253MA after ageing for 1000 hours at 500-900°C, Dhooge et al. [6] observed coarse precipitation of $Cr_{23}C_6$ and sigma-phase on grain boundaries, with fine precipitates found throughout the matrix.

A metallographic sample from the 253MA control test, exposed to 1040°C for 1.6 hours, was etched with glyceregia. Clearly visible carbides were observed along

grain boundaries, Figures 6.23-6.25. Additionally, these micrographs show creep voids aligned in the circumferential direction, predominantly formed on grain boundaries. The typical grain size in the control sample post-test was measured to be approximately 32 ± 10 μm.

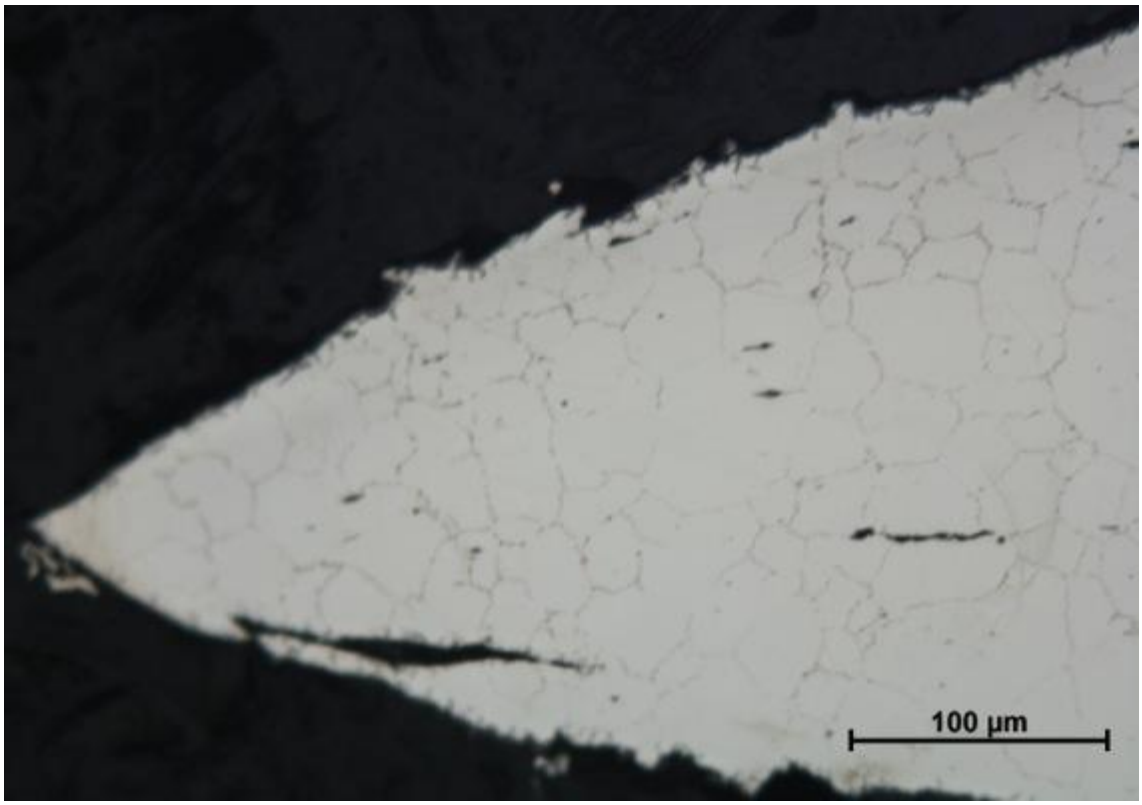

Figure 6.23. *Creep void formation in unreinforced control sample, etched with glyceregia. Material tip on left is necking at the point of rupture.*

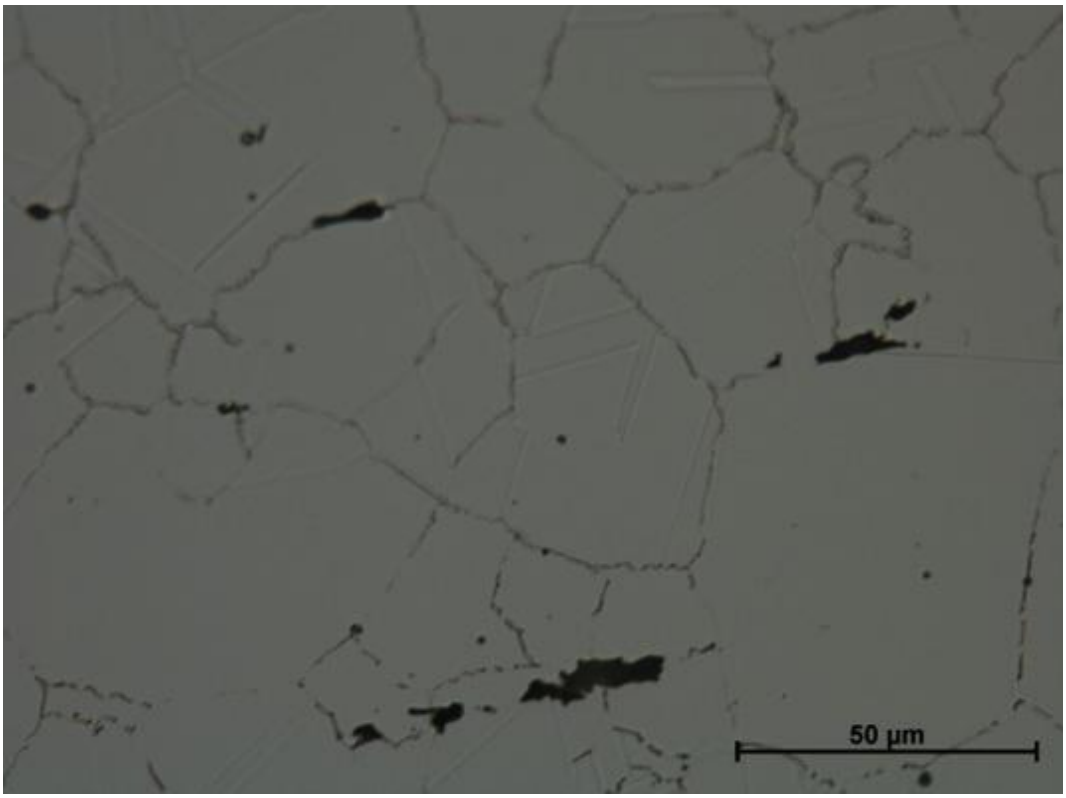

Figure 6.24. *Creep void and carbide formation in unreinforced control sample, etched with glyceregia.*

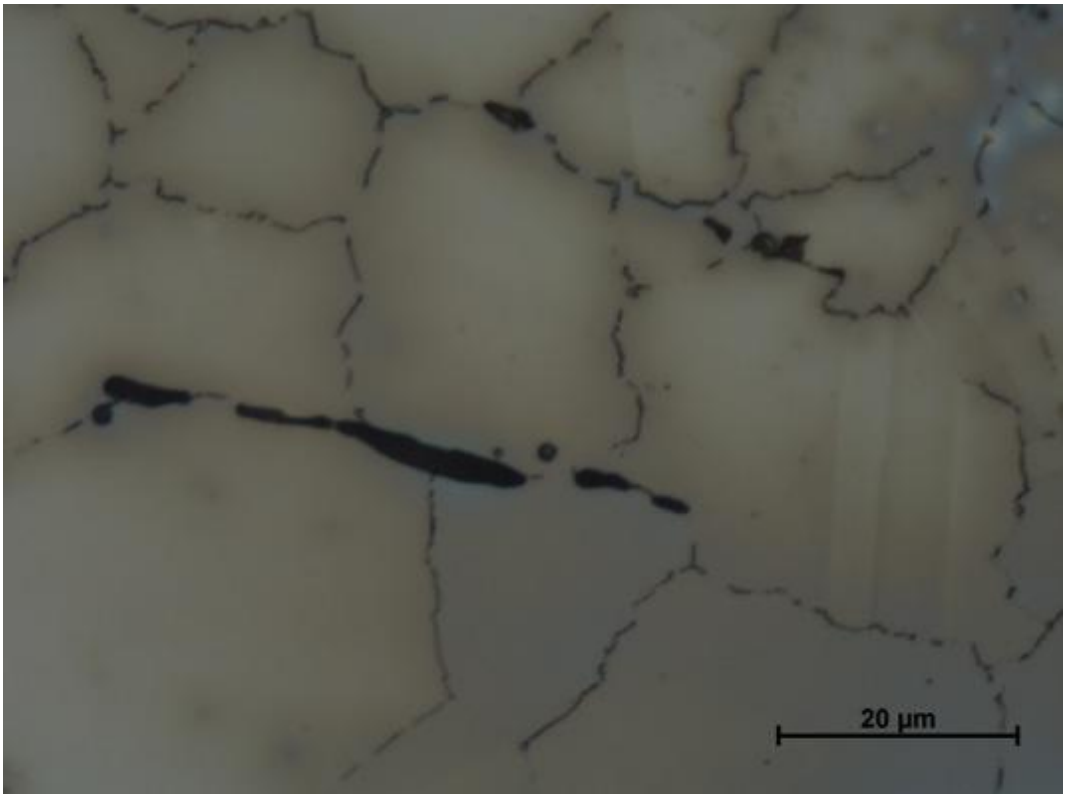

Figure 6.25. *Large, aligned creep voids on grain boundaries in unreinforced control sample, etched with glyceregia.*

A metallographic sample from the W-53° (optimized tungsten braid) test, exposed to 1040°C for 570 hours, was etched with glyceregia. This section was cut away from the anomalous point of rupture where the braid failed, but chosen such that an embedded fragment of tungsten wire was present, Figure 6.26.

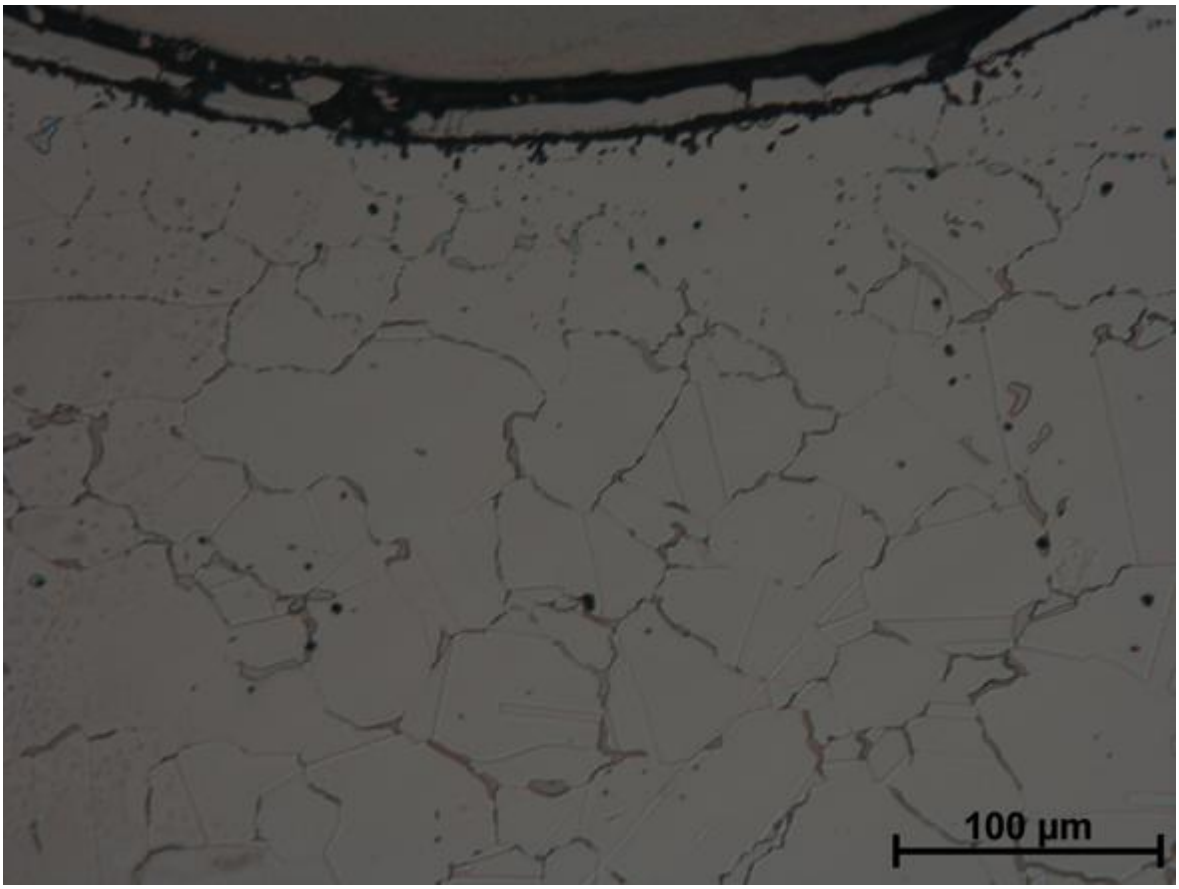

Figure 6.26. *W-53° sample. Tungsten wire, top, 253MA liner, bottom, with intermetallic layer in between.*

As observed by Dhooge et al. [6] for 253MA aged for 1000 hours at 500-900°C, coarse $Cr_{23}C_6$ precipitates are present on grain boundaries, with fine precipitates throughout the matrix. In the sampled region of the W-53° test piece, no visible creep voids were observed. This is consistent with the measured 2.7% effective strain at the liner away from the point of rupture.

6.5.4 Secondary damage mechanisms

In these accelerated tests, creep and damage to the reinforcement layer presented themselves as issues of primary concern. However, damage mechanisms which were less prevalent in accelerated testing may become more problematic when given a longer timescale in which to operate. Consideration of these long-term effects is particularly relevant for industry applications, and will be discussed in more detail in Section 7.3.

Oxidation of the 253MA sheath pipes was superficial after 570 hours at 1040°C. This was largely expected, as 253MA is specified as having excellent oxidation resistance up to 1100°C. However, oxidation still requires a great deal of consideration, particularly given the potentially catastrophic consequences of exposing the tungsten reinforcement to an oxidising environment. Other forms of environmental attack, such as carburization, may also be present in the industry context.

Recalling Section 3.6.2, a particular strength of the hybrid tube geometry is the avoidance of liquid metal interaction which leads to traditional wire-matrix diffusion. Despite diffusion over a mechanical interface being a largely unexplored field, observations in the present study led to the theory that contact stresses at the liner-reinforcement interface may be sufficient for an intermetallic layer to form. Figures 6.27-6.30 document intermetallic formation at the interface between the 253MA liner and the W-53° braid reinforcement layer after 570 hours at 1040°C.

In the W-53° test, the intermetallic layer formed was sufficiently large and coherent that small pieces of tungsten braid were left bonded to the surface of the liner. This intermetallic layer was further investigated at 20keV using a JEOL

7000F field emission scanning electron microscope (SEM) equipped with a JEOL JED-2300 EDS detector, Figures 6.27-6.30.

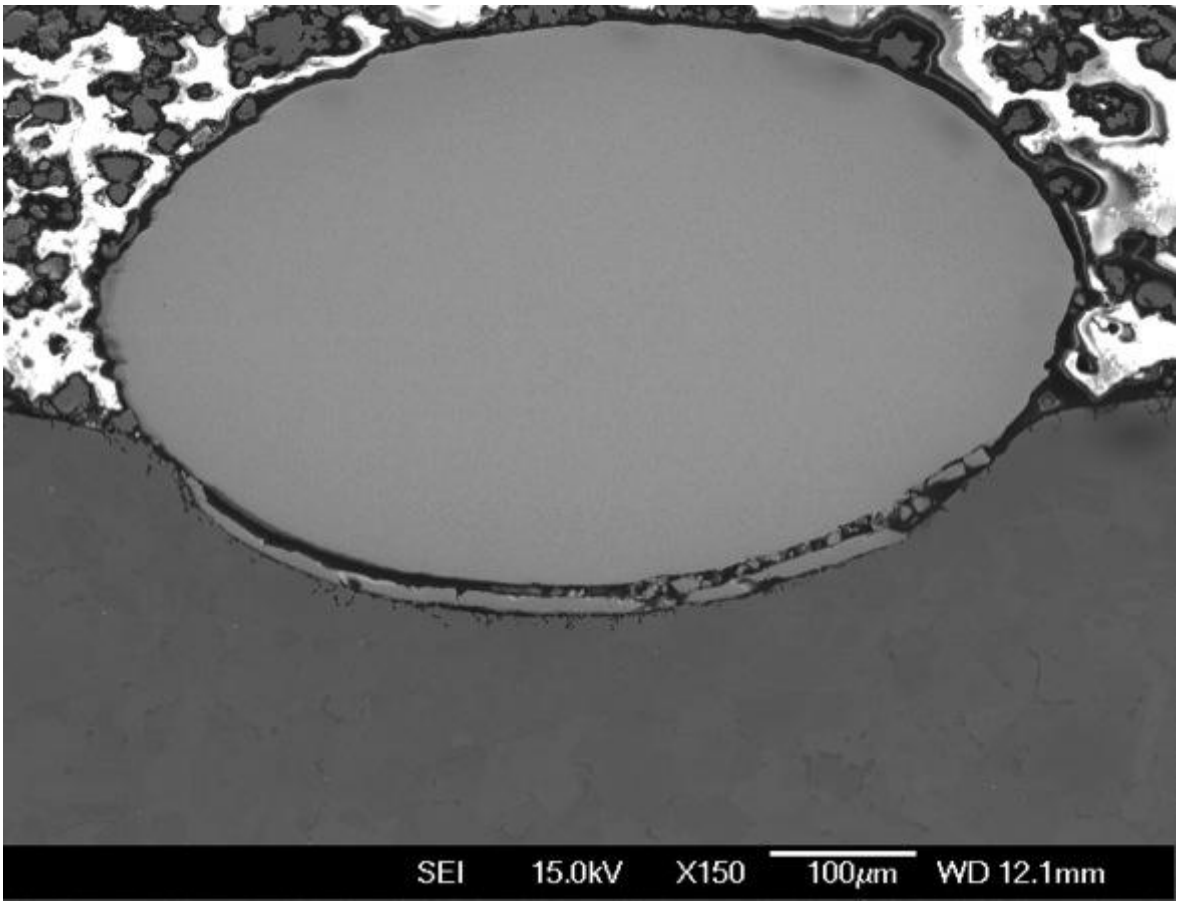

Figure 6.27. *W-53° sample. Section of wire bonded to outer surface of liner by intermetallic phase, formed over 570 hours at 1040°C.*

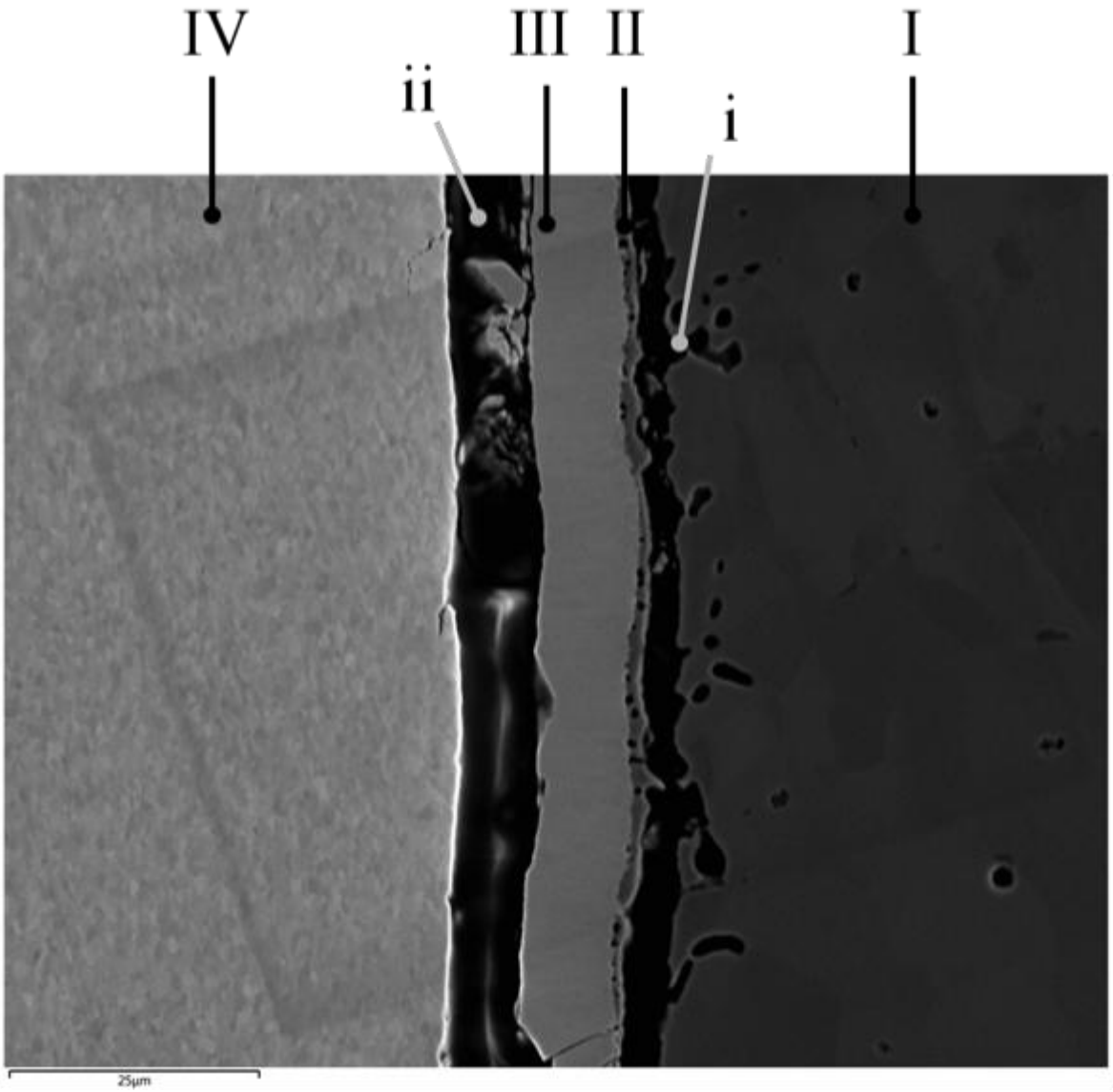

Figure 6.28. *W-53° sample. High magnification image of intermetallic phase between embedded tungsten wire and 253MA liner, formed over 570 hours at 1040°C.*

As well as leaving an indentation on the surface on the order of 135 µm, approximately one-third the original wire diameter, there is a clear multi-layered intermetallic which has formed between the reinforcement and liner. From Figure 6.28, two distinct intermetallic phases can be seen in between the base metal layer (I) and embedded wire (IV). Energy dispersive x-ray spectroscopy (EDS) is utilized to produce compositional maps, Figures 6.29 and 6.30, to clarify the transition between phases as well as characterizing the size and composition of these intermetallic layers formed over 570 hours at 1040°C.

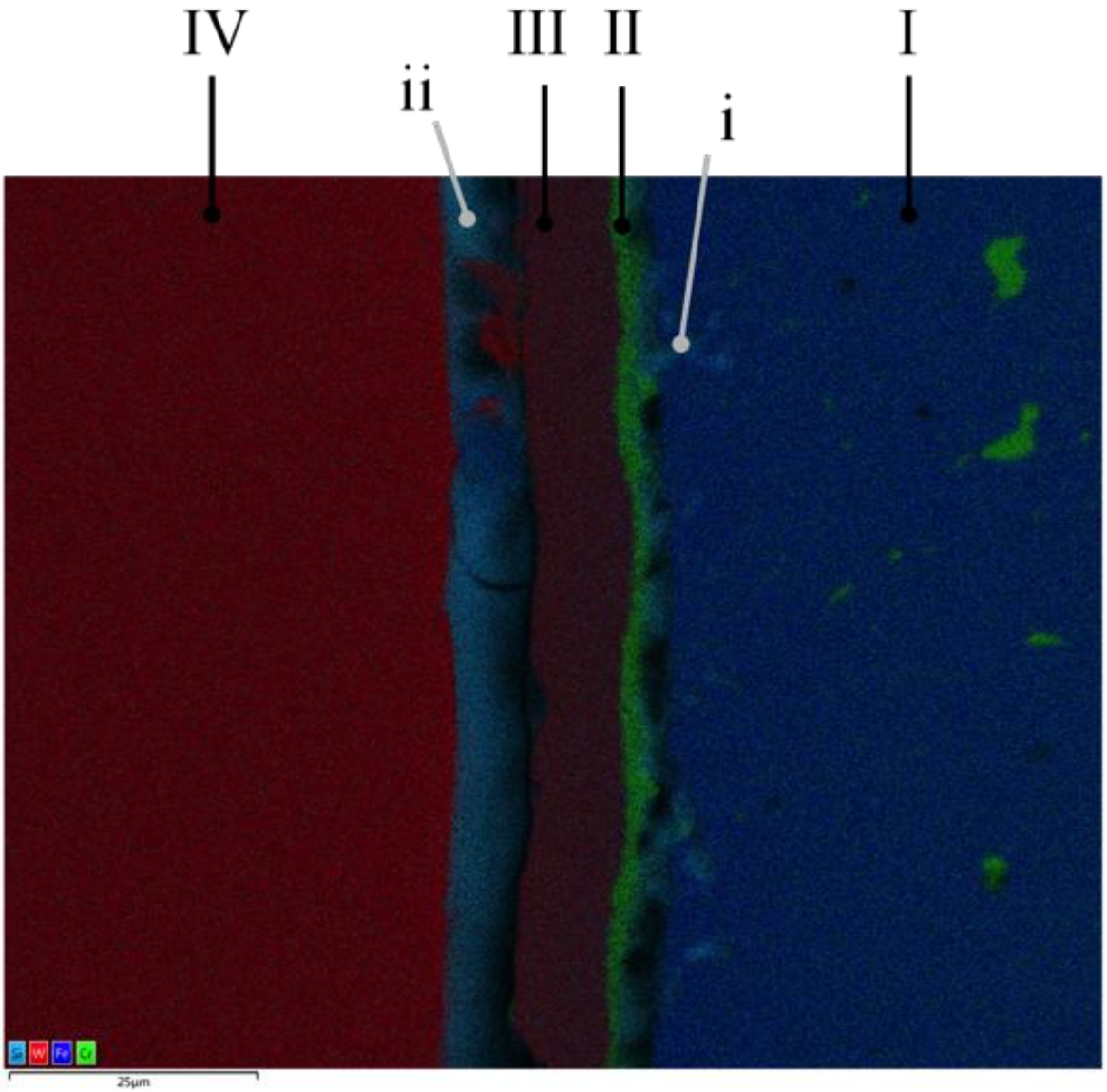

Figure 6.29. *W-53° sample. EDS map overlay of intermetallics formed at outer surface of liner after 570 hours at 1040°C. Major constituents coloured: tungsten (red), silicon (cyan), iron (blue) and chromium (green).*

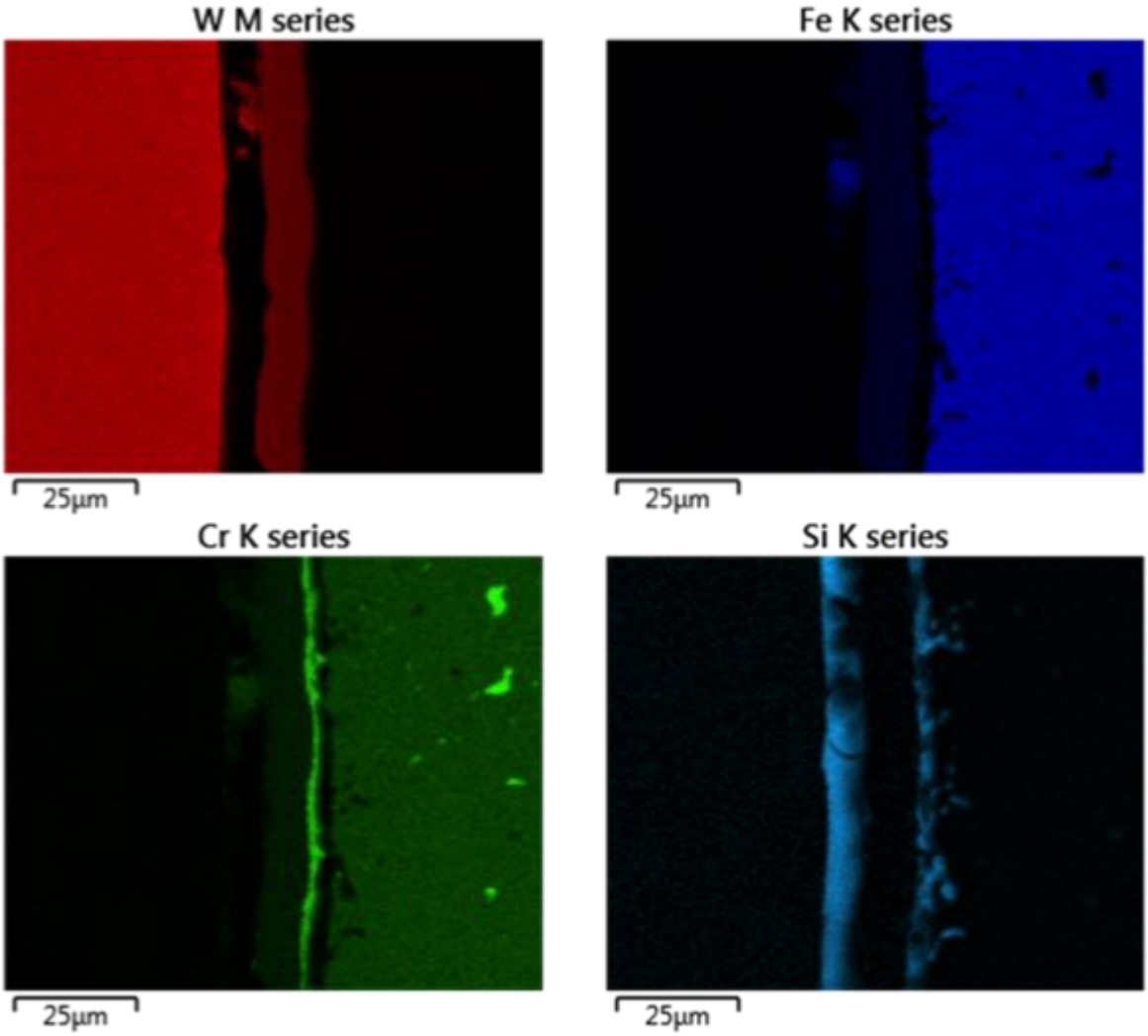

Figure 6.30. *Individual maps for major constituents overlaid in Figure 6.29.*

Figure 6.29 reveals two additional regions, labelled *i* and *ii*, which have the appearance of being empty space in the micrographs shown in Figure 6.27 and Figure 6.28. These spaces are presumed to have formed during cooling of the sample, where the difference in thermal expansion coefficients caused the tungsten to pull away from the 253MA liner. The silicon-rich reading in region *ii* is attributed to the voids collecting silicon during the sample preparation process. While region *i* also consists of some empty space resulting from the thermal expansion mismatch, the presence of silicon oxides is expected in regions of the 253MA matrix where Cr has been depleted. This internal oxidation phenomenon

is discussed further in the analysis of phases formed at the inner surface of the pipe, Figures 6.31 and 6.32.

Compositional information from EDS utilised in conjunction with crystallographic information from indexed EBSPs was used to identify the intermetallic phases which formed between the base metal and tungsten wire, Table 6.4. The EDS mapping technique used to produce Figures 6.29 and 6.30 gave nominal compositional information for each phase. From these nominal compositions, phase diagrams could then be used to identify a pool of candidate phases [7]. As performed by Buchanan et al [8, 9], indexing of phases was carried out using Pearson's Handbook [10] to obtain crystallographic parameters for candidate phases and examining the sample at 20 keV using a JEOL JSM 6100 SEM equipped with the Oxford eXL EDS system and HKL Technology electron backscatter diffraction (EBSD) system. EBSD patterns (or EBSPs) were recorded in spot mode and indexed in three locations in each of the phases labelled I-IV in Figure 6.29.

Table 6.4. *Characterization of intermetallic phases formed at liner-reinforcement interface after 570 hours at 1040°C.*

	Nominal Composition[a] (at %)	**Phase**	**Approximate Layer Thickness (μm)**
I	67%Fe, 21%Cr, 12%Ni	253MA base metal	-
II	59%Cr, 7.5%W, 14%Fe, 19.5%C	CrW	2
III	33%W, 48%Fe, 20%Cr	Fe_7W_6	10
IV	76%W, 24%C	W	-

[a] atomic percentages determined via EDS.

Neglecting the silicon rich 'phases', the intermetallic between W wire and 253MA tube has two distinct layers – Fe_7W_6 and CrW, the combined thickness of which is on the order of 12 μm. Depending on the space between the wire and outer surface of the Fe_7W_6 layer, and how damaged that layer has been by the cooling process,

Figure 6.29 and Figure 6.30 show the tungsten diffused 12-20 μm into the surface of the 253MA. Kumar [11] observed that interfacial phases in both W-316 stainless steel and W-HP alloy composites are isostructural with M_7W_6.

While the growth of these intermetallic layers had no significant effect on the tungsten reinforcement's ability to restrict the hybrid tube from creeping in the present study, long-term exposure to service conditions may lead to the embrittlement or complete dissolution of the reinforcement layer, as investigated by Kumar [11] for tungsten-reinforced austenitic stainless steel matrices.

As alluded to in Section 6.5.2, it is theorized that the formation of these brittle intermetallic phases may in part be responsible for the localised failure of the W-53° braid. Recall that this sample was tested in two stages, with a period of cooldown in between. Although the braid failure has clearly taken place in a small, localized region, it is also notable that the braid provided a significant life extension over the first stage of testing. The delay in the onset of failure suggests a potential gradual weakening of the braid. The formation of a brittle intermetallic bonded the reinforcement to the liner surface, as evidenced by Figure 6.27. This was followed by the cooling of the sample, which involves the 253MA liner contracting on the order of four times more than the tungsten reinforcement layer, Table 6.2. The resultant thermal contraction stresses, coupled with the intermetallic bond formed between reinforcement and liner may very well have resulted in damage to the braid in addition to the pre-existing defects. As thermal cycling is an unavoidable aspect of real-world reformer furnace operation and maintenance, it is important to consider its potential impact on reinforcement integrity.

Figure 6.29 also reveals the presence of a chromium-rich phase in the 253MA matrix. As seen in Figure 6.26, these are the $Cr_{23}C_6$ precipitates which have formed

on grain boundaries, with fine precipitates throughout the matrix. This is an expected effect of ageing 253MA [6]. Figures 6.31 and 6.32 show these chromium carbides in more detail, with larger precipitates clearly forming on grain boundaries.

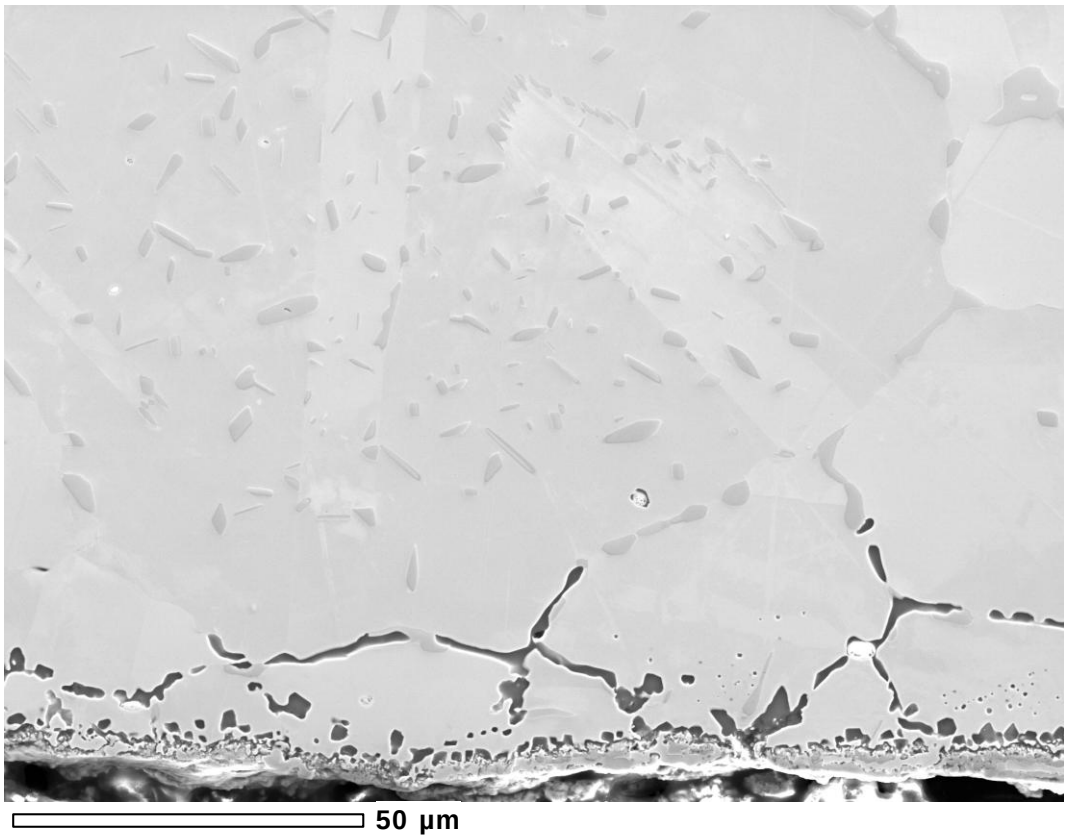

Figure 6.31. *W-53° sample. SEM micrograph of chromium carbide formation at inner wall.*

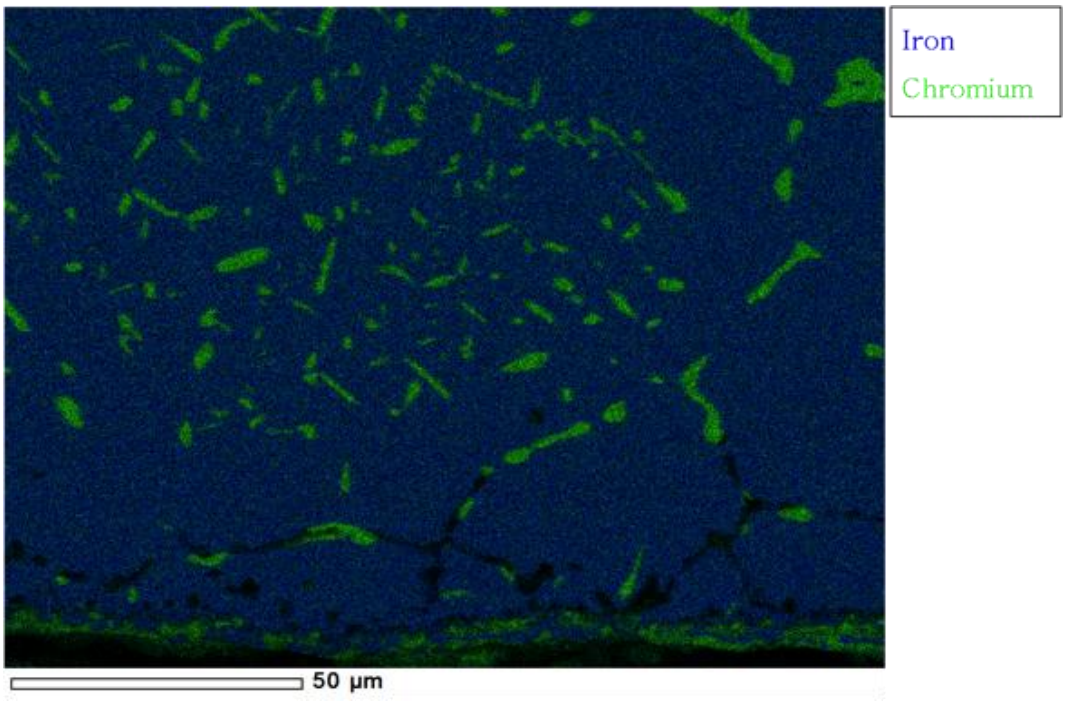

Figure 6.32. *W-53° sample. EDS map of chromium carbide formation at inner wall over 570 hours at 1040°C. Major constituents coloured: iron (blue) and chromium (green).*

As detailed in Section 3.6.3, chromium oxide is a principal scale phase formed for oxidation protection. The 3-6 µm thick chromium-rich layer at the inner-most surface of the pipe was identified as Cr_2O_3. The dark regions in Figures 6.31 and 6.32, predominantly along grain boundaries and beneath the Cr_2O_3 scale on the inner surface, were identified as being rich in silicon. As a result of the chromium oxide layer being formed, chromium is depleted from the adjacent matrix. Silicon oxides tend to form in 253MA following the depletion of chromium from the matrix via a process known as internal oxidation [12], creating the dark region observed immediately underneath the Cr_2O_3 layer in Figures 6.31 and 6.32. Sustaining the protective outer scale leads to the exhaustion of chromium from the matrix and dissolution of the chromium carbides, as seen over the 12-25 µm layer nearest to the inner surface of the pipe, Figures 6.31 and 6.32. Silicon oxides then tend to form preferentially along the grain boundaries in place of these chromium carbides [12].

In the process of considering long-term effects in an industry context, Section 7.3 discusses potential methods of mitigating this risk of embrittlement or dissolution of the reinforcement, including the use of a coating/stable intermetallic layer to act as a diffusion barrier.

6.6 Conclusions

An order of magnitude life extension was observed in the unoptimized (W-46°) test. At the time of rupture, bulk deformation was minimal and snaking due to non-uniform longitudinal creep was negligible. This result shows potential for the future of using braided reinforcement in this high temperature application, and in creep-limited industry applications first outlined in Chapter 1. Failure was attributed to the formation of a localised creep blister in a region where defects and breakages in the braid were sufficiently large for a section of the liner to creep.

With braided reinforcement as close as practicable to the empirical optimum orientation of 54.7 ± 1.5°, the W-53° sample exhibited a 724-times life extension over its control. After 500 hours (309-times life extension), bulk deformation was negligible. As well as being due to the optimization of the reinforcement, this observation is largely attributed to the avoidance of large defects in the braid, and keeping defects as far as possible from the hot zone in the furnace. Ultimately, failure was observed due to localised creep at a region where the braid had failed, possibly exacerbated by cooling the sample after phase one before ramping back up to phase two at a higher pressure. Final strain readings for this W-53° test gave a mean effective creep rate 10,000-times lower than was recorded for the control test.

The post-test braid angle was measured to be 54.4 ± 1.6° after 570 hours (compared to the initial braid angle of 52.6 ± 1.4°). This increase in braid angle confirms that the neutral angle is indeed higher than 52.6° and is consistent with a predicted neutral angle of 54.7°, suggesting that the behaviour of the high temperature 253MA/W system complies with the empirical model derived in Chapter 4 for a model system of brass and stainless steel.

Despite the considerable self weight of the 253MA tube, and the horizontal sample orientation, no snaking was observed. Therefore, it can be concluded that braided reinforcement architecture is an effective means of controlling the non-uniform longitudinal snaking phenomenon observed in the wrap-reinforced samples.

It was discovered that diffusion over the mechanical liner-reinforcement interface is possible, with intermetallic layers of Fe_7W_6 and CrW observed to form at the interface. Tungsten was observed to have diffused 12-20 μm into the surface of the liner after 570 hours at 1040°C.

CHAPTER REFERENCES

[1] M. V. Kral and C. K. H. Dharan, "Improved Tubes For High Temperature Industrial Application And Methods For Producing Same," US provisional patent application no. 61/157011, 2009.

[2] RA 253MA Data Sheet, http://content.rolledalloys.com/technical-resources/databooks/RA-253-MA_DB_US_EN.pdf, [Accessed 2011].

[3] G. F. Vander Voort, G. M. Lucas, and E. P. Manilova, "Metallography and Microstructures of Stainless Steels and Maraging Steels," in *ASM Metals HandBook, Volume 9: Metallography and Microstructures*, ed, 1991.

[4] F. Windhösel, 38x7x0.4 Data Sheet, (personal communication with B. Reyngoud, November 29th, 2013)

[5] HAYNES HR-120 Alloy, http://www.haynesintl.com/pdf/h3125.pdf, [Accessed 2014].

[6] A. Dhooge, W. Hoek, W. Provost, and M. Steen, "High Temperature Behaviour of the Austenitic Stainless Steel ASTM UNS S30815 (253 MA) and Weldments.," *ACOM,* vol. 4, pp. 1-16, 1985.

[7] H. Okamoto, "Nickel - Tungsten Phase Diagram," in *ASM Metals HandBook, Volume 3: Alloy Phase Diagrams*, ed, 1991.

[8] K. G. Buchanan and M. V. Kral, "Crystallography and Morphology of Niobium Carbide in As-Cast HP-Niobium Reformer Tubes," *Metallurgical and Materials Transactions A,* vol. 43A, pp. 1760-1769, 2012.

[9] K. G. Buchanan, M. V. Kral, and C. M. Bishop, "Crystallography and Morphology of MC Carbides in Niobium-Titanium Modified As-Cast HP Alloys," *Metallurgical and Materials Transactions A,* vol. 45A, pp. 3373-3385, 2014.

[10] P. Villars and L. D. Calvert, *Pearson's Handbook of Crystallographic Data for Intermetallic Phases*, 2nd ed. Materials Park, OH: ASM International, 1991.

[11] P. Kumar, "Studies of wire/matrix interactions in some tungsten wire reinforced stainless steels," PhD, Mechanical Engineering, University of Canterbury, 2014.

[12] F. A. Jones, "The Effect of a High-Temperature High-Pressure Nitrogen Environment with Carbonaceous Impurities on the Performance of Three Austenitic Alloys," Master of Engineering, Department of Mechanical Engineering, University of Canterbury, 2007.

CHAPTER 7: IMPLICATIONS FOR INDUSTRY

A life extension on the order of 720-times effectively halts creep as a primary mode of failure. However, in order to be truly relevant and useful to the 'real world', it is important to shift away from an academic standpoint and consider what hurdles there are between these accelerated tests and successful implementation in industry. Furthermore, it must be asked if this result adequately meets the needs of the steam reforming industry, Methanex in particular.

7.1 Balance Between Life and Temperature

As alluded to in Section 2.2, when reformer furnace operating conditions were outlined, the limited availability of resources, and the finite life of other components, means that it is not necessarily ideal to seek to increase creep life indefinitely. These methane reformer plants are not intended to be in operation for hundreds of years, yet alone the tens of thousands of years a 720-times creep life extension would give. Rather than a total focus on life extension, a balance between increased operating temperature and a more moderate life increase would be preferable.

In a modern reformer furnace configuration, the maximum possible operating temperature is limited to approximately 1050°C by components downstream of the reformer which are exposed to flue gases at the outlet. As a typical Methanex reformer furnace currently operates at 930-950°C, accounting for expected thermal losses in the system still leaves room for a temperature gain on the order of 50°C, if materials within the furnace were to permit such an increase. As outlined in

Section 1.2, this 50°C operational temperature increase at a single plant would translate to approximately NZ$1.25 million per year in increased revenue due to improved process efficiencies.

From the Rolled Alloys 253MA data sheet [1], average stresses to cause rupture in 1,000, 10,000 and 100,000 hrs are shown in Figure 7.1, with trends extrapolated to give points for 10 and 100 hour rupture times. Linear interpolation was used to predict behaviour at 950°C and 1000°C, and power trend lines were fitted to generate stress-rupture life relationships of $\sigma = 76.084t^{-0.222}$ for T = 950°C and $\sigma = 49.164t^{-0.208}$ for T = 1000°C.

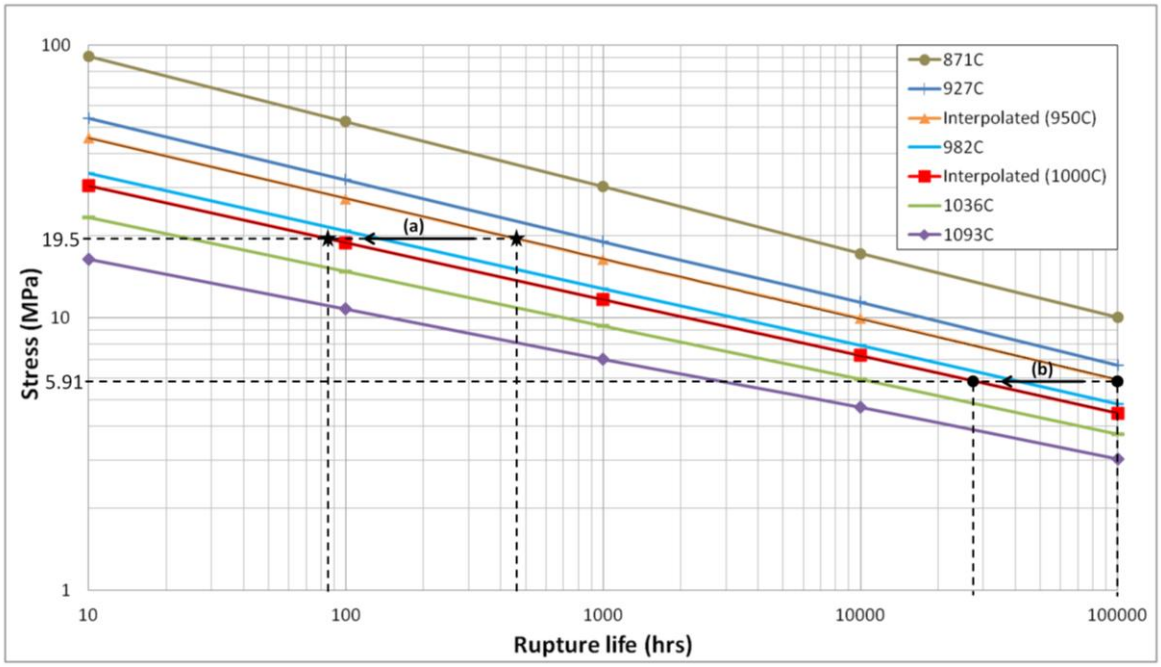

Figure 7.1. *Effect of 50°C temperature increase on 253MA creep rupture life when under typical reformer furnace conditions. Case (a) – matching stress and temperature conditions. Case (b) – matching life and temperature conditions.*

In case (a) highlighted on Figure 7.1, under operating conditions typical to a reformer furnace (950°C, 19.5 MPa), a 460.6 hour creep life is calculated for

253MA. At this stress state, increasing the temperature to 1000°C results in creep life reducing to 85.3 hours (18.5% of original life).

In case (b) shown in Figure 7.1, stress is set such that there is a 100,000 rupture life at 950°C (σ = 5.91 MPa), reflective of the typical design life of a HP-alloy reformer tube, rather than the stress state as was considered in case (a). From this 100,000 hour rupture life, increasing temperature to 1000°C results in creep life reducing to 26,500 hours (26.5% of original life).

Therefore, for 253MA operating in the 950-1000°C range, a 50°C temperature increase results in a reduction of creep rupture life by a factor of approximately 4-5. Without comprehensive creep rupture data for HP-alloy, it should be noted that these projections cannot reliably be directly applied to the reformer furnace case. There is also a base assumption that these calculations hold in the case of a hybrid pipe if temperature were to be raised by 50°C.

Thus it can be deduced that rather than a life extension in excess of 700-times, as seen in current hybrid pipe tests, a life extension on the order of 140-times coupled with a 50°C operating temperature increase may be achievable. A 140-times life extension would still be viewed as excessive for the industry application, presenting an opportunity for material thicknesses to be reduced, thereby saving mass (and cost) at the expense of increased stresses. This reduction in material cost, coupled with a balance of an extension in life and an increased operating temperature, is well suited to the requirements of the petrochemical industry.

7.2 Critical Flaw Size

From failure analysis of the unoptimized tungsten braid, Figure 6.16 revealed that an elliptical gap in the reinforcement, approximately 13x7.5 mm, led to highly localized creep which resulted in the rupture of the liner. While a single case makes it difficult to draw conclusions with any degree of certainty, let 7.5 mm be defined as the critical flaw size. That is, regular empty spaces between yarns (strands of wires in the braid) should be less than 7.5 mm to help mitigate the risk of localized creep deformation resulting in rupture of the liner.

For a typical tungsten braid construction of 48 yarns, each made up of 12 individual ø0.4 mm wires, optimized to give a braid angle of 54.7° when on a typical ø133 mm reformer tube, Windhösel estimates that a regular gap size of 7.5 mm corresponds to a braid coverage of approximately 72%. To avoid the potential for localized creep deformation, it is recommended that a minimum braid coverage of 80% be specified. Additionally, spot checks should be performed to confirm that unreinforced spaces in the braid are no larger than 5x5 mm (applying a safety factor of 1.5 to the critical flaw size).

7.3 Long-Term Effects in Reformer Application

Given long-term exposure to elevated temperature and pressure, evolution of the reformer tube microstructure is inevitable. As such, special considerations should be made before applying the findings of the accelerated tests back into industry. These tests were specifically designed to accelerate the effects of creep, and may fail to adequately capture slower-acting phenomenon.

Evidence of tungsten diffusing at 12-20 μm into the liner surface over 570 hours at 1040°C, despite no permanent bond at the interface is potentially problematic, and diffusion over mechanical interfaces remains a largely unexplored field. Continued growth of these interfacial intermetallics may lead to the embrittlement or complete dissolution of the reinforcement layer.

In Section 3.6.2, it was shown that all superalloy-based matrices have a tendency to react with tungsten wire reinforcement at high temperatures (1000°C to 1200°C) [2, 3]. Nickel-based composites are particularly prone to wire-matrix interaction. This Ni/W based compound in the interfacial region is unstable at high temperature and decomposes to W and Ni solid solutions at around 1050°C, causing deterioration in the high temperature properties of the composite [4]. This interaction may cause dissolution of the wire, accelerated recrystallization, and embrittlement due to its reaction with the matrix.

Iron-based matrices are reported to have shown the least interaction with tungsten wires [5]. The solubility of tungsten is much lower in iron than in nickel at 1000°C, and the Fe_7W_6 formed can be stable up to 1640°C [6]. The work of Kumar [7] suggests that a Fe/Ni ratio of < 0.5 is required in the matrix material to suppress the formation of a tungsten intermetallic phase at the matrix-reinforcement interface. This knowledge may be used to formulate a diffusion barrier between the reinforcement and liner pipe layers in the hybrid geometry, Figure 7.2.

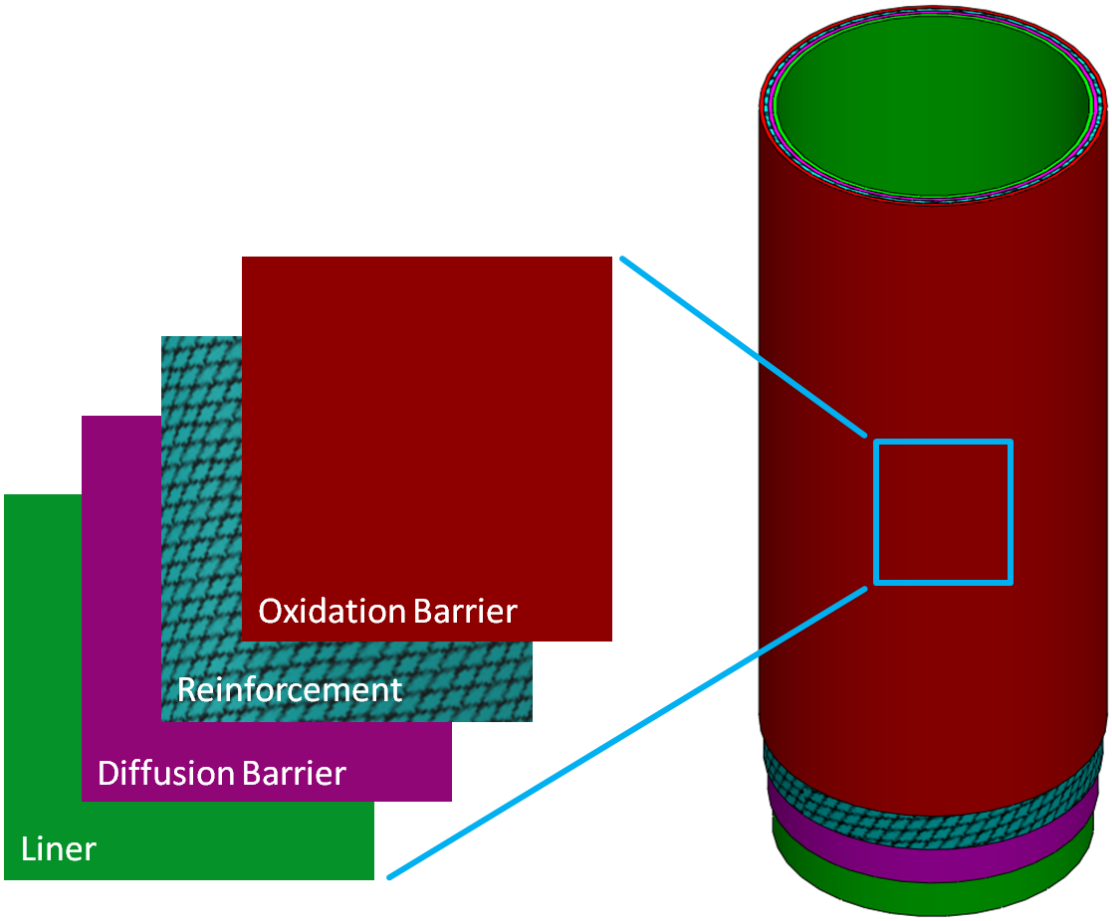

Figure 7.2. *Hybrid pipe schematic with diffusion barrier.*

Another attractive solution to this diffusion problem is to coat or plate the tungsten wire prior to braiding. Nickel electroplating is well established, commercially available process which is commonly applied for corrosion resistance. However, this would produce a new nickel-tungsten interface which would be prone to the formation of brittle intermetallics and the dissolution of the tungsten reinforcement. Alternatively, it may be possible to coextrude the tungsten wire with a secondary metal which has low solubility in tungsten, Figure 7.3.

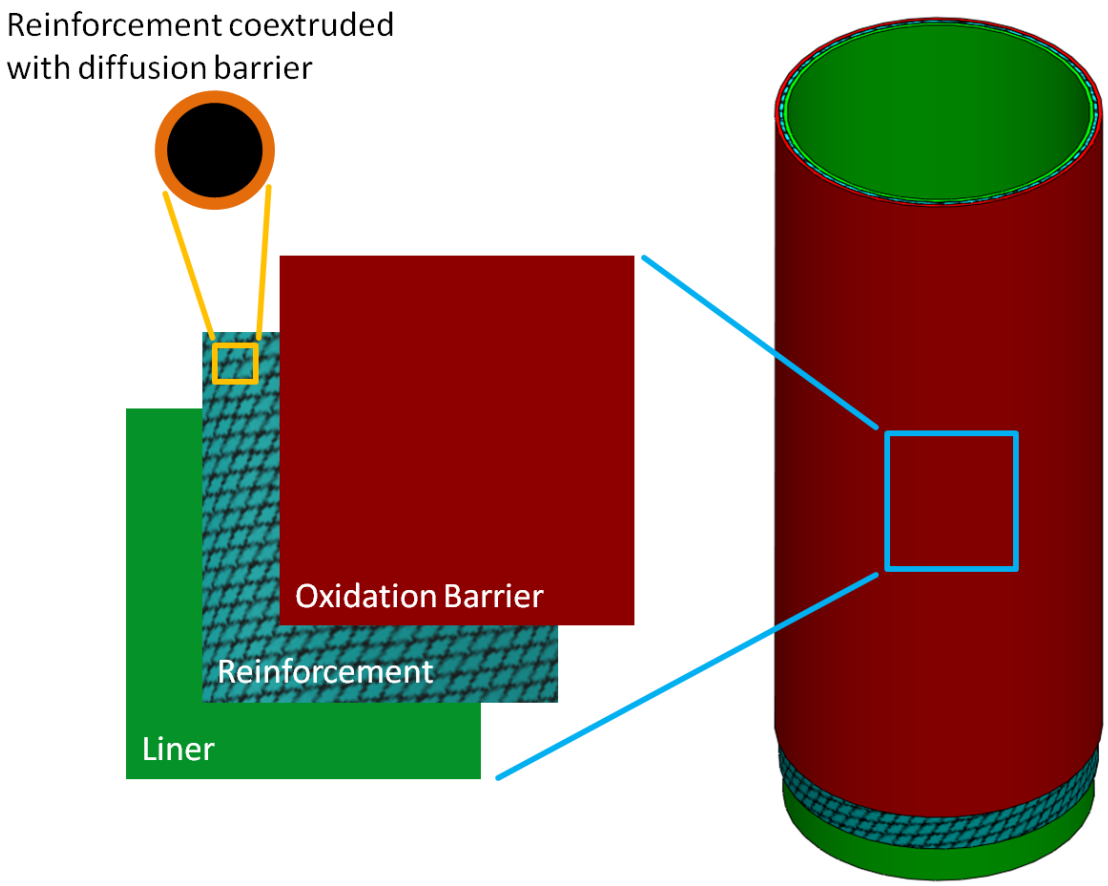

Figure 7.3. *Hybrid pipe schematic with coextruded reinforcement.*

Copper is a particularly good candidate for this extruded oxidation barrier due to its high ductility and relatively low cost. Molybdenum may also be coextruded with tungsten wire, and has the added benefit of being a refractory metal with excellent creep properties, in addition to its low solubility in tungsten.

This concept of coating the wires with a diffusion barrier has the added benefit of potentially serving as protection from environmental attack, rendering the sheath pipe redundant. However, one must be aware of the inherent risks associated with removing the sheath pipe in favour of a wire coating. As was seen in Section 6.2.2, thinning down of the sheath resulted in dramatic snaking in the design 2 test. This was attributed to there being less material away from the neutral axis to resist bending. Chapter 5 has shown that more uniform temperature distribution, and

vertical sample orientation, helps to negate the snaking issue. However, this may not be the case in industry, where large thermal gradients are commonly observed in the reformer furnace.

7.4 Additional Stresses in Reformer Application

In Section 2.3.1, the stress state of a typical reformer tube was considered. This analysis showed that the significant self weight of the tube, when oriented vertically, increases σ_z from approximately 8 MPa to 9 MPa. However, this analysis assumed thick-walled pressure vessel behaviour. In Section 4.2.4, the brass/stainless steel hybrid system was shown to behave as a thin-walled pressure vessel despite not meeting the $t/r_i < 0.05$ criterion. As designed, the stress-bearing component of the hybrid pipe is the reinforcement layer and the pipe effectively acts as a shell which transmits load to the reinforcement.

However, there may be cases where changes to geometry or loading conditions alter the optimal reinforcement orientation. From the theoretical neutral angle derivation in Section 3.3.1, it can be seen that θ_N is essentially:

$$\theta_N = tan^{-1}\left(\sqrt{\frac{\sigma_t}{\sigma_z}}\right) \tag{7.1}$$

Using Lamé's equations for stresses in a thick-walled pressure vessel, the nominal reformer tube geometry gives a tangential/longitudinal stress ratio of 2–2.44, depending on the variation of σ_t through the wall thickness. This gives a theoretical neutral angle of 54.7–57.4°.

Accounting for maximum self weight, the tangential/longitudinal stress ratio drops to 1.78–2.17, giving a neutral angle of 53.1–55.8°. That is, the presence of the

considerable self weight of the reformer tube decreases the theoretical optimal braid angle by approximately 1.5°. This observation holds for the case of a thin-walled pressure vessel under the same degree of self weight.

It is not uncommon for reformer tubes to be suspended by counterweights, with the tubes left free at the bottom to expand longitudinally. There is potential for a counterweight system such as this to be manipulated such that net longitudinal stress is reduced. This reduction in longitudinal stress would increase the optimal braid angle, and allow the reinforcement to be focused primarily on controlling creep in the tangential direction. Additionally, reducing net longitudinal stress minimizes the risk of snaking when exposed to the non-uniform thermal gradients of a reformer furnace.

In some industrial applications with particularly low internal pressure, resultant stresses may be primarily the result of self weight. It is known that in an ethylene cracking furnace, creep of pyrolysis tubes is driven primarily by self weight. Using nominal tube dimensions of an 80 mm outer diameter, 8 mm wall thickness and a 20 m length, as well as a typical internal pressure of 0.5 MPa [8] gives pressure stresses of σ_t = 1.8-2.3 MPa and σ_z = 0.9 MPa as well as a maximum longitudinal self weight stress of σ_{sw} = 1.5 MPa. Superimposing longitudinal stresses gives a tangential/longitudinal stress ratio of 0.74-0.95, with a corresponding neutral angle of 41-44°.

7.5 Thermal Conductivity

Ultimately, these hybrid tubes are intended for use in a reformer furnace application, where they exist to facilitate an endothermic reaction. This reaction is driven by heat generated in the furnace, effectively making the core role of the

reformer tubes to transfer heat from the furnace to the gasses inside the tube. Therefore, thermal conductivity of the hybrid should be assessed.

By introducing a thermal bridge, it is possible to assess how overall thermal resistivity is affected by the bridge surface area, Figure 7.4. That is, the width of the thermal bridge (x) is varied to control how much heat, Q, is transferred through the bridges and how much goes through the 'air + tungsten' section (L-x). Subsequent resistivity calculations are based upon currently used design materials and layer thicknesses, although these parameters are intended only for testing, and may be altered before implementation in the reformer furnace.

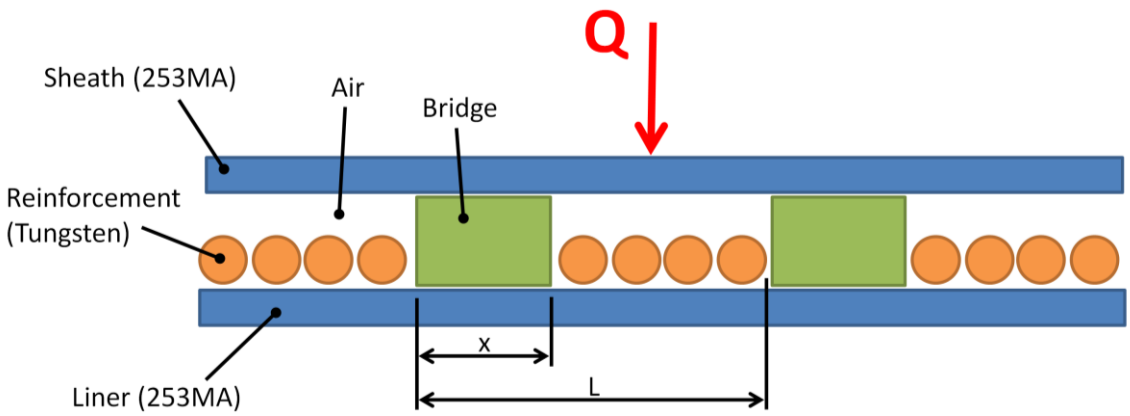

Figure 7.4. *Hybrid tube layer schematic, with thermal bridges.*

To aid in the resistivity analysis, consider the schematic shown in Figure 7.4 as a system of (thermal) resistors in series and parallel, Figure 7.5.

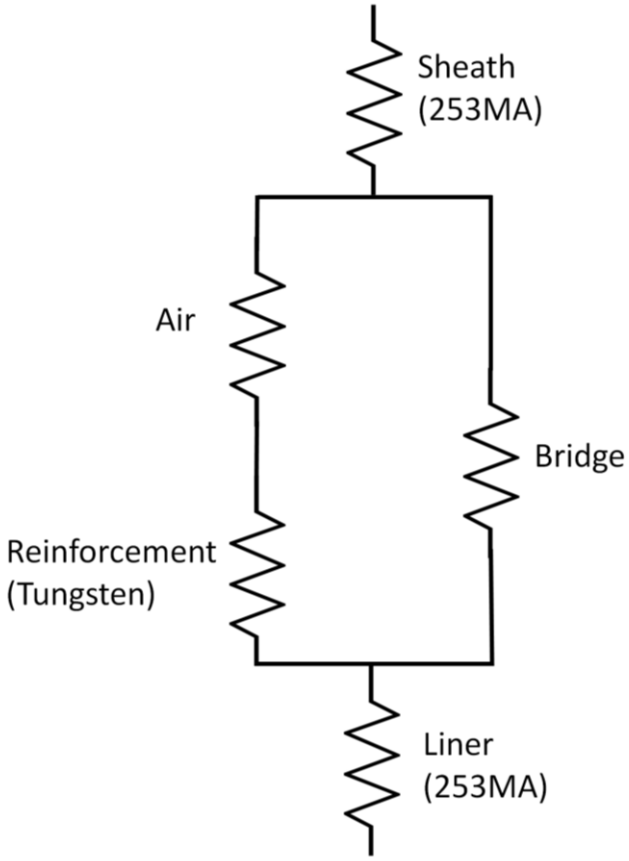

Figure 7.5. *Thermal resistor diagram for hybrid tube layer.*

Total resistivity, R_{Tot}, is calculated as:

$$R_{Tot} = R_{sheath} + \left(\frac{1}{R_{air}+R_{reinf}} + \frac{1}{R_{bridge}}\right)^{-1} + R_{liner} \tag{7.2}$$

$$R_{Tot} = \frac{t_{sheath}}{k_{sheath}} + \left[\frac{1}{\left(\frac{t_{air}}{k_{air}(1-f)} + \frac{1}{h_{air,rad}(1-f)} + \frac{t_{reinf}}{k_{reinf}(1-f)}\right)} + \frac{1}{\left(\frac{t_{bridge}}{k_{bridge}(f)}\right)}\right]^{-1} + \frac{t_{liner}}{k_{liner}} \tag{7.3}$$

Where subscripts denote components in the hybrid, t is the layer thickness, k is component conductivity, h is the radiation heat transfer coefficient, and $f = x/L$ is the length fraction of the liner surface occupied by the bridge.

Note that convective heat transfer is assumed to be zero in the enclosed volume between the sheath and liner layers, with only conductive and radiative terms considered. Exceptions to Equation 7.3 are applied when $f = 1$ and $f = 0$ (to avoid dividing by zero). i.e. when $f = 1$, the reinforcement and air terms are removed completely as the entire surface is bridged.

The bridge material was varied in a sensitivity analysis, with low and high conductivity materials trialled (253MA and tungsten, respectively). Thermal conductivity values, sourced from [9-11], are given in Table 7.1 alongside layer thicknesses and the radiation heat transfer coefficient, h_{rad}.

For a surface of area A, temperature T_S, and emissivity ε, radiative heat flux, q_{rad}, is defined by [12] as:

$$q_{rad} = \sigma \varepsilon A(T_S^4 - T_\infty^4) \tag{7.4}$$

$$q_{rad} = h_{rad} A(T_S - T_\infty) \tag{7.5}$$

Where σ is the Stefan-Boltzmann constant (5.67×10^{-8} W/m^{2}K^4), and T_∞ is the surrounding temperature. Assuming black-body radiation, ε = 1. A typical reformer furnace operates at approximately T_∞ = 950°C (1223K). The surface temperature of the outside of the liner, T_S, is estimated to be 900°C (1173K). Defining mean temperature as $\bar{T} = (T_S + T_\infty)/2$, and equating Equations 7.4 and 7.5, gives:

$$h_{rad} = 4\sigma\varepsilon\bar{T}^3 \tag{7.6}$$

$$= 4 * 5.67\text{x}10^{-8} * 1 * (1198)^3$$

$$= 390 \ \frac{W}{m^2 K}$$

Table 7.1. *Thermal properties used for hybrid tube heat transfer calculation.*

Component	Material	Thickness, t (m)	Conductivity, k (W/mK)	Radiation heat transfer coefficient, h_{rad} (W/m^2K)
Sheath	253MA	3.95E-3	29	-
Air gap	Air	1.48E-3	0.052	390
Reinforcement	Tungsten	4.50E-4	113	-
Bridge 1	253MA	1.93E-3	29	-
Liner	253MA	1.49E-3	29	-
Bridge 2	Tungsten	1.93E-3	113	-

Taking the values summarized in Table 7.1, Equation 7.3 can be used to determine overall hybrid resistivity for varying values of *f*, Figure 7.6.

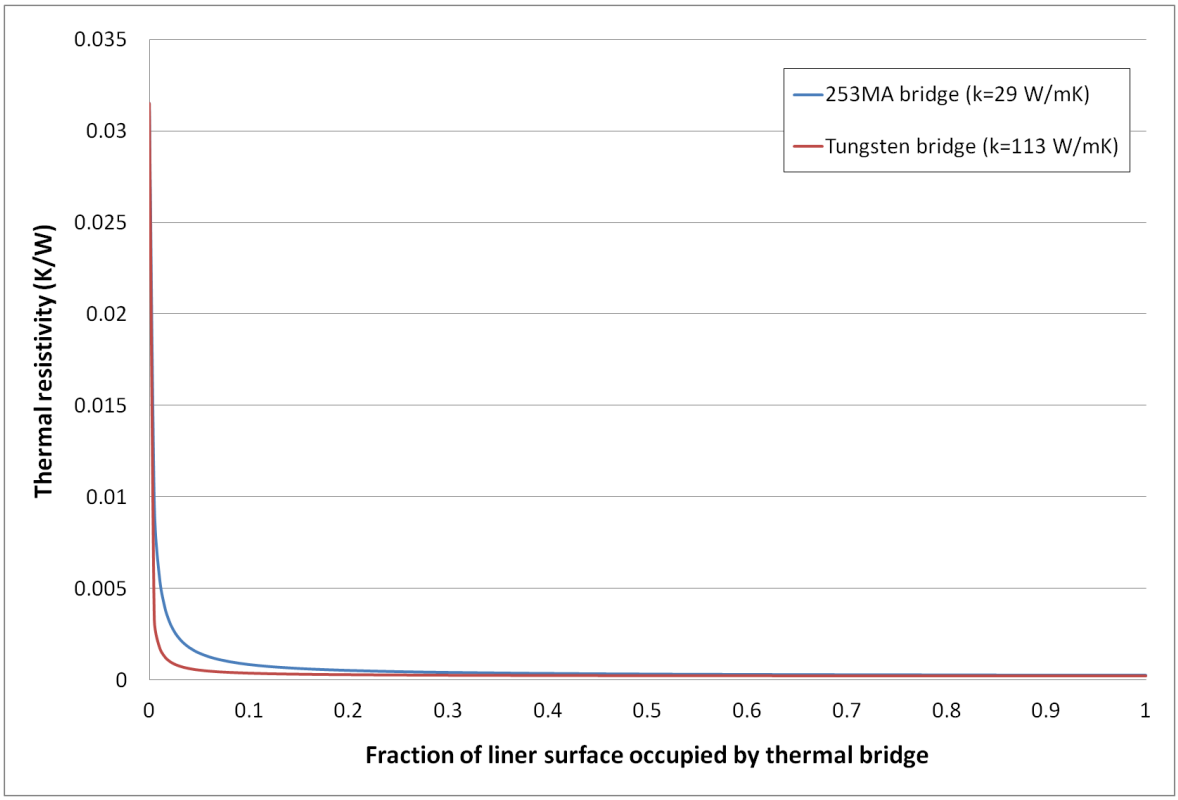

Figure 7.6. *Effect of thermal bridge on total resistivity of pipe hybrid.*

From Table 7.1, it can be seen that the air gap itself makes up the majority of overall resistivity (lowest conductivity), and Figure 7.6 reveals that any alternative path of lesser resistance immediately has a dramatic effect. Even with the less conductive 253MA bridge, bridging 2.5% of the surface results in a 92% drop in thermal resistivity.

However, Figure 7.6 reveals that there are rapidly diminishing returns, and the mere presence of some form of bridge is more important than the thermal conductivity of the bridging material. Tungsten is impractical as a bridging material, as differences in thermal expansion coefficients mean that maintaining physical contact with inner and outer layers would be very difficult (as 253MA expands approximately four times more than tungsten, Table 3.4). Additionally, the effect of thermal bridges on the overall hybrid creep response must be considered, as there would be no creep reinforcement in these areas, and bridges are also likely to create hot spots.

7.6 Comparison with Existing Technology

While relatively simple and well standardised, the Ashby creep performance index method outlined in Section 3.1.2 is difficult to apply in practice. This is particularly true for recently developed materials, where manufacturers are interested in protecting intellectual property rather than publishing materials constants and activation energies.

Instead, the hybrid pipe technology can be compared against the historical performance of reformer tube materials, introduced in Figure 2.8, by considering a 100,000 hour stress rupture plot, Figure 7.7 [13]. Note that data for these reformer tube materials has been extrapolated for temperatures above 1000°C, as indicted

by dashed lines. A 300-times life extension was observed in 253MA at 1040°C without rupture, and a total life extension on the order of 700-times was recorded at rupture. From Section 6.4.2, it is known that the stress-rupture relationship for 253MA at 1040°C is governed by $\sigma = 36.132 t_r^{-0.198}$. This equation suggests that in the *unreinforced* case, a 700-times life extension can be achieved by reducing stress by a factor of 3.7. Therefore, it can be deduced that the 700-times minimum life extension created by the presence of the reinforcement is equivalent to maintaining a 100,000 hour life and instead increasing permissible stress by a factor of 3.7, as long as the material does not yield.

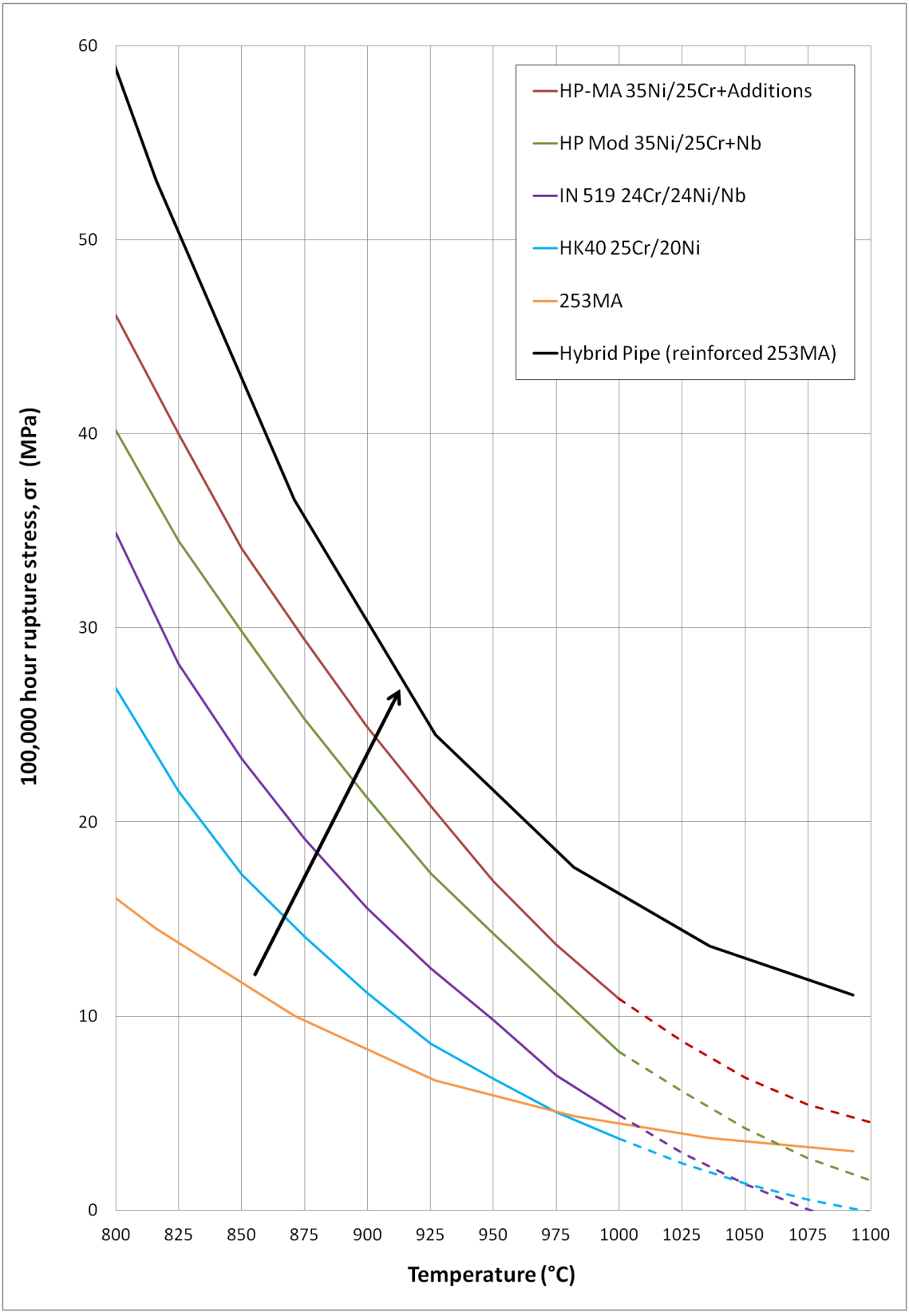

Figure 7.7. *Stress-rupture plot for 100,000 hour tube lifetimes for various reformer tube materials. Adapted from Beyer et al. [13] to include 253MA with and without reinforcement.*

This increase in permissible stress facilitates a reduction in tube wall thickness, thereby increasing catalyst volume and plant capacity. For example, to maintain operating conditions and a 100,000 hour life, a 14 mm thick reformer tube made out of HP-MA would need a wall thickness of 17 mm if made out of HP Mod, or over 30 mm if made out of HK-40 [13].

Using typical reformer tube dimensions of 120 mm OD and a 10 mm wall thickness, and an internal pressure of 3.5 MPa, increasing permissible stress by a factor of 3.7 allows the nominal wall thickness to be reduced to 2.9 mm, translating to a potential 70% reduction in tube mass. Based on the observed increase in 253MA rupture stress brought about by the presence of a braided reinforcement layer, Figure 7.7 suggests that even greater rupture stresses are achievable if the braided reinforcement is applied to a modern alloy developed specifically for use in reformer furnaces, such as HP Mod or HP-MA.

7.7 Conclusions

Premature braid failure was attributed to the formation of a localised creep blister in a region where defects and breakages in the braid were sufficiently large for a section of the liner to creep. To avoid the potential for localized creep deformation, it is recommended that a minimum braid coverage of 80% be specified. Additionally, spot checks should be performed to confirm that unreinforced spaces in the braid are no larger than 5x5 mm (applying a safety factor of 1.5 to the critical flaw size).

It was discovered that diffusion over the mechanical liner-reinforcement interface is possible, with intermetallic layers of Fe_7W_6 and CrW observed to form at the interface. Tungsten was observed to have diffused 12-20 μm into the surface of the

liner after 570 hours at 1040°C. While the growth of these intermetallic layers had no significant effect on the tungsten reinforcement's ability to restrict the hybrid tube from creeping, long-term exposure to service conditions may lead to the embrittlement or complete dissolution of the reinforcement layer, as investigated by Kumar [7] for tungsten-reinforced austenitic stainless steel matrices.

For 253MA operating in the 950-1000°C range, a 50°C temperature increase results in a reduction of creep rupture life by a factor of approximately 4-5. Therefore, it can be deduced that rather than a life extension in excess of 700-times, as seen in current hybrid pipe tests, a life extension on the order of 140-times coupled with a 50°C operating temperature increase may be achievable. This 140-times life extension presents an opportunity for material thicknesses to be reduced, thereby saving mass (and cost) at the expense of increased stresses. This reduction in material cost, coupled with a balance of an extension in life and an increased operating temperature, is well suited to the requirements of industry partners.

Based on the reduction in stress associated with a 700-times extension in life, it is projected that the hybrid pipe technology allows for this life extension to be traded off for a potential 70% reduction in liner tube mass.

Using nominal reformer tube dimensions to account for maximum self weight, the tangential/longitudinal stress ratio drops to 1.78–2.17, giving a neutral angle of 53.1–55.8°. That is, the presence of the considerable self weight of the reformer tube decreases the theoretical optimal braid angle by approximately 1.5°. Based on the empirical model generated in Chapter 4, this result suggests an optimal angle of approximately 53.2° when reformer self weight is considered. For low pressure systems such as ethylene cracking furnaces, where creep is primarily driven by self weight, an optimal braid angle of less than 45° is predicted.

Bridging 2.5% of the surface between the sheath and liner pipes results in a 92% drop in thermal resistivity, largely independent of the thermal conductivity of the bridging material. The air gap between the reinforcement and sheath layers makes up the majority of overall resistivity, and any alternative path of lesser resistance immediately has a dramatic effect, with bridging to 2.5% of the surface resulting in a 92% drop in thermal resistivity. However, returns diminish rapidly, and the mere presence of some form of bridge is more important than the thermal conductivity of the bridging material.

CHAPTER REFERENCES

[1] RA 253MA Data Sheet, http://content.rolledalloys.com/technical-resources/databooks/RA-253-MA_DB_US_EN.pdf, [Accessed 2011].

[2] T. Caulfield and J. Tien, "High Temperature Reaction Zone Growth in Tungsten Fiber Reinforced Superalloy Composites: Part I. Application of the Movig Boundary Equations," *Metallurgical and Materials Transactions A,* vol. 20, pp. 255-266, 1989.

[3] J. Tien, T. Caulfield, and Y. Wu, "High Temperature Reaction Zone Growth in Tungsten Fiber Reinforced Superalloy Composites: Part II. Matrix Chemistry Effects," *Metallurgical and Materials Transactions A,* vol. 20, pp. 26-272, 1989.

[4] K. E. Poulsen, S. Rabaek, and E. W. Langer, *Scripta Met,* vol. 8, pp. 267-272, 1984.

[5] R. Warren, L. O. Larsson, and C. H. Andersson, "Fibre/matrix Interactions in a Tungsten Alloy Wire-Reinforced Stainless Steel Composite," *Composites,* vol. 10, pp. 121-125, 1979.

[6] H. Baker, *ASM Handbook, Vol.3: Alloy Phase Diagrams*. Ohio: ASM International, 1992.

[7] P. Kumar, "Studies of wire/matrix interactions in some tungsten wire reinforced stainless steels," PhD, Mechanical Engineering, University of Canterbury, 2014.

[8] H. Zimmermann and R. Walzi, *Ullmann's Encyclopedia of Industrial Chemistry, Ethylene*: John Wiley and Sons, Inc, 2009.

[9] EngineeringToolbox. Air Properties, http://www.engineeringtoolbox.com/air-properties-d_156.html, [Accessed August 5th 2014].

[10] MatWeb. Tungsten, http://www.matweb.com/search/DataSheet.aspx?MatGUID=41e0851d2f3c417ba69ea0188fa570e3&ckck=1, [Accessed August 2nd 2014].

[11] MatWeb. Outokumpu 253MA® High Temperature Austenitic Stainless Steel, http://www.matweb.com/search/DataSheet.aspx?MatGUID=cde513f9b216440a8578764db8dada30, [Accessed August 2nd 2014].

[12] A. Faghri, Y. Zhang, and J. Howell, *Advanced Heat and Mass Transfer*. Columbia, MO: Global Digital Press, 2010.

[13] F. Beyer, J. Brightling, P. Farnell, and C. Foster, "Steam Reforming - 50 years of Development, and Challenges for the Next 50 years.", Uhde GmbH, Johnson Matthey Catalysts, 2005.

CHAPTER 8: SUMMARY AND CONCLUDING REMARKS

This chapter provides a summary of the main achievements of this research, and reflects on the initial objectives outlined in Chapter 1. Contributions this work has made to the broader field of materials intended for use in high temperature environments and the study of creep reinforcement are detailed. Future work is outlined, and consideration is given to the steps required for this hybrid pipe technology to be utilized in the steam reforming industry.

8.1 Summary of Achievements

The preceding chapters draw a number of significant conclusions. In light of the initial research objectives, a select few of the most significant findings made in this research are detailed below.

8.1.1 Multiaxial strain measurement

Three pressurized pipe creep testing rigs were developed for high and low temperature testing, with apparatus gradually developed to incorporate in-situ longitudinal strain measurement and an IFL to improve temperature uniformity. These rigs facilitated the multiaxial creep strain measurement of samples under a complex stress state. This study into the interrelatedness of creep in tangential and longitudinal directions concluded that:

- Restricting tangential creep with helically wound reinforcement leads to the acceleration of longitudinal creep such that the failure mode shifts from longitudinal to circumferential cracking.

- Creep strains in both the tangential and longitudinal directions can be manipulated by exploiting the anisotropic nature of a braided reinforcement layer, particularly the coupling between its behaviour in the longitudinal and tangential directions.

8.1.2 Reinforcement architecture

Reinforcement structure-property relationships were investigated, with the significance of specific architectural features assessed in light of creep performance. An experimental means of measuring the longitudinal stiffness of a braid was devised, and compared to a stiffness model produced using a modified version of classical lamination theory. It was concluded that:

- Reinforcement angle is the key parameter of reinforcement architecture.
- Stiffness is an indicator of the collective effort of multiple architectural features, including surface area coverage, wire diameter, number of yarns, packing fraction and wires per yarn.
- The longitudinal stiffness of a helical wrap is four orders of magnitude lower than that of a braid of comparable size.
- Although the braid is free from matrix material, the transverse stiffness, E_2, is non-zero due to internal friction related to the braid-braid contact area. Using a nonlinear least squares fit, this pseudo-matrix effect was quantified to give E_2 = 2.77 GPa.

8.1.3 Effective creep rate model

An empirical model was derived for the dependence of effective multiaxial creep rate on reinforcement angle. This empirical model, based on fitting trigonometric functions to experimental data, has a correlation coefficient of 0.976, and allowed for a number of important conclusions to be drawn:

- A braid angle of approximately 54.7 ± 1.5° is optimal to minimize the effective multiaxial creep rate of a hybrid pipe under internal pressure.

- A 2° deviation from the ideal braid angle leads to a 40-60x increase in the effective creep rate.
- In the brass-stainless steel system, orienting the reinforcement at 54.7° is projected to reduce creep rate to the point that it is negligible.

8.1.4 Change in braid angle

Using indents left in the surface of the pipe, post-test measurements of the braid angle were made. Additionally, in-situ longitudinal strain measurement allowed for change in creep rate to be tracked and related back to a predicted change in θ. Through this combination of experimental and analytical observations, it was concluded that:

- Creep deformation is the mechanism which allows θ shifts towards the neutral angle θ_N, but only for initial vales of $\theta < \theta_N$.
- In theory, $\dot{\theta}$ and $\dot{\varepsilon}$ are zero at θ_N (54.7°) due to force equilibrium being reached. In practice, reaching this point of equilibrium from an initial angle of 50° takes longer than 920 hours, and further testing is required to investigate the asymptotic behaviour of $\dot{\varepsilon} \rightarrow 0$ as $\theta \rightarrow \theta_N$.
- $\dot{\theta}$ is zero (and $\dot{\varepsilon}$ is constant but non-zero) for $\theta > \theta_N$. The inability for the braid to reduce its angle from $\theta > \theta_N$ is related to the contact condition between the liner and reinforcement layers which dictates that $\dot{\varepsilon}_t \geq 0$ i.e. the pipe cannot contract tangentially while the reinforcement is not bonded to its surface.
- In the high temperature tests, the tungsten braid angle was 52.6 ± 1.4° pre-test and 54.4 ± 1.6° after 570 hours, suggesting that the neutral angle for the high temperature system is consistent with the theoretical value of 54.7° for thin-walled pressure vessels. Additionally, the behaviour of the high temperature 253MA/W system appears to comply with the empirical model derived in Chapter 4 for a model brass/stainless steel system.

8.1.5 Effect of reinforcement

Through strain measurement as well as micro- and macro-scale investigation for signs of creep, it was possible to quantify the effect of the reinforcement layer in terms of life extension gain and the change in the stress state of the liner. A number of conclusions were drawn with regards to the effectiveness of using an architectured reinforcement for creep reduction:

- Through careful geometric application and design considerations, *overall* hybrid creep strength can be controlled by the creep strength of the refractory *reinforcement*.
- In the brass-stainless steel system, all braid-reinforced samples were ended after a 10-times life extension over the control. This also implies that even in an unoptimized state, braided reinforcement out-performs a simple helical wrap by at least 22%.
- Using braided reinforcement architecture, creep life extensions in excess of 10-times were observed without rupture, and a reduction in creep rate in excess of 45-times was measured (for the F-50° reinforcement architecture).
- In the high temperature 253MA-W system, a life extension in excess of 700-times is achievable through the use of braided reinforcement oriented at 53°, as close as practicable to the empirical optimal angle of 54.7°. After 500 hours (309-times life extension), bulk deformation was negligible.
- Upon further acceleration of this W-53° sample, failure via localised tangential creep expansion was observed at a region of failure in the braid after an equivalent life extension of 709-times over the unreinforced control.
- Tangential expansion at this localised failure was 21% and longitudinal expansion was 0.26%. This translates to a mean effective creep rate 1,000-times lower than the control test. Using the 2% tangential strain recorded away from this anomalous region of localized creep, the mean effective creep rate is 10,000-times lower than the control test.
- It was demonstrated that sheathing is an effective means of isolating the tungsten reinforcement from oxidation.

- For α-brass at 400°C, the mean creep rate approximation was shown to overestimate the minimum creep rate by 80 ± 40%, as observed in unreinforced samples which were tested to rupture and experienced tertiary creep. For reinforced tests ended before tertiary creep and rupture, the difference between the mean creep rate approximation and the minimum creep rate was on the order of 55 ± 8%, though this is a function of test duration.
- In the high temperature tests with a simple wrapped tungsten reinforcement architecture, longitudinal creep manifested as 'snaking' - a unique phenomenon driven by non-uniform creep due to hot spots in the furnace. This phenomenon was minimized by orienting samples vertically as well as utilising braided reinforcement architecture and an IFL to produce a more uniform temperature gradient.

8.1.6 Industry implications

Experimental observations were assessed in light of the targeted end-use in reformer furnaces. When considering the potential for longer exposure to lesser temperatures in service, a number of significant conclusions were drawn and practical recommendations were made:

- Over 570 hours at 1040°C, tungsten from the reinforcement diffused 12-20 μm into the surface of the 235MA liner, forming intermetallic layers of Fe_7W_6 and CrW at the interface.
- In the hybridized pipe, creep is no longer believed to be the primary mode of failure. For longer-term exposure at typical service conditions, environmental attack and intermetallic formation were identified as potential sources of failure. Particularly as this intermetallic formation is likely to result in embrittlement or complete dissolution of the reinforcement.

- Care must be taken to avoid large defects in the braid, with approximately 7.5x7.5 mm identified as the critical flaw size. A minimum surface area coverage of 80% is recommended.
- Rather than a life extension in excess of 700-times, a life extension on the order of 140-times coupled with a 50°C increase in operating temperature may be achievable. This 140-times life extension presents an opportunity for wall thickness to be reduced, thereby saving mass/cost and improving thermal conductivity as well as plant capacity.
- Based on the ratio of tangential to longitudinal stress, the considerable self weight of the reformer tube decreases the theoretical optimal braid angle by 1.5°. Based on the empirical model generated in Chapter 4, this result suggests an optimal angle of approximately 53.2° when reformer self weight is considered.
- In the case of unreinforced 253MA, a 700-times life extension can be achieved by reducing stress by a factor of 3.7. This implies that the 700-times minimum life extension created by the presence of the reinforcement is equivalent to maintaining a 100,000 hour life and increasing permissible stress by a factor of 3.7.
- Based on the reduction in stress associated with a 700-times extension in life, it is projected that the hybrid pipe technology allows for this life extension to be traded off for a potential 70% reduction in liner tube mass, so long as the material does not yield.

8.2 Concluding Remarks

The primary objective of the current research was to expand on the field of reinforcement of piping for creep reduction, and exploit the creep strength of refractory metals. This was achieved by altering refractory reinforcement

architecture to control the stress state of a hybrid pipe, effectively utilizing structure-property relationships to control creep rate.

It was successfully demonstrated that, through careful geometric application and design considerations, creep strength of the refractory reinforcement was successfully used to control the overall hybrid creep strength – creating a 'best of both' scenario rather than being limited by the rule of mixtures.

Through a combination of modelling and experimentation, reinforcement angle was identified as the dominant architectural feature. Additionally, reinforcement stiffness was identified as representative of the collective impact peripheral architectural features such as surface area coverage, wire diameter, number of yarns, packing fraction and wires per yarn.

In the low temperature brass-stainless steel system, the predicted empirical optimal braid angle of 54.7° is projected to reduce creep rate by a factor of 3500 over an unreinforced control test.

The significance of experimentally observing a life extension on the order of 700-times cannot be overstated. For some perspective, the life expectancy of an average New Zealander is 81 years. The life extensions being considered here are analogous to extending that to 57,000 years.

These gains have created possibilities for increased operating temperature and a wall thickness reduction, coupled with a more modest increase in service life. Gains are on the order of a 50°C temperature increase coupled with either a 60-times life extension, or a 70% reduction in tube mass. While intricately inter-

related, and difficult to precisely predict the impact of these changes, the approximate financial implications are on the order of:

- 50°C temperature increase → NZD$1.25 million per plant per year in improved process efficiency.
- 60x life extension → NZD$126 million per plant in saved capital expenditure from not replacing tubes every 11 years[2].
- 70% reduction in mass → NZD$14.5 million per plant every 11 years in saved capital expenditure from reduced material usage[1].

Potential wall thickness reductions, as well as the ability to replace the liner material with something less creep-resistant than HP-alloy, mean that these hybrid pipes may very well be implemented without any significant increase in capital cost. Additionally, it is forecast that the hybrid layup will have minimal effect on heat transfer characteristics, particularly if wall thickness is reduced, as long as at least 2.5% of the liner surface area is thermally bridged to the outer sheath surface.

8.3 Future Work

The present research has addressed the initial scope of study. Inevitably though, expanding the field of knowledge has resulted in a host of questions being raised. It is beneficial from both scientific and industrial perspectives to pursue certain avenues of thought further. This section details specific areas which the author believes warrant further investigation.

[2] Based on a capital cost of NZD$21 million for a typical reforming plant (250-450tubes), as reported in Chapter 1.

8.3.1 Tangential creep rate measurement

While longitudinal strain measurement can be used to track the progression of multiaxial creep, it is strain in the tangential direction with is of primary concern for cylindrical pressure vessels.

To further explore the relationship between creep in the tangential and longitudinal directions, it would be useful to measure tangential strain during testing by means other than periodic interruption.

As was seen in [1] it is possible to employ non-contact strain measurement techniques to measure creep strain. Such techniques could potentially be automated to track the outer surface of the tube, through a viewing point in the furnace, to continuously log tangential strain. Alternatively, McAllister et al. [2] developed special ceramic extensometry to take axial and tangential measurements at 900°C. Both of these techniques measure strain of the outer surface only, and would struggle to accurately capture tangential creep behaviour of a layered hybrid pipe.

On a reformer scale, measurements of tube ID can currently be made during maintenance shutdowns using a robotic probe ('mole') which travels through the reformer tube. There is the potential for this technology to be applied to track the creep rate of large-scale hybrid tubes.

8.3.2 Suppression of intermetallic formation

It was discovered that diffusion over the mechanical liner-reinforcement interface is possible, with intermetallic layers of Fe_7W_6 and CrW forming at the interface. Tungsten was observed to have diffused 12-20 μm into the surface of the liner after 570 hours at 1040°C.

Further investigation is required to fully understand the growth and evolution of the tungsten-based intermetallic layers which form at the mechanical interface between the reinforcement and liner. This does not need to occur during creep testing, and therefore much simpler layered sample geometries could be exposed to high temperature in a dedicated investigation of intermetallic formation. In addition to looking at specific intermetallics formed and their growth rates, the ductility of these intermetallics as well as their resistance to cyclic loading and thermal shock should be considered.

The exact material system expected in industry should be used in this investigation, this may mean HP-alloy if retrofitting the reinforcement to existing reformer tubes. Alternatively, in addition to a stress reduction or potential wall thickness increase, it may be attractive from a financial standpoint to use a material other than HP-alloy for the liner pipe, as this component of the hybrid pipe no longer requires great creep resistance.

Once a full appreciation of the nature of the intermetallic formation is gained, practical strategies can be implemented to suppress intermetallic formation, or minimize its impact. As outlined in Section 7.3, the solubility of tungsten is much lower in iron than in nickel at 1000°C, and the Fe_7W_6 formed can be stable up to 1640°C [3]. A diffusion barrier with a Fe/Ni ratio of < 0.5, applied between the reinforcement and liner pipe layers, is required in the matrix material to suppress the formation of a tungsten intermetallic phase at the matrix-reinforcement interface [4].

Alternatively, it may be possible to apply a protective coating to the tungsten wire prior to braiding. Copper and molybdenum both have low solubility in tungsten, and may be coextruded with the wire to form a diffusion barrier.

8.3.3 Reformer furnace conditions

A subtle but significant step towards practical industry implementation involves not only reproducing results on a reformer scale (see Section 8.3.4 for increasing the size of the tungsten braid), but also reproducing the operating conditions of a reformer furnace. While creep was rightly presented as the primary concern in the high temperature reformer furnace, environmental attack is also a contributing factor to pipe failure.

A step between the lab and full-scale implementation of a set of hybrid pipes in a full reformer furnace, a miniature single tube reformer is recommended. Johnson Matthey uses such furnaces for proving catalysts [5, 6]. The environment created by true reforming conditions provides potential for carburization as well as exposing the hybrid tube to hydrogen, both of which are essential to consider before full-scale implementation.

Additionally, this step towards true reforming conditions offers the perfect opportunity to expose the hybrid pipe to cyclic loading and non-uniform temperature gradients, and assess the impact on the effectiveness of the reinforcement. It may also be possible to conduct the intermetallic formation investigation outlined in Section 8.3.2 simultaneously. This would also allow for the impact of thermal cycling to be assessed in terms of its interaction with the intermetallic phases, and the significant thermal expansion mismatch between the 253MA liner and tungsten reinforcement.

8.3.4 Reformer-sized braid

An optimized tungsten braid, manufactured with a reinforcement angle of 54.7° and a 133 mm diameter to fit over a reformer tube, has structure of 48x12x0.4 i.e. 48 strands, 12 wires per strand and 0.4mm wire. Note that the largest Windhösel braiding machine is limited to a maximum of 48 strands. In this configuration, the

braid has a surface area coverage of approximately 72%. From this coverage, it is predicted that the spaces between yarns is on the order of 6.6x6.6 mm. This is dangerously close to the critical flaw size of 7.5 mm determined in Section 6.6.2.

In order to increase surface area coverage for a braid of this size, a larger braiding machine must be sourced which is capable of braiding more strands. In practice, braids even larger than 305 mm (12") OD are routinely manufactured, but these are commonly made of stainless steel and find use in hydraulic applications as reinforcement for hoses [7]. Few international braiders have expertise with braiding tungsten. From Windhösel's experience, the high stiffness and brittle nature of tungsten wire makes it very difficult to braid [8]. While coextrusion/plating the tungsten may alter the ease of braiding, it could be difficult to convince the owner of a sufficiently large braiding machine to experiment with trial runs of tungsten braid.

8.3.5 Counterweights

While specific to individual plant arrangements, it is not uncommon for reformer tubes to be suspended by counterweights, with the tubes left free at the bottom to expand longitudinally. By manipulating these counterweights, it may be possible to utilize the compressive load induced by self weight to counter a portion of the stresses driving longitudinal creep.

Reducing net longitudinal stress minimizes the risk of snaking when exposed to the non-uniform thermal gradients of a reformer furnace. Any reduction in longitudinal stress would also increase the optimal braid angle, allowing the reinforcement to be focused primarily on controlling creep in the tangential direction.

To determine the potential usefulness of this counterweight manipulation scheme, a feasibility study is required. Finite element analysis (FEA) is required to quantify the maximum achievable longitudinal stress reduction resulting from balancing compressive self weight stress against internal pressure stress. Statistical analysis of existing plants is also required, to determine the proportion of sites where counterweights are in use and implementation would be possible.

8.3.6 Additional creep tests

A major contribution of the present work has been the design and development of a means to measure longitudinal creep strain in-situ. In order to ensure the future utilization of this test apparatus, and a deepened understanding of $\dot{\varepsilon}_z - \theta - t$ relationships, the following tests are outlined as an extension to the present work:

- In order to assess the long-term behaviour of the F-50° sample, it should be tested for at least 2000 hours. This will reveal if the longitudinal creep rate eventually stabilizes at $\dot{\varepsilon}_z = 0$, or at least clearly approaches some asymptote as $\theta \rightarrow \theta_N$.
- Repeating the tests outlined in Chapter 5, but interrupting periodically to take tangential strain measurements will allow for braid orientation information to be gleaned and plotted against creep rate, as was done in Figure 4.18 for the periodically interrupted F-42° sample.
- By producing a braid with $\theta < 50°$ and a tighter clearance on the pipe than the C-36° braid had (i.e. target a radial clearance of < 0.5mm), $\ddot{\varepsilon}_z$ and $t_{\dot{\varepsilon}=0}$ can be assessed for multiple reinforcement architectures with initial reinforcement angles below the neutral angle.
- At present, the as-received brass grain size is 18.3 ± 3.2 μm, a variation of approximately 17%. By developing a standardized pre-test heat treatment schedule, it is hoped that grain size in the pre-test condition can be tightly controlled, thereby reducing variation in the minimum creep rate of the control tests (recorded in Chapter 5 as currently varying from 6.1×10^{-5} %/hour to 3.6×10^{-4} %/hour).

8.3.7 Modifications to creep testing apparatus

During creep testing, room temperature was observed to cycle by as much as ±15°C, driven by both weather effects and the automated switching on and off of heating and ventilation systems. Conducting future creep tests in a temperature-controlled room would significantly reduce noise in both furnace temperature and sample strain recordings.

In order to effectively test multiple samples in the same rig, it is important that samples are fully isolated from one another. Figure 8.1 illustrates the importance of having a completely reliable means of shutting off gas flow once a sample has ruptured.

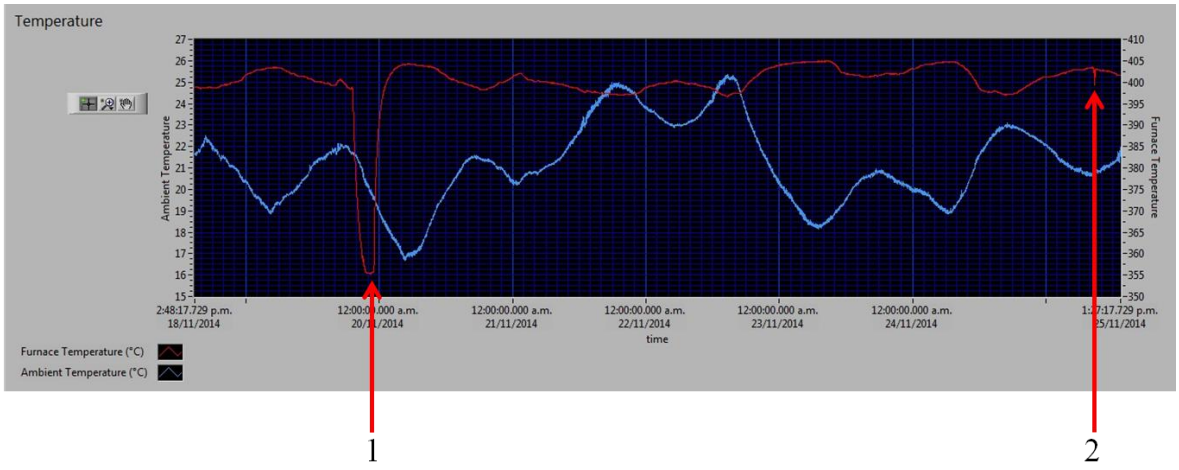

Figure 8.1. *Temperature profile during sample rupture.*

Points 1 and 2 highlighted in Figure 8.1 show the drop in furnace temperature brought about by the rupture of pressurized creep samples. Point 2 indicates a fully functional solenoid valve which correctly shuts off after sample pressure drops below a set threshold. As a result of this automated shutoff, furnace temperature drops no more than 3°C, and temperature is recovered within 15 minutes. In contrast to this, point 1 indicates a pipe rupture which failed to trigger the solenoid shutoff immediately. As a result, room temperature argon from the

gas supply was vented into the furnace, reducing the furnace temperature by 50°C and taking approximately six hours to return to set temperature.

It was also revealed that the need for active cooling of the brazed joints and LVDTs leads to approximately 44% of the sample length being heated to the set temperature of 400°C. The use of a mechanical seal in place of a brazed joint for the end cap, Figure 8.2, would circumvent the limitation that brazed joints must be kept under 200°C. With a mechanical seal, the full sample length could be heated to the test temperature, and thorough insulation coupled with active cooling would be required to keep the LVDT temperature below 100°C.

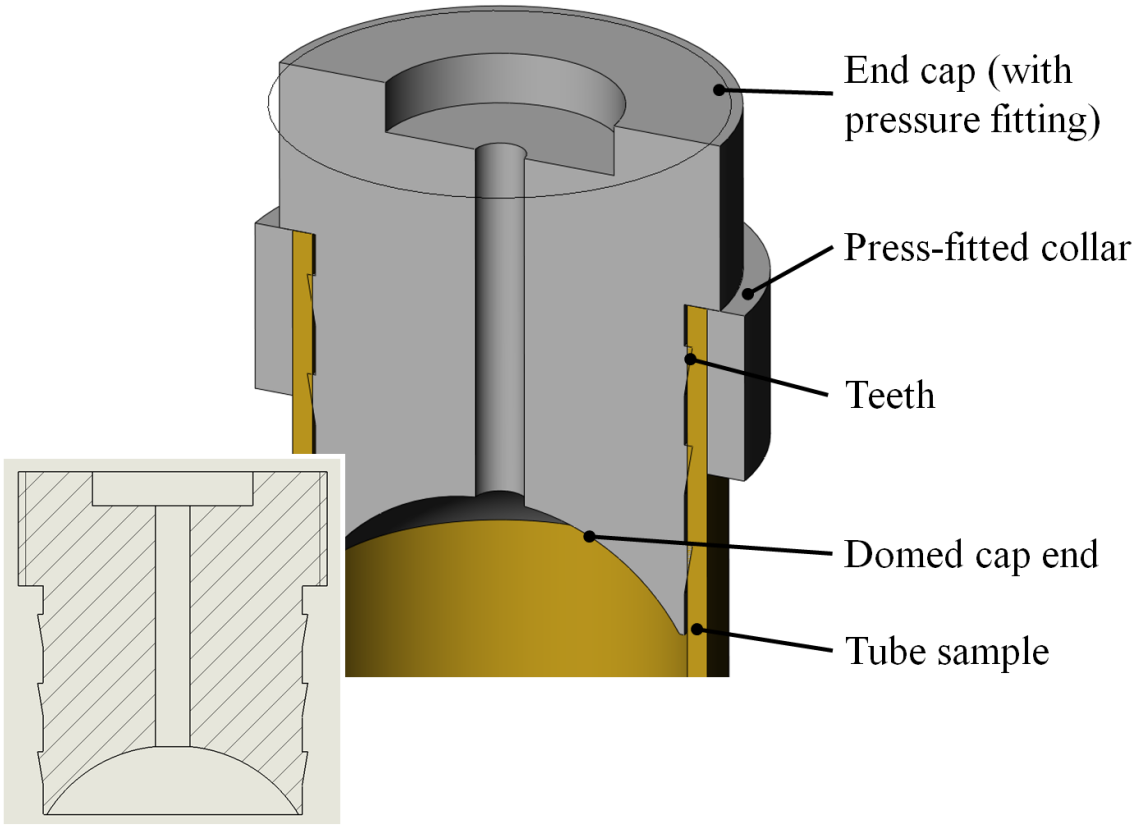

Figure 8.2. *Design for mechanical end cap to circumvent need for brazed joints. Schematic of mechanical sealing features. Inset: engineering drawing of end cap.*

CHAPTER REFERENCES

[1] J. Lee, R. C. Bradshaw, R. W. Hyers, J. R. Rogers, T. J. Rathz, J. J. Wall*, et al.*, "Non-contact measurement of creep resistance of ultra-high-temperature materials," *Materials Science and Engineering A,* vol. 463, pp. 185-196, 2007.

[2] S. McAllister, R. C. Hurst, and T. E. Chung, "Modelling the Multiaxial Creep Behaviour of Alloy 800H," *International Journal of Pressure Vessels and Piping,* vol. 47, pp. 355-370, 1991.

[3] H. Baker, *ASM Handbook, Vol.3: Alloy Phase Diagrams*. Ohio: ASM International, 1992.

[4] P. Kumar, "Studies of wire/matrix interactions in some tungsten wire reinforced stainless steels," PhD, Mechanical Engineering, University of Canterbury, 2014.

[5] P. Tait, Methanex Corporation, (personal communication with B. Reyngoud, 2013)

[6] P. I. Goni, Schmidt-Clemens, (personal communication with B. Reyngoud, June 19th, 2013)

[7] USHoseCorporation. Large Diameter Metal Hose and Braid, http://www.ushosecorp.com/product/metal-hose-braid/large-diameter-metal-hose-braid/, [Accessed September 15th 2014].

[8] F. Windhösel, (personal communication with B. Reyngoud, May 24th, 2014)

APPENDIX A: PUBLICATIONS

A journal paper was published during the course of this research. This paper is included in full in the following pages of this Appendix.

B.P. Reyngoud, C.M. Bishop and M.V. Kral, *"Hybrid Materials Design to Control Creep in Metallic Pipes",* Materials and Design, vol. 84, pp. 25-35, 2015.

Materials and Design 84 (2015) 25–35

Contents lists available at ScienceDirect

Materials and Design

journal homepage: www.elsevier.com/locate/jmad

Hybrid materials design to control creep in metallic pipes

B.P. Reyngoud, C.M. Bishop, M.V. Kral *

University of Canterbury, Department of Mechanical Engineering, P.O. Box 4800, Christchurch 8041, New Zealand

ARTICLE INFO

Article history:
Received 10 December 2014
Received in revised form 13 June 2015
Accepted 17 June 2015
Available online 25 June 2015

Keywords:
Hybrid
Creep
Architectured reinforcement
Neutral angle

ABSTRACT

A hybrid material has been developed to improve creep performance in pressurized metallic pipes subjected to high-temperatures. Model materials were selected for an investigation of reinforcement design parameters in architectured materials. Brass pipes (65 wt.% Cu/35 wt.% Zn) with austenitic stainless steel reinforcement were pressurized and creep rupture tested at 673 K. Compared to unreinforced pipes of equal dimensions, a 47-times reduction in the effective strain rate was observed with a 50° reinforcement angle. A 'neutral angle' of 54.7 ± 1.5° was determined experimentally, where tangential (hoop) and longitudinal stresses on the pipe can be balanced and strains minimized. For initial angles below the neutral angle, creep strain was shown to facilitate a shift in orientation towards the neutral angle. For an initial angle of 42°, this shift towards the neutral angle resulted in instantaneous creep rate dropping from 170% of the mean creep rate to 60% of the mean creep rate over 820 h, when the final angle was measured to be 50°. A high-temperature prototype (tungsten braid oriented at 53° over a 253MA stainless steel pipe) was shown to give a creep life extension in excess of 300-times at 1313 K.

1. Introduction

There is constant demand for improved materials that can perform at higher temperatures to increase efficiency and reliability of systems such as gas turbine engines and petrochemical facilities [1,2]. Bulk materials have been continuously improved via alloying and manufacturing processes to obtain substantial gains in performance over the past few decades, e.g., in gas turbine engines [3,4] steam reformer and steam cracker furnace tubes [5]. However, improvements are made in relatively small steps and it may be argued that such materials are reaching the limit of their potential. The present research focuses on industrial applications, such as steam methane reformers, in which relatively large pipes (ca. 10 cm diameter and 13 m in length) operate under ~1–5 MPa internal pressure at approximately 1173 K. Since these pipes operate at temperatures greater than 1/3 the absolute melting temperature (T_M) of the alloys presently employed in these applications, the pipes are subject to failure by creep mechanisms, and cracks eventually develop along the longitudinal axis of the pipe due to tangential (hoop) stress.

The present work seeks insight into the design of "hybrid materials" as an alternative pathway to obtain substantial performance improvements over bulk materials and even composite materials in high temperature piping applications. Ashby [6] defined hybrid materials as "combinations of two or more materials or of materials and space, configured in such a way as to have attributes not offered by any one material alone". The simple hybrid design under consideration here involves externally reinforcing a pipe with an architectured layer of a material having substantially greater creep rupture life than the pipe material. This architectured reinforcement layer may be comprised of filament windings or a braided sleeve. Utilizing a hybrid layup allows the property space between rule of mixtures and 'greatest of both' scenarios to be exploited for a substantial life extension, utilizing the structural strength and chemical resistance of the pipe and the creep strength of the reinforcement layer.

A significant amount of work has been done in the area of fibre and braid-reinforced polymeric or elastomeric pipes [7] which operate at relatively low temperatures (less than 473 K). These reinforced composite materials have shown a great deal of success in improving both mechanical and creep strength. The cost-effectiveness of glass-fibre reinforced composites, coupled with their well-balanced combination of impact toughness and strength/stiffness properties makes them suitable for the development of aerospace components such as propeller shafts and turbine casings as well as automotive parts such as transmission drive shafts [7]. A polyethylene pipe containing aramid fibres can permit operating pressures of around ten-times the capability of conventional polyethylene pipe [8].

For fibre reinforcement oriented at an angle θ from the pipe axis, the theoretical angle at which stresses due to internal pressure are balanced by the reinforcement restorative force is known as the neutral angle (θ_N). This θ_N notation is used to refer to a general case, dependant on tube geometry and loading conditions (i.e. self weight or tension in addition to internal pressure). In a thin-walled pressure vessel where internal pressure is the only applied load, the tangential stress (σ_t) is twice the longitudinal stress (σ_z). It can be shown that when forces

* Corresponding author.
E-mail addresses: ben.reyngoud@pg.canterbury.ac.nz (B.P. Reyngoud), catherine.bishop@canterbury.ac.nz (C.M. Bishop), milo.kral@canterbury.ac.nz (M.V. Kral).

http://dx.doi.org/10.1016/j.matdes.2015.06.089
0264-1275/

are in a state of equilibrium and the reinforcement is in tension, the theoretical neutral angle for thin-walled vessels (θ_N^*) is 54.7° [8,9].

$$\theta_N^* = tan^{-1}\left(\sqrt{\frac{\sigma_t}{\sigma_z}}\right) = tan^{-1}(\sqrt{2}) = 54.7°. \quad (1)$$

In composite systems where the reinforcement is embedded in a pipe matrix with low stiffness and/or strength, under applied internal pressure the reinforcement shifts to orient itself at the equilibrium position of θ_N. When $\theta > \theta_N$, the pipe will increase in length and its diameter will decrease. When $\theta < \theta_N$, the pipe will shorten in length and its diameter will increase [9]. This means of actuation for a given internal pressure is often utilized in pneumatic artificial muscles as well as muscular hydrostats in biological systems [10–12], where the deformation is elastic.

Refractory metals have been previously considered as good reinforcement candidates for achieving considerable gains in the creep rupture life of stainless steels and nickel-based super-alloys, materials commonly used in high temperature piping applications (1173 K and above) [13–18]. It must be noted that refractory metals themselves are limited by their poor oxidation resistance at service temperatures and can only be used in air when protected by suitable coating materials [15]. As a result, most creep tests on refractory composite and alloy systems have been performed under vacuum with the intended application being high temperature components for use in space [19]. For some applications with shorter life requirements, it may be practical to minimize the rate of oxidation by alloying or coating materials such that they form a stable, dense surface oxide [15]. However, in order to form an effective oxide layer, a critical Cr, Si or Al content is required in the alloy and such high levels of these alloying components cause brittle intermetallic phases to form with refractory metals [15,20].

Prior to the present work, a proof-of-concept 43-mm diameter, schedule 160 alloy 800H pipe was reinforced using helically wound 0.38 mm diameter tungsten wires, and creep tested at 1303 K and 3.5 MPa internal pressure (analytical grade argon). To combat oxidation, the reinforced pipe was coated with a plasma sprayed 79E nickel-based alloy. This proof-of-concept test showed at least a 4-times life extension over a monolithic pipe of equal dimensions tested simultaneously under the same conditions. Although the prototype pipe did not rupture, there were signs of oxidation in the tungsten reinforcement, which was considered the life-limiting factor [21].

The main purpose of the present work was to optimize the architecture of the reinforcement. A model materials system of brass pipes reinforced with austenitic stainless steel was selected for study, which was convenient to avoid oxidation of refractory metal, facilitate fabrication, improve availability of materials and lower test temperatures. A series of model materials prototypes, having systematically altered reinforcement architecture, were built and creep tested under internal pressure until failure. Post-test assessment and periodically interrupted tests revealed the strains that were obtained during the tests. While a similar approach to creep testing has been used for polymeric composites at low temperature [22,23], the use of pressurized pipe tests to assess the creep rupture performance of metals at high temperature has only been considered in a few select cases [24–26] and never, to the authors' knowledge, for metallic composites or hybrids.

2. Methodology

Structural pipes are widely used in fluid and gas transportation in the petrochemical industry, where they often contend with aggressive environments, high temperatures and elevated pressures, and are prone to failure via creep. The multiaxial mechanical properties of the pipe become extremely important when the material or structure is anisotropic or orthotropic, as is the case for composites and hybrids [27].

2.1. Life prediction of unreinforced materials

Shigley [28] states that a pressure vessel can be assumed to be thin-walled when the ratio of the wall thickness to inner radius (t/r_i) is < 0.05. For typical test pipe dimensions, 25.4 mm outer diameter and $t = 1.22$ mm, this assumption is invalid as $t/r_i = 0.106$. Therefore, Lamé's equations for stresses in a thick-walled pressure vessel were reduced for zero external pressure (Eqs. (2)–(4)). Von Mises equation (Eq. (5)) was used to resolve these multiaxial stresses into an equivalent stress, σ_{VM}. Principal stresses in a cylindrical coordinate system σ_r, σ_t and σ_z are functions of radial distance at a given point (r), internal pressure (p_i) and outer and inner radii (r_o and r_i) of the cylinder. Tangential and von Mises stresses are largest at the inner wall of the pipe.

$$\sigma_r = \frac{p_i r_i^2}{r_o^2 - r_i^2}\left[1 - \frac{r_o^2}{r^2}\right] \quad (2)$$

$$\sigma_t = \frac{p_i r_i^2}{r_o^2 - r_i^2}\left[1 + \frac{r_o^2}{r^2}\right] \quad (3)$$

$$\sigma_z = \frac{p_i r_i^2}{r_o^2 - r_i^2} \quad (4)$$

$$\sigma_{VM} = \sqrt{\frac{\left[(\sigma_r - \sigma_t)^2 + (\sigma_t - \sigma_z)^2 + (\sigma_r - \sigma_z)^2\right]}{2}} \quad (5)$$

Eqs. (2)–(5) were then solved for typical test piece dimensions and 2 MPa of internal pressure, to find an equivalent stress, σ_{VM}, of 18.9 MPa at the inner wall. This value was used for the life prediction of an unreinforced control pipe.

2.2. Model pipe material selection

The brass used in this study has a nominal composition of 65 wt.% Cu/35 wt.% Zn, with a copper composition typically in the range of 64–68.5% [29]. While some β' may exist in this composition at room temperature, it is in solution at 673 K and the alloy may be considered single phase α-brass during creep testing [30]. For a 673 K test temperature and $\sigma_{VM} = 18.9$ MPa, interpolating from the creep curve provided for 70–30 α-brass by Evans and Wilshire [31] gives an estimated creep rupture life of 83.5 h for the unreinforced pipe.

2.3. Reinforcement architecture

The 304 and 316 L stainless steel reinforcement configurations tested were defined by parameters relating to their architecture. These include surface area coverage, braid/wrap angle, wire packing fraction, longitudinal stiffness, wire size, number of yarns and number of wires per yarn. Modelling [32] reveals that overall braid stiffness is a function of braid angle, wire diameter, packing fraction, yarn sectional area and length and angle of undulation (crimp angle) through the thickness of the braid.

These reinforcement configurations and their characteristics prior to testing are summarized in Table 1. Reinforcement angle, θ, was measured relative to the pipe axis (0°) and defined from $0° \le \theta \le 90°$. At least six measurements of θ were taken for each reinforcement type, with the mean and standard deviation reported in Table 1. Braid naming convention was selected based on the wire coarseness (C or F to denote 'coarse' and 'fine' wires, respectively) and nominal reinforcement angle.

'C-65°' (Fig. 1b) refers to a braided structure with an overall reinforcement layer thickness comparable to the 0.4 mm wire wrap (Fig. 1a). By comparison to C-65°, F-42° (Fig. 1d) is comprised of many finer wires arranged in a tighter weave to give increased surface coverage.

Table 1
Reinforcement architecture characterization.

	Wrap	C-65°	F-50°	C-36°	F-42°
Material	316 L	304	304	304	304
Wire diameter (mm)	0.4	0.254	0.127	0.254	0.127
~Wrap/braid angle[a] (°)	86.2 ± 0.8	65.3 ± 1.1	49.5 ± 2.4	36.2 ± 1.2	41.5 ± 1.0
Surface area coverage (%)	100	94	95	80	98
Yarns (strands)	1	24	48	36	48
Wires per yarn	1	8	11	8	15
Total wires	1	192	528	288	720

[a] Mean ± standard deviation.

While a helically wound wrap serves as an extremely effective means of restricting tangential expansion, it has low longitudinal stiffness and thus a very limited ability to control longitudinal expansion. By altering the reinforcement angle, a braided reinforcement sacrifices some of this tangential stiffness, but gains the ability to more effectively constrain the pipe in the longitudinal direction, particularly due to its interlocking nature.

2.4. Pressurized pipe tests

1 m lengths of 65 wt.% Cu/35 wt.% Zn brass pipe liner with a typical outer diameter of 25.4 mm and 1.22 mm wall thickness were brazed sealed and reinforced with austenitic stainless steel wire in the form of either a helical wrap (316 L SS) or a braided sleeve (304 SS), as shown in Fig. 1. These tube samples were placed in a horizontal tube furnace at 673 K, pressurized to 2 MPa with argon and allowed to creep until rupture or 820 h (~10-times the predicted life of an unreinforced tube) had elapsed. This 2 MPa internal pressure was selected to give a von Mises equivalent stress of approximately 19 MPa, a slight acceleration from the 16–18 MPa seen in typical reformer furnace conditions. The present pressurized pipe tests are similar to previous methods [24–26,33,34]. ASTM E139-11 [35] outlines standard testing methods for creep testing of metallic materials, and was adhered to for heating, temperature measurement and post-mortem strain measurement guidelines.

The test temperature was selected such that the brass was subjected to creep conditions (approximately 42% of its melting point) while the stainless steel reinforcement was only exposed to approximately 30% of its melting point, leaving it unaffected by creep — confirmed by a lack of measurable deformation and the absence of creep voids in post-test microstructural analysis. Therefore, the model materials serve as analogues of the behaviour of stainless steel (e.g., 253MA) pipe and refractory (e.g., tungsten) at high temperature (1313 K).

Internal pressure and temperature were logged every 60 s during all tests, and maintained stability to within ±0.2 MPa and ±1 K. A sustained pressure drop indicated pipe rupture, in which case the test was ended. Unlike conventional uniaxial creep tests and some more sophisticated multiaxial creep tests where strains may be measured in-situ [25,27,36], the multilayered nature of the hybrid pipe made in-situ strain measurements problematic. Therefore, strain measurements were made during interruptions or after test completion.

Post-test longitudinal creep strain was measured at room temperature over a 50 mm gauge length across the midspan of the tube, positioned in the middle of the hot zone of the furnace. At least five measurements were made using digital callipers and the readings

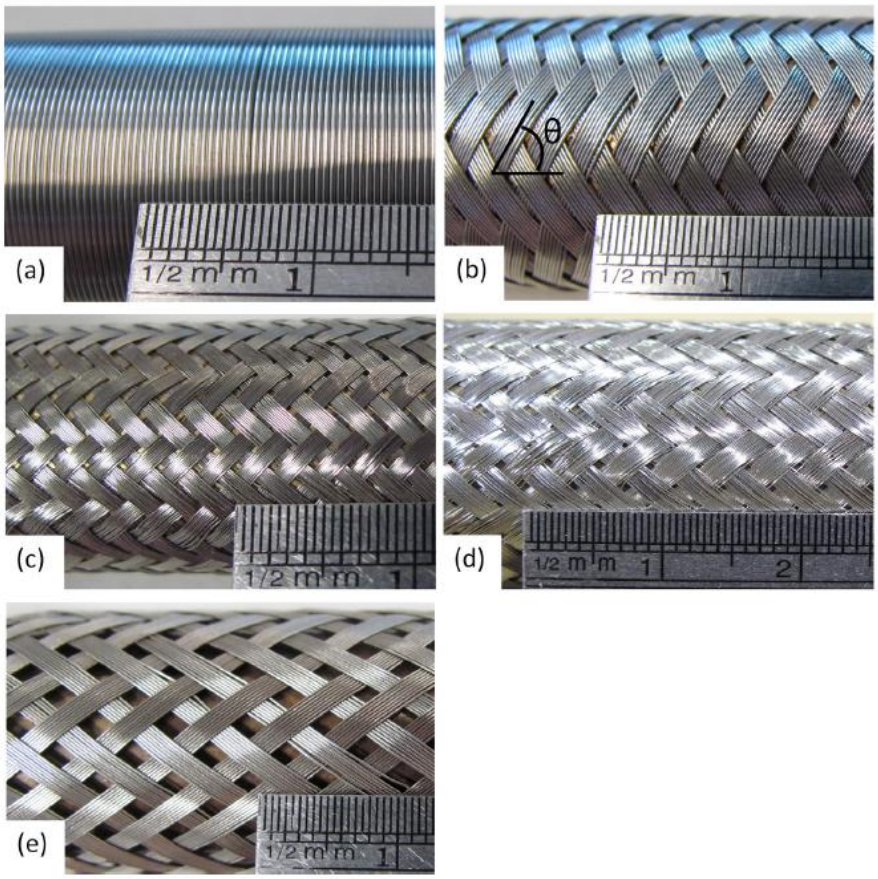

Fig. 1. Reinforcement configurations tested (a) 0.4 mm diameter wire wrap, (b) C-65°, (c) F-50°, (d) F-42° and (e) C-36°.

Table 2
Creep rupture testing programme.

Reinforcement designation	Number of tests performed	Average duration (hours)
Control (unreinforced)	3	83
Wrap-86°	1	647
C-65°	2	818[a]
F-50°	1	817[a]
F-42° (uninterrupted)	2	818[a]
F-42° (interrupted)	1	819[a]
C-36°	1	818[a]

[a] Denotes test samples that did not fail.

were averaged. Post-test measurements of the inside and outside diameter were made on a length of pipe sectioned from the midspan and positioned vertically in a 3-jaw chuck. A Giddings and Lewis Discovery D12 Cordax Series coordinate-measuring machine (CMM) with an Ø8 mm probe was used to take 12 diameter coordinate measurements to 1 μm resolution. These diameter measurements allowed tangential and radial creep strains to be determined.

In order to enhance understanding of strain behaviour during testing, an F-42° sample was interrupted periodically and the reinforcement was removed to enable strain measurements on the pipe. This method of periodic interruption to take strain measurements has been used previously on unreinforced metallic creep rupture specimens under internal pressure [26,33]. To quantify the effect of this periodic interruption, two additional tests of F-42° samples were performed without interruption.

Table 2 details the number and duration of creep rupture tests performed. A wide range of braid angles was tested in order to determine the effect on creep strain rate. All reinforced tests were ended either after rupture or after 820 h had elapsed. Final strains in the tangential, longitudinal and radial directions were determined upon failure. Mean creep strain rates were determined by final strain divided by test duration.

3. Results and discussion

3.1. Pressurized pipe tests

The average life of the three creep rupture control tests was 83 ± 5 h, which is consistent with the predicted life of 83.5 h. These tests provide a control against which reinforced cases could be compared. A post-mortem average tangential expansion of 12.9% was observed at the midspan of the ruptured unreinforced pipes, with a corresponding average of 0.30% longitudinal expansion over the gauge length.

All of the braid-reinforced pipes achieved a 10-times life extension over the control pipe without rupturing, at which point testing was ended due to practicality. The helically wound reinforcement (Wrap-86°) failed after ~647 h, a 7.8-times life extension over the control pipe, with a circumferential crack. A failed control pipe with a longitudinal crack is presented in Fig. 2 alongside the failed wrap-reinforced pipe. This shift in the primary mode of failure between the control and wrap-reinforced pipe affirmed that tangential creep had effectively been arrested by the reinforcement, and identified longitudinal creep as a new failure mode for pipes exposed to internal pressure.

Figs. 3 and 4 show mean creep rates in the tangential and longitudinal directions, respectively, for each reinforcement type. Error bars denote variation in repeated tests.

The data shows that tangential creep rates decrease with increasing reinforcement angle, and that longitudinal creep rates increase with increasing reinforcement angle. Both tangential and longitudinal creep appear to be minimized between the 50° and 65° samples. The braid architecture parameters such as wire diameter, number of yarns and number of wires per yarn appear to have little effect on the observed trends, i.e., reinforcement angle appears to be dominant. In the case of the wrap and C-65° reinforcement, a substantial reduction in average tangential creep strain compared to the control pipe was observed, while the average longitudinal strain rate increased in these cases. As expected, Figs. 3 and 4 show that for initial reinforcement angles below the neutral angle, the pipe expands tangentially and shortens longitudinally and vice versa for initial reinforcement angles above the neutral angle. In contrast to the near-instantaneous and largely elastic deformation observed in polymeric and elastomeric braid-reinforced pipes, this creep strain occurs gradually and is inelastic and non-recoverable.

The results of the periodically interrupted F-42° pressurized pipe test are shown in Fig. 5 as a plot of tangential and longitudinal strain versus time. Power laws provide good fits for the strain and show that the magnitudes of the creep rates decrease with time compared to a linear trend over a 10-times control life test duration.

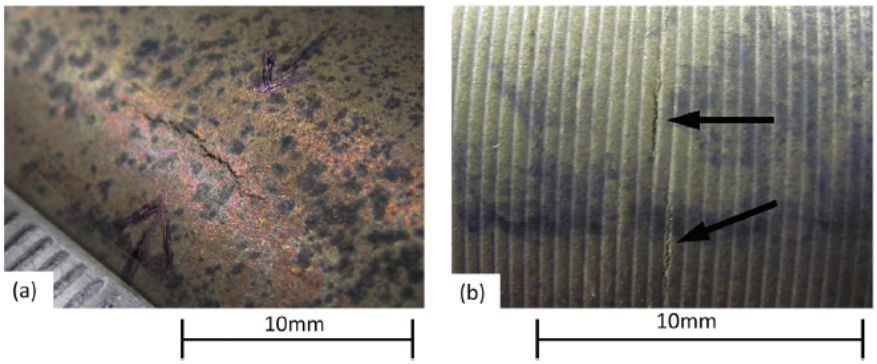

Fig. 2. Cracks and impressions on pipe outer diameter after rupture (reinforcement removed). (a) Longitudinal crack in control pipe, (b) circumferential crack in wrap-reinforced pipe, where helical windings have left impressions on the pipe.

and undulation.

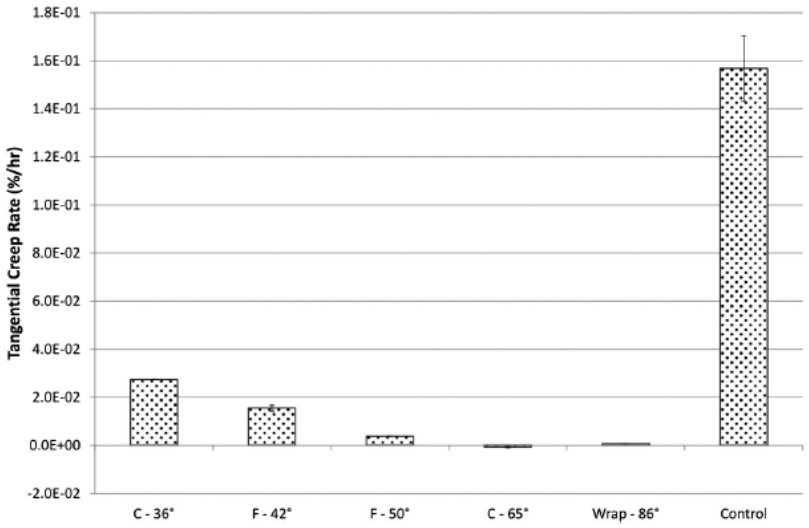

Fig. 3. Mean tangential creep rates from final tangential strain measurements of pipes with various reinforcement architectures. All braid-reinforced pipes stopped after 10-times life extension. Error bars denote variation in repeated tests.

This periodically interrupted test allows for an investigation of strain behaviour during testing, and a quantification of the effectiveness of the mean creep rate approximation. The instantaneous creep rate, calculated from the power law fits, differs by 8% at most from the mean creep rate approximation, which consistently overestimates creep rate. This relatively small discrepancy supports the use of the mean creep rate in other tests.

At the end of the interrupted F-42° test, 13.4% tangential strain and −8.19% longitudinal strain were recorded. Comparatively, the two uninterrupted F-42° tests strained 11.7% to 13.5% in the tangential direction and −5.67% to −6.61% longitudinally, putting the tangential strain of the interrupted test within the range of observed tangential strains in the uninterrupted tests. The periodic interruptions, involving regularly cooling the sample and removing the reinforcement layer to take strain measurements, appear to have caused a ratcheting effect which has enhanced strain in the longitudinal direction, causing an additional contraction on the order of 0.8 mm across the 50 mm gauge length when compared to equivalent uninterrupted tests.

3.2. Creep strain rate analysis

A major purpose of the present work is to determine the effect of braid architecture on creep strain rate. As mentioned previously, the neutral angle for internally pressurized, thin-walled pressure vessels with reinforcement in tension is $\theta_N^* = 54.7^\circ$ [8,9,37], and systems with compliant matrices and stiff reinforcement deform elastically under pressure at low temperature so that the stiff reinforcement assumes this orientation [9]. In contrast to braid-reinforced polymeric and elastomeric tubes, the modulus of the pipe relative to the reinforcing material is comparatively large

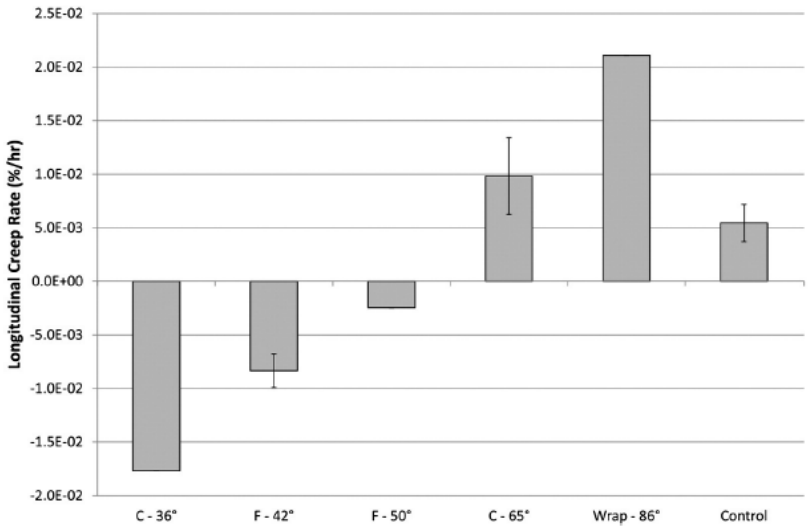

Fig. 4. Mean longitudinal creep rates from final longitudinal strain measurements of pipes with various reinforcement architectures. All braid-reinforced pipes stopped after 10-times life extension. Error bars denote variation in repeated tests.

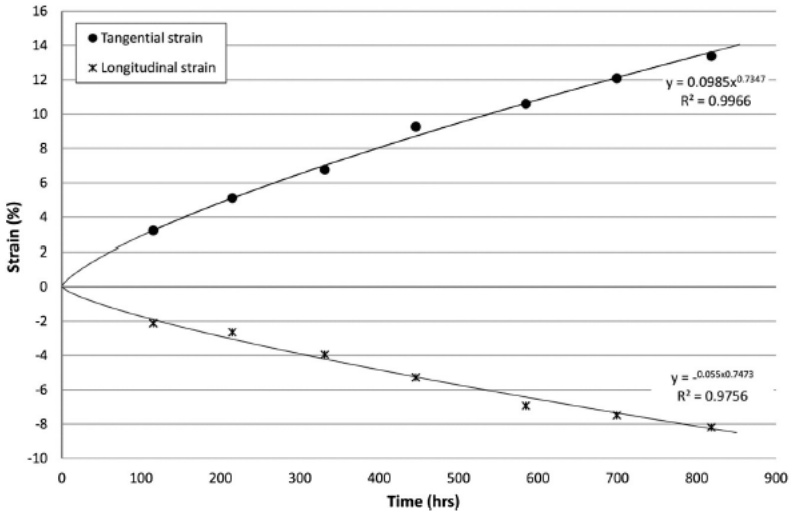

Fig. 5. Tangential and longitudinal strain measurements at periodic interruptions for a pipe with F-42° reinforcement architecture. Test stopped after 10-times life extension over control.

in the present study. As a result of this relatively large pipe stiffness, coupled with the high test temperature, creep deformation rather than elastic deformation is expected to be the mechanism for reorientation of the reinforcement in the present experiments. As the tube is not thin-walled ($t/r_i > 0.05$), it is expected that a geometry dependent neutral angle (θ_N) will be obtained where $\theta_N \rightarrow \theta_N^*$ as $t/r_i \rightarrow 0.05$.

In the present case, the braid left indentations on the pipe surface (see Fig. 2), so it was possible to ascertain whether reorientation of the reinforcement is also observed in the hybrid pipe geometry deforming by creep. As indicated by Table 3, post-test braid angle measurements confirm that during testing, the braid angle shifts by $\Delta\theta$ towards some θ_N, which is dependent on the particular tube geometry and the tangential/longitudinal stress ratio, Eq. (1). However, the 50°, 65° and 86° samples all showed relatively small changes that are not significantly different from the range of measured braid angles in the as-manufactured condition. Predictably, $\Delta\theta$ is smaller in magnitude for initial angles around $\boldsymbol{\theta_N^*}$. The observation of small to negligible values of $\Delta\theta$ for initial angles greater than θ_N is related to the inability of this system to reduce the braid angle via a reduction in diameter due to the interfacial interaction between the reinforcement and the liner, resulting in a requirement that $\dot{\varepsilon}_t \geq 0$. In order for a tangential contraction and concomitant reduction of larger braid angles towards θ_N to occur, the reinforcement would have to be bonded to the surface of the liner pipe or embedded within the pipe itself.

Rather than the near-instantaneous shift upon application of pressure seen with reinforced elastomeric or polymeric hoses [9], the shift in braid angle in reinforced metallic pipes occurs primarily through creep. All braid-reinforced brass pipe tests were interrupted prior to rupture after approximately 820 h, so it is likely that all initial angles below θ_N would have continued to shift towards θ_N over time, limited only by the creep ductility of the brass.

Measured mean creep rates are plotted against mean reinforcement angle in Fig. 6. Error bars for the mean reinforcement angle $\Delta_{mean} = \sqrt{\Delta_{pre}^2 + \Delta_{post}^2}$ were determined from standard deviations in the pre- and post-test angle measurements, Δ_{pre} and Δ_{post}, respectively. The fitted trend lines are based on an analysis of the stresses in a thin-walled pressure vessel at internal pressure p, reinforced with n fibres per unit length of pipe oriented at angle θ to the longitudinal axis and which transmit tension T. The radial stress in the pipe is zero. From force balances in the tangential and longitudinal directions, stresses in these respective directions are derived to be:

$$\sigma_t = \frac{pr_i}{t} - \frac{nT}{t}\sin\theta$$
$$\sigma_z = \frac{pr_i}{2t} - \frac{nT}{t}\frac{\cos\theta}{\tan\theta} \tag{6}$$

and can be generalized to have the following dependences on θ:

$$\sigma_t = A - B\sin\theta$$
$$\sigma_z = \frac{A}{2} - B\frac{\cos\theta}{\tan\theta}. \tag{7}$$

Table 3
Post-test braid angle measurement.

Designation	Pre-test braid angle (°)	Post-test braid angle (from indentations) (°)	Change in reinforcement angle (°)
C-36°	36.2 ± 1.2	47.8 ± 1.4	+11.6
F-42°	41.5 ± 1.0	50.0 ± 2.6	+8.5
F-50°	49.5 ± 2.4	50.7 ± 1.9	+1.2
C-65°	65.3 ± 1.1	63.8 ± 1.5	−1.5
Wrap	86.2 ± 0.8	86.6 ± 0.7	+0.4

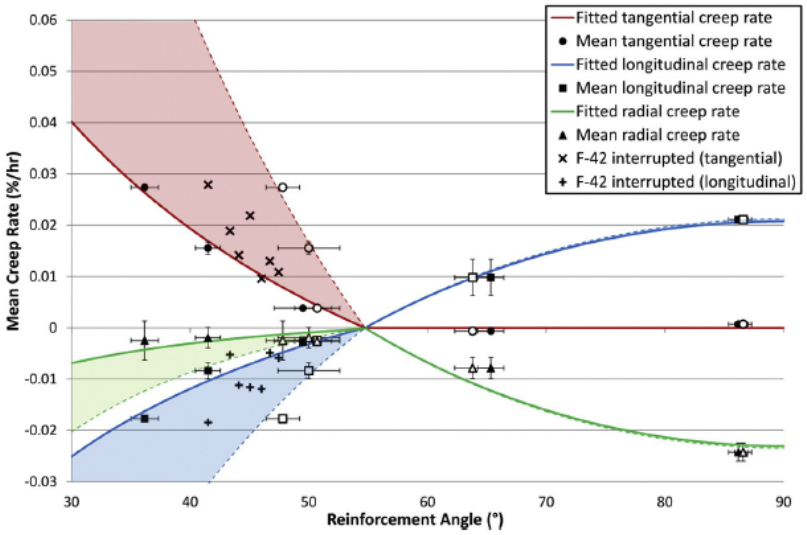

Fig. 6. Measured mean tangential, longitudinal and radial creep rates plotted against initial reinforcement angle (solid points) and final angle (unfilled points), with creep rate trends superimposed. Shaded bands cover range of predicted behaviour from initial angle (solid line) to final angle at t = 820 h or failure (dashed line). Creep strain data from the interrupted F-42° test is superimposed, with × and + symbols, showing tangential and longitudinal creep rates, respectively.

Following Dowling [38], a time hardening model for multiaxial creep rates is used to associate multiaxial stress components to component strain rates:

$$\dot{\varepsilon}_t = \frac{1}{\eta}[\sigma_t - 0.5(\sigma_r + \sigma_z)]$$
$$\dot{\varepsilon}_z = \frac{1}{\eta}[\sigma_z - 0.5(\sigma_r + \sigma_t)] \tag{8}$$

where η, the tensile viscosity, is the ratio of the effective creep rate to the von Mises stress and is, in general, a function of stress and time, given by:

$$\frac{1}{\eta} = \frac{\dot{\varepsilon}_{eff}}{\sigma_{VM}} = D_3 \emptyset \sigma_{VM}^{\delta-1} t^{\emptyset-1} \tag{9}$$

with D_3, $\emptyset$ and δ empirical constants related to creep data.

The effective creep rate is much like von Mises stress and is given by:

$$\dot{\varepsilon}_{eff} = \frac{\sqrt{2}}{3}\sqrt{(\dot{\varepsilon}_t - \dot{\varepsilon}_r)^2 + (\dot{\varepsilon}_r - \dot{\varepsilon}_z)^2 + (\dot{\varepsilon}_z - \dot{\varepsilon}_t)^2}. \tag{10}$$

Substituting the expressions from Eq. (7) into Eq. (8) gives:

$$\dot{\varepsilon}_t = \frac{1}{\eta}\left[\frac{3A}{4} - B\left(\sin\theta - \frac{\cos\theta}{\tan\theta}\right)\right]$$
$$\dot{\varepsilon}_z = \frac{1}{\eta}\left[B\left(\frac{\sin\theta}{2} - \frac{\cos\theta}{\tan\theta}\right)\right]. \tag{11}$$

Incompressibility requires that volumetric strain and therefore volumetric strain rate are zero [38] and gives:

$$\dot{\varepsilon}_r = -(\dot{\varepsilon}_t + \dot{\varepsilon}_z). \tag{12}$$

Eqs. (11) and (12) can then be used to generate a $\dot{\varepsilon}_r - \theta$ curve against which measured radial creep strains can be compared in order to validate the incompressibility assumption of Eq. (12). Eqs. (11) and (12) suggest that this $\dot{\varepsilon}_r - \theta$ curve is of the form $-A + B(\sin\theta + \frac{\cos\theta}{\tan\theta})$.

A boundary condition has been applied such that the tangential fit for the tangential strain rate is terminated at the x-axis to ensure that $\dot{\varepsilon}_t \geq 0$. The reason for this boundary condition is that tangential contraction would result in the reinforcement disengaging. If the reinforcement were to disengage, tangential creep would occur, and the pipe would begin to expand until the reinforcement was once again engaged. Therefore, in other words, in this model the pipe is not allowed to contract tangentially. From Eq. (8), the condition that $\dot{\varepsilon}_t = 0$ implies that $(\sigma_t - 0.5\sigma_z) = 0$. This modifies the longitudinal fit to be of the form $A - B\frac{\cos\theta}{\tan\theta}$, and the radial fit of the form $-A + B\frac{\cos\theta}{\tan\theta}$ for regions where the $\dot{\varepsilon}_t = 0$ boundary condition is applied.

Neglecting the stress- and time-dependency of η, least squares fits using the trigonometric relationships of Eqs. (11) and (12) were used to fit the strain rate data and are shown on Fig. 6, with curves generated at the initial angles (solid lines) and final angles at $t = 820$ h (dashed lines), to create lower and upper bounds, respectively. To allow for goodness of fit to be assessed, as well as illustrating the transition made by individual samples

from initial to final angle, measured mean creep rates are plotted at both the initial angles (filled points) and final angles at $t = 820$ h (unfilled points).

Strain measurements taken during the periodically interrupted test shown in Fig. 5 can be related to the instantaneous reinforcement angle geometrically. This in turn allows the change in creep rate to be explored as the F-42° sample reinforcement reorients itself from 41.5° to 50.0°. The instantaneous creep rate and reinforcement angle are superimposed in Fig. 6, showing the transition of the F-42° sample from the lower to the upper band.

Up to a value of $\theta \leq 54.7°$, the measured tangential creep rate varies with initial reinforcement angle as $\dot{\varepsilon}_t = 0.0117 - 0.0286(\sin\theta - \frac{\cos\theta}{\tan\theta})$ and has a coefficient of determination of $R^2 = 0.968$. At the least squares-fit generated using the final braid angle values, this R^2 value drops to 0.643.

The negligible shift observed in braid angle for initial angles above $\theta_N \approx \theta_N^*$ can be attributed to the lack of a driver for tangential contraction of the pipe, which is also responsible for the $\dot{\varepsilon}_t \geq 0$ boundary condition. As stated previously, to make tangential contraction (and reduction of larger braid angles towards θ_N) possible the reinforcement would need to be bonded to the surface of the liner, or embedded within the pipe itself.

From Fig. 6 it can be seen that for $\theta < \theta_N$ the measured longitudinal creep rate varies with initial braid angle as $\dot{\varepsilon}_z = 0.0319(\frac{\sin\theta}{2} - \frac{\cos\theta}{\tan\theta})$, has an R^2 value of 0.939, and is zero at $\theta = 54.7°$. For $\theta > \theta_N$, this relationship is $\dot{\varepsilon}_z = 0.0204 - 0.0407\frac{\cos\theta}{\tan\theta}$ and has an R^2 value of 0.869. Note that the $\dot{\varepsilon}_z$ curve is negative for angles below θ_N. Unlike the tangential and radial trends, the $\dot{\varepsilon}_z$ curve exists both above and below the x-axis.

The measured values of radial creep rate conform to the general behaviour of the predicted radial creep rate trend, remaining negative and increasing in magnitude away from θ_N. For initial angles below θ_N, this radial creep rate trend is $\dot{\varepsilon}_r = -0.0104 + 0.0086(\sin\theta + \frac{\cos\theta}{\tan\theta})$ and has an R^2 value of 0.734. Above θ_N, the $\dot{\varepsilon}_r - \theta$ trend is $\dot{\varepsilon}_r = -0.0228 + 0.0455\frac{\cos\theta}{\tan\theta}$ and has an R^2 value of 0.708.

Comparing the instantaneous creep rate from the periodically interrupted data with the mean creep rate for the F-42° sample, Fig. 6 reveals that initial creep rate is on the order of 1.7-times greater than the mean rate, and decays to approximately 60% of the mean rate after 820 h (i.e. at the final angle). From measured strains, and knowledge of the initial angle, a final braid angle of 47.5° is calculated. While lower than expected, this calculated final angle is within a single standard deviation of the measured final angle of $50.0 \pm 2.6°$. The geometric relationship between braid angle and pipe dimensions is based upon a single fibre in continuous contact with the pipe surface, and does not account for three-dimensional effects of the reinforcement architecture such as curvature and undulation.

From Eq. (11), it can be seen that the constant associated with the trigonometric terms in both the $\dot{\varepsilon}_t$ and $\dot{\varepsilon}_z$ expressions is B/η. The B/η terms at the initial reinforcement angle are 0.0286 and 0.0319 for the $\dot{\varepsilon}_t$ and $\dot{\varepsilon}_z$ trends, respectively — a difference of 11%.

The theoretical neutral angle (θ_N) is geometry and load-dependent, and is not necessarily $\theta_N^* = 54.7°$, as derived for thin-walled pressure vessels. Effective strain rate, $\dot{\varepsilon}_{eff}$, is evaluated in order to consider the collective effect of the multiaxial strains presented in Fig. 6. The optimum reinforcement angle (θ_{min}) is determined to be at the point where this effective strain rate is minimized, and is expected to approach θ_N^* as $t/r_i \to 0.05$.

Using Eq. (10) to combine the fitted trigonometric functions from Fig. 6, a plot of effective strain rate is generated, Fig. 7, from which an optimum reinforcement angle can be predicted where multiaxial creep rates are minimized. Additionally, this plot reveals the nature of multiaxial strain behaviour away from the neutral angle, which to the authors' knowledge is previously unseen in the literature. Vertical error bars for the effective creep rate data are determined from propagation of uncertainty from each of the creep rate components, which are reflective of variation in repeated tests.

Applying the trigonometric trend line formulae for the tangential and longitudinal fits to Eqs. (10) and (12) reveals the relationship between effective strain rate and reinforcement angle as:

$$\dot{\varepsilon}_{eff} = \begin{cases} \frac{\sqrt{2}}{3}\sqrt{0.0029\sin^2\theta - 0.0025\sin\theta - 0.0053\cos^2\theta + 0.0036\frac{\cos^2\theta}{\tan^2\theta} + 0.0014\frac{\cos\theta}{\tan\theta} + 0.0007} & \text{if } \theta < 54.7° \\ \frac{\sqrt{2}}{3}\sqrt{0.0112\frac{\cos^2\theta}{\tan^2\theta} - 0.0112\frac{\cos\theta}{\tan\theta} + 0.0028} & \text{if } \theta \geq 54.7° \end{cases} \quad (13)$$

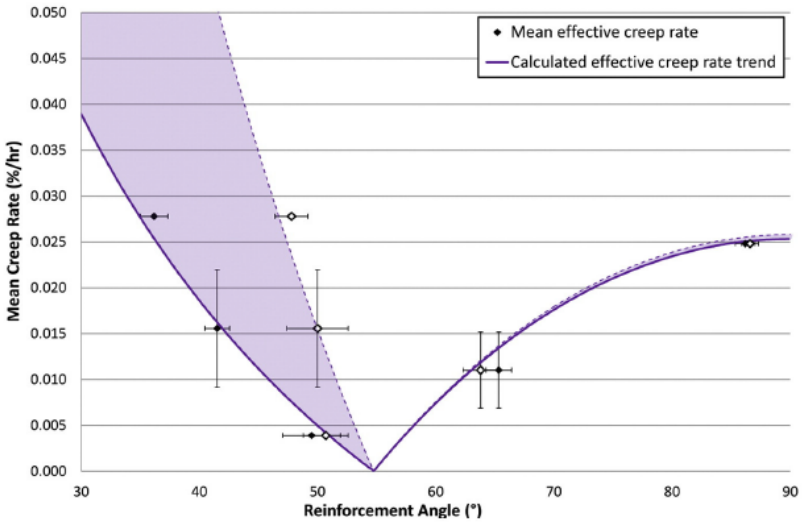

Fig. 7. Calculated mean effective creep rates plotted against initial reinforcement angle (solid points) and final angle (unfilled points). Shaded bands cover range of predicted behaviour from initial angle (lower band) to final angle at t = 820 h or failure (upper band).

A minimum effective strain rate is found at a reinforcement angle of $\theta_{min} = 54.7 \pm 1.5°$, with uncertainty based on typical variation in the measured braid angles. From observation of Fig. 6, the location of this minima in the multiaxial curve is entirely expected as all three directional creep rate curves reach zero strain at approximately $\theta = 54.7°$. The final effective creep rate curve, generated by combining fitted trends, has a coefficient of determination of $R^2 = 0.976$ using initial angle values. In this instance, θ_{min} appears to be equal to θ_N^*, suggesting that the hybrid pipe behaves as a thin-walled pressure vessel despite not meeting the $t/r_i < 0.05$ criterion. As designed, the stress-bearing component of the hybrid pipe is the reinforcement layer and the pipe effectively acts as a shell that transmits load to the reinforcement.

By magnitude, creep in the radial direction is the smallest contributor to the effective creep rate, particularly for $\theta < \theta_{min}$, where measurements of radial creep rate are an order of magnitude lower than those for the tangential and longitudinal directions. Referring to Fig. 6, measured values of $\dot{\varepsilon}_r$ are consistently lower than expected for $\theta < \theta_{min}$. Because of the much smaller initial length scale, the error associated with radial strain measurement is proportionally much higher than the errors in the longitudinal and tangential directions. For the mean reinforcement angle trend, the absolute difference between measured and calculated strains in the radial direction lies in the range of 7–54 μm.

In the as-received condition, wall-thickness was found to only have a 0.4% standard deviation (on the order of 5 μm), suggesting it was not a significant contributor to variations in repeated tests. For diffusional creep, creep rate is proportional to $1/d^m$ where d is grain size and m is a constant typically between 2 and 3[38]. Neglecting twin boundaries, the as-received grain size was determined to be 18.3 ± 3.2 μm, a variation of approximately 17%.

The F-50° sample has an effective strain rate of $\dot{\varepsilon}_{eff} = 4.06 \times 10^{-3}$%/h. By comparison, the average unreinforced control test has an effective strain rate of 0.190%/h, a reduction of creep rate by a factor of 47. The predicted effective strain rate at the optimum braid angle of θ_{min} is calculated to reduce creep rate by a factor of over 3500, increasing the creep life from 83 h to almost 300,000 h and essentially negating creep as the primary mode of failure.

The effective creep rate modelled in Fig. 7 changes significantly with deviation from the optimum angle. For example, a 2° deviation leads to a 40–60× increase in the effective creep rate. However, it should be noted that when the braid seeks to obtain this optimum angle, this elevated creep rate reduces as net stress is reduced and the braid approaches a position of force equilibrium.

The empirically derived neutral angle of $\theta_{min} = 54.7 \pm 1.5°$ in the present case is consistent with the theoretical neutral angle of 54.7° for a thin-walled pressure vessel, predicted to give zero net stress and thus eliminate the driving force for creep deformation. The observed location and magnitude of this minimum is consistent with literature and modelling. The generated trends have a strong physical basis related to the trigonometric relationship between stress and reinforcement angle, and conform closely to the experimental data points. The shape of the $\dot{\varepsilon}_{eff} - \theta$ curve, as well as knowledge of the change in θ towards θ_N in creep applications, but only for $\theta < \theta_N$ when the reinforcement is unbonded, are unique observations with significant implications for industry when considering manufacturing guidelines and tolerances for braids.

The focus of the present study was to explore the relationship between creep rate and braid angle over a wide range of braid angles. Measured mean creep rates in Figs. 6 and 7 have been plotted against the mean braid angle. From Table 3, it can be seen that during testing, the braid orientation shifts towards the optimum angle for initial angles below θ_N. Therefore, it is expected that the majority of creep deformation happens early in the test, while the braid angle is at its furthest from θ_{min}. As this deformation permits the shifting of the braid towards the optimum angle, it is theorized that the creep rate drops as the braid angle shifts. This theory is supported by instantaneous creep rate and reinforcement angle information collected during periodically interrupted testing, with a clear decrease in creep rate observed in Fig. 6 as the F-42° sample tends to an angle of 50° after 820 h. The time-dependent behaviour of the braid angle and its relationship with the creep rate is a concept that will be further explored via in-situ longitudinal strain measurement.

Work following the present study is intended to provide considerable gains in the creep rupture life of stainless steels and nickel-based superalloys, materials commonly used in high temperature piping applications (1173 K and above). In order to apply the findings of this reinforcement architecture optimization study with a model system to a truly high temperature application, a tungsten/stainless steel system was tested. A tungsten braid was manufactured with a 53° braid angle – as close as possible to the empirical optimum of 54.7 ± 1.5° – and used to reinforce a Ø37.5 mm 253MA pipe with a 1.5 mm wall thickness. To combat oxidation of the reinforcement, a second 253MA sheath pipe was fitted concentrically and welded in place, as shown in Fig. 8.

This high temperature hybrid pipe was tested at 1313 K with 5 MPa argon, giving a von Mises equivalent stress of 22 MPa. This was designed to be an acceleration of typical steam methane reformer furnace conditions, while maintaining the diffusional creep mechanism seen in industry.

In order to compare this high temperature system with the previously tested model system, and assess the validity of applying the findings of the reinforcement architecture optimization study, it is useful to compare stiffness (E), thermal expansion (α), test temperatures and melting points for each material system, Table 4. The single most important factor in the success of the reinforcement is its melting point relative to the test temperature. It is imperative that the reinforcement material does not undergo creep. In order to effectively restrain the pipe, it is also important that the reinforcement material has a relatively high stiffness compared to the pipe material. Thermal expansion characteristics are predicted to influence the nature by which the reinforcement first engages the pipe, and how rapidly creep strains are halted. However, the stiffness and thermal expansion characteristics of the reinforcement layer are complicated by the braid geometry, which does not behave as a monolithic material.

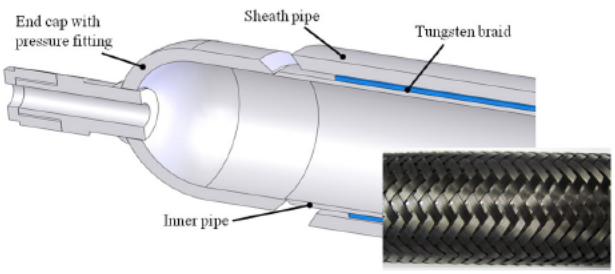

Fig. 8. High temperature hybrid tube sectional schematic. Inset: 53° tungsten braid configuration.

Table 4
Comparison between reinforcement effectiveness in low and high temperature materials systems.

Material system	Reinforcement/liner ratio		$T_{test}/T_{M,\ reinf}$
	E (GPa)	α (μm/m °C)	
SS/brass	1.84	0.8–0.9	0.28
W/253MA	2.0	0.24	0.31

At 1313 K with 5 MPa of internal pressure, an unreinforced 253MA control pipe ruptured after 1.6 h. A hybrid prototype of equivalent size was tested for 500 h (309-times life extension), exhibiting no measurable tangential or longitudinal strain, thereby proving the hybrid pipe concept at high temperatures with a braided refractory reinforcement layer.

As expected, examination of the interface between the inner pipe and the tungsten reinforcement revealed 12–20 μm layers of Fe_7W_6 and CrW. Under long-term service and temperature cycling, interfacial intermetallics will eventually lead to failure of the reinforcement. For implementation in an industrial application these issues will need to be addressed and are the focus of on-going investigation by the present authors.

As shown in Eq. (1), the tangential/longitudinal stress ratio influences the neutral angle for a given pipe geometry. Therefore, designing an effective reinforcement layer for a hybrid pipe requires analysis of the specific application. In some industrial applications, resultant stresses are not solely the result of internal pressure. It is useful to consider how a change in stress state affects the optimal reinforcement angle. For example, in an ethylene cracking furnace, internal pressure is sufficiently low that creep of ethylene pyrolysis tubes is driven primarily by self weight. Using nominal tube dimensions of an 80 mm outer diameter, 8 mm wall thickness and an 20 m length, as well as a typical internal pressure of 0.5 MPa [39] gives pressure stresses of $\sigma_t = 1.8–2.3$ MPa and $\sigma_z = 0.9$ MPa as well as a maximum longitudinal self weight stress of $\sigma_{sw} = 1.5$ MPa. Superimposing longitudinal stresses gives a tangential/longitudinal stress ratio of 0.74–0.95, with a corresponding neutral angle of 41–44°. Utilizing a volume-average tangential/longitudinal stress ratio is recommended to calculate the optimal θ for use as a design guide.

4. Summary and conclusions

A hybrid metallic pipe design was conceived to reduce or eliminate creep in high temperature applications (1173 K and above). A model system (brass reinforced with austenitic stainless steel braid/wires) was selected to determine the effects of varying braid/wire angles.

Pipes reinforced with helical windings obtain approximately 8-times creep life extension compared to unreinforced pipes of the same dimensions. While pressurized unreinforced pipes normally fail through cracking in the longitudinal direction due to tangential stress, helical reinforcement shifts the failure mode to cracking in the tangential direction due to longitudinal stress.

When a braided architecture is employed, creep strains in both the tangential and longitudinal directions can be controlled. A simple analytical model predicts a neutral angle of 54.7°, at which both tangential and longitudinal creep strain rates are zero in thin-walled pressure vessels. In the model material system, an optimal braid angle was empirically determined to be $54.7 \pm 1.5°$. In the present case, for a model materials prototype with braid reinforcement angle of 50°, creep life extensions in excess of 10-times were observed without rupture, and a reduction in creep rate in excess of 45-times was measured. Understanding the effects of varying braid angle on performance in metallic pipes is critical, since the precise optimum angle will be difficult to manufacture in industrial applications. Furthermore, hybrid architecture can be designed with specific braid angles to offset any combination of self-weight and internal pressure.

The shape of the $\dot{\varepsilon}_{eff} - \theta$ curve, as well as knowledge of the change in θ towards θ_N in creep applications, but only for $\theta < \theta_N$ when the reinforcement is unbonded, are unique observations with significant implications for industry when considering manufacturing guidelines and tolerances for braids. A 2° deviation in the initial angle is predicted to cause a 40–60× increase in the effective creep rate. However, it should be noted that the braid is constantly shifting to seek θ_N if the initial θ value is less than θ_N, and this elevated creep rate would be short lived as the braid approaches a position of force equilibrium and the rate of reduction of creep rate follows Eq. (13), dropping rapidly for angles near θ_N. For an initial angle of 42°, this shift towards the neutral angle resulted in the instantaneous creep rate dropping from 170% of the mean creep rate to 60% of the mean creep rate over 820 h, when the final angle was measured to be 50°. As seen in Table 3, the braid angle typically varies by 1–2.5°. Assuming a similar level of control during production, it would be advisable to produce a braid slightly below the neutral angle, so that it is able to tend to θ_N during service.

The optimized architecture is directly applicable to any hybrid materials system, as long as the reinforcement is able to be braided and has substantially greater creep resistance than the pipe material. The present results show potential for high temperature industrial applications: a hybrid materials prototype (253MA stainless steel sheath/liner with tungsten-braid reinforcement oriented at 53°) survived 500 h at 1313 K and 5 MPa internal pressure, with no evidence of creep strain and greater than 300-times creep life compared to unreinforced 253MA pipes tested under the same conditions. The success of this prototype suggests that relatively low cost/creep performance stainless steel pipes can be reinforced with refractory metals for greatly improved creep resistance over monolithic materials. For further progress in high temperature applications, intermetallic growth and oxidation must be addressed through continued development.

Acknowledgements

The authors recognize the generous financial support of Schmidt-Clemens (Spain) S.A.U (UC Grant Number E5789).

References

[1] Z. Huda, P. Edi, Materials selection in design of structures and engines of supersonic aircrafts: a review, Mater. Des. 46 (2013) 552–560.
[2] Q. Lu, W. Xu, S. Van Der Zwaag, Computational design of precipitation strengthened austenitic heat-resistant steels, Philos. Mag. 93 (2013) 3391–3412.
[3] J.A. Lemberg, R.O. Ritchie, Mo–Si–B alloys for ultrahigh-temperature structural applications, Adv. Mater. 24 (2012) 3445–3480.
[4] R.A. MacKay, T.P. Gabb, A. Garg, R.B. Rogers, M.V. Nathal, Influence of composition on microstructural parameters of single crystal nickel-base superalloys, Mater. Charact. 70 (2012) 83–100.
[5] V. Javaheri, F. Shahri, M. Mohammadnezhad, M. Tamizifar, M. Naseri, The effect of Nb and Ti on structure and mechanical properties of 12Ni–25Cr–0.4C austenitic heat-resistant steel after aging at 900 °C for 1000 h, J. Mater. Eng. Perform. 23 (2014) 3558–3566.
[6] M. Ashby, Designing architectured materials, Scr. Mater. 68 (2013) 4–7.
[7] L. Srikanth, R.M.V.G.K. Rao, Strength and stiffness behaviour of braided and filament wound glass epoxy composites – simultaneous studies and comparison, J. Compos. Mater. (2013) 1–8.
[8] T. Safford, Plastics in pressure pipes, in: R. Dobley (Ed.), Rapra Review Reports, Rapra Technology Ltd, Shropshire, UK, 1998.
[9] C.W. Evans, Hose Technology, 2nd ed. Applied Science Publishers Ltd, London, UK, 1979.

[10] J.L. VanLeeuwen, W.M. Kier, Functional design of tentacles in squid: linking sarcomere ultrastructure to gross morphological dynamics, Philos. Trans. R. Soc. Lond. B 352 (1997) 551–571.
[11] R. Tiwari, M.A. Meller, K.B. Wajcs, C. Moses, I. Reveles, E. Garcia, Hydraulic artificial muscles, J. Intell. Mater. Syst. Struct. 23 (2012) 301–312.
[12] C. Laschi, M. Cianchetti, B. Mazzolai, L. Margheri, M. Follador, P. Dario, Soft robot arm inspired by the octopus, Adv. Robot. 26 (2012) 709–727.
[13] G. Frommeyer, R. Rablbauer, High temperature materials based on the intermetallic compound NiAl reinforced by refractory metals for advanced energy conversion technologies, Steel Res. Int. 79 (2008) 507–513.
[14] D.W. Petrasek, R.H. Titran, Creep Behaviour of Tungsten/Niobium and Tungsten/Niobium—1 Percent Zirconium Composites. Fifth Symposium on Space Nuclear Power Systems, NASA Lewis Research Center, Albuquerque, New Mexico, 1988.
[15] B.A. Pint, J.R. DiStefano, I.G. Wright, Oxidation resistance: one barrier to moving beyond Ni-based superalloys, Mater. Sci. Eng. A (2006) 255–263.
[16] D.N. Robinson, W.K. Binienda, M. Miti-Kavuma, Creep and creep rupture of metallic composites, J. Eng. Mech. 118 (1992) 1646–1660.
[17] J.R. Stephens, D.W. Petrasek, R.H. Titran, Refractory Metal Alloys and Composites for Space Power Systems. Spring Meetings of the Materials Research Society, NASA Lewis Research Center, Reno, Nevada, 1988.
[18] R.H. Titran, T.L. Grobstein, Advanced refractory metals and composites for extraterrestrial power systems, JOM 42 (1990) 8–10.
[19] T. Grobstein, H.M. Yun, The role of the interface in refractory metal alloy composites, Am. Inst. Phys. (1991) 186–192.
[20] D. Young, High Temperature Oxidation and Corrosion of Metals, Elsevier, Great Britain, 2008.
[21] M.V. Kral, C.K.H. Dharan, Improved Tubes for High Temperature Industrial Application and Methods for Producing Same, 2009.
[22] U. Andersson, Which Factors Control the Lifetime of Plastic Pipes and how the Lifetime can be Extrapolated, Plastic Pipes XII, Munchen, Germany, 2001.
[23] Z.W. Guan, J.C. Boot, Creep analysis of polymeric pipes under internal pressure, Polym. Eng. Sci. 41 (2001) 955–961.
[24] R.J. Browne, Creep rupture testing of tubular model components, in: D.J. Gooch (Ed.), Techniques for Multiaxial Creep Testing, Elsevier Applied Science Publishers Ltd 1986, pp. 311–332.
[25] S. McAllister, R.C. Hurst, T.E. Chung, Modelling the multiaxial creep behaviour of alloy 800H, Int. J. Press. Vessel. Pip. 47 (1991) 355–370.
[26] T. Mitsueda, K. Fujii, S. Ohnuki, Comparison of Creep Damage Appearances Among Low Alloy Steel Pipes. Creep and Fatigue and Elevated Temperatures 8, ASME, San Antonio, Texas, 2007.
[27] S. Arsene, J. Bai, A new approach to measuring transverse properties of structural tubing by a ring test, J. Test. Eval. 24 (1996) 386–391.
[28] J.E. Shigley, R.G. Budynas, J.K. Nisbett, Mechanical Engineering Design, 10th ed. McGraw-Hill Education, New York, NY, 2015.
[29] AustralWrightMetals, Metal Alloys — Properties and Application of Brass and Brass Alloys, 2013.
[30] A.P. Miodownik, Phase diagrams of binary copper alloys, in: P.R. Subramanian, D.E. Laughlin (Eds.),ASM International 1994, pp. 487–496.
[31] W.J. Evans, B. Wilshire, The high temperature creep and fracture behaviour of 70–30 alpha-brass, Metall. Trans. 1 (1970) 2133–2139.
[32] J. Byun, The analytical characterization of 2-D braided textile composites, Compos. Sci. Technol. 60 (2000) 705–716.
[33] S.N. Gundarev, A.F. Gurov, V.V. Dement'ev, A.S. Demidov, A.E. Rusanov, A.A. Khomyakov, High-temperature creep tests on specimens of single crystal molybdenum with a complex stress state, Probl. Prochn. 22 (7) (1990) 1012–1015.
[34] I. Nonaka, T. Ito, F. Takemasa, K. Saitou, Y. Miyachi, A. Fujita, Full size internal pressure creep test for welded P91 hot reheat elbow, Int. J. Press. Vessel. Pip. 84 (2007) 97–103.
[35] ASTM, E139-11 Standard Test Methods for Conducting Creep, Creep-Rupture, and Stress-Rupture Tests of Metallic Materials, 2011.
[36] J. Lee, R.C. Bradshaw, R.W. Hyers, J.R. Rogers, T.J. Rathz, J.J. Wall, et al., Non-contact measurement of creep resistance of ultra-high-temperature materials, Mater. Sci. Eng. A 463 (2007) 185–196.
[37] T. Hunt, N. Vaughan, The Hydraulic Handbook, 9th ed. Elsevier Advanced Technology, Oxford, UK, 1996.
[38] N.E. Dowling, Mechanical Behaviour of Materials, 4th ed. Person Prentice Hall, Boston MA, 2013.
[39] H. Zimmermann, R. Walzi, Ullmann's Encyclopedia of Industrial Chemistry, John Wiley and Sons, Inc., Ethylene, 2009..